Optimal Vehicle Dynamics Control and State Estimation for a Low-Cost GNSS-based Collision Avoidance System

Von der Fakultät für Maschinenwesen der Rheinisch-Westfälischen Technischen Hochschule Aachen zur Erlangung des akademischen Grades eines Doktors der Ingenieurwissenschaften genehmigte Dissertation

vorgelegt von
Alexander Katriniok

Berichter: Univ.-Prof. Dr.-Ing. Dirk Abel
Prof. Dr.-Ing. habil. Ansgar Trächtler

Tag der mündlichen Prüfung: 24. Oktober 2013

Diese Dissertation ist auf den Internetseiten der Hochschulbibliothek online verfügbar.

Fortschritt-Berichte VDI

Reihe 8

Mess-, Steuerungs- und Regelungstechnik

Dipl.-Inf. Alexander Katriniok, Aachen

Nr. 1230

Optimal Vehicle Dynamics Control and State Estimation for a Low-Cost GNSS-based Collision Avoidance System

BERICHTE AUS DEM INSTITUT FÜR REGELUNGSTECHNIK RWTH AACHEN

Katriniok, Alexander
Optimal Vehicle Dynamics Control and State Estimation for a Low-Cost GNSS-based Collision Avoidance System
Fortschr.-Ber. VDI Reihe 8 Nr. 1230. Düsseldorf: VDI Verlag 2014.
208 Seiten, 65 Bilder, 14 Tabellen.
ISBN 978-3-18-523008-0, ISSN 0178-9546,
€ 71,00/ VDI-Mitgliederpreis € 63,90.

Keywords: Collision avoidance – Autonomous vehicle guidance – Intelligent transportation systems – Navigation systems – Vehicle state estimation – Vehicle dynamics control – Optimal control – Adaptive control – Model predictive control – Adaptive estimation

This dissertation deals with the investigation and experimental evaluation of a concept for conducting autonomous evasion maneuvers in the context of a global navigation satellite system (GNSS) based automotive collision avoidance system. Thereby, this contribution focuses on the aspects of navigation, vehicle state estimation and vehicle control. The proposed concept is based on a low-cost GNSS receiver while previous publications commonly rely on centimeter-precision navigation systems. As the driver should generally be able to avoid an accident by himself, an autonomous intervention should take place as late as possible. Thus, the presented algorithms have to be designed for the application at high horizontal accelerations and at the limits of vehicle handling respectively. This thesis introduces an appropriate estimation and model predictive control approach to achieve this aim. Finally, experimental results prove the feasibility of the proposed concept.

Bibliographische Information der Deutschen Bibliothek
Die Deutsche Bibliothek verzeichnet diese Publikation in der Deutschen Nationalbibliographie; detaillierte bibliographische Daten sind im Internet unter http://dnb.ddb.de abrufbar.

Bibliographic information published by the Deutsche Bibliothek
(German National Library)
The Deutsche Bibliothek lists this publication in the Deutsche Nationalbibliographie (German National Bibliography); detailed bibliographic data is available via Internet at http://dnb.ddb.de.

D 82 (Diss. RWTH Aachen University, 2013)

ISSN 0178-9546
ISBN 978-3-18-523008-0

Preface

The research results of this dissertation have been gained during my time as research associate in the automotive control group at the Institute of Automatic Control of RWTH Aachen University. Thereby, the project *Galileo above* which has been funded by the Federal Ministry of Economics and Technology has been the background of my research activities. In the context of this project, my work focused on the investigation, implementation and experimental evaluation of an automotive collision avoidance system which is based on global navigation satellite systems (GNSS).

I would like to thank my supervisor Univ.-Prof. Dr.-Ing. Dirk Abel for the support of my thesis and the opportunity to work on such an exciting research project. Furthermore, I thankfully appreciate Prof. Dr.-Ing. habil. Ansgar Trächtler's willingness to act as my co-supervisor, his interest in my thesis as well as his valuable feedback regarding my work. Finally, I would like to express my gratitude to Univ.-Prof. Dr.-Ing. Lutz Eckstein and Univ.-Prof. em. Dr.-Ing. Heinrich Rake for being part of the examination board.

For the excellent research cooperation I would like to express my appreciation and thanks to the Institute of Automotive Engineering (ika) of RWTH Aachen University, especially to Univ.-Prof. Dr.-Ing. Lutz Eckstein, Fréderic Christen and the numerous student assistants who had to bear lots of evasion maneuvers to finally determine an appropriate parameter setup. This cooperation and support allowed to us to successfully finish the research work and experimentally evaluate the algorithms we have developed so far.

Furthermore, I would like to thank my colleagues at the Institute of Automatic Control, especially Dr.-Ing. Jan P. Maschuw, René Rütters and Thivaharan Albin for several valuable discussions regarding my research work. I also truly enjoyed numerous jogging tours during the lunch brakes and after work together with Frank Schrödel, Thomas

Lammersen and Felix Nolteernsting. These tours enabled me to clear my mind and get new energy and ideas for my daily (research) work. I also greatly appreciate that my friends made me forget work in my spare time.

Especially, I would like to express my appreciation and thanks to my parents who have always supported me in all concerns during my entire education and thus enabled me to come that far. Likewise, I would like to thank my girlfriend Martina by heart for her lovely and unconditional support and her patience during the stressful time of writing the dissertation.

Aachen, January 2014. Alexander Katriniok

Contents

Abstract

The context of this dissertation is the investigation and experimental evaluation of a global navigation satellite system (GNSS) based automotive collision avoidance system in the scope of the project *Galileo above*. While the application of collision avoidance comprises a variety of research topics, this thesis focuses on the issues of navigation, vehicle state estimation and vehicle guidance at the handling limits. The main aim of this thesis is to investigate and implement a concept for conducting autonomous evasion maneuvers based on a low-cost GNSS receiver (absolute horizontal position accuracy of about 4 m) and inertial sensors. In previous publications, centimeter-precision high-cost navigation systems (absolute horizontal position accuracy in the centimeter range) have commonly been employed for this purpose.

To solve the navigation task, a navigation concept based on relative positioning is introduced that is appropriate for evasion maneuvers having high horizontal accelerations greater than $7\,\mathrm{m/s^2}$. Vehicle state estimation is related to determining key drive dynamic vehicle states (especially the longitudinal and lateral velocity at the center of gravity) which can generally not be measured using series production sensors but are required for the considered control concept. The estimator is designed in such a way that these vehicle states can be determined appropriately even at the handling limits. Furthermore, the concept allows for being adaptive with respect to uncertainties in the tire-road contact. As the evasion path respectively trajectory is considered to be given over a finite time horizon and physical constraints like actuator limitations and the tire-road friction limit are taken into account, a model predictive control scheme is employed to guide the vehicle autonomously. Besides the discussion of the proposed algorithms, experimental results are presented and evaluated.

Zusammenfassung

Der Kontext dieser wissenschaftlichen Arbeit ist die Erforschung und experimentelle Evaluierung eines auf einem Satellitennavigationssystem (GNSS, Global Navigation Satellite System) basierendem Kollisionsvermeidungssystem für Personenkraftwagen im Rahmen des öffentlich geförderten Forschungsprojekts *Galileo above*. Während die Kollisionsvermeidung eine Vielzahl an Forschungsthemen umfasst, fokussiert sich die vorliegende Dissertation dabei auf die Schwerpunkte der Navigation, Fahrzustandsschätzung und Fahrzeugführung im fahrdynamischen Grenzbereich. Ziel der wissenschaftlichen Arbeit ist dabei, autonome Ausweichmanöver auf Basis eines low-cost GNSS-Empfängers (absolute horizontale Positionsgenauigkeit von ca. 4 m) und Inertialsensorik darstellen zu können. In Vorarbeiten kommen dagegen meist hochgenaue, kostenintensive Navigationssysteme (absolute horizontale Positionsgenauigkeit im Bereich weniger Zentimeter) zum Einsatz.

Zur Lösung der Navigationsaufgabe wird ein Ansatz präsentiert, der auf Basis von Relativpositionierung für Ausweichmanöver mit hohen Horizontalbeschleunigungen von mehr als $7\,\mathrm{m/s^2}$ geeignet ist. Die Fahrzustandsschätzung ermittelt die Fahrzustände (insbesondere die longitudinale und laterale Schwerpunktgeschwindigkeit), die mit konventionellen Sensoren nicht direkt messbar jedoch zur Umsetzung des verwendeten Regelungskonzepts notwendig sind. Der entworfene Schätzer ist dabei so ausgelegt, dass sowohl die fahrdynamischen Größen im Grenzbereich adäquat ermittelt werden als auch eine Adaption an Unsicherheiten im Rad-Straße-Kontakt stattfinden kann. Zur autonomen Fahrzeugführung im Grenzbereich wird ein modellprädiktiver Regelungsansatz verfolgt, da zum einen die Ausweichbahn bzw. -trajektorie a prioi bekannt ist, zum anderen aber auch Aktorbeschränkungen und die Haftreibungsgrenze zwischen Rad und Straße explizit berücksichtigt werden sollen. Neben der Diskussion der methodischen Ansätze werden die erzielten experimentellen Ergebnisse vorgestellt und evaluiert.

1 Introduction

1.1 Motivation

While the number of road fatalities in the European Union (EU) has decreased by about 45% from 2000 to 2010, there are still more than 31.000 people who died in road accidents in 2010, see [7]. For this reason, the European Union (EU) has launched its new road safety programme having the main objective to reduce the number of road fatalities by 50% from 2011 to 2020, see [8]. Passive safety systems like seat belts, airbags or constructive measures, which aim at protecting the vehicle occupants from serious injuries when an accident is going to happen, are already part of almost each vehicle. Therefore, the European road safety programme 2010 puts a special emphasis on advanced driver assistance systems (ADAS) respectively active safety systems (a subclass of ADAS) that actively support the driver in preventing accidents and are thus supposed to be able to significantly contribute to further reduce the number of road fatalities.

Focusing on Germany, Figure 1.1 illustrates that the absolute number of road fatalities shows a declining trend since the 1970s while the number of road vehicles has increased by more than 200% simultaneously. Besides passive safety systems, especially the introduction of active safety systems like anti-lock braking systems (ABS) in the late 1970s or electronic stability controls (ESC) in 1995, which are employed to stabilize the ego-vehicle (i.e. the vehicle under consideration that employs the active safety system) in critical driving situations, has made this trend possible, see [10]. In the last decade, ADAS like lane departure warning (LDW) or lane keeping support (LKS) systems that warn the driver from leaving the lane respectively intervene by steering back into the lane have been implemented in new vehicles. As statistics in [9] show that more than 60% of all road accidents in Germany are caused by collisions between vehicles, collision warning (CW), collision mitigation

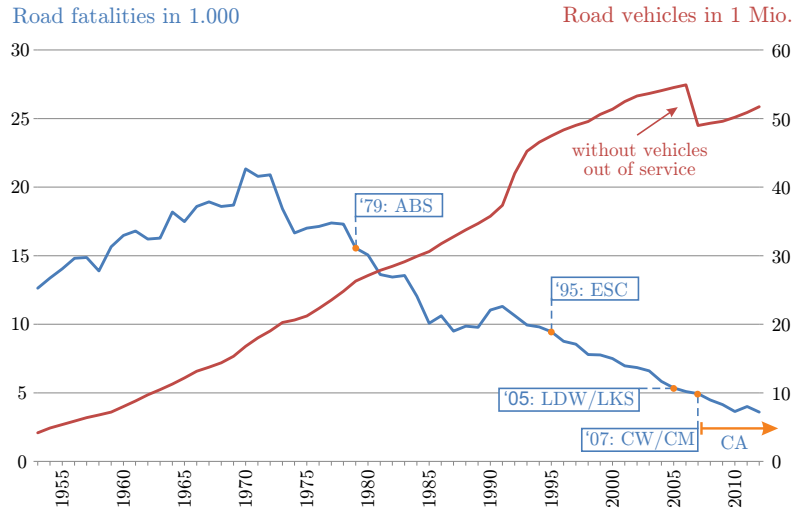

Figure 1.1: Road fatalities and road vehicles in Germany along with the introduction of ADAS from 1953 to 2012 (derived from [9, 10])

(CM) and even collision avoidance (CA) systems are currently focused to improve road safety. These systems that warn the driver and intervene by partial or full braking maneuvers when an accident is imminent have already been implemented in modern passenger vehicles in recent years. ADAS that even conduct autonomous evasion maneuvers are currently still in conflict with the Vienna Convention on Road Traffic 1968 which claims that the driver has always full supervision of the vehicle. Nonetheless, these ADAS are part of several research projects, see e.g. [1] and [10], which contribute to the development of new innovative ADAS.

In order to be generally capable of avoiding road accidents by warning the driver or even by autonomous interventions, a reliable knowledge of the ego-vehicle's position relative to its environment is essential. Contrarily, the development of innovative ADAS is often restricted by the limited detection range and the limited usability of commonly employed, cost-optimized sensors (e.g. camera, LiDAR or radar sensors)

under various environmental conditions. In this regard, a significant improvement can be achieved by the additional use of global navigation satellite systems (GNSS) in combination with digital road maps and vehicle-to-vehicle (V2V) communication, see [11, 12]. When these systems complement each other, accuracy, reliability as well as availability can significantly be improved and the detection range decisively be extended.

Motivated by the improvements that can be gained through GNSS-based ADAS, a GNSS-based CA system has been subject of research at RWTH Aachen University in the scope of the project *Galileo above* which has been funded by the Federal Ministry of Economics and Technology, see [1]. These research activities have been conducted by the Institute of Automatic Control in cooperation with the Institute of Automotive Engineering (ika). The intended behavior of CA is to keep track of the surrounding environment and to perform an autonomous emergency braking or evasion maneuver if the driver does not react appropriately in time. Regarding research topics, the application can basically be subdivided into *sensor fusion* (estimation of relevant ego-vehicle states and the recognition of the surrounding environment), *maneuver coordination* (decision for driver warning, emergency braking or evasive maneuver), *path/trajectory planning* (computation of a feasible, collision-free (time-dependent) evasion path) and *vehicle control* (longitudinal and lateral vehicle guidance at the handling limits along an evasion path/trajectory). This thesis mainly focuses on sensor fusion (regarding the ego-vehicle) and vehicle control issues assuming that an evasion maneuver has to be conducted and the time of intervention as well as the evasion path/trajectory are a priori known. As the CA system is supposed to intervene as late as possible to permit the driver to avoid accidents by himself, these algorithms have to be capable of being applied at the vehicle handling limits. Thus, this contribution deals with a concept for autonomous driving at the handling limits in the context of autonomous evasion maneuvers rather than the entire application of CA. In the following, an overview of the thesis' main contribution is given.

1.2 Aim of the Thesis

The main aim of this thesis is to investigate, implement and experimentally evaluate a concept for GNSS-based autonomous vehicle guidance at the handling limits in the context of autonomous evasion maneuvers using low-cost sensors. Thereby, the term low-cost has to be seen in a research context rather than referring to low-cost series production sensors in automotive industry. In particular low-cost refers to an experimental setup comprising a single antenna, single frequency GNSS receiver, micro-electro-mechanical systems (MEMS) based inertial sensors (i.e. accelerometers and gyroscopes) as well as series production on-board sensors which e.g. provide information on the wheel speeds. In literature, GNSS-based navigation concepts for autonomous vehicle guidance at the handling limits commonly rely on centimeter-precision real-time kinematic Global Positioning System (RTK-GPS) aided navigation systems [13, 14] which are highly cost-intensive. Contrarily, [15] employs series production sensors and proposes to numerically integrate the estimated longitudinal and lateral vehicle velocity with respect to a local maneuver reference frame to obtain a navigation solution without any aiding measurement. This approach, also known as dead reckoning, might suffer from increasing positioning errors in time due to open-loop integration, e.g. a longitudinal or lateral velocity error of just 0.1 m/s causes a systematic position error of 0.5 m for a maneuver having a duration of 5 s.

This thesis demonstrates that autonomous evasion maneuvers at the handling limits are feasible when using a low-cost GNSS, having an absolute horizontal position accuracy of 4.1 m at a 95.4% confidence level (2σ), and a MEMS-based inertial measurement unit (IMU) for navigation purposes. The achievable navigation performance can be seen superior to dead reckoning approaches and as an appropriate alternative to highly cost-intensive navigation systems when considering relative instead of absolute positioning. The entire concept for autonomous evasion maneuvers at the handling limits has not been investigated so far and can be seen as the main contribution of this dissertation. Thereby, the main emphasis of this thesis is put on sensor fusion, i.e. aggregating multiple sensor information in the context of navigation and vehicle

state estimation, and vehicle control algorithms. Consecutively, a brief outline of the main research topics as well as the contribution compared to previous published approaches is given.

Navigation basically deals with the estimation of the ego-vehicle's pose in terms of position, velocity and attitude. As inertial navigation systems (INS) suffer from increasing navigation errors in time due to the open-loop integration of inertial sensors (i.e. accelerometers, gyroscopes) or other motion-sensing devices, this thesis considers an approach that complements an INS with GNSS. In literature, this concept is known as the integration of GNSS and INS or as GNSS/INS integration, see [16]. In this contribution, a linearized Kalman filter [17] based approach that complements a MEMS-based IMU with a low-cost GNSS will be considered. This integration is based on the navigation solution (i.e. position and velocity) provided by the GNSS receiver which is known as loosely coupled GNSS/INS integration, see [16]. To improve the estimated heading, the author proposes to incorporate the GNSS course angle (i.e. the direction of travel) as aiding measurement when driving almost straight. In order to assess the requirements on the navigation solution for autonomous evasion maneuvers, a requirement analysis is carried out. In this context, only relative positioning with respect to the initial maneuver position turns out to be feasible. To fulfill all the specified requirements, an appropriate navigation concept is introduced. The main idea is to calibrate the MEMS-based IMU during normal operation (i.e. to estimate and finally compensate sensor biases) and mainly rely on the calibrated INS during the evasive maneuver. Therefore, the navigation filter is still operated closed-loop to avoid significant sensor drifts but with an appropriately decreased weight on the GNSS measurements.

Vehicle state estimation is related to determining key drive dynamic states such as the yaw rate, the longitudinal and lateral velocity at the center of gravity (CG) which are required to apply the considered vehicle control algorithms. While the yaw rate can generally be measured directly using series production sensors, this is commonly not the case for the vehicle's longitudinal and lateral velocity at CG when not using cost-intensive sensors. Although the navigation filter provides the vehicle's velocity and attitude, its accuracy is not sufficient to derive an appropriate estimate of the longitudinal and lateral velocity at CG,

especially at the vehicle handling limits. Therefore, these states are determined by an additional EKF-based estimator that relies on a dynamic vehicle model. The estimator is designed in such a way that it is capable of adapting the tire model by scaling tire forces to account for uncertainties in the tire-road contact. For the purpose of adaptation, two additional estimator states are introduced. As the estimation problem becomes ill-conditioned when having low excitation, a major contribution can be seen in assessing the local observability as well as handling the loss of observability. Furthermore, the filter employs the horizontal velocity at CG resulting from the navigation filter instead of wheel speeds as aiding measurement. Especially the independence from wheel slip and the achievable accuracy of GNSS-based velocity measurements, e.g. $0.05\,\mathrm{m/s}$ at a 68.3% confidence level (1σ) for the Global Positioning System (GPS) [18], promise a gain in estimation performance. Furthermore, it allows for an improved estimation of further vehicle states like the longitudinal tire slip.

In order to guide the vehicle along an evasion path/trajectory, an appropriate *vehicle control* approach is required. As the evasion path/trajectory is considered to be given over a finite time horizon and physical constraints like actuator limitations and the tire-road friction limit are into account, a model predictive control (MPC) scheme [19, 20] is investigated. In the scope of this thesis, a steering-only path following controller and a steering/braking trajectory following controller will be introduced. Both controllers employ successive linearizations of the nonlinear prediction model, thus obtaining linear time-varying MPC (LTV-MPC) control schemes. While similar LTV-MPC strategies (see e.g. [13]) are not always able to guide and stabilize the vehicle in the nonlinear tire region, both controllers are capable of handling the limits of static friction. For the steering-only controller, the potential of using the vehicle state estimator's adaptation states to adapt the controller's internal plant model as well is studied, thus resulting in an adaptive LTV-MPC control scheme which has not been examined in previous publications. The steering/braking controller is designed in the sense of an integrated vehicle dynamics control approach employing the wheel steering angle and the vehicle's longitudinal deceleration (in contrast to differential braking in [21]) as control inputs. Finally, a disturbance estimator is proposed to compensate steady-state offsets of the lateral

displacement from the evasion path. These steady-state offsets result from orientation errors which act as a ramp disturbance on the controlled output. This issue is mentioned in [13] but has not been solved yet.

To evaluate the sensor fusion as well as vehicle control algorithms outlined above, experimental tests have been carried out. These investigate the real-time capability of the introduced concepts as well as their estimation respectively control performance for maneuvers at the handling limits. Finally, the feasibility of low-cost GNSS-based autonomous driving and thus the interaction of the proposed algorithms is examined.

1.3 Structure

In the following, chapter 2 introduces the basics of vehicle dynamics, tire modeling and relative kinematics of the vehicle and an evasion path. Furthermore, the experimental setup (i.e. the test vehicle and its sensors and actuators) and a survey of the software components that are required for the GNSS-based CA system as well as their potential fields of research are considered. Then, the chapter narrows the survey down to the main focus of GNSS-based autonomous driving at the handling limits. The thesis' main research topics *navigation*, *vehicle state estimation* and *vehicle control* are discussed in chapter 3, 4 and 5. A detailed analysis of experimental vehicle control results is conducted in chapter 6. Finally, this thesis ends up with a conclusion and provides an outlook for future work.

2 Preliminaries

2.1 Vehicle Dynamics and Relative Kinematics

2.1.1 Vehicle Modeling

This section provides a basic introduction to longitudinal and lateral vehicle dynamics, tire modeling as well as relative kinematics of the vehicle and the evasion path. These modeling approaches are required for the purpose of vehicle state estimation and vehicle control. The level of detail for modeling longitudinal and lateral vehicle dynamics ranges from multi-body vehicle models to a simplified single-track model, see [22]. To reduce the computational complexity and to allow for a real-time execution of sensor fusion and vehicle control algorithms, simplified vehicle models like single- or two-track models are applied in the scope of this thesis. These are introduced consecutively.

2.1.1.1 Single-track Model

The single-track model is a simplified approach to describe horizontal vehicle dynamics. In particular, the two tires of an axle are reduced to a single one, thus obtaining a bicycle-like vehicle. In literature, the single-track model does not refer unambiguously to a particular mathematical representation but is commonly used in the scope of lateral vehicle dynamics. Hereafter, it will be employed to model pure lateral as well as combined longitudinal and lateral vehicle dynamics. In this section, a nonlinear single-track model according to [23] is introduced. The corresponding free-body diagram is illustrated in Figure 2.1. In this regard, it is assumed that the height of CG is zero, thus neglecting roll and pitch dynamics, and that rolling resistances, aerodynamic drag as well as road bank and grade are negligible.

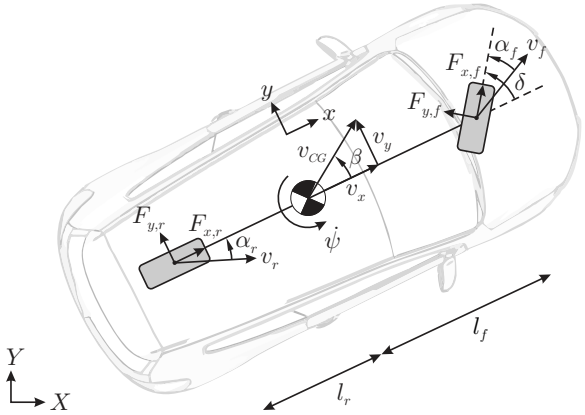

Figure 2.1: Free-body diagram of the single-track model

Newton-Euler equations (2.1)-(2.2) describe the longitudinal and lateral momentum with respect to CG in the vehicle reference frame. Yaw dynamics, i.e. the rotational degree of freedom with respect to the vertical vehicle axis, are modeled by (2.3).

$$m(\dot{v}_x - \dot{\psi} v_y) = F_{x,f}\cos(\delta) + F_{x,r} - F_{y,f}\sin(\delta) \tag{2.1}$$

$$m(\dot{v}_y + \dot{\psi} v_x) = F_{y,f}\cos(\delta) + F_{y,r} + F_{x,f}\sin(\delta) \tag{2.2}$$

$$J_z \ddot{\psi} = \Big(F_{y,f}\cos(\delta) + F_{x,f}\sin(\delta)\Big) l_f - F_{y,r} l_r \tag{2.3}$$

Thereby, v_x denotes the longitudinal velocity at CG, v_y the lateral velocity at CG, $\dot{\psi}$ the yaw rate, δ the wheel steering angle, m the vehicle mass, J_z the mass moment of inertia with respect to the vertical axis and l_f respectively l_r the distance between CG and the front respectively rear axle. Tire forces $F_{x,i}$ and $F_{y,i}$ with $i \in \{f,r\}$ at the front (f) respectively the rear axle (r) are determined using a nonlinear tire model that is introduced in section 2.1.2. In literature, the angle β between the longitudinal and lateral velocity is known as the vehicle sideslip angle

$$\beta = \arctan\left(\frac{v_y}{v_x}\right), \tag{2.4}$$

see [23]. Although this contribution describes vehicle dynamics with respect to v_x and v_y, a formulation in terms of the vehicle sideslip angle β and the horizontal velocity v_{CG} at CG is used in other contributions as well. Furthermore, the reader should be aware that all definitions that are related to vehicle dynamics in the scope of this thesis refer to driving forward.

2.1.1.2 Two-track Model

Due to its simplifications, the single-track model does not allow to account for the tire forces at each wheel. This might result in severe modeling errors, e.g. in situations with different tire-road friction coefficients (i.e. μ-split situations), see [22]. If individual tire forces have to be considered, the two-track model is an appropriate choice. To incorporate load transfer due to steering and braking into the vehicle model, a common approach in literature is to determine the steady-state vertical load at each tire in dependence of the longitudinal and lateral acceleration at CG, see [23]. In this way, vertical vehicle dynamics as well as roll and pitch motion can be neglected, thus simplifying the resulting vehicle model (2.5)-(2.7) which considers three degrees of freedom. As for the single-track model, rolling resistances, aerodynamic drag as well as road bank and grade are considered to be negligible.

$$\begin{aligned} m(\dot{v}_x - \dot{\psi} v_y) &= (F_{x,fl} + F_{x,fr})\cos(\delta) - (F_{y,fl} + F_{y,fr})\sin(\delta) \\ &\quad + F_{x,rl} + F_{x,rr} \end{aligned} \tag{2.5}$$

$$\begin{aligned} m(\dot{v}_y + \dot{\psi} v_x) &= (F_{y,fl} + F_{y,fr})\cos(\delta) + (F_{x,fl} + F_{x,fr})\sin(\delta) \\ &\quad + F_{y,rl} + F_{y,rr} \end{aligned} \tag{2.6}$$

$$\begin{aligned} J_z \ddot{\psi} &= (F_{x,rr} - F_{x,rl})\frac{tw_r}{2} - (F_{y,rl} + F_{y,rr})l_r \\ &\quad + \Big((F_{x,fr} - F_{y,fl})\cos(\delta) + (F_{y,fl} - F_{y,fr})\sin(\delta)\Big)\frac{tw_f}{2} \\ &\quad + \Big((F_{y,fl} + F_{y,fr})\cos(\delta) + (F_{x,fl} + F_{y,fr})\sin(\delta)\Big)l_f \end{aligned} \tag{2.7}$$

Particularly, (2.5)-(2.6) describe the longitudinal and lateral momentum with respect to CG while (2.7) accounts for yaw dynamics. Compared to the single-track model, it can be recognized that the two-track model

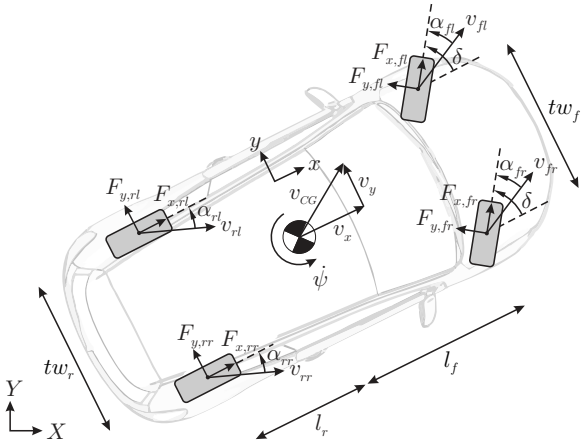

Figure 2.2: Free-body diagram of the two-track model

contains the longitudinal tire forces $F_{x,i}$ and lateral tire forces $F_{y,i}$ with $i \in \{fl,fr,rl,rr\}$ at the front left (fl), front right (fr), rear left (rl) and rear right (rr) wheel. The applied tire model as well as the incorporation of load transfer is outlined in the following. Furthermore, tw_f and tw_r denote the track width at the front and rear axle respectively.

2.1.2 Tire Modeling

2.1.2.1 Longitudinal Slip

Longitudinal and lateral tire forces in (2.1)-(2.3) and (2.5)-(2.7) are obtained through a tire model that is described consecutively. As this tire model relies on the longitudinal slip respectively sideslip, these terms are introduced first. Thereby, longitudinal slip as well as sideslip depend on the wheel velocities v_x^w and v_y^w in the wheel reference frame (x^w, y^w) that has its origin in center of the tire contact patch, see Figure 2.3. In particular, the longitudinal tire slip is defined as the difference of the longitudinal velocity v_x^w of the (actual) wheel (transmitting longitudinal forces) and the longitudinal velocity $v_{x,free}^w$ of the (virtual) free

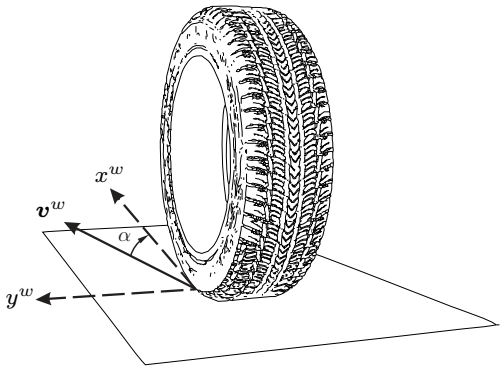

Figure 2.3: Velocities in the wheel reference frame

rolling (passive) wheel, see [23]. This relative velocity results from the longitudinal deformation of the tire patch which causes a sheer stress and thus a longitudinal reaction force. The longitudinal slip ratio λ_i at tire i which is one of the primary quantities to compute longitudinal tire forces can be expressed as

$$\lambda_i = \begin{cases} 1 - \frac{v^w_{x,i,free}}{v^w_{x,i}} & , v^w_{x,i} - v^w_{x,i,free} \geq 0 \text{ (acceleration slip)} \\ \frac{v^w_{x,i}}{v^w_{x,i,free}} - 1 & , v^w_{x,i} - v^w_{x,i,free} < 0 \text{ (braking slip)}, \end{cases} \tag{2.8}$$

while λ_i is positive for accelerating and negative for braking, see [23]. For the two-track model, $v^w_{x,i,free}$ at the front axle can be determined by transferring the velocity vector at CG to the corresponding wheel and rotating the resulting vector to the wheel fixed reference frame, i.e.

$$v^w_{fl/fr,x,free} = (v_x \mp \frac{tw_f}{2}\dot{\psi})\cos(\delta) + (v_y + l_f\dot{\psi})\sin(\delta). \tag{2.9}$$

Likewise, for the velocities of the free rolling wheels at the rear axle holds

$$v^w_{rl/rr,x,free} = v_x \mp \frac{tw_r}{2}\dot{\psi}. \tag{2.10}$$

As these quantities are consecutively not required when using the single-track model, the corresponding velocities are omitted for reasons of clarity.

2.1.2.2 Sideslip

According to [23] and as depicted in Figure 2.3, the tire sideslip angle α is defined as the angle between the velocity vector $\boldsymbol{v}^{w,T} = [v_x^w,\, v_y^w]$ and the longitudinal wheel axis x^w in the wheel reference frame, i.e.

$$\alpha = -\arctan\left(\frac{v_y^w}{v_x^w}\right). \tag{2.11}$$

The sideslip angle results from the deformation of the tire contact patch in the lateral direction. The corresponding shear stress in the tire patch induces the lateral reaction force. Thus, the sideslip angle is one of the primary quantities when modeling tire side forces. In order to be used in the single-track model, the sideslip angles α_f at the front and α_r at the rear axle have to be expressed in dependence of the vehicle states v_x, v_y and $\dot{\psi}$ as well as the wheel steering angle δ, thus yielding

$$\alpha_f = \delta - \arctan\left(\frac{v_y + l_f\dot{\psi}}{v_x}\right), \tag{2.12}$$

$$\alpha_r = -\arctan\left(\frac{v_y - l_r\dot{\psi}}{v_x}\right). \tag{2.13}$$

For the two-track model, these quantities at the front left (fl), front right (fr), rear left (rl) and rear right (rr) tire can be expressed as

$$\alpha_{fl/fr} = \delta - \arctan\left(\frac{v_y + l_f\dot{\psi}}{v_x \mp 0.5 \cdot tw_f\dot{\psi}}\right), \tag{2.14}$$

$$\alpha_{rl/rr} = -\arctan\left(\frac{v_y - l_r\dot{\psi}}{v_x \mp 0.5 \cdot tw_r\dot{\psi}}\right). \tag{2.15}$$

2.1.2.3 Longitudinal Tire Forces

When accounting for vehicle dynamics at the handling limits, a nonlinear tire model describing the longitudinal respectively lateral tire forces in dependence of longitudinal tire slip respectively sideslip is required. Furthermore, the regions of static and sliding friction should be taken into account. In literature, the Pacejka Magic Formula tire model [24]

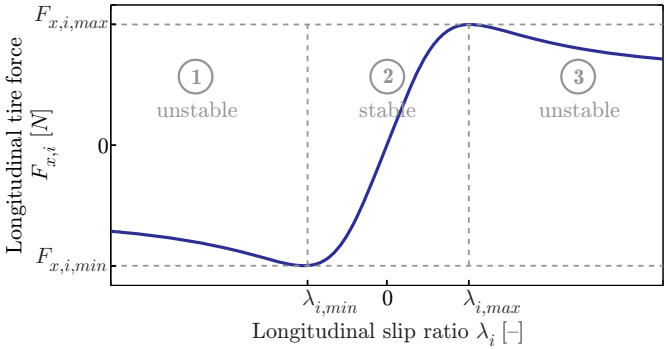

Figure 2.4: Pacejka Magic Formula tire model: Longitudinal tire forces

is frequently employed for this purpose. This semi-empirical tire model describes the steady-state tire force when having pure longitudinal slip respectively pure sideslip. An example of this tire model showing the longitudinal tire force $F_{x,i}$ in dependency on the longitudinal slip ratio λ_i is depicted in Figure 2.4. In particular, region 2 corresponds to the (stable) slip interval of static friction, i.e. an increased longitudinal slip ratio λ_i results in an increased tire force $F_{x,i}$ until a maximum tire force $F_{x,i,max}$ is reached according to Coulomb's law of friction. When increasing the tire slip any further, the tire force decreases as the tire's sheer stress cannot be supported by the road any more. Consequently, the tire enters (unstable) region 3 of sliding friction. The same principle holds for negative values of the longitudinal tire slip.

With regard to [24] and assuming a curve which is point-symmetric with respect to the origin, the longitudinal tire force for pure longitudinal slip, i.e. no lateral forces are applied at the tire, can be expressed as

$$F_{x,i} = D_{x,i} \cdot f_{x,i} \tag{2.16}$$
$$f_{x,i} = \sin[C_{x,i} \arctan\{B_{x,i}\lambda_i - E_{x,i}(B_{x,i}\lambda_i - \arctan(B_{x,i}\lambda_i))\}]$$

where λ_i denotes the longitudinal slip ratio at tire i as introduced in (2.8). Thereby, $B_{x,i}$ influences the curve's slope at the origin, $C_{x,i}$ denotes the shape factor, $D_{x,i}$ the maximum feasible longitudinal tire force and $E_{x,i}$ defines the curvature near the maximum/minimum tire force

$F_{x,i,max/min}$ as well as the maximum/minimum slip ratio $\lambda_{i,max/min}$ itself. Actually, these parameters have to be identified for the particular tire through experimental tests.

Instead of a pure data-driven identification, these parameters have been chosen according to their physical interpretation. $C_{x,i}$ is assigned to 1.65 as it is recommended in [24]. According to Coulomb's law of friction, the maximum tire force is assumed to be proportional to the maximum tire-road friction coefficient μ and the vertical tire load $F_{z,i}$, i.e.

$$D_{x,i} = \mu F_{z,i}. \tag{2.17}$$

While $D_{x,i}$ can vary due to load transfer (see section 2.1.2.6) and a changing friction coefficient, $B_{x,i}$ is determined once in dependence of $D_{x,i,nom}$ (i.e. for the nominal tire load and a nominal friction coefficient) and $C_{x,i}$, i.e.

$$B_{x,i} = \frac{c_{\lambda_i}}{C_{x,i} \cdot D_{x,i,nom}} \tag{2.18}$$

where

$$c_{\lambda_i} = \left. \frac{\partial F_{x,i}}{\partial \lambda_i} \right|_{\lambda_i = 0} \tag{2.19}$$

corresponds to the nominal longitudinal tire stiffness c_{λ_i} for $\lambda_i = 0$, see [23]. Finally, $E_{x,i}$ is calculated in dependence of $\lambda_{i,max}$, i.e.

$$E_{x,i} = \frac{B_{x,i} \cdot \lambda_{i,max} - \tan\left(\frac{\pi}{2C_{x,i}}\right)}{B_{x,i} \cdot \lambda_{i,max} - \arctan(B_{x,i} \cdot \lambda_{i,max})}. \tag{2.20}$$

A good estimate of c_{λ_i} as well as $\lambda_{i,max}$ can be obtained through parameter identification in experimental tests.

2.1.2.4 Lateral Tire Forces

Similar to the computation of longitudinal tire forces, the lateral tire forces at pure cornering, i.e. no longitudinal forces are applied at the tire, are obtained using the Pacejka tire model. Figure 2.5 depicts an

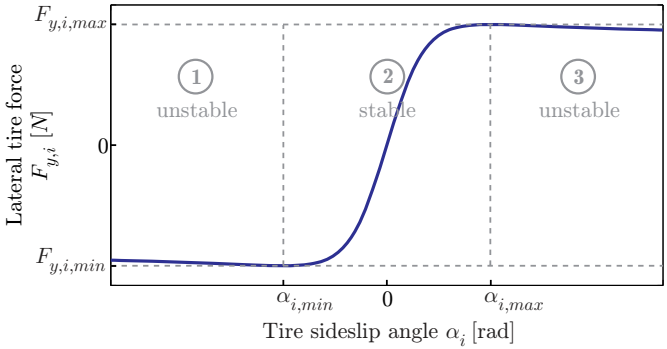

Figure 2.5: Pacejka Magic Formula tire model: Lateral tire forces

example for the lateral tire force $F_{y,i}$ as a nonlinear function of the sideslip angle α_i. Similar to longitudinal tire forces, the same principle of static and sliding friction holds for increasing/decreasing the sideslip angle to a maximum/minimum value $\alpha_{i,max/min}$.

Thus, the lateral tire force at pure cornering can be expressed in dependence of the sideslip angle α_i as

$$\begin{aligned} F_{y,i} &= D_{y,i} \cdot f_{y,i} \\ f_{y,i} &= \sin[C_{y,i} \arctan\{B_{y,i}\alpha_i - E_{y,i}(B_{y,i}\alpha_i - \arctan(B_{y,i}\alpha_i))\}] \end{aligned} \tag{2.21}$$

where $B_{y,i}$, $C_{y,i}$, $D_{y,i}$ and $E_{y,i}$ can be interpreted in the same way as discussed in section 2.1.2.3. As far as the parameterization is concerned, $C_{y,i}$ is set to 1.3 as advised in [24]. Furthermore, the maximum lateral tire force is assigned by applying Coulomb's law of friction, thus yielding

$$D_{y,i} = \mu F_{z,i}. \tag{2.22}$$

With regard to [24], for $B_{y,i}$ holds

$$B_{y,i} = \frac{c_{\alpha_i}}{C_{y,i} \cdot D_{y,i,nom}} \tag{2.23}$$

where $D_{y,i,nom}$ depends on the nominal tire load and friction coefficient and

$$c_{\alpha_i} = \left.\frac{\partial F_{y,i}}{\partial \alpha_i}\right|_{\alpha_i=0} \tag{2.24}$$

denotes the nominal cornering stiffness c_{α_i} for $\alpha_i = 0\,\mathrm{rad}$, see [23]. Finally, $E_{y,i}$ is determined according to (2.20) in dependence of $\alpha_{i,max}$, i.e.

$$E_{y,i} = \frac{B_{y,i} \cdot \alpha_{i,max} - \tan\left(\frac{\pi}{2C_{y,i}}\right)}{B_{y,i} \cdot \alpha_{i,max} - \arctan(B_{y,i} \cdot \alpha_{i,max})}. \tag{2.25}$$

As for the longitudinal tire forces, particular values of c_{α_i} and $\alpha_{i,max/min}$ can been gained in experimental tests.

2.1.2.5 Combined Slip

An extension of the Pacejka tire model that allows for considering combined slip, i.e. the simultaneous transmission of longitudinal and lateral tire forces, is proposed in [24]. As this approach requires additional parameters to be identified, a simplified concept according to [25] is employed in this contribution that is independent from the particular tire model. Thereby, the required model parameters are reduced to a minimum. Let $F_{y,i,0}$ denote the lateral tire force at pure cornering with regard to (2.21). As illustrated in Figure 2.6, the lateral tire force $F_{y,i}$ for combined slip can be determined by reducing $F_{y,i,0}$ depending on the transmission of longitudinal forces in accordance to the friction ellipse, i.e.

$$F_{y,i} = F_{y,i,0}\sqrt{1 - \left(\frac{F_{x,i}}{F_{x,i,max}}\right)^2}. \tag{2.26}$$

If longitudinal tire forces are determined by employing the Pacejka tire model, (2.26) can further be simplified to

$$F_{y,i} = F_{y,i,0}\sqrt{1 - {f_{x,i}}^2} \tag{2.27}$$

as $F_{x,i} = F_{x,i,max} \cdot f_{x,i}$ holds with respect to (2.16).

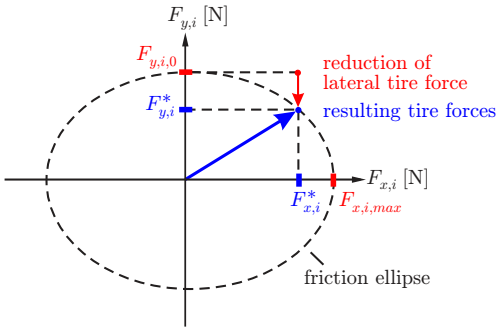

Figure 2.6: Friction ellipse to determine resulting lateral tire force $F^*_{y,i}$ depending on transmitted longitudinal tire force $F^*_{x,i}$

2.1.2.6 Nominal Tire Load and Load Transfer

As previously indicated, the dynamic tire load is determined in dependence of the longitudinal and lateral acceleration at CG. In this way, vertical vehicle dynamics as well as roll and pitch motion can be neglected in the vehicle model. As far as the tire model is concerned, the vertical tire load $F_{z,i}$ defines the Pacejka parameters $D_{x,i}$ and $D_{y,i}$. In the following, the particular computation of $F_{z,i}$ is introduced for the single-track as well as the two-track model.

While roll motion cannot be considered in the single-track model (due to the reduction to a single track), pitch motion is neglected consecutively. Thus, only the nominal tire load $F_{z,i}$ with $i \in \{f,r\}$ at the front and the rear axle is relevant for the subsequent considerations. These quantities are obtained by

$$F_{z,f} = \frac{m \cdot g \cdot l_r}{l_f + l_r}, \quad F_{z,r} = \frac{m \cdot g \cdot l_f}{l_f + l_r} \tag{2.28}$$

where g denotes the gravitational acceleration. On the contrary, load transfer due to steering and braking is incorporated into the two-track model. For this purpose, the actual tire load is approximated by the steady-state tire load in dependence of the measured longitudinal and

lateral acceleration at CG, i.e. a_x and a_y respectively. Thus, for the vertical tire load at tire $i \in \{fl,fr,rl,rr\}$ holds

$$F_{z,fl/fr} = m\left(\frac{l_r}{l}g - \frac{h_{CG}}{l}a_x\right)\left(\frac{1}{2} \mp \frac{h_{CG}}{tw_f \cdot g}a_y\right), \tag{2.29}$$

$$F_{z,rl/rr} = m\left(\frac{l_f}{l}g + \frac{h_{CG}}{l}a_x\right)\left(\frac{1}{2} \mp \frac{h_{CG}}{tw_r \cdot g}a_y\right) \tag{2.30}$$

where h_{CG} indicates the height of CG and $l = l_f + f_r$ the wheelbase. When load transfer due to steering and braking is neglected, i.e. when the longitudinal acceleration a_x and lateral acceleration a_y are assumed to be zero, the nominal tire load can be obtained by

$$F_{z,nom,fl/fr} = \frac{m \cdot g \cdot l_r}{2 \cdot l}, \quad F_{z,nom,rl/rr} = \frac{m \cdot g \cdot l_f}{2 \cdot l}. \tag{2.31}$$

2.1.3 Relative Kinematics of Vehicle and Evasion Path

For autonomous vehicle guidance with respect to an evasion path, relative kinematics of the vehicle and the corresponding path have to be taken into account. Basically, this relative motion can be modeled with respect to the inertial frame [13], relative to the path reference frame [14] and relative to the vehicle's body frame [23]. This thesis focuses on the third concept which is illustrated in Figure 2.7. In particular, the relative rotational and translational movement of the vehicle's CG and the evasion path is described in accordance to [2]. In this regard, the relative yaw rate $\Delta\dot{\psi}$ is defined as the difference of the vehicle's yaw rate $\dot{\psi}$ and the evasion path's yaw rate $\dot{\psi}_{path}$ while the latter can be expressed as the product of the path's curvature κ (which is positive for a left and negative for a right turn) and the vehicle velocity v_{CG} at CG, thus obtaining

$$\begin{aligned} \Delta\dot{\psi} &= \dot{\psi} - \dot{\psi}_{path} \\ &= \dot{\psi} - \kappa \cdot v_{CG} \\ &= \dot{\psi} - \kappa\sqrt{{v_x}^2 + {v_y}^2}. \end{aligned} \tag{2.32}$$

Furthermore, the relative lateral velocity $\Delta\dot{y}$ is defined as the difference of the vehicle's lateral velocity v_y and the corresponding path velocity

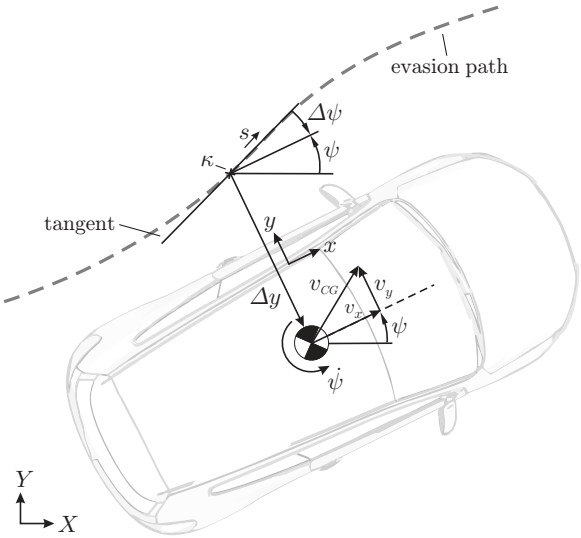

Figure 2.7: Free-body diagram of relative kinematics

$v_{y,path}$ with respect to the vehicle's body frame. The path velocity can be formulated in terms of v_{CG} and the relative yaw angle $\Delta\psi$, i.e.

$$\begin{aligned} \Delta\dot{y} &= v_y - v_{y,path} \\ &= v_y - v_{CG} \cdot \sin(-\Delta\psi) \\ &= v_y + \sqrt{{v_x}^2 + {v_y}^2}\sin(\Delta\psi). \end{aligned} \tag{2.33}$$

These two equations of motion are sufficient to fully describe relative kinematics of the vehicle's CG and the corresponding evasion path in the horizontal plane.

2.2 Experimental Setup

This section provides an overview of the experimental setup that is especially used for autonomous evasion maneuvers, assuming that the

decision for an intervention and the evasion path/trajectory is a priori known, instead of the entire application of CA. Particularly, a Volkswagen Passat CC 3.6 V6 which has been provided by the Institute of Automotive Engineering (ika) of RWTH Aachen University is employed as test vehicle, see Figure 2.8. To conduct autonomous steering interventions the vehicle is equipped with an electric power steering (EPS) system that allows for demanding a wheel steering angle. Furthermore, a brake booster that permits full braking maneuvers has been implemented in the vehicle such that even combined steering and braking interventions are feasible. In this section, the employed sensor and actuator setup is outlined in detail. Moreover, the physical interconnection of sensors, actuators and electronic control units (ECU) is presented.

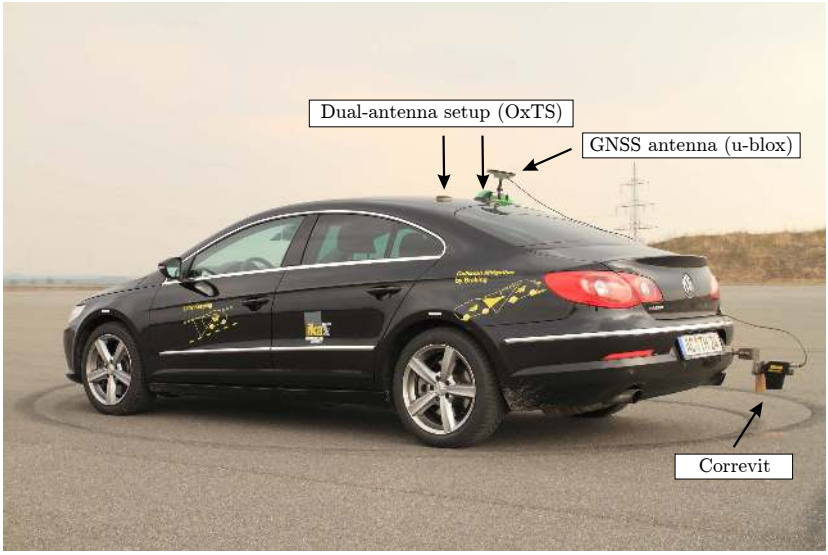

Figure 2.8: Volkswagen Passat CC 3.6 V6 test vehicle

2.2.1 Sensors

A basic overview of the employed setup is given in Table 2.1, classifying the sensors into standard sensors (STD), which are used to implement the algorithms that have been outlined in section 1.2, and reference sensors (REF), which are applied to validate these algorithms. Consecutively, a detailed description of this setup is given.

Table 2.1: Overview of employed standard (STD) and reference (REF) sensors

Sensor	STD	REF	Description
On-board sensors	×		Series prod. sensors (CAN bus)
u-blox LEA-6T	×		Low-cost GNSS receiver
OxTS RT3003		×	High-precision nav. system
	×		MEMS IMU
Correvit		×	Optical velocity sensor

2.2.1.1 On-board Series Production Sensors

On-board series production sensors refers to sensors that are already available in the test vehicle. These are connected via the controller area network (CAN) bus. The sensor signals that are subsequently used comprise the individual wheel speeds $\boldsymbol{v}^{w,T} = [v^w_{fl},\, v^w_{fr},\, v^w_{rl},\, v^w_{rr}]$ at the front left (fl), front right (fr), rear left (rl) and rear right (rr) wheel in the direction of travel as well as the wheel steering angle δ. Particularly, the wheel steering angle δ cannot be obtained directly form the CAN bus such that it has to be derived from the EPS actuator's bevel angle (i.e. the angle of the electrical motor), see section 2.2.2.1. Thereby, each signal is provided with an update rate of 100 Hz.

2.2.1.2 u-blox LEA-6T GNSS Receiver

The u-blox LEA-6T GNSS receiver [26] serves as standard low-cost GNSS receiver with a single-antenna, single-frequency setup. It pro-

vides the navigation solution, comprising the vehicle's position, velocity and course angle (i.e. the direction of travel), with an update rate of 5 Hz via a serial RS-232 interface. Thereby, the receiver utilizes the European Geostationary Navigation Overlay Service (EGNOS) to improve the horizontal position accuracy from 5.25 m to 4.1 m (2σ), see [26]. With respect to [27], a 1σ-accuracy specifies that 68.3% of all measurements are located in a circle having a radius which corresponds to the 1σ-accuracy centered at the true position. The same holds for 95.4% of the measurements when referring to the 2σ-accuracy. Furthermore, the receiver provides a precise digital time pulse each Universal Time Coordinated (UTC) [28] second. By using this pulse, GNSS measurement time delays, which result from the receiver's internal signal processing and data transmission [29], can be determined and finally compensated by the navigation filter. Particularly, a mean time delay of 0.18 s has been observed in experimental tests. Finally, Table 2.2 provides an overview of the most relevant sensor properties.

Table 2.2: u-blox LEA-6T signal properties

Navigation Solution (L1 freq. + EGNOS)

Property	Value	Unit
Update rate	5	Hz
Horizontal position accuracy (2σ)	4.1	m
Horizontal velocity accuracy (1σ)	0.1	m/s
Course angle accuracy (1σ)	0.5	deg
Time delay (mean)*	0.18	s

Time Pulse

Property	Value	Unit
Update rate	1	Hz
Timing accuracy (2σ)	30	ns

* Determined in experimental tests (not specified in [26])

2.2.1.3 Oxford Technical Solutions (OxTS) RT3003

The OxTS RT3003 centimeter-precision navigation system [30] is used as standard as well as reference sensor and is interconnected via a CAN bus interface. First, the RT3003 provides raw inertial sensor measurements, i.e. accelerations and angular rates, with an update rate of 100 Hz. Although, the OxTS RT3003 is a highly cost-intensive sensor, the IMU is still based on low-cost MEMS technology. Hence, it allows for an investigation of low-cost sensor based collision avoidance respectively autonomous vehicle guidance. Second, the RT3003 is used as reference centimeter-precision navigation system to evaluate the low-cost navigation solution. In particular, the centimeter-precision navigation solution is determined by an internal sensor fusion of the IMU and a two-antenna RTK-GPS. Thereby, differential corrections are obtained via N-TRIP V3 using a GPRS-modem. A summary of the most relevant signal properties according to [30] is given in Table 2.3.

Table 2.3: OxTS RT3003 signal properties

IMU (MEMS-based inertial measurement unit)

Property	Value	Unit
Update rate	100	Hz
Accelerometer noise (1σ)*	0.02	m/s^2
Accelerometer bias (1σ)	0.01	m/s^2
Angular rate noise (1σ)*	0.20	deg/s
Angular rate bias (1σ)	0.01	deg/s

Navigation Solution (L1/L2 frequency)

Property	Value	Unit
Update rate	100	Hz
Horizontal position accuracy (2σ)	0.04	m
Horizontal velocity accuracy (1σ)	0.05	m/s
Heading accuracy (1σ)	0.10	deg

* Determined in experimental tests (not specified in [30])

2.2.1.4 Correvit

A Correvit sensor is employed as optical reference sensor to measure the longitudinal and lateral velocity with respect to the sensor's mounting position. It is mainly applied to validate vehicle state estimation results. As the sensor is mounted at the rear bumper, its measurements have to be aligned with the longitudinal vehicle axis and to be transferred to CG to be used as reference. The sensor is interconnected via an analog interface which is sampled with 100 Hz.

2.2.2 Actuators

2.2.2.1 Electric Power Steering

To realize steering interventions, the vehicle provides an interface to the EPS steering system which is actually used by the park assist. Power steering systems support the driver by applying an additional torque at the steering rack which is supplied by an electric motor. Besides classical hydraulic or electro-hydraulic power steering systems, EPS systems are increasingly implemented in modern vehicles not least due to their efficiency. However, the EPS-based steering system allows for demanding the actuator's bevel angle $\varphi_{bevel,ref}$ at the steering rack with an update rate of 50 Hz. As vehicle control algorithms require to demand the wheel steering angle δ instead of the bevel angle φ_{bevel}, a lookup table that maps the reference wheel steering angle δ_{ref} on a reference

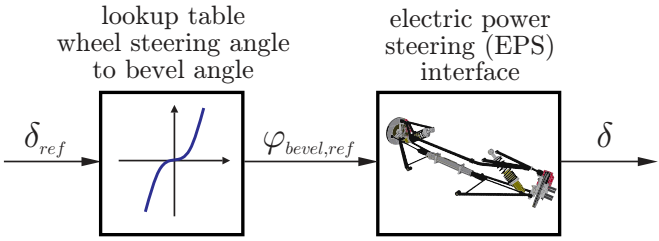

Figure 2.9: Electric power steering interface

bevel angle $\varphi_{bevel,ref}$ is employed, see Figure 2.9. Likewise, the wheel steering angle δ can be derived from the bevel angle φ_{bevel} which is obtained from the vehicle CAN bus. For the purpose of vehicle control, a mathematical model of the steering actuator has to be determined. Therefore, the dynamic behavior is approximated as a first-order lag element neglecting higher-order dynamics, i.e.

$$T_\delta \dot{\delta} + \delta = \delta_{ref}, \tag{2.34}$$

where T_δ denotes the dynamic time constant which has been identified as 0.15 s. Figure 2.10 shows the actual and simulated wheel steering angle δ for stepwise changes of the reference value δ_{ref}. In this regard, the simulated plant response matches the actual wheel steering angle closely. For a detailed consideration, a zoom of the time interval between $t = 11$ s and $t = 13$ s is additionally illustrated. In contrast to the plant model, the actual wheel steering angle shows overshootings for large steps of its reference value resulting from higher order dynamics which have been neglected. Furthermore, some minor steady-state offsets occur which are mainly caused by uncertainties in the lookup table and the accuracy of CAN bus signals. Consecutively, the dynamic

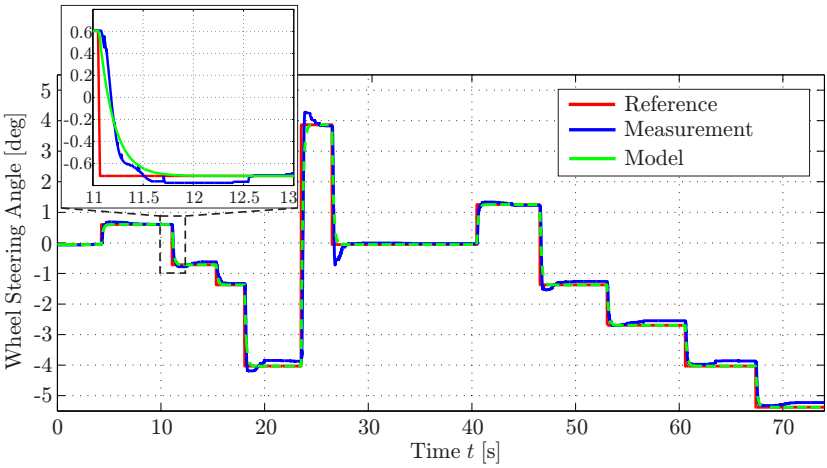

Figure 2.10: Measured and simulated step response of EPS actuator

actuator model is used by the predictive control schemes that are discussed in chapter 5. As no major control issues can be observed due to the simplified actuator model and the estimated wheel steering angle generally tracks its reference closely, the model is considered to be able to describe the plant's dynamic behavior in a satisfying way.

2.2.2.2 Brake Booster

In series production vehicles, a brake booster is employed to amplify the brake force that is induced by the driver hitting the brake pedal. In general, a commonly employed brake booster is not capable of conducting full braking maneuvers as it is not able to supply the required brake pressure. Therefore, a brake booster that is able to establish the required pressure for such a maneuver has been implemented in the test vehicle. The corresponding interface allows for demanding the brake pressure in the main brake cylinder p_{bc} with an update rate of 100 Hz. Regarding vehicle control, a deceleration interface is more applicable than a brake pressure interface. For this reason, a low-level proportional-integral (PI) deceleration controller has been designed which establishes the reference longitudinal vehicle deceleration $a_{x,ref}$ by demanding the reference brake pressure $p_{bc,ref}$, see Figure 2.11.

To design the PI controller, the dynamic behavior of the brake pressure interface has been identified as a first-order lag element with time delay which decreases with increasing brake pressure. The time delay results from the buildup of the brake pressure as the actuator does not have any

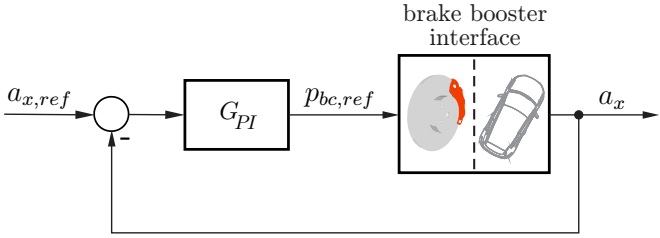

Figure 2.11: Low-level PI deceleration controller

pre-charge mechanism to provide the demanded pressure immediately. The closed-loop behavior of the low-level deceleration interface has finally been optimized by reducing the response time while maximizing the damping ratio simultaneously. Similar to the steering actuator, a mathematical model of the deceleration interface is required. For the sake of simplicity, the dynamic behavior is modeled as first-order lag element while higher-order dynamics as well as time delays are neglected, i.e.

$$T_{a_x}\dot{a}_x + a_x = a_{x,ref} \tag{2.35}$$

where T_{a_x} denominates the dynamic time constant which has been identified as 0.15 s, $a_{x,ref}$ the reference and a_x the actual longitudinal acceleration. For validation purposes, Figure 2.12 illustrates the actual and estimated system response when changing the reference value in a stepwise manner. Thereby, the response when neglecting the time delay as well as when assuming a time delay of 0.1 s is shown. When considering the actual system response, it can be noticed that the initial time delay for $a_{x,ref} = -2\,\mathrm{m/s^2}$ has a magnitude of about 0.2 s. After the initial buildup of the brake pressure, the time delay decreases to 0.1 s for $a_{x,ref} = -4\,\mathrm{m/s^2}$ and $a_{x,ref} = -6\,\mathrm{m/s^2}$. The estimated longitudi-

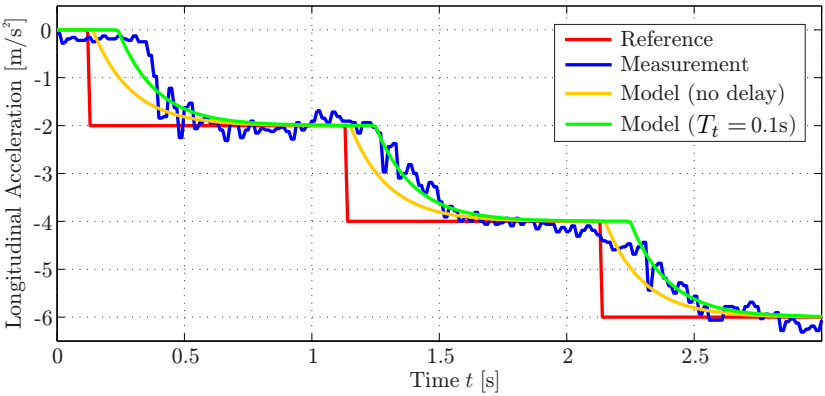

Figure 2.12: Measured and simulated step response of the low-level deceleration interface

nal deceleration tracks the actual plant response closely when assuming a time delay of 0.1 s. When neglecting the time delay, larger errors can especially be observed for the initial buildup of the brake pressure while these errors decrease with increasing decelerations. Hereafter, the plant model is used in the prediction model of the MPC-based steering/braking controller. As the controller requires a plant model in (discrete) state space representation, disregarding the time delay has been preferred to simplify the corresponding prediction model. Experimental control results show that just the initial time delay due to the buildup of the brake pressure is an issue as far as control performance is concerned. But as this time delay cannot be avoided and the reference is tracked satisfyingly for increasing decelerations, the simplified plant model is considered to be sufficient for the purpose of controller design.

2.2.3 Physical Interconnection

Figure 2.13 illustrates the experimental setup in the trunk of the test vehicle. Besides the sensors that have been introduced in section 2.2.1, it is apparent that two dSPACE MicroAutoBox II units are applied as rapid control prototyping ECUs. Due to the computational complexity, algorithms that are related to sensor fusion (i.e. navigation and vehicle state estimation) are executed on the first ECU while vehicle control algorithms are assigned to the second. A schematic of the physical interconnection of sensors, actuators and ECUs is depicted in Figure 2.14. For navigation and vehicle state estimation purposes, the u-blox low-cost GNSS receiver, the OxTS RT3003 (using raw IMU outputs) as well as the vehicle's CAN bus are connected to the sensor fusion ECU. A required subset of the sensor fusion outputs is transmitted to the vehicle control ECU via a dedicated CAN bus. At the same time, the vehicle control ECU is able to influence the sensor fusion parameters via the same interface. Furthermore, the vehicle control ECU is interconnected to the vehicle CAN bus to send commands to the actuators and thus guide the vehicle autonomously. Moreover, it receives the navigation solution from the OxTS RT3003 aided navigation system in order to be able to switch from the low-cost to the centimeter-precision navigation solution. In this way, the influence of the position accuracy on the control results can be investigated. For the sake of completeness, it has to

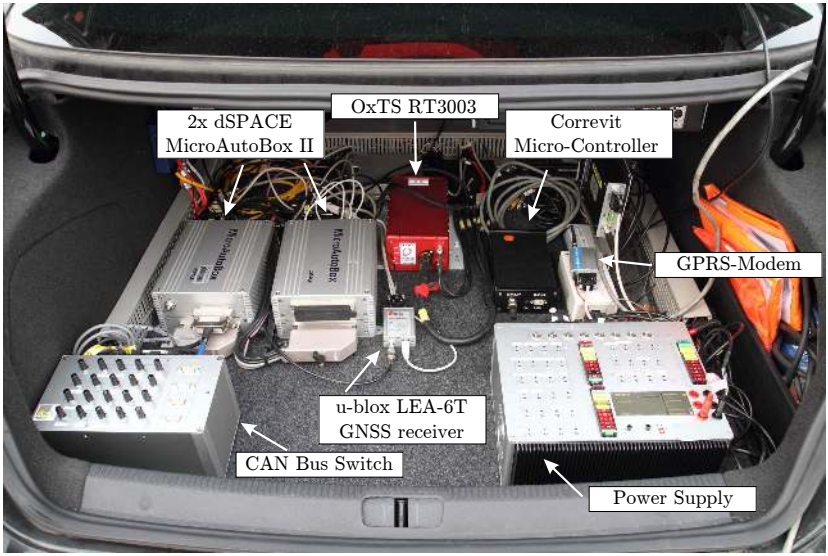

Figure 2.13: Overview of hardware integration in test vehicle

be noted that reference signals originating from the OxTS RT3003 and the Correvit sensor are additionally recorded on both ECUs for validation purposes. This interconnection is discarded for reasons of clarity.

2.3 GNSS-based Collision Avoidance

Although the main focus of this thesis is on GNSS-based autonomous vehicle guidance rather than the entire application of CA, a brief survey of the main issues that have to be considered when implementing the GNSS-based CA system is provided consecutively. As illustrated in Figure 2.15, the application of CA can basically be subdivided into the tasks of *sensor fusion*, *maneuver coordination*, *path/trajectory planning* and *vehicle control*. For each field of research, a brief overview will be

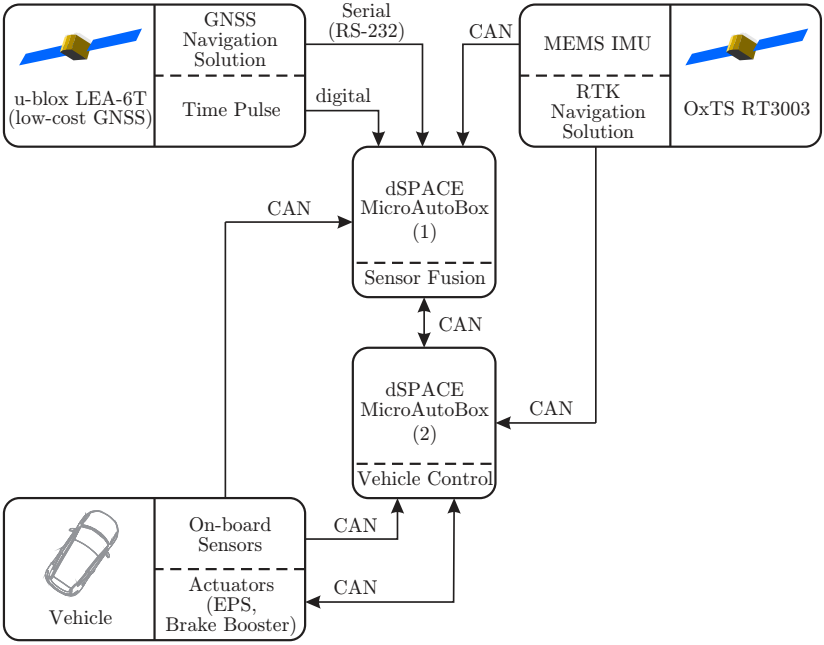

Figure 2.14: Physical interconnection scheme

given subsequently.

When considering sensor fusion, it can further be subdivided into the estimation of ego-vehicle states and environment recognition. As far as the estimation of ego-vehicle states is concerned, the main issues are navigation and vehicle state estimation. These are related to determining the vehicle's position, velocity, attitude and further vehicle states that are required to apply the control scheme. Consecutively, these issues will be addressed in chapter 3 and 4. On the other hand, environment recognition aims at determining information about the surrounding environment, i.e. the road geometry in front of and behind the vehicle (e.g. current lane, lane width, number of lanes) as well as (non-)moving vehicles (e.g. position, velocity, heading) that are a potential collision risk. Particularly, the information about the road can

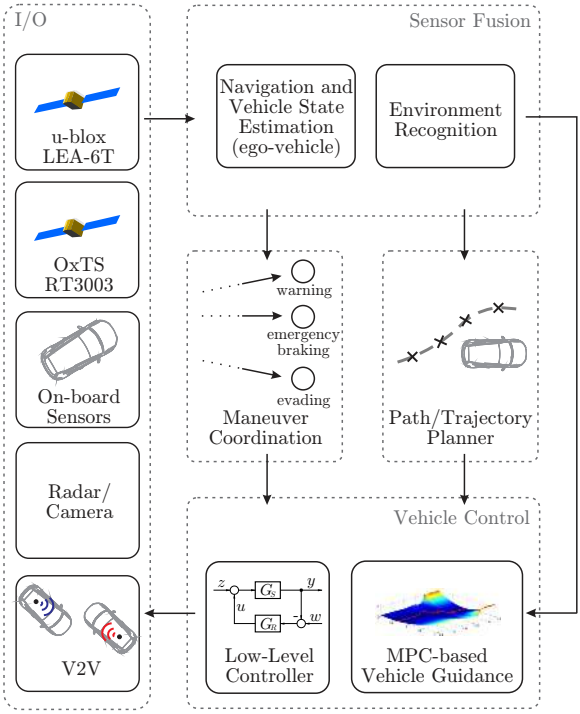

Figure 2.15: System scheme for GNSS-based collision avoidance

be gained through a camera or by matching the vehicle's position onto a digital map that contains all the relevant road properties, see [31, 32]. To detect surrounding vehicles, a radar, a mono-camera as well as V2V communication are incorporated into the sensor setup. These sensors have previously been omitted for reasons of brevity as they are not considered in this thesis. The information that is obtained from each sensor has to be integrated in a multi-sensor fusion approach to obtain a consistent list of objects. In literature, several multi-sensor fusion concepts that aggregate LiDAR, radar and camera sensor information are proposed, see [33, 34]. Finally, a classification of moving and non-moving objects and a perception of their future behavior is performed which is

essential for maneuver coordination as well as path/trajectory planning algorithms, see [35, 36].

Maneuver coordination is generally dedicated to deciding whether the driver should be warned or an emergency braking respectively evasion maneuver should be conducted. Thereby, the decision depends on the distance to surrounding vehicles as well as their perceived behavior. Mostly, the particular decision is based on the time to collision (TTC), i.e. the estimated time until the accident is going to happen, and depends on several boundary conditions like maximum feasible longitudinal and lateral accelerations, see [37, 38].

When the maneuver coordinator demands an evasive maneuver, a feasible collision-free evasion path/trajectory has to be determined by the path/trajectory planner. Thereby, several physical limitations like maximum feasible accelerations and the boundaries of the road have to be taken into account. In literature, a variety of concepts can be found comprising amongst others potential field based methods [39, 40], optimal control based approaches [41–44] as well as sigmoid-based concepts [3], [37].

Finally, the vehicle control layer is responsible of guiding the vehicle on the path/trajectory that has been determined by the path/trajectory planner. In this regard, the controller has to guide the vehicle with minimum deviations from the reference value while stabilizing the vehicle during the entire maneuver even at the handling limits. A solution to this particular issue is introduced in chapter 5.

2.4 Low-cost GNSS-based Autonomous Vehicle Guidance

After providing a brief survey of the main tasks related to the entire application of CA, the focus is narrowed down to low-cost GNSS-based autonomous vehicle guidance in the context of CA and thus to the main focus of this thesis. As previously stated, it is assumed that the maneuver coordinator demands an evasion maneuver and that the time of intervention as well as the evasion path/trajectory are a priori known

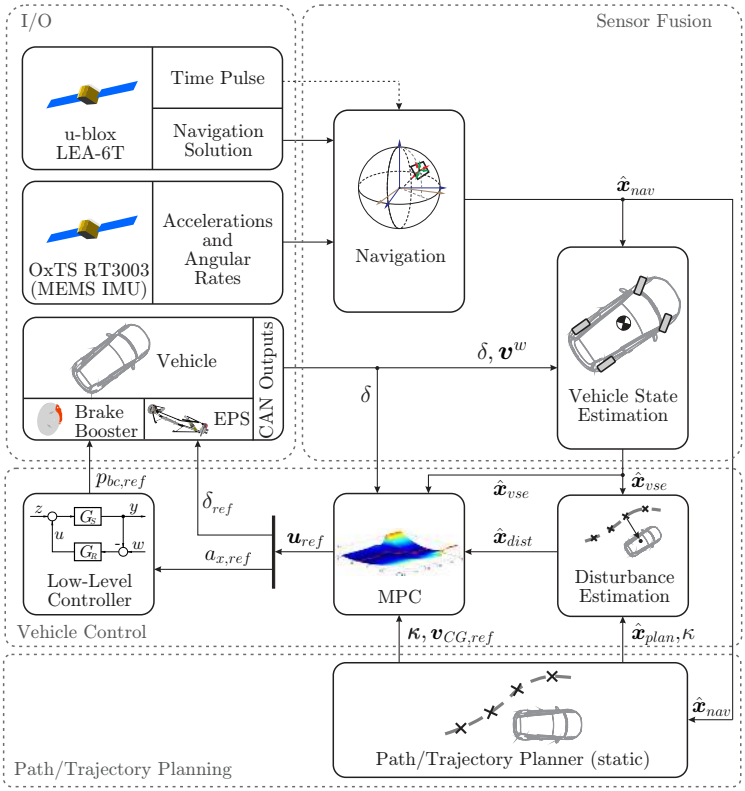

Figure 2.16: System scheme for autonomous vehicle guidance

such that the subsequent considerations concentrate on *navigation*, *vehicle state estimation* and *vehicle control*. The corresponding reduced system scheme is depicted in Figure 2.16.

In the sensor fusion layer, a kinematic navigation filter integrates inertial sensor measurements with a low-cost GNSS with an update rate of 100 Hz to determine the navigation solution $\hat{\boldsymbol{x}}_{nav}$ containing the vehicle's position, velocity and attitude, see chapter 3. As the longitudinal and lateral velocity at CG cannot be derived from the navigation so-

lution with an appropriate accuracy, a second EKF-based vehicle state estimator that relies on a dynamic vehicle model is employed to provide these quantities with a sampling rate of 100 Hz, see chapter 4. Thereby, a subset of the navigation solution, i.e. the horizontal velocity and (calibrated) inertial sensor measurements, are processed in this estimator. Further quantities like wheel velocities $\boldsymbol{v}^w$ as well as the wheel steering angle δ are obtained from the vehicle CAN bus.

The navigation solution $\hat{\boldsymbol{x}}_{nav}$ is used by the (static) path/trajectory planner to compute the relative orientation to and the lateral displacement from the a priori known evasion path, see section 5.5. These quantities are summarized as $\hat{\boldsymbol{x}}_{plan}$. Furthermore, the current and future path's curvature $\boldsymbol{\kappa}$ as well as the velocity reference trajectory $\boldsymbol{v}_{CG,ref}$ (when applying the steering/braking controller) is provided to the vehicle control layer. While the scheme that is illustrated in Figure 2.16 solely relies on the low-cost navigation solution, the actual software structure allows for switching to the OxTS RT3003 reference navigation system to analyze the influence of the position accuracy on the control performance, see chapter 6. In this case, the input $\hat{\boldsymbol{x}}_{nav}$ to the path/trajectory planner is composed of the corresponding outputs of the OxTS RT3003 navigation solution. At the same time, the vehicle state estimator still relies on the low-cost navigation solution (not requiring any position information) as studies have shown that estimation results are almost equal when using the OxTS RT3003.

The outputs of the sensor fusion as well as path/trajectory planning layer are used to employ the MPC-based control scheme that determines the control inputs by solving an online optimization problem, see chapter 5. Thereby, the sample rate depends on the applied control scheme in terms of computational complexity. While the steering-only controller can be executed in real-time with a sample rate of 50 Hz, only 25 Hz are feasible for the steering/braking controller. In addition to the predictive controller, an EKF-based disturbance estimator is applied with an update rate of 50 Hz to suppress external disturbances and thus to avoid steady-state offsets in the lateral displacement from the evasion path. Finally, the control inputs that are determined by the predictive controller, i.e. the reference wheel steering angle δ_{ref} and the deceleration $a_{x,ref}$ (when applying the steering/braking controller), are made available to the steering as well as the braking system.

3 Navigation

3.1 Motivation and Related Work

In the scope of autonomous vehicle guidance, a precise knowledge of the vehicle's pose in terms of position, velocity and attitude is required to guide the vehicle along a desired path or trajectory. As the navigation scheme relies on a low-cost GNSS and MEMS-based inertial sensors, an appropriate concept is required to achieve the aim of a precise navigation solution. In this chapter, a concept that is able to fulfill all the requirements on the navigation solution for autonomous evasion maneuvers is introduced.

Generally, navigation concepts for autonomous vehicle guidance that can be found in literature comprise vision-based navigation systems [45] which are even complemented by LiDAR sensors [46], inertial navigation systems (INS) [15] as well as aided inertial navigation systems that use GNSS, LiDAR or camera information as aiding measurements [47–49]. To give a brief outline of these approaches, the use of an IMU or other motion-sensing devices (e.g. wheel speed sensors) to determine a navigation solution in terms of position, velocity and attitude is referred to as INS. As a main drawback of INS, navigation errors increase in time when sensor measurements, which are usually impaired by errors like biases or scale factor errors, are integrated numerically. The performance of a pure vision/LiDAR- or GNSS-based navigation system does not suffer from increasing errors in time but might be impaired under various environmental conditions. Thus, it is reasonable to employ a sensor fusion of different sensors such that they complement each other. With regard to literature, GNSS are frequently integrated with INS to an aided inertial navigation system in order to achieve a high update rate and to avoid long-term sensor drifts as they occur for pure INS, see [16]. As far as GNSS-based navigation concepts for autonomous vehicle guidance at the limits of vehicle dynamics are concerned, [13, 14] rely

on centimeter-precision RTK-GPS aided navigation system which are highly cost-intensive.

In the following, a concept for an aided inertial navigation system that is based on a sensor fusion of a low-cost GNSS and MEMS-based inertial sensors is considered. Referring to [16, 28], this approach is known as GNSS/INS integration. Although, a radar and a camera are part of the experimental setup that has been introduced in section 2.3, the incorporation of these sensors in the navigation concept is still part of future work. When using the GNSS receiver's navigation solution in terms of position and velocity, this approach is referred to as loosely coupled GNSS/INS integration while tightly coupled integration schemes rely on raw navigation data like pseudo- and doppler-ranges (i.e. signal transit time and doppler frequency shifts due to the relative movement of the receiver's antenna and the corresponding satellite). One of the major advantages of tightly coupled approaches is the ability to compute a navigation solution even if less than four satellites are available. Due to the fact that at least four satellites are considered to be available in experimental tests, a loosely coupling integration scheme according to [28] is applied in the scope of this contribution. This assumption is reasonable as the proving ground is not surrounded by any buildings or trees that may impair the reception of satellite signals. Furthermore, GNSS-denied environments such as urban canyons which are characterized by poor GNSS signal reception are not part of this thesis. For the design of the integration scheme, time delays in GNSS measurements that are caused by internal receiver signal processing and data transmission [29] have to be taken into account and finally to be compensated. Otherwise, these delays can significantly degrade the navigation performance, especially when having large horizontal accelerations. In addition to conventional integration schemes, an approach for improving the heading estimate by additionally using the GNSS course angle (indicating the direction of travel) as aiding measurement when driving almost straight is proposed.

A requirement analysis will point out that the horizontal position accuracy of 4.1 m (2σ), provided by the u-blox receiver, is not sufficient for autonomous evasion maneuvers. As the achievable absolute position accuracy of the integrated navigation solution is always limited by the aiding GNSS, this chapter proposes to rely on relative positioning

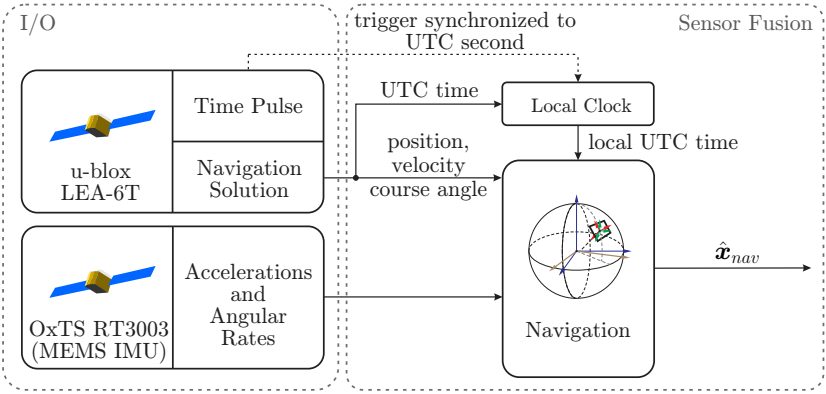

Figure 3.1: Navigation scheme

to meet the accuracy requirement. According to [50], it is assumed that the errors that impair the GNSS receiver's navigation solution are approximately constant in a close local environment. Thus, relative positioning can achieve a much higher positional accuracy than absolute positioning. Additionally, occasional position jumps and growing positioning errors are identified to be an issue when having large horizontal accelerations as they might cause severe steering interventions. Thus, the task of autonomous vehicle guidance at the handling limits becomes demanding, see [51]. The main idea of the proposed solution is to compensate inertial sensor biases during nominal operation and mainly rely on the INS during an evasive maneuver. For this purpose, the weights on the GNSS measurements are appropriately reduced during the maneuver while the filter is still operated closed-loop to avoid severe sensor drifts which are apparent in dead reckoning approaches. Finally, the introduced concept is validated using actual measurements that have been gained in experimental tests. The resulting navigation performance fulfills all the specified requirements is thus assessed to be suited for the purpose of autonomous vehicle guidance at the handling limits.

Figure 3.1 shows the part of the system scheme for autonomous vehicle guidance in section 2.4 that is related to navigation. As previously

indicated, accelerations and angular rates originating from the MEMS-based IMU as well as the low-cost GNSS receiver's navigation solution, i.e. the position, velocity and course angle, are integrated in the navigation filter. In order to determine the time delay of GNSS measurements, an internal (software) clock which is synchronized with UTC time is employed. For synchronization purposes, the u-blox time pulse (no time delay) as well as the UTC message timestamp (delayed) are employed to obtain the precise UTC time. Basically, the resulting navigation solution $\hat{\boldsymbol{x}}_{nav}$ provides the vehicle's pose in terms of position, velocity and attitude with an update rate of 100 Hz.

3.2 Requirements on Navigation Solution

In order to implement an appropriate navigation concept for autonomous evasion maneuvers, the requirements on the navigation solution have to be analyzed first. Based on [52, 53], the following basic requirements have been derived:

- *Accuracy:* Accuracy refers to the amount of error in the estimated compared to the actual vehicle position. Due to the focus on an automotive application, subsequent considerations refer to the horizontal position accuracy whose particular performance requirement is deduced consecutively.
- *Bandwidth:* Bandwidth specifies the update rate of the aided navigation system. For autonomous vehicle guidance, an update rate of 100 Hz is considered to be appropriate [52] and achieved through the sensor fusion of inertial sensors and GNSS measurements.
- *Availability:* The aided navigation system should provide continuous uninterrupted information on the vehicle's pose. As for the bandwidth, this requirement is met through the integration of inertial sensors and GNSS measurements. Thereby, GNSS-denied environments are not covered in this thesis.
- *Integrity:* Integrity is defined as the ability of the navigation system to detect anomalies in the navigation solution and provide an indication of the current reliability to the underlying application.

> In this thesis, integrity aspects are not taken into account but are part of future work.

Hence, the horizontal position accuracy is the only basic requirement that has to be deduced consecutively. In literature, only few investigations have been carried out to specify the required minimum horizontal position accuracy for autonomous vehicle guidance in urban and rural environments. [54] evaluates the minimum horizontal position accuracy (2σ) when using GNSS-based positioning as well as V2V communication for collision warning (CW) systems comprising forward collision warning (FCW) and lane change collision warning (LCCW). For both systems, a sub-meter accuracy is assessed to be necessary while 0.5 m is advisable for a reliable FCW and 0.7 m for LCCW. [55] recommends a horizontal position accuracy (2σ) of 0.3 m for a cooperative rear-end collision avoidance system on a multi-lane road to distinguish between adjacent lanes.

In the following, an upper bound of the admissible horizontal position error for the feasibility of autonomous evasion maneuvers is deduced by considering simple evasion maneuvers to adjacent lanes. Assuming that the ego-vehicle changes to the center of an adjacent lane while the obstacle remains in its own lane, the admissible lateral position error budget can be determined in dependence of the vehicle's track width as well as the road lane width, see Figure 3.2. Considering a lane width of 3.75 m, which is commonly present in European countries [56], and subtracting the test vehicle's track width of 1.6 m, the total admissible lateral position error budget amounts to 1.075 m for each side of the vehicle. To obtain the maximum acceptable horizontal position error, the lateral position error is assessed to be more critical than the longitudinal error. As the longitudinal position error should not exceed the lateral error, the maximum admissible horizontal position error is assessed to be 1 m. Thereby, it has to be taken into account that the error budget refers to navigation as well as vehicle control errors. As both issues are quite challenging as far as autonomous vehicle guidance is concerned, it has been decided to fix the resulting upper (feasibility) bound of the acceptable horizontal position error due to navigation issues to the half of the error budget, i.e. 0.5 m. This requirement is comparable to [55] when referring to the 3σ-accuracy of 0.45 m which approximately corresponds to a maximum admissible error. Particu-

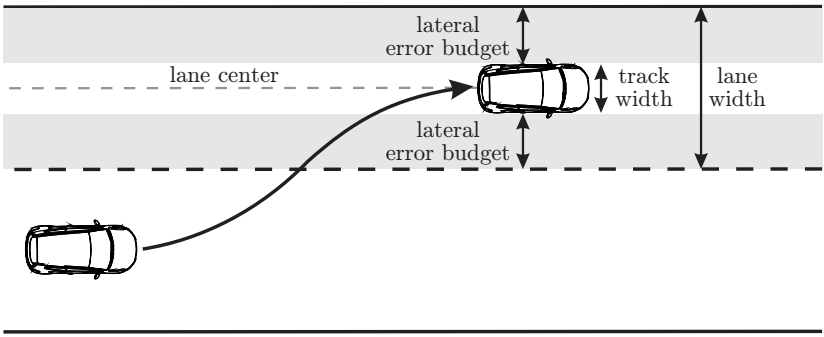

Figure 3.2: Scheme to determine max. admissible horizontal position error

larly, the 3σ position accuracy specifies that 99.7% of all measurements show a maximum deviation of 0.45 m from its actual position.

As previously indicated, the horizontal position accuracy of the integrated navigation solution is limited by the aiding GNSS having an accuracy of 4.1 m (2σ), see section 2.2.1. Thus, autonomous vehicle guidance is considered not to be feasible when the vehicle has to be guided with respect to absolute position set-points. Assuming that the errors that impair the GNSS receiver's navigation solution (e.g. ionospheric, tropospheric errors [27]) are approximately constant in a close local environment, relative instead of absolute positioning is assessed to be an appropriate solution to satisfy the accuracy requirement and is thus studied subsequently. Furthermore, the integrated navigation solution shows discontinuities, i.e. steps-wise changes in the position and velocity estimate, and also increasing positioning errors when conducting maneuvers with high horizontal accelerations greater than $7\,\mathrm{m/s^2}$. These errors are mainly caused by discontinuities in GNSS measurements as well as the fact that assumptions in the filter design (e.g. for real-time compensation of time delays) become less accurate. Investigations have shown that position jumps of more than 0.2 m lead to severe steering interventions or even heavy oscillations that can cause instabilities in the vehicle control layer and thus have to be avoided. Contrarily, no issues have been observed for discontinuities of less than

0.1 m. Hence, the resulting specific requirements for autonomous evasion maneuvers can be summarized as:

- *(Relative Position) Accuracy:* The (relative) horizontal position error should be less than 0.5 m even for maneuvers with high horizontal accelerations greater than $7\,\mathrm{m/s^2}$.
- *Smoothness:* The position trajectory should be smooth to avoid severe steering interventions, i.e. stepwise changes in the position solution should be less than 0.1 m.

Hereafter, the basic integration scheme for absolute positioning is introduced first before discussing further extensions such as relative positioning to satisfy the specified requirements.

3.3 Basic Definitions and Integration Scheme

3.3.1 Reference Frames

Before introducing the particular integration scheme, some basic principles regarding reference frames and their relative orientation are outlined first. In literature, there are basically four relevant reference frames which are required to express the quantities of the navigation solution. For two of these coordinate systems, the actual geodetic shape of the earth has to be approximated using a reference ellipsoid. Therefore, this contribution applies the World Geodetic System 1984 (WGS84), see [27]. An illustration of the corresponding reference frames whose definitions refer to [28] is depicted in Figure 3.3.

- The origin of *inertial reference frame (i-frame)* is the center of the earth's reference ellipsoid, the x^i- and y^i-axis are located in the equatorial plane while the z^i-axis and rotational axis of the earth coincide with each other. The orientation of the i-frame is related to the fixed stars.
- The *earth-centered, earth-fixed (ECEF) reference frame (e-frame)* commonly refers to a Cartesian as well as a geodetic frame to

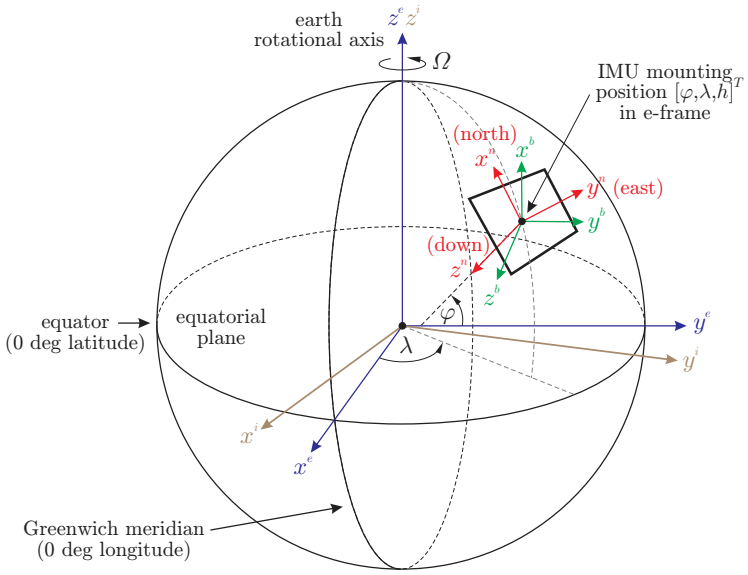

Figure 3.3: Navigation reference frames

denote the position in the ECEF frame. As far as the Cartesian coordinate system is concerned, the e- and the i-frame are the same except the x^e-axis intersects the Greenwich meridian (i.e. for 0 deg longitude) and the equator (i.e. for 0 deg latitude). When using the geodetic coordinate system, a position is generally expressed in terms of latitude φ, longitude φ and altitude h above the WGS84 reference ellipsoid, see Figure 3.3. The latitude φ denotes the angle between the equatorial plane and the local ellipsoidal normal vector (i.e. in the direction of z^n). The longitude λ refers to the angle between the Greenwich meridian and the projection of the current position on the equatorial plane. Finally, the altitude h represents the distance between the reference ellipsoid and the current position along the ellipsoidal normal vector. In accordance to commonly employed definitions, the altitude is negative when the vehicle is located above the reference ellipsoid.

- The axes of the *body-fixed reference frame (b-frame)* are aligned with the vehicle axes. In this regard, the x^b-axis is directed forward while the y^b- and z^b-axis are directed right and downwards. Furthermore, the origin of the b-frame corresponds to the mounting position of the IMU and the IMU's axes coincide with the vehicle axes.
- The *navigation reference frame (n-frame)* has the same origin as the b-frame while the x^n-, y^n- and z^n-axis are orientated north, east and downwards.

As indicated in section 3.1, relative instead of absolute positioning is considered for evasive maneuvers. Therefore, an additional Cartesian reference frame is introduced.

- The *maneuver reference frame (m-frame)* has its origin at the position when the evasion maneuver is initiated. In this regard, the position always refers to the vehicle's CG instead of the IMU mounting position. The x^m-axis coincides with vehicle longitudinal axis when the maneuver is started, the y^m- and z^m-axis are directed left and upwards. Further information regarding the m-frame is provided in section 3.7.1.

Consecutively, the frame abbreviations (i, e, b, n, m) are used as super- and subscripts to denote the corresponding reference frames. E.g. the subscript ib of $\{\cdot\}_{ib}^{b}$ indicates a quantity describing a movement of the b-frame with respect to the i-frame while the superscript denotes that the quantity is given in coordinates of the b-frame.

3.3.2 Euler Angles and Quaternions

The relative orientation of two Cartesian reference frames can be expressed by the corresponding Euler angles. These angles describe three subsequent rotations to transfer one reference frame to the other, see [28]. In the following, the transformation of the n- to the b-frame will be used to exemplify this issue. In order to transfer the n- to the b-frame, the z^n-axis is rotated by the yaw angle ψ, the resulting $y^{n'}$-axis by the pitch angle θ and finally the resulting $x^{n''}$-axis by the roll angle ϕ.

These subsequent rotations can be formulated in terms of a direction cosine matrix (DCM), i.e.

$$\boldsymbol{R}_n^b = \boldsymbol{R}_{n,x^{n''}}^b(\phi)\ \boldsymbol{R}_{n,y^{n'}}^b(\theta)\ \boldsymbol{R}_{n,z^n}^b(\psi) \tag{3.1}$$

where $\boldsymbol{R}_{n,z^n}^b(\psi)$, $\boldsymbol{R}_{n,y^{n'}}^b(\theta)$ and $\boldsymbol{R}_{n,x^{n''}}^b(\phi)$ indicate the corresponding rotation matrices. The particular definition of these matrices can be found in section C.1. As the DCM is an orthogonal matrix, for the inverse transformation from the b- to the n-frame holds

$$\boldsymbol{R}_b^n = \boldsymbol{R}_n^{b,T}. \tag{3.2}$$

A major disadvantage of Euler angles is that certain configurations can lead to singularities. To solve this issue, a common approach is the use of an orientation vector $\boldsymbol{\sigma}$ describing the relative orientation of two reference frames. In particular, the vector

$$\boldsymbol{\sigma}_b^{n,T} = [\sigma_x,\, \sigma_y,\, \sigma_z] \tag{3.3}$$

specifies the axis in the three dimensional space that is used to transfer the b- and the n-frame into each other by a single rotation. Thereby, the Euclidean vector norm $\|\boldsymbol{\sigma}_b^n\|$ denotes the corresponding rotation angle. In general, the orientation vector $\boldsymbol{\sigma}_b^n$ is stored as a normalized quaternion, i.e.

$$\boldsymbol{q}_b^n = \begin{bmatrix} \cos(\|\boldsymbol{\sigma}_b^n\|/2) \\ (\sigma_x/\|\boldsymbol{\sigma}_b^n\|)\sin(\|\boldsymbol{\sigma}_b^n\|/2) \\ (\sigma_y/\|\boldsymbol{\sigma}_b^n\|)\sin(\|\boldsymbol{\sigma}_b^n\|/2) \\ (\sigma_z/\|\boldsymbol{\sigma}_b^n\|)\sin(\|\boldsymbol{\sigma}_b^n\|/2) \end{bmatrix}. \tag{3.4}$$

Further details on Euler angles and quaternions are provided in [28].

3.3.3 Loosely Coupled GNSS/INS Integration

Aided inertial navigation systems are commonly applied to complement the properties of an INS (i.e. high update rate but long-term sensor drifts) and GNSS (i.e. low update rate, no long-term sensor drifts). In this section, the basic concept of the implemented loosely coupled integration scheme will be described while the subsequent sections provide

further details regarding the particular parts of the integration scheme. From a structural point of view, GNSS/INS integration schemes can be subdivided into three parts as depicted in Figure 3.4, i.e.

1. INS mechanization,
2. the estimation of the corresponding mechanization errors and
3. error correction.

Generally speaking, the INS mechanization determines an a priori navigation solution $\hat{\boldsymbol{x}}^-$, i.e. the attitude by integrating angular rates, the velocity by integrating accelerations and the position by integrating the estimated velocity. In this context, the notation $\{\hat{\cdot}\}$ corresponds to an estimated variable.

To determine the errors that are introduced through the forward integration of inertial sensors, an estimator to determine the corresponding mechanization error $\delta\hat{\boldsymbol{x}}$ is required. For this purpose, several integration schemes comprising amongst others loosely and tightly coupled approaches as well as different estimator concepts like linearized Kalman

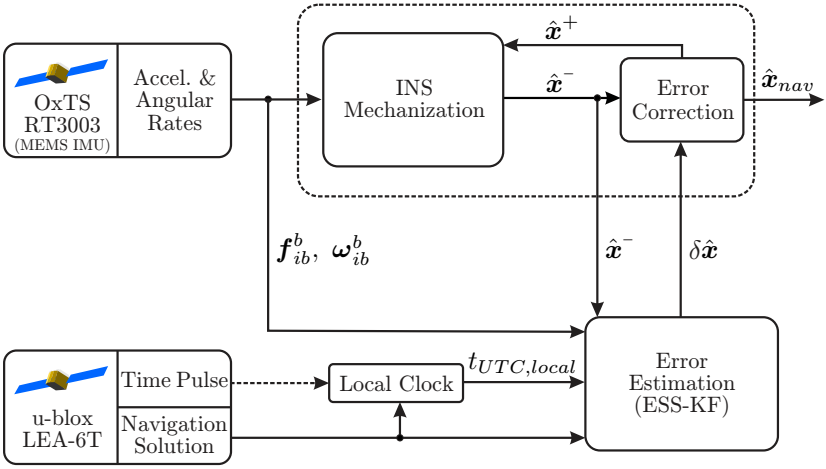

Figure 3.4: Loosely coupled GNSS/INS integration scheme

filters [28], sigma-point Kalman filters (SPKF) [57] and particle filters (PF) [58] can be found in literature. Assuming that at least four satellites are available all the time, a loosely coupled GNSS/INS integration scheme that is based on a linearized Kalman filter to determine the estimation error $\delta\hat{\boldsymbol{x}}$ by processing GNSS position, velocity and course angle measurements is used in this contribution. Compared to ordinary EKF-based estimator concepts, only the estimation error is determined by the linearized Kalman filter while the actual state vector estimate is stored outside the filter. Thus, the prediction of the state vector is excluded from the filter and conducted in the INS mechanization algorithm. For this reason, the linearized Kalman filter is commonly denoted as error state space Kalman filter (ESS-KF).

Finally, the a posteriori navigation solution $\hat{\boldsymbol{x}}^{+}$ is obtained by subtracting the estimated error $\delta\hat{\boldsymbol{x}}$ from the a priori navigation solution $\hat{\boldsymbol{x}}^{-}$. Thereby, the resulting navigation solution $\hat{\boldsymbol{x}}_{nav}$ generally provides the vehicle's pose in terms of position, velocity and attitude with respect to the IMU's mounting position.

3.4 INS Mechanization

As stated in section 3.3.3, the INS mechanization basically determines the a priori navigation solution by integrating accelerations $\boldsymbol{f}_{ib}^{b}$ and angular rates $\boldsymbol{\omega}_{ib}^{b}$, see Figure 3.5. In this context, $\boldsymbol{f}_{ib}^{b}$ refers to the specific force measured by the IMU in the b-frame that is composed of the actual kinematic acceleration $\boldsymbol{a}_{ib}^{b}$ and the gravitational acceleration $\boldsymbol{g}^{b}$, i.e.

$$\boldsymbol{f}_{ib}^{b} = \boldsymbol{a}_{ib}^{b} - \boldsymbol{g}^{b}, \tag{3.5}$$

see [28]. In the following, the employed dynamic model to compute the vehicle's position, velocity and attitude based on inertial measurements is introduced. While the dynamic model is given in terms of differential equations, the a priori navigation solution is obtained through numerical integration of these differential equations. For this purpose, an explicit forth-order Runge-Kutta integration algorithm [59] is employed as higher order integration technique to reduce numerical errors.

According to [17], this approach is commonly used as a good trade-off between accuracy and computational complexity. In the following, this thesis just covers the most important issues to generally comprehend the mechanization algorithm. For further details, the interested reader is referred to [28].

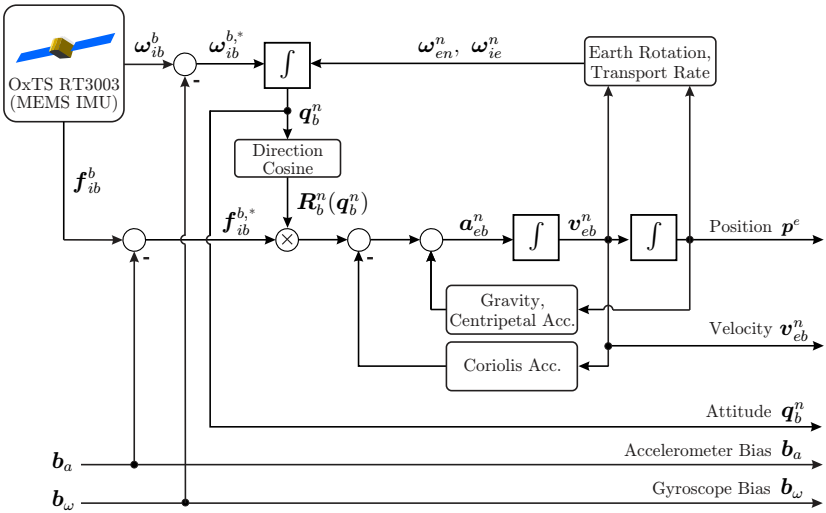

Figure 3.5: INS mechanization scheme (derived from [28])

3.4.1 Sensor Error Model

As MEMS-based inertial sensors are affected by several error sources like biases, scale factor errors, sensor non-orthogonalities and nonlinearities [16], a sensor model is employed to allow for considering these errors in the navigation filter. As the number of filter states and thus the computational complexity increases with the number of considered errors, only sensor biases are investigated consecutively. Thus, the sensor measurements are assumed to be composed of the actual signal (i.e. accelerations and angular rates), a sensor bias which corresponds to a

measurement offset and zero-mean Gaussian white noise, i.e.

$$\tilde{\boldsymbol{f}}_{ib}^{b} = \boldsymbol{f}_{ib}^{b} + \boldsymbol{b}_a + \boldsymbol{n}_a, \tag{3.6}$$

$$\tilde{\boldsymbol{\omega}}_{ib}^{b} = \boldsymbol{\omega}_{ib}^{b} + \boldsymbol{b}_\omega + \boldsymbol{n}_\omega \tag{3.7}$$

where $\{\tilde{\cdot}\}$ denotes an actually measured quantity, $\boldsymbol{n}_a$ and $\boldsymbol{n}_\omega$ the sensor noise and $\boldsymbol{b}_a$ and $\boldsymbol{b}_\omega$ the sensor biases. These biases are assumed to be a random walk process, i.e.

$$\dot{\boldsymbol{b}}_a = \boldsymbol{n}_{b_a}, \tag{3.8}$$

$$\dot{\boldsymbol{b}}_\omega = \boldsymbol{n}_{b_\omega} \tag{3.9}$$

where $\boldsymbol{n}_{b_a}$ and $\boldsymbol{n}_{b_\omega}$ represents the zero-mean Gaussian white bias noise. By incorporating sensor biases in the estimation problem, the filter design allows for an online calibration of inertial sensors. When compensating these biases, for the calibrated IMU measurements holds

$$\boldsymbol{f}_{ib}^{b,*} = \boldsymbol{f}_{ib}^{b} - \boldsymbol{b}_a, \tag{3.10}$$

$$\boldsymbol{\omega}_{ib}^{b,*} = \boldsymbol{\omega}_{ib}^{b} - \boldsymbol{b}_\omega. \tag{3.11}$$

3.4.2 Attitude

Attitude dynamics are commonly described by Bortz's differential equation with respect to the orientation vector $\boldsymbol{\sigma}_b^n$. For the purpose of navigation, the simplified differential equation

$$\dot{\boldsymbol{\sigma}}_b^n = \boldsymbol{\omega}_{ib}^{b,*} - \boldsymbol{R}_b^{n,T}(\boldsymbol{\omega}_{ie}^{n} + \boldsymbol{\omega}_{en}^{n}) \tag{3.12}$$

describing the change of the relative orientation between the n- and b-frame is employed where $\boldsymbol{\omega}_{ie}^n$ denotes the earth rotation rate and $\boldsymbol{\omega}_{en}^n$ the transport rate. As the implemented INS mechanization algorithm is based on quaternions, (3.12) is solved iteratively. The change of orientation between time $k-1$ and k can be obtained by

$$\boldsymbol{\Delta\sigma}_{b,k}^{n} = \int_{(k-1)\cdot T_s}^{k\cdot T_s} \boldsymbol{\omega}_{ib}^{b,*} - \boldsymbol{R}_b^{n,T}(\boldsymbol{\omega}_{ie}^{n} + \boldsymbol{\omega}_{en}^{n})\, dt \tag{3.13}$$

where T_s indicates the INS mechanization sample time. Finally the quaternion $\boldsymbol{q}_{b,k}^n$ at time k is determined by deriving a quaternion $\boldsymbol{r}_k$ from $\boldsymbol{\Delta\sigma}_{b,k}^n$ and conducting a quaternion multiplication, i.e.

$$\boldsymbol{r}_k = \begin{bmatrix} \cos(\|\boldsymbol{\Delta\sigma}_{b,k}^n\|/2) \\ (\boldsymbol{\Delta\sigma}_{b,k}^n/\|\boldsymbol{\Delta\sigma}_{b,k}^n\|)\sin(\|\boldsymbol{\Delta\sigma}_{b,k}^n\|/2) \end{bmatrix}, \tag{3.14}$$

$$\boldsymbol{q}_{b,k}^n = \boldsymbol{q}_{b,k-1}^n \circ \boldsymbol{r}_k. \tag{3.15}$$

For a definition of quaternion multiplications, the reader is referred to section C.2.

3.4.3 Velocity

The n-frame velocity $\boldsymbol{v}_{eb}^n$ directing north (n), east (e) and downwards (d) is obtained by numerically integrating the IMU accelerations in the n-frame. To obtain these accelerations, the calibrated IMU measurement $\boldsymbol{f}_{ib}^{b,*}$ has to be transferred to the n-frame and Coriolis acceleration as well as gravity (including gravitational attraction and centripetal accelerations due to the earth's rotation) have to be compensated, i.e.

$$\dot{\boldsymbol{v}}_{eb}^n = \begin{bmatrix} \dot{v}_{eb,n}^n \\ \dot{v}_{eb,e}^n \\ \dot{v}_{eb,d}^n \end{bmatrix} = \boldsymbol{R}_b^n \boldsymbol{f}_{ib}^{b,*} - \underbrace{(2\boldsymbol{\omega}_{ie}^n + \boldsymbol{\omega}_{en}^n) \times \boldsymbol{v}_{eb}^n}_{\text{Coriolis acceleration}} + \underbrace{\boldsymbol{g}^n}_{\text{gravity}}. \tag{3.16}$$

3.4.4 Position

Finally, the IMU position $p^{e,T} = [\varphi,\ \lambda,\ h]$ in the e-frame regarding latitude φ, longitude λ and altitude h can be obtained by integrating

$$\dot{\varphi} = \frac{v_{eb,n}^n}{R_n(\varphi) - h}, \tag{3.17}$$

$$\dot{\lambda} = \frac{v_{eb,e}^n}{(R_e(\varphi) - h)\cos(\varphi)}, \tag{3.18}$$

$$\dot{h} = v_{eb,d}^n \tag{3.19}$$

numerically where $R_e(\varphi)$ denotes the east-west and $R_n(\varphi)$ the north-south radius of curvature of the WGS84 reference ellipsoid in dependence of the latitude φ.

3.4.5 A Priori Navigation Solution

Summing up, the augmented state vector

$$\boldsymbol{x}^T = [\bar{\boldsymbol{x}}^T, \boldsymbol{b}^T] \tag{3.20}$$

of the a priori navigation solution contains the actual navigation solution

$$\bar{\boldsymbol{x}}^T = [\boldsymbol{p}^{e,T}, \boldsymbol{v}_{eb}^{n,T}, \boldsymbol{q}_b^{n,T}], \tag{3.21}$$

comprising the IMU position $\boldsymbol{p}^e$, the IMU velocity $\boldsymbol{v}_{eb}^n$ and the orientation quaternion $\boldsymbol{q}_b^n$, and the sensor biases

$$\boldsymbol{b}^T = [\boldsymbol{b}_a^T, \boldsymbol{b}_\omega^T] \tag{3.22}$$

where $\boldsymbol{b}_a$ and $\boldsymbol{b}_\omega$ correspond to the accelerometer and gyroscope biases respectively. The input vector

$$\boldsymbol{u}^T = [\boldsymbol{f}_{ib}^{b,T}, \boldsymbol{\omega}_{ib}^{b,T}] \tag{3.23}$$

that is used for the purpose of INS mechanization is composed of the accelerations $\boldsymbol{f}_{ib}^b$ and angular rates $\boldsymbol{\omega}_{ib}^b$ measured by the IMU.

3.5 Loosely Coupled Error Estimation

3.5.1 Estimator Design

While the a priori navigation solution $\hat{\boldsymbol{x}}^-$ is determined by integrating INS mechanization equations numerically, the corresponding mechanization error $\delta\hat{\boldsymbol{x}}$ is estimated through an ESS-KF-based estimator. As the actual state estimate is stored outside the filter, the basic concept of an ESS-KF-based estimator is to determine the estimation error

covariance matrix in the prediction step and to compute the estimation errors of the actual state estimate when a measurement $\tilde{\boldsymbol{y}}$ is available, see [28]. Therefore, the nonlinear plant model is linearized along the estimated state trajectory. For numerical reasons, the estimator's state vector contains the position errors

$$\delta \boldsymbol{p}^{n,T} = [\delta p_n^n,\, \delta p_e^n,\, \delta p_d^n] \tag{3.24}$$

in the n- instead of the e-frame. Furthermore, attitude errors are denoted as Euler angle errors $\delta\boldsymbol{\epsilon}$, i.e.

$$\delta \boldsymbol{\epsilon}^T = [\delta\phi,\, \delta\theta,\, \delta\psi] \tag{3.25}$$

where $\delta\phi$ describes the roll error, $\delta\theta$ the pitch error and the $\delta\psi$ yaw error. While a detailed deduction of the nonlinear and linearized model equations can be found in [28], these are consecutively omitted for reasons of clarity. A general overview of the particular implementation is provided in section C.4. When linearizing the nonlinear plant model with respect to the current state estimate and assuming that the measured inputs are superimposed by zero-mean Gaussian white noise, the following continuous-time linear plant model yields

$$\begin{aligned}
\frac{d}{dt}\underbrace{\begin{bmatrix} \delta\boldsymbol{p}^n \\ \delta\boldsymbol{v}_{eb}^n \\ \delta\boldsymbol{\epsilon} \\ \delta\boldsymbol{b}_a \\ \delta\boldsymbol{b}_\omega \end{bmatrix}}_{\delta\boldsymbol{x}(t)} &= \underbrace{\begin{bmatrix} \boldsymbol{F}_{p,p} & \boldsymbol{I} & \boldsymbol{0} & \boldsymbol{0} & \boldsymbol{0} \\ \boldsymbol{F}_{v,p} & \boldsymbol{F}_{v,v} & \boldsymbol{F}_{v,\epsilon} & -\boldsymbol{R}_b^n & \boldsymbol{0} \\ \boldsymbol{F}_{\epsilon,p} & \boldsymbol{F}_{\epsilon,v} & \boldsymbol{F}_{\epsilon,\epsilon} & \boldsymbol{0} & -\boldsymbol{R}_b^n \\ \boldsymbol{0} & \boldsymbol{0} & \boldsymbol{0} & \boldsymbol{0} & \boldsymbol{0} \\ \boldsymbol{0} & \boldsymbol{0} & \boldsymbol{0} & \boldsymbol{0} & \boldsymbol{0} \end{bmatrix}}_{\boldsymbol{F}} \underbrace{\begin{bmatrix} \delta\boldsymbol{p}^n \\ \delta\boldsymbol{v}_{eb}^n \\ \delta\boldsymbol{\epsilon} \\ \delta\boldsymbol{b}_a \\ \delta\boldsymbol{b}_\omega \end{bmatrix}}_{\delta\boldsymbol{x}(t)} \\
&+ \underbrace{\begin{bmatrix} \boldsymbol{0} & \boldsymbol{0} & \boldsymbol{0} & \boldsymbol{0} \\ -\boldsymbol{R}_b^n & \boldsymbol{0} & \boldsymbol{0} & \boldsymbol{0} \\ \boldsymbol{0} & -\boldsymbol{R}_b^n & \boldsymbol{0} & \boldsymbol{0} \\ \boldsymbol{0} & \boldsymbol{0} & \boldsymbol{I} & \boldsymbol{0} \\ \boldsymbol{0} & \boldsymbol{0} & \boldsymbol{0} & \boldsymbol{I} \end{bmatrix}}_{\boldsymbol{G}} \underbrace{\begin{bmatrix} \boldsymbol{n}_a \\ \boldsymbol{n}_\omega \\ \boldsymbol{n}_{b_a} \\ \boldsymbol{n}_{b_\omega} \end{bmatrix}}_{\boldsymbol{w}(t)}
\end{aligned} \tag{3.26}$$

where $\boldsymbol{0}$ respectively $\boldsymbol{I}$ denote the zero matrix respectively the identity matrix of appropriate dimension and

$$\delta \boldsymbol{x}^T = [\delta \boldsymbol{p}^{n,T},\, \delta \boldsymbol{v}_{eb}^{n,T},\, \delta \boldsymbol{\epsilon}^T,\, \delta \boldsymbol{b}_a^T,\, \delta \boldsymbol{b}_\omega^T] \tag{3.27}$$

the error state vector containing the position error $\delta\boldsymbol{p}^n$, velocity error $\delta\boldsymbol{v}^n_{eb}$, attitude error $\delta\boldsymbol{\epsilon}$, accelerometer bias error $\delta\boldsymbol{b}_a$ and the gyroscope bias error $\delta\boldsymbol{b}_\omega$. Furthermore,

$$\boldsymbol{w}^T = [\boldsymbol{n}_a^T,\, \boldsymbol{n}_\omega^T,\, \boldsymbol{n}_{b_a}^T,\, \boldsymbol{n}_{b_\omega}^T] \tag{3.28}$$

indicates the process noise which originates from the accelerometer and gyroscope measurements (i.e. $\boldsymbol{n}_a$ and $\boldsymbol{n}_\omega$) as well as the sensor biases (i.e. $\boldsymbol{n}_{b_a}$ and $\boldsymbol{n}_{b_\omega}$). Thereby, $\boldsymbol{w}$ is assumed to be zero-mean Gaussian white noise with the covariance $\boldsymbol{Q}$, i.e. $\boldsymbol{w} \sim \mathcal{N}(\boldsymbol{0},\boldsymbol{Q})$.

To conduct the measurement update, the corresponding measurements have to be put into context to the states of the plant model (3.26). In a loosely coupled GNSS/INS integration scheme, the measured variables comprise the GNSS position

$$\boldsymbol{p}_A^{e,T} = [\varphi_A,\, \lambda_A,\, h_A] \tag{3.29}$$

in terms of latitude φ_A, longitude λ_A and altitude h_A as well as the GNSS velocity

$$\boldsymbol{v}_{eA}^{n,T} = [v^n_{eA,n},\, v^n_{eA,e},\, v^n_{eA,d}] \tag{3.30}$$

in terms of north, east and vertical velocity referring to the mounting position of the GNSS antenna. Therefore, the estimated quantities have to be transferred to the mounting position of the antenna. Finally, linearizing the nonlinear measurement equations with respect to the current state estimate while assuming that the measured outputs are superimposed by zero-mean Gaussian white noise, the following linear measurement model is gained

$$\underbrace{\begin{bmatrix}\delta\boldsymbol{p}^n_A\\ \delta\boldsymbol{v}^n_{eA}\end{bmatrix}}_{\delta\boldsymbol{y}(t)} = \underbrace{\begin{bmatrix}\boldsymbol{I} & \boldsymbol{0} & \boldsymbol{H}_{p,\epsilon} & \boldsymbol{0} & \boldsymbol{0}\\ \boldsymbol{0} & \boldsymbol{I} & \boldsymbol{H}_{v,\epsilon} & \boldsymbol{0} & \boldsymbol{H}_{v,b_\omega}\end{bmatrix}}_{\boldsymbol{H}} \underbrace{\begin{bmatrix}\delta\boldsymbol{p}^n\\ \delta\boldsymbol{v}^n_{eb}\\ \delta\boldsymbol{\epsilon}\\ \delta\boldsymbol{b}_a\\ \delta\boldsymbol{b}_\omega\end{bmatrix}}_{\delta\boldsymbol{x}(t)} + \underbrace{\begin{bmatrix}\boldsymbol{n}_p\\ \boldsymbol{n}_v\end{bmatrix}}_{\boldsymbol{v}(t)} \tag{3.31}$$

where

$$\delta\boldsymbol{y}^T = [\delta\boldsymbol{p}_A^{n,T},\, \delta\boldsymbol{v}_{eA}^{n,T}] \tag{3.32}$$

corresponds to the measurement residuals comprising the position $\delta \boldsymbol{p}_A^n$ and velocity residual $\delta \boldsymbol{v}_{A,eb}^n$ with respect to the antenna mounting position. Moreover,

$$\boldsymbol{v}^T = [\boldsymbol{n}_p^T,\, \boldsymbol{n}_v^T] \tag{3.33}$$

denominates the measurement noise which is assumed to be zero-mean Gaussian white noise with the covariance $\boldsymbol{R}$, i.e. $\boldsymbol{v} \sim \mathcal{N}(\boldsymbol{0},\boldsymbol{R})$. The position and velocity measurement residuals are determined in dependence of the INS mechanization state vector. In particular, the position residual $\delta \boldsymbol{p}_A^n$ can be expressed as

$$\delta \boldsymbol{p}_A^n = \begin{bmatrix} \delta p_n^n \\ \delta p_e^n \\ \delta p_d^n \end{bmatrix} = \begin{bmatrix} (\hat{\varphi} - \tilde{\varphi}_A) \cdot (R_n - \hat{h}) \\ (\hat{\lambda} - \tilde{\lambda}_A) \cdot (R_e - \hat{h}) \cos(\hat{\varphi}) \\ \hat{h} - \tilde{h}_A \end{bmatrix} + \hat{\boldsymbol{R}}_b^n \boldsymbol{r}_{IMU,A}^b. \tag{3.34}$$

where $\boldsymbol{r}_{IMU,A}^b$ denotes the vector pointing from the IMU to the antenna mounting position, R_n the north-south and R_e the east-west radius of curvature of the WGS84 reference ellipsoid. For the velocity residual $\delta \boldsymbol{v}_{A,eb}^n$ holds

$$\delta \boldsymbol{v}_{eA}^n = \hat{\boldsymbol{v}}_{eb}^n + \hat{\boldsymbol{R}}_b^n (\hat{\boldsymbol{\omega}}_{ib}^{b,*} \times \boldsymbol{r}_{IMU,A}^b) - \tilde{\boldsymbol{v}}_{eA}^n. \tag{3.35}$$

To be used in the ESS-KF-based estimator, the linearized estimator model (3.26),(3.31) has to be transferred to a discrete-time representation, thus yielding

$$\delta \boldsymbol{x}_{k+1} = \boldsymbol{F}_k \delta \boldsymbol{x}_k + \boldsymbol{G}_k \boldsymbol{w}_k \tag{3.36}$$

$$\delta \boldsymbol{y}_k = \boldsymbol{H}_k \delta \boldsymbol{x}_k + \boldsymbol{v}_k. \tag{3.37}$$

Due to the fact that the prediction of state variables is excluded from the ESS-EKF and conducted in the INS mechanization algorithm, the ESS-EKF prediction step is reduced to determining the estimation error covariance matrix $\boldsymbol{P}_k^-$ in accordance to [17]

$$\boldsymbol{P}_k^- = \boldsymbol{F}_{k-1} \boldsymbol{P}_{k-1}^+ \boldsymbol{F}_{k-1}^T + \boldsymbol{G}_{k-1} \boldsymbol{Q}_{k-1} \boldsymbol{G}_{k-1}^T \tag{3.38}$$

where $\boldsymbol{Q}_k = \boldsymbol{Q}/T_s$ indicates the discrete-time covariance matrix of the process noise $\boldsymbol{w}_k$ while T_s corresponds to the sampling time of the

Kalman filter. When a GNSS measurement is available without any time delay, the a posteriori error state vector $\delta\hat{\boldsymbol{x}}_k^+$ and covariance matrix $\boldsymbol{P}_k^+$ is obtained by

$$\boldsymbol{K}_k = \boldsymbol{P}_k^- \boldsymbol{H}_k^T (\boldsymbol{H}_k \boldsymbol{P}_k^- \boldsymbol{H}_k^T + \boldsymbol{R}_k)^{-1} \tag{3.39}$$

$$\delta\hat{\boldsymbol{x}}_k^+ = \boldsymbol{K}_k \underbrace{(\boldsymbol{h}(\hat{\boldsymbol{x}}_k^-, \boldsymbol{u}_k) - \tilde{\boldsymbol{y}}_k)}_{\delta\hat{\boldsymbol{y}}_k} \tag{3.40}$$

$$\boldsymbol{P}_k^+ = (\boldsymbol{I} - \boldsymbol{K}_k \boldsymbol{H}_k) \boldsymbol{P}_k^- \tag{3.41}$$

where $\boldsymbol{R}_k = \boldsymbol{R}$ denotes the discrete-time covariance matrix of the measurement noise $\boldsymbol{v}_k$. As previously stated, GNSS measurements are commonly affected by time delays. As far the u-blox GNSS receiver is concerned, a mean time delay of 0.18 s (see section 2.2.1) has been observed in experimental evaluations. Assuming that the measurements are available in time would cause serious systematic errors that cannot be tolerated for the considered application. To solve this issue, section 3.5.2 provides an approach to already compensate time delays in the estimator design.

3.5.2 Time Delayed Measurements

While the time interval between validity and availability of a measurement can commonly be neglected, this is in general not the case for GNSS measurements. Figure 3.6 illustrates the situation of time delayed measurements, i.e. a GNSS measurement is valid at time t_{valid} but available at time t_{avail}. Basically, this issue occurs due to internal receiver signal processing and data transmission, see [29]. Considering the mean time delay of 0.18 s for the u-blox receiver, neglecting this delay would e.g. cause a mismatch between the estimated a priori and measured position of about 2.5 m when moving with a velocity of 14 m/s. As the ESS-KF basically determines a weighted mean value of the estimated a priori and the measured variables, the systematic errors that are introduced in this way would be crucial for the considered application and would cause a violation of the horizontal accuracy and smoothness requirement. As previously indicated, an internal (software)

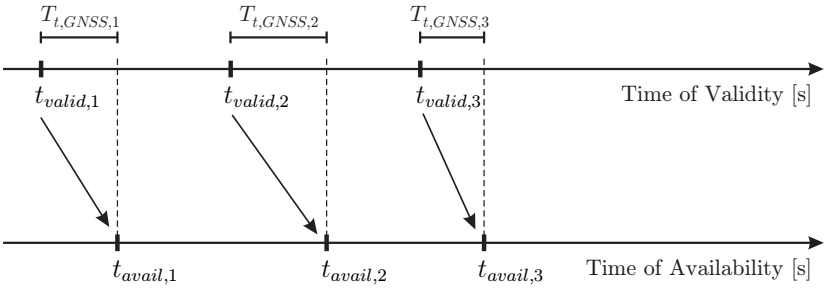

Figure 3.6: Time delayed GNSS measurements

clock is employed to determine the GNSS time delay

$$T_{t,GNSS} = t_{avail} - t_{valid}. \tag{3.42}$$

Particularly, this clock is synchronized with UTC time and uses the u-blox time pulse as well as the UTC message timestamp to determine the precise (delay-free) UTC time. In this context, t_{valid} corresponds to the GNSS message timestamp while t_{avail} refers to the internal clock's time when the measurement is available.

3.5.2.1 Full Reprocessing

An optimal solution to account for time delayed measurements is to reprocess the filter when the measurement is available at time step k_{avail}, see [60]. Therefore, recent filter states and inputs have to be stored and the filter has finally to be rolled back to time step k_{valid} when the GNSS data has been valid. Then, the update step is conducted at time k_{valid} and INS mechanization as well as covariance prediction is performed until the current time step $k = k_{avail}$. Thereby, the time delay is handled in an optimal way thus that the same estimate $\hat{\boldsymbol{x}}_k$ and estimation error covariance matrix $\boldsymbol{P}_k$ is obtained as if the measurement would have been available at time k_{valid}. Although this approach is optimal in order to compensate measurement time delays, its computational burden is too high to calculate the navigation solution in real-time. Therefore,

an sub-optimal approximation has been applied which is described in the following section.

3.5.2.2 Sub-Optimal Approximation

As full reprocessing the navigation filter is not feasible in real-time using the hardware setup described in section 2.2, a sub-optimal approximation is employed to compensate the time delay of a measurement $\tilde{\boldsymbol{y}}_k^{k-n}$ that is valid at time $k-n$ but available at time k. According to [28], modified measurement update equations are employed for this purpose

$$\boldsymbol{K}_k^* = \boldsymbol{C}_{k,k-n}\boldsymbol{H}_{k-n}^T(\boldsymbol{H}_{k-n}\boldsymbol{P}_{k-n}^-\boldsymbol{H}_{k-n}^T + \boldsymbol{R}_{k-n})^{-1} \tag{3.43}$$

$$\delta\hat{\boldsymbol{x}}_k^+ = \boldsymbol{K}_k^* \underbrace{(\boldsymbol{h}(\hat{\boldsymbol{x}}_{k-n}^-, \boldsymbol{u}_{k-n}) - \tilde{\boldsymbol{y}}_k^{k-n})}_{\delta\hat{\boldsymbol{y}}_k^{k-n}} \tag{3.44}$$

$$\boldsymbol{P}_k^+ = \boldsymbol{P}_k^- - \boldsymbol{K}_k^*\boldsymbol{H}_{k-n}\boldsymbol{C}_{k,k-n}. \tag{3.45}$$

Thereby, the calculation of the modified Kalman gain $\boldsymbol{K}_k^*$ as well as the a posteriori covariance matrix $\boldsymbol{P}_k^+$ rely on the measurement and covariance matrices at time $k-n$, i.e. when the processed measurement $\tilde{\boldsymbol{y}}_k^{k-n}$ has been valid. In this context, $\boldsymbol{C}_{k,k-n}$ indicates the approximated estimation error covariance at time k that would have been obtained if the measurement update had been conducted in time, i.e. at time $k-n$. To obtain the estimation error $\delta\hat{\boldsymbol{x}}_k^+$ at time k, the residual $\delta\hat{\boldsymbol{y}}_k^{k-n}$ at time $k-n$ is weighted with the modified Kalman gain $\boldsymbol{K}_k^*$. To simplify the computation of $\boldsymbol{C}_{k,k-n}$ and to allow for a real-time execution of the filter, it is assumed that the estimation error covariance matrix remains unchanged between time $k-n$ of validity and time k of availability, i.e.

$$\boldsymbol{C}_{k,k-n} \approx \boldsymbol{P}_{k-n}^- \approx \boldsymbol{P}_k^-. \tag{3.46}$$

It has to be noted that this assumption becomes less accurate for increasing time delays and increasing trajectory dynamics. Further details and a deduction of (3.43)-(3.45) can be found in [28].

To illustrate the influence of time delays in GNSS measurements on the considered application, a manually driven double lane change maneuver with high lateral accelerations of $\pm 1g$ is considered, see Figure 3.7. For the subsequent investigations, the data that has been recorded in experimental tests has been used in offline simulations. In order to develop solutions for all the issues that are related to navigation successively, the same maneuver will be examined subsequently. Figure 3.7

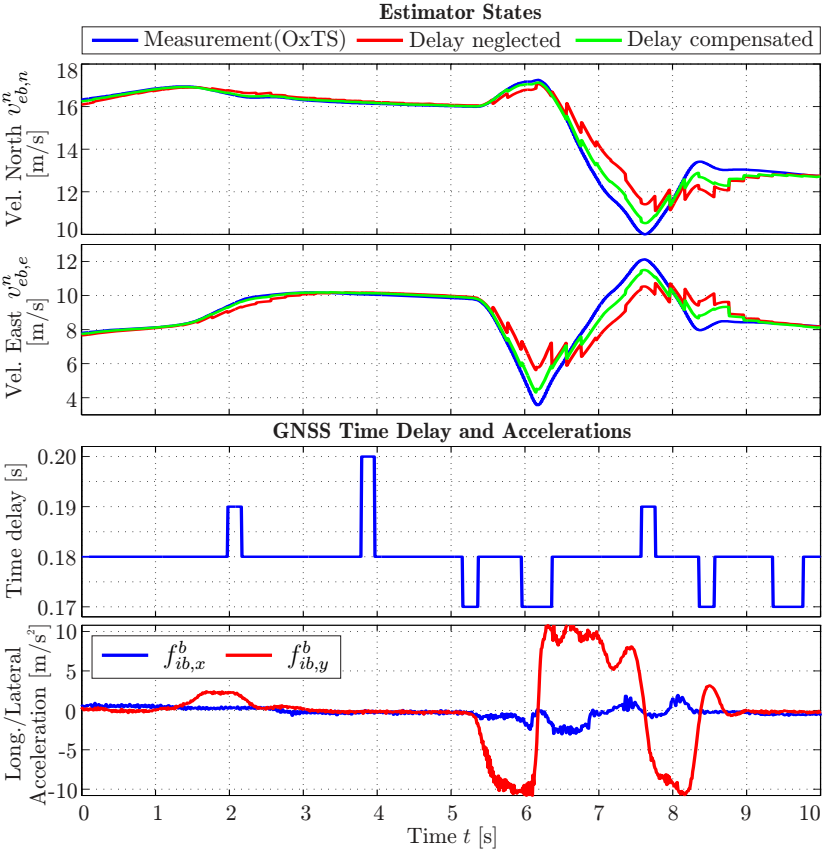

Figure 3.7: Estimated velocity with and without accounting for time delays

shows the estimated n-frame velocity when and when not accounting for time delays using the sub-optimal approximation. For the illustrated maneuver, GNSS time delays range from 0.17 to 0.2 s which is of the same magnitude as the GNSS receiver's sampling time. It can be noticed that estimation errors are considerably small from $t = 0$ to 5 s, i.e. before the maneuver is started and when having small lateral accelerations. Thereby, slightly larger errors can be noticed when time delays are neglected within this time interval. During the maneuver, i.e. from $t = 5$ to 10 s, velocity errors increase even when time delays are compensated. These errors are mainly caused by discontinuities in the aiding GNSS measurements as well as the fact that assumptions that have been made during filter design (especially for compensating time delays) become less accurate when having high horizontal accelerations. Nevertheless, velocity errors are significantly less and discontinuities (stepwise changes) occur less frequently when compensating time delays. Furthermore, the filter extensions that are introduced in section 3.7.2 to fulfill the accuracy and smoothness requirements allow for a further significant reduction of these errors during the maneuver.

3.5.3 Aided Heading Estimation

The vehicle's yaw angle with respect to true north (geodetic north) can directly be determined with high accuracy when using a multi-antenna configuration, see [18]. When considering the single-antenna setup that is employed in this contribution, the yaw angle is estimated through the numerical integration of inertial sensors and by processing GNSS position as well as velocity measurements in the error estimator according to section 3.4 and 3.5. Experimental evaluations have shown that the maximum error of the yaw angle estimate is about ± 4 deg compared to the OxTS RT3003 reference navigation system (having a dual-antenna setup). To improve the attitude estimate, a magnetic compass measuring the Earth's magnetic field is frequently utilized as additional aiding measurement [49], especially in the scope of Unmanned Aerial Vehicles (UAVs) to aid the roll and pitch estimate. However, these measurements are very sensitive to local electro-magnetic fields that might even originate from unpredictable sources like high-voltage power lines. Furthermore, the improvement of estimation performance is limited by

the accuracy of the aiding magnetometer measurement which is commonly less than the already achieved precision of the yaw angle estimate. E.g. in [61], the accuracy of the employed magnetometer is declared as $\pm 5\,\mathrm{deg}$. Therefore, the use of a magnetometer is discarded in the scope of this thesis.

On the contrary, this contribution incorporates kinematic vehicle constraints to aid the yaw angle estimate. As the vehicle is only able to move in the horizontal plane, the GNSS course angle ψ_{course}, i.e. the horizontal orientation of the velocity vector with respect to true north, is processed in the error estimator under certain conditions as subsequently discussed. Referring to section 2.2.1, the u-blox GNSS receiver provides the course angle with an accuracy of $0.5\,\mathrm{deg}$ (1σ), thus offering the potential for a further improvement of the yaw angle accuracy. For the filter modification, it has to be taken into account that

- the GNSS course angle ψ_{course} and the vehicle's yaw angle ψ coincide when driving almost straight, i.e. for small vehicle sideslip angles $\beta \approx 0\,\mathrm{deg}$ and thus for small lateral accelerations, see section 2.1.1. On the contrary, when the vehicle performs maneuvers with high lateral accelerations, the vehicle sideslip angle β and thus the yaw angle errors increase simultaneously when using the course angle as aiding measurement. It has turned out that a yaw rate threshold is an appropriate way to assess if the vehicle is driving straight, i.e. $|\dot{\psi}| < \dot{\psi}_{thld}$.
- the GNSS course angle's measurement variance increases significantly for low velocities, see [62]. Thus, the course angle is only employed as aiding measurement when a horizontal velocity threshold $v_{hor,thld}$ is exceeded.

Summing up, the corresponding measurement equation, i.e. the relationship between the estimator states and the additional aiding measurement $\tilde{\psi}_{course}$, can be formulated as

$$\tilde{\psi}_{course} = \begin{cases} \psi & \text{, if } |\dot{\psi}| \leq \dot{\psi}_{thld} \ \wedge \ v_{hor} \geq v_{hor,thld} \\ 0 & \text{, otherwise} \end{cases} \tag{3.47}$$

where $\dot{\psi}_{thld}$ denotes the upper absolute yaw rate threshold, $v_{hor,thld}$ the lower velocity threshold for processing the course angle in the update

step of the error estimator and

$$v_{hor} = \sqrt{{v_{eb,n}^n}^2 + {v_{eb,e}^n}^2} \tag{3.48}$$

the horizontal velocity in the n-frame. Hence, (3.31) is modified with respect to (3.47) thus yielding

$$\underbrace{\begin{bmatrix} \delta \boldsymbol{p}^n \\ \delta \boldsymbol{v}_{eb}^n \\ \delta \psi \end{bmatrix}}_{\delta \boldsymbol{y}(t)} = \underbrace{\begin{bmatrix} \boldsymbol{I} & \boldsymbol{0} & \boldsymbol{H}_{p,\epsilon} & \boldsymbol{0} & \boldsymbol{0} \\ \boldsymbol{0} & \boldsymbol{I} & \boldsymbol{H}_{v,\epsilon} & \boldsymbol{0} & \boldsymbol{H}_{v,b_\omega} \\ \boldsymbol{0} & \boldsymbol{0} & \boldsymbol{H}_{\psi,\epsilon} & \boldsymbol{0} & \boldsymbol{0} \end{bmatrix}}_{\boldsymbol{H}} \underbrace{\begin{bmatrix} \delta \boldsymbol{p}^n \\ \delta \boldsymbol{v}_{eb}^n \\ \delta \boldsymbol{\epsilon} \\ \delta \boldsymbol{b}_a \\ \delta \boldsymbol{b}_\omega \end{bmatrix}}_{\delta \boldsymbol{x}(t)} + \underbrace{\begin{bmatrix} \boldsymbol{n}_p \\ \boldsymbol{n}_v \\ \boldsymbol{n}_\psi \end{bmatrix}}_{\boldsymbol{v}(t)} \tag{3.49}$$

with

$$\boldsymbol{H}_{\psi,\epsilon} = \begin{cases} [0\ 0\ 1], & \text{if } |\dot{\psi}| \leq \dot{\psi}_{thld} \ \wedge \ v_{hor} \geq v_{hor,thld} \\ [0\ 0\ 0], & \text{otherwise.} \end{cases} \tag{3.50}$$

Finally, the yaw angle residual $\delta\psi$ can be expressed as

$$\delta\psi = \hat{\psi} - \tilde{\psi}_{course}. \tag{3.51}$$

Figure 3.8 depicts the estimated yaw angle when and when not using the additional aiding GNSS course angle measurement for the double lane change maneuver that has already been considered using a velocity threshold $v_{hor,thld}$ of 2 m/s and a yaw rate threshold $\dot{\psi}_{thld}$ of 2 deg/s. Before the maneuver is started at $t = 8$ s, the yaw angle error is about 0.4 deg less than in the non-aided case while the yaw angle is aided when driving straight (indicated by the value one of the binary yaw aiding flag). In other scenarios, the difference is even noticeably larger and has a magnitude of about 2 to 3 deg. During the maneuver, the non-aided yaw angle error increases significantly when processing a GNSS measurement (i.e. position and velocity) at $t = 9.6$ s. This effect is not present in the aided case as the yaw angle has been updated using the GNSS course angle just before the maneuver starts at $t = 8.6$ s. Thus, the believe in this estimate is higher which corresponds to a lower

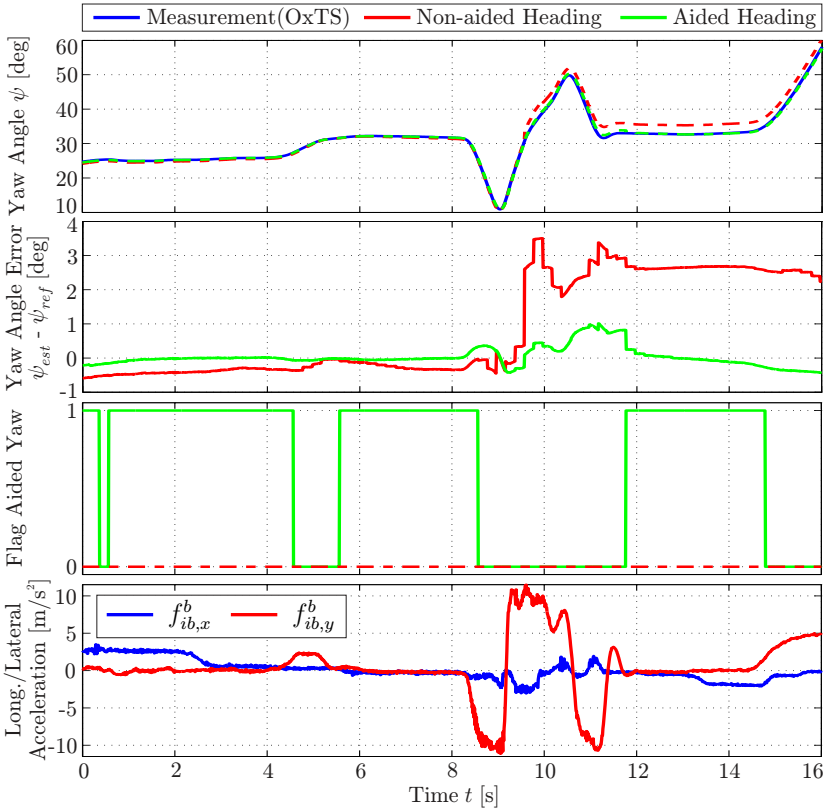

Figure 3.8: Aided heading: Experimental results

estimation error covariance of the yaw angle. The error of the non-aided yaw angle estimate increases up to 3.5 deg and remains at about 2.6 deg after the maneuver. Contrarily, the yaw angle error in the aided case just increases up to 1 deg during the maneuver and decreases to 0.25 deg when the heading is aided again after the maneuver end at $t = 11.8$ s. Overall, a root mean square error (RMSE) of 0.28 deg is obtained when aiding the yaw angle estimate while the RMSE amounts to 1.70 deg in the non-aided case. Concluding, introducing the additional aiding

GNSS course angle measurement is an appropriate measure to further improve the vehicle's heading estimate noticeably.

3.6 Error Correction and Navigation Solution

3.6.1 Error Correction

To obtain the a posteriori navigation solution $\hat{\boldsymbol{x}}^+$, the a priori navigation solution $\hat{\boldsymbol{x}}^-$ that results from the INS mechanization has to be corrected with respect to the estimated error $\delta\hat{\boldsymbol{x}}$. As explained in section 3.5, position errors are estimated in the n-frame (e-frame is used for INS mechanization) and attitude errors are expressed as Euler angle errors (quaternions are used for INS mechanization) for numerical reasons. Referring to [28], the a posteriori position estimate $\hat{\boldsymbol{p}}^{e,+}$ is obtained by transferring the a posteriori position error $\delta\hat{\boldsymbol{p}}^{n,+}$ to the e-frame, i.e.

$$\hat{\varphi}^+ = \hat{\varphi}^- - \frac{\delta\hat{p}_n^{n,+}}{R_n - \hat{h}^-}, \tag{3.52}$$

$$\hat{\lambda}^+ = \hat{\lambda}^- - \frac{\delta\hat{p}_e^{n,+}}{(R_e - \hat{h}^-)\cos(\hat{\varphi}^-)}, \tag{3.53}$$

$$\hat{h}^+ = \hat{h}^- - \delta\hat{p}_d^{n,+}. \tag{3.54}$$

The a posteriori velocity estimate $\hat{\boldsymbol{v}}_{eb}^{n,+}$ can be determined by subtracting the error $\delta\hat{\boldsymbol{v}}_{eb}^{n,+}$ from the a priori estimate $\hat{\boldsymbol{v}}_{eb}^{n,-}$ as both refer to the same reference frame, i.e.

$$\hat{\boldsymbol{v}}_{eb}^{n,+} = \hat{\boldsymbol{v}}_{eb}^{n,-} - \delta\hat{\boldsymbol{v}}_{eb}^{n,+}. \tag{3.55}$$

To compute the a posteriori quaternion $\hat{\boldsymbol{q}}_b^{n,+}$ describing the vehicle attitude, the quaternion $\boldsymbol{q}_c$ is derived from the estimated attitude error $\delta\hat{\boldsymbol{\epsilon}}^+$ and the orientation vector $\boldsymbol{\sigma}_c$

$$\boldsymbol{\sigma}_c = -\delta\hat{\boldsymbol{\epsilon}}^+, \tag{3.56}$$

$$\boldsymbol{q}_c = \begin{bmatrix} \cos(\|\boldsymbol{\sigma}_c\|/2) \\ (\boldsymbol{\sigma}_c/\|\boldsymbol{\sigma}_c\|)\sin(\|\boldsymbol{\sigma}_c\|/2) \end{bmatrix} \tag{3.57}$$

and multiplied with the a priori attitude estimate $\hat{\boldsymbol{q}}_b^{n,-}$

$$\hat{\boldsymbol{q}}_b^{n,+} = \boldsymbol{q}_c \circ \hat{\boldsymbol{q}}_b^{n,-}. \tag{3.58}$$

Finally, the a posteriori sensor biases are gained through

$$\hat{\boldsymbol{b}}_a^{+} = \hat{\boldsymbol{b}}_a^{-} - \delta\hat{\boldsymbol{b}}_a^{+}, \tag{3.59}$$

$$\hat{\boldsymbol{b}}_\omega^{+} = \hat{\boldsymbol{b}}_\omega^{-} - \delta\hat{\boldsymbol{b}}_\omega^{+}, \tag{3.60}$$

and can be used to derive the bias compensated IMU measurements

$$\boldsymbol{f}_{ib}^{b,*} = \tilde{\boldsymbol{f}}_{ib}^{b} - \hat{\boldsymbol{b}}_a^{+}, \tag{3.61}$$

$$\boldsymbol{\omega}_{ib}^{b,*} = \tilde{\boldsymbol{\omega}}_{ib}^{b} - \hat{\boldsymbol{b}}_\omega^{+}. \tag{3.62}$$

3.6.2 Resulting Navigation Solution

Concluding, the resulting a posteriori navigation solution that is supplied by the GNSS/INS integration scheme comprises

- the position $\boldsymbol{p}^{e,T} = [\varphi,\ \lambda,\ h]$ of the IMU in the WGS84 reference frame with respect to latitude φ, longitude λ and altitude h.
- the velocity $\boldsymbol{v}_{eb}^{n,T} = [v_{eb,n}^{n},\ v_{eb,n}^{e},\ v_{eb,n}^{d}]$ of the IMU orientated north, east and downwards in the n-frame.
- the orientation quaternion $\boldsymbol{q}_b^{n,T} = [q_{b,1}^{n},\ q_{b,2}^{n},\ q_{b,3}^{n},\ q_{b,4}^{n}]$ describing the relative orientation of the b- and the n-frame.
- the bias compensated IMU accelerations $\boldsymbol{f}_{ib}^{b,*,T} = [f_{ib,x}^{b,*},\ f_{ib,y}^{b,*},f_{ib,z}^{b,*}]$ and angular rates $\boldsymbol{\omega}_{ib}^{b,*,T} = [\omega_{ib,x}^{b,*},\ \omega_{ib,y}^{b,*},\ \omega_{ib,z}^{b,*}]$.

3.7 Further Extensions for Autonomous Vehicle Guidance

Now that the basic integration scheme has been introduced, further extensions to satisfy the requirements on the navigation solution (see

section 3.2) are discussed in this section. Referring to section 3.2, autonomous driving in the context of CA has been assessed not to be feasible when relying on absolute positioning. Instead, relative positioning can solve this issue when assuming that navigation errors are approximately constant in a close local environment and thus do not influence the (relative) vehicle position significantly. Section 3.7.1 outlines the corresponding transformation from absolute e-frame coordinates to the local Cartesian m-frame. Furthermore, the accuracy and smoothness requirements in section 3.2 cannot be fulfilled when operating the navigation filter as introduced previously. Therefore, an appropriate filter modification that solves this problem is presented in section 3.7.2.

3.7.1 Transformation to Maneuver Reference Frame

For the purpose of relative positioning, the (local) Cartesian m-frame has been introduced in section 3.3.1. Recapitulating, the m-frame generally refers to the vehicle's CG position while the origin of the m-frame is defined by the initial maneuver position. Due to the fact that the navigation solution provides the IMU position

$$\boldsymbol{p}_{IMU}^{e,T} = [\varphi_{IMU},\, \lambda_{IMU},\, h_{IMU}] \tag{3.63}$$

in the e-frame, a transformation from the e- to the m-frame as well as from the IMU's mounting position to CG has to be conducted to obtain the vehicle's CG position

$$\boldsymbol{p}_{CG}^{m,T} = [x_{CG}^{m},\, y_{CG}^{m},\, z_{CG}^{m}] \tag{3.64}$$

in the m-frame, see Figure 3.9. Let $\boldsymbol{p}_{IMU,0}^{e}$ denote the initial position and ψ_0 the initial yaw angle with respect to the e-frame when the evasive maneuver is initiated. As a first step, the initial position $\boldsymbol{p}_{IMU,0}^{e}$ as well as the current position $\boldsymbol{p}_{IMU}^{e}$ are considered in a local n-frame and transferred to CG, thus yielding

$$\boldsymbol{p}_{CG,0}^{n} = \boldsymbol{p}_{IMU,0}^{n} + \boldsymbol{R}_{b,0}^{n}\boldsymbol{r}_{IMU,CG}^{b}, \tag{3.65}$$

$$\boldsymbol{p}_{CG}^{n} = \boldsymbol{p}_{IMU}^{n} + \boldsymbol{R}_{b}^{n}\boldsymbol{r}_{IMU,CG}^{b} \tag{3.66}$$

where $\boldsymbol{p}_{IMU,0}^{n}$ and $\boldsymbol{p}_{IMU}^{n}$ denote the initial and current IMU position in the n-frame respectively. To transfer these positions to CG, the

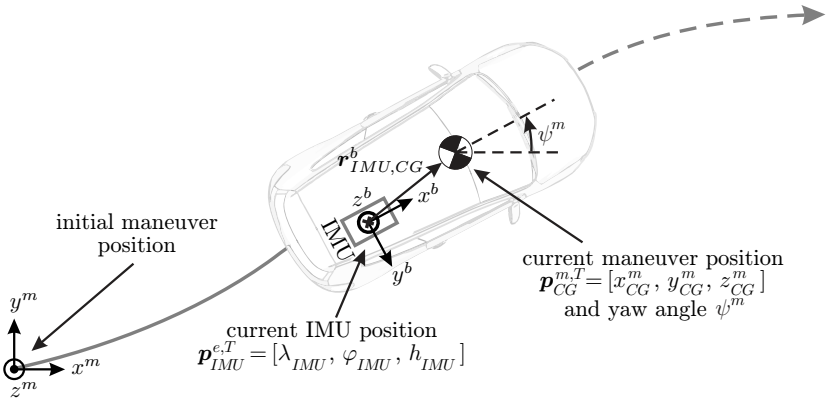

Figure 3.9: Maneuver reference frame

vector that points from the IMU to CG in the n-frame has to be added. Therefore, the vector $\boldsymbol{r}_{IMU,CG}^{b}$ has to be rotated from the b- to the n-frame using the initial DCM $\boldsymbol{R}_{b,0}^{n}$ respectively the current DCM $\boldsymbol{R}_{b}^{n}$. Second, the vector $\boldsymbol{r}_{CG}^{n}$ pointing from $\boldsymbol{p}_{CG,0}^{n}$ to $\boldsymbol{p}_{CG}^{n}$ is determined by

$$\boldsymbol{r}_{CG}^{n} = \boldsymbol{p}_{CG}^{n} - \boldsymbol{p}_{CG,0}^{n} \tag{3.67}$$

$$= \underbrace{(\boldsymbol{p}_{IMU}^{n} - \boldsymbol{p}_{IMU,0}^{n})}_{\boldsymbol{r}_{IMU}^{n}} + \boldsymbol{R}_{b}^{n}\boldsymbol{r}_{IMU,CG}^{b} - \boldsymbol{R}_{b,0}^{n}\boldsymbol{r}_{IMU,CG}^{b}. \tag{3.68}$$

Neglecting the initial yaw angle ψ_0, $\boldsymbol{r}_{CG}^{n}$ represents a position vector in a local Cartesian reference frame having $\boldsymbol{p}_{CG,0}^{n}$ as origin. In this context, the vector

$$\boldsymbol{r}_{IMU}^{n,T} = [r_{n}^{n},\, r_{e}^{n},\, r_{d}^{n}] \tag{3.69}$$

pointing from the initial position $\boldsymbol{p}_{IMU,0}^{e,T} = [\varphi_{IMU,0},\, \lambda_{IMU,0},\, h_{IMU,0}]$ to the current position $\boldsymbol{p}_{IMU}^{e}$ in the n-frame with origin $\boldsymbol{p}_{IMU,0}^{e}$ can be expressed as

$$r_{n}^{n} = (\varphi_{IMU} - \varphi_{IMU,0}) \cdot (R_{n} - h_{IMU,0}), \tag{3.70}$$

$$r_{e}^{n} = (\lambda_{IMU} - \lambda_{IMU,0}) \cdot (R_{e} - h_{IMU,0}) \cdot \cos(\varphi_{IMU,0}), \tag{3.71}$$

$$r_{d}^{n} = h_{IMU} - h_{IMU,0}. \tag{3.72}$$

Finally, the vehicle position $\boldsymbol{p}_{CG}^{m,T} = [x_{CG}^{m},\, y_{CG}^{m},\, z_{CG}^{m}]$ in the m-frame can be obtained by rotating $\boldsymbol{r}_{CG}^{n}$ from the n- to the m-frame, i.e.

$$\boldsymbol{p}_{CG}^{m} = \boldsymbol{R}_{n}^{m}\ \boldsymbol{r}_{CG}^{n} \tag{3.73}$$

where $\boldsymbol{R}_{n}^{m}$ indicates the corresponding DCM. According to section 3.3.1, the m-frame's x-axis coincides with longitudinal vehicle axis when the maneuver is initiated while its orientation is forward, left and upwards. Considering that the n-frame is directed forward, right and downwards, $\boldsymbol{R}_{n}^{m}$ performs a rotation by $-\psi_0$ with respect to the z^n-axis to align the x^n-axis with the initial vehicle orientation and by 180 deg with respect to the resulting $x^{n'}$-axis to obtain the desired m-frame orientation.

The vehicle's yaw angle ψ^m with respect to the m-frame is determined by subtracting the initial yaw angle $0 \leq \psi_0 < 2\pi$ from the current yaw angle $0 \leq \psi < 2\pi$. As the m-frame is directed upwards, the corresponding sign of the yaw angle has finally to be inverted, thus obtaining

$$\psi^m = -(\psi - \psi_0) = \psi_0 - \psi. \tag{3.74}$$

In order to obtain $0 \leq \psi^m < 2\pi$, 2π has to be added if $\psi^m < 0$ respectively 2π has to be subtracted if $\psi^m \geq 2\pi$. Consequently, (3.74) is modified to

$$\psi^m = \begin{cases} \psi_0 - \psi & , 0 \leq \psi_0 - \psi < 2\pi \\ \psi_0 - \psi - 2\pi \cdot \mathrm{sign}(\psi_0 - \psi) & , \text{otherwise.} \end{cases} \tag{3.75}$$

3.7.2 Filter Modifications

In this section, a filter modification is proposed to overcome the problem of growing position errors and discontinuities for large horizontal accelerations. In this way, the navigation requirements that have been formulated in section 3.2 can be satisfied. To comprehend why this measure becomes necessary, the vehicle's m-frame position when operating the filter conventionally is analyzed. Figure 3.10 depicts the estimated and the reference position solution in the m-frame for the double lane change maneuver which has already been considered previously. In this regard, the reference position is obtained by applying the m-frame transformation to the OxTS RT3003 navigation solution. When examining

horizontal position errors it can be noticed that these errors increase up to 1.1 m during the maneuver. Furthermore, stepwise position changes of about 0.3 m are present in the navigation solution. Thus, the conventional closed-loop operation is not applicable for the purpose of autonomous vehicle guidance when having high horizontal accelerations as it meets neither the accuracy nor the smoothness requirements. To fulfill the requirements on the navigation solution during the maneuver, the following two concepts have mainly been considered:

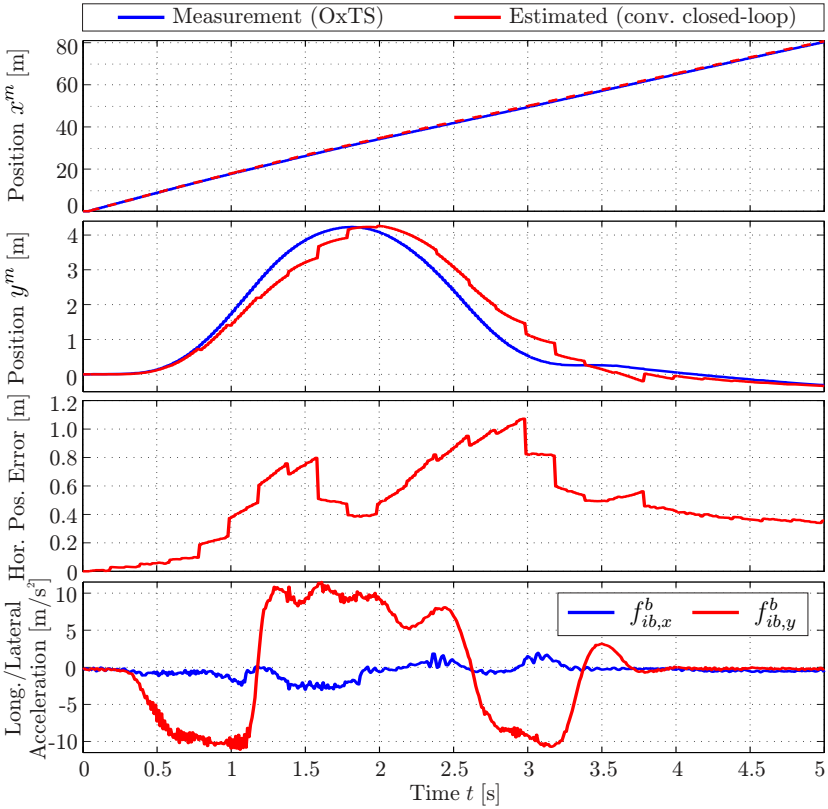

Figure 3.10: Position solution for conventional closed-loop operating mode

- Dead reckoning (subsequently referred to as DR), i.e. operating the navigation filter open-loop.
- Closed-loop operation but with an appropriately decreased weight on the GNSS measurements (consecutively referred to as LWM).

For DR, the navigation filter is operated open-loop during the maneuver such that GNSS measurements are discarded and the navigation solution solely relies on the INS mechanization. Contrarily, the strat-

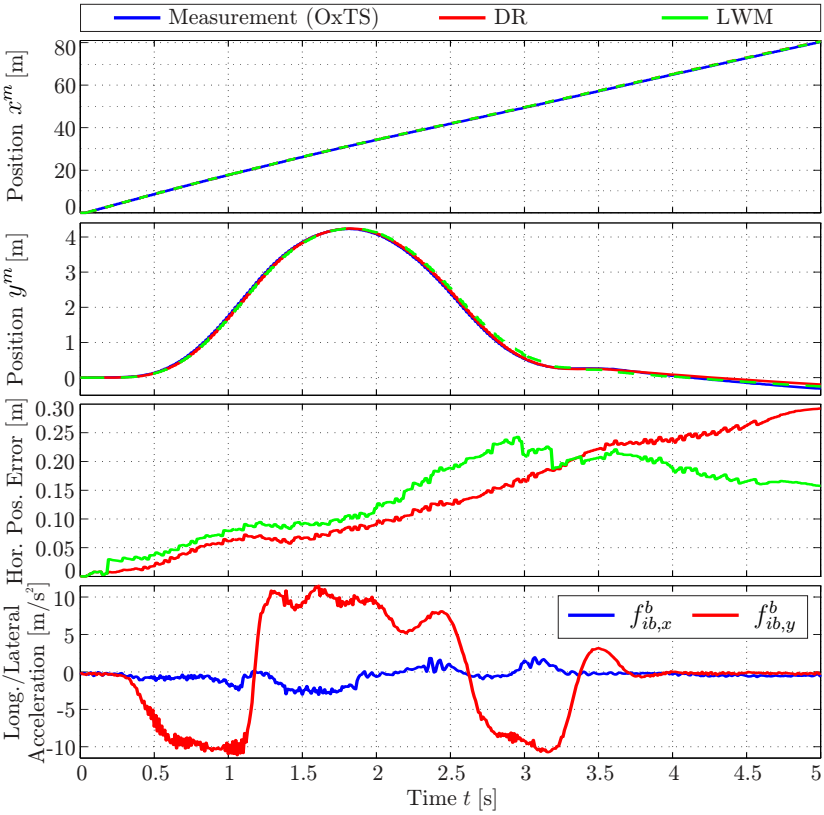

Figure 3.11: Position solution for operating modes DR and LWM

egy LWM employs a low-weight measurement covariance matrix $\boldsymbol{R}_{lw}$ during the maneuver, i.e. GNSS position and velocity measurements covariances are chosen large to decrease the corresponding weight in the update step while the covariance of the GNSS course angle remains unchanged in order to aid the yaw angle estimate appropriately. When not conducting an evasion maneuver, a nominal measurement covariance matrix $\boldsymbol{R}_{nom}$ is employed to calibrate inertial sensors, i.e. to compensate sensor biases.

A comparison of LWM and DR is illustrated in Figure 3.11. It can be recognized that position errors for LWM are larger in the first half of the maneuver. Nonetheless, these errors increase almost monotonically for DR and thus are larger in the second half of the maneuver. For the entire maneuver, the horizontal position error increases up to 0.25 m for LWM and 0.3 m for DR. Overall, position errors are comparable for both modes of operation and the accuracy requirement is met in both cases. Furthermore, both operating modes provide a smooth position trajectory such that only small stepwise position changes of about 0.05 m can be observed. Finally, LWM is preferred because position errors do not increase monotonically in time due to its closes-loop operation. Especially when larger position errors occur early during the maneuver, the use of DR has turned out to be disadvantageous as it leads to unacceptable position errors that violate the accuracy requirement. Consequently, LWM is assessed to be the superior approach and is thus applied subsequently.

3.8 Experimental Results

3.8.1 Test Scenario and Filter Parameterization

Now that a low-cost GNSS-based navigation concept for autonomous evasion maneuvers with high horizontal accelerations has been developed successfully, this section finally provides an overview of the estimation results that are gained when using LWM as operating mode. Therefore, the double lane change maneuver that has been investigated previously will be used as test scenario. For reasons of clarity, the focus

of the following results relies on the horizontal position in the m-frame, the horizontal velocity in the n-frame and the yaw angle with respect to true north. According to section 3.1, a sampling rate of 100 Hz has been chosen for INS mechanization as well as the error estimator.

As far as filter parameterization is concerned, most of the variances in the process noise covariance matrix $\boldsymbol{Q}$ and the nominal measurement noise covariance matrix $\boldsymbol{R}_{nom}$ can be derived from sensor specification or experimental evaluations. In this regard, the standard deviations of the IMU's noise and its biases, the GNSS velocity and the GNSS course angle are basically known by specification or have been identified in experimental tests, see section 2.2.1. Due to several error sources like atmospheric or receiver clock errors the assumption of zero-mean Gaussian white noise is generally not valid for GNSS position measurements, see [27]. Thus, the corresponding measurement noise covariance has been determined by optimizing the nominal system performance in a variety of test scenarios. For the navigation mode LWM, the low-weight measurement covariance matrix $\boldsymbol{R}_{lw}$ has been obtained by tuning the covariance of the GNSS position and velocity measurements such that the average estimation performance becomes optimal. As indicated in section 3.7.2, the GNSS course angle covariance is chosen equal for $\boldsymbol{R}_{nom}$ and $\boldsymbol{R}_{lw}$ to aid the yaw angle estimate appropriately. For further details on the filter parameterization, see section C.5.

3.8.2 Position

Figure 3.12 illustrates the estimated position $\boldsymbol{p}_{est}^{m,T} = [x_{est}^{m},\, y_{est}^{m}]$ and the OxTS RT3003 reference position $\boldsymbol{p}_{ref}^{m,T} = [x_{ref}^{m},\, y_{ref}^{m}]$ in the m-frame. Compared to Figure 3.11, longitudinal and lateral position errors are additionally depicted. It can be recognized that the horizontal position error $\|\boldsymbol{p}_{est}^{m} - \boldsymbol{p}_{ref}^{m}\|$ is mainly dominated by the longitudinal position error $x_{est}^{m} - x_{ref}^{m}$ which has a maximum absolute value of 0.21 m and a RMSE of 0.14 m. On the contrary, the lateral position error $y_{est}^{m} - y_{ref}^{m}$ is noticeably less and increases up to an absolute value of 0.15 m while having a RMSE of 0.07 m. Overall, the horizontal position error has an absolute maximum value of 0.24 m and a RMSE of 0.15 m for a maneuver at the handling limits having lateral accelerations of $\pm 1g$. At

the same time, the largest position steps can be observed in the lateral position and have a magnitude of 0.07 m.

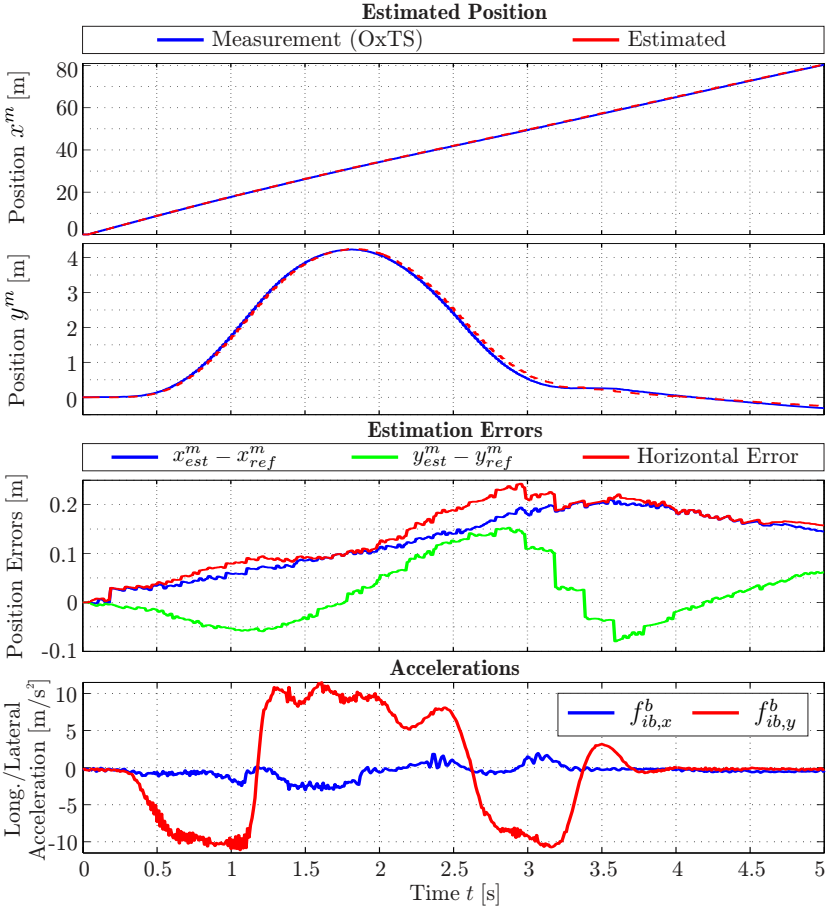

Figure 3.12: Position estimate in the m-frame for LWM navigation mode

3.8.3 Velocity

In the following, the n-frame velocity is considered for evaluation purposes as it is important to derive further quantities, e.g. the velocity at CG in section 4.2, while the m-frame velocity is not of major importance. The estimated n-frame velocity is depicted along with its reference values and corresponding estimation errors in Figure 3.13. When comparing Figure 3.13 with Figure 3.7, it can initially be observed that the velocity estimate matches the reference closer such that velocity errors can indeed further be reduced when using LWM as filter operating mode. Specifically, the velocity with respect to true north shows

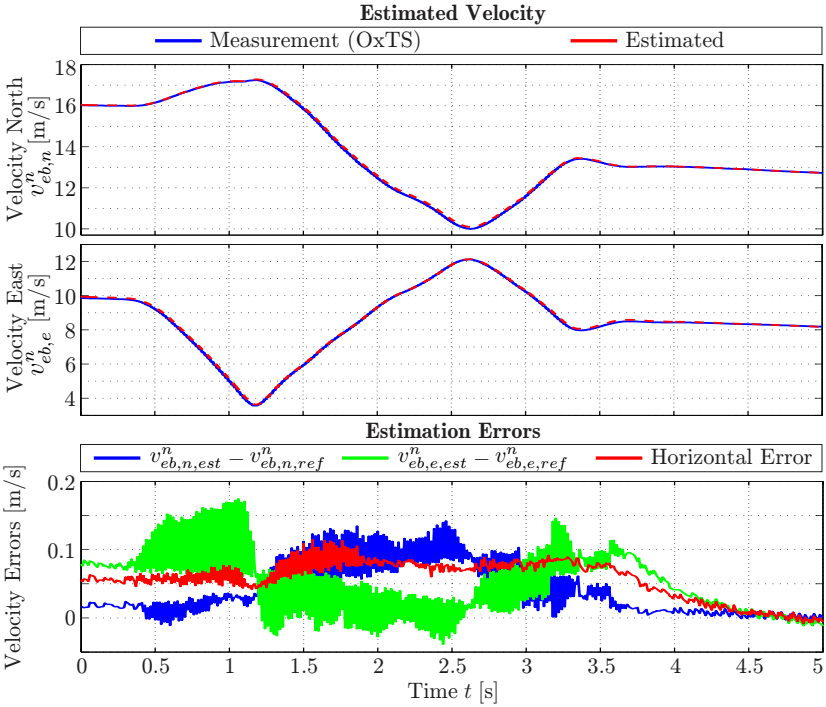

Figure 3.13: Velocity estimate in the n-frame for LWM navigation mode

a maximum absolute error of 0.14 m/s and a RMSE of 0.06 m/s while a maximum absolute error of 0.17 m/s and a RMSE of 0.07 m/s can be observed for the estimated velocity with respect to east. Finally, the horizontal velocity error increases up to 0.11 m/s while the RMSE amounts to 0.06 m/s.

3.8.4 Attitude

In this section, the estimated yaw angle with respect to true north (i.e. in the n-frame) is evaluated. As the yaw angle with respect to the n- and m-frame just differs in an offset (see section 3.7.1), the following conclusions are valid for the m-frame as well. According to Figure 3.14, it is apparent that the reference yaw angle is tracked very close. Particularly, the estimated yaw angle shows a maximum absolute deviation of 0.49 deg from its reference. The discontinuity at $t = 3.7$ s occurs when the yaw angle is aided again after the maneuver is ended, i.e. when driving approximately straight. Overall, a RMSE of 0.29 deg results for the entire maneuver.

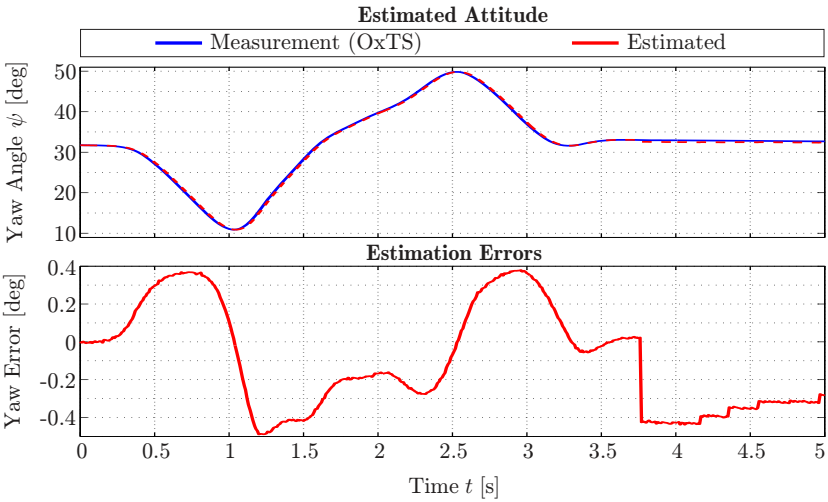

Figure 3.14: Yaw angle estimate in n-frame for LWM navigation mode

3.8.5 Assessment of Navigation Performance

Table 3.1 summarizes the results that have been gained in terms of maximum absolute errors and RMSE. Recapitulating the requirements imposed on the position accuracy and its smoothness, a maximum position error of 0.5 m and a maximum stepwise position change of 0.1 m have been identified to be tolerable. These requirements are indeed satisfied while the maximum horizontal position error is considerably less than the upper feasibility bound. However, the reader should be aware that there might be (rare) disadvantageous situations in which the accuracy requirement is not fulfilled, e.g. when sensor biases are not estimated appropriately. In order to improve reliability and accuracy, further aiding sensor measurements of a radar, LiDAR or camera can be incorporated in the filter design, see [63, 64]. As far as the velocity estimate is concerned, experimental results are assessed to be satisfying especially when considering that the achievable 1σ-accuracy of u-blox velocity measurements is 0.1 m/s. The same conclusion can be drawn for the yaw angle estimate when taking into account that the 1σ-accuracy of u-blox course angle measurements is 0.5 deg. Finally, the navigation performance is assessed to be appropriate for the considered application as it fulfills all the specified requirements.

Table 3.1: Navigation performance for maneuver with $1g$ hor. acceleration

	Max.	RMSE
Position Errors [m] (m-frame)		
x^m-direction	0.21	0.14
y^m-direction	0.15	0.07
Horizontal	0.24	0.15
Stepwise changes (x^m, y^m, hor.)	0.07	-
Velocity Errors [m/s] (n-frame)		
Velocity north	0.14	0.06
Velocity east	0.17	0.07
Horizontal	0.11	0.06
Attitude Errors [deg]		
Yaw angle	0.49	0.29

4 Vehicle State Estimation

4.1 Motivation and Related Work

To employ the optimal vehicle dynamics control scheme indicated in section 1.2, key vehicle states such as the yaw rate, longitudinal and lateral vehicle velocity at CG are required. While the yaw rate can be measured directly using commonly employed sensors, this is in general not the case for the vehicle's longitudinal and lateral velocity when not using cost-intensive (optical) sensors. Studies have shown that these quantities cannot be derived from the navigation solution with an appropriate accuracy. For this reason, an additional EKF-based estimator relying on a dynamic vehicle model is introduced in this chapter.

In literature, the estimation of key vehicle states has widely been discussed. Previously published approaches comprise Luenberger observers [65], nonlinear observers [66, 67] as well as Kalman filter (KF) [68] and extended Kalman filter (EKF) based estimators [69]. While all these contributions solely rely on a nominal vehicle and tire model, there are approaches that are designed to deal with model uncertainties. Especially tire parameters are difficult to identify and change under different environmental conditions, e.g. when changing from a dry to a wet road surface. In this context, [70, 71] present an EKF-based estimator that incorporates the tire forces in the state vector instead of using a particular tire model. The studies carried out in [72] tend in the same direction whereas a linear tire model (using additional information about tire force generation) is used and the cornering stiffness is estimated and thus adapted online. [73] proposes a combination of a sliding-mode observer and an EKF, including the cornering stiffness at the front and the rear axle in the EKF's state vector for adaptation purposes. In [74], the vehicle sideslip angle is derived from a simple algebraic equation while the relevant parameters such as the cornering stiffness at the front and rear axle are estimated online. An observer that is explicitly

designed such that it is robust with respect to model uncertainties can be found in [68]. As an extension of [67], [75] additionally proposes an adaptation of the friction coefficient to apply the observer even when road conditions are uncertain or change during operation. To cope with changing model parameters like the vehicle mass or the mass moment of inertia, [76] introduces a dual extended Kalman filter (DEKF) that employs two EKF in parallel for state and parameter estimation. In recent years, the additional use of GNSS velocity measurements for the purpose of vehicle state estimation has been investigated, see [77–79]. Generally, the main advantage of using GNSS-based velocity measurements can be seen in the achievable accuracy, e.g. $0.05\,\mathrm{m/s}$ (1σ) for GPS [18], as well as the independence from tire slip. On the contrary, ABS wheel speeds may significantly be impaired by wheel slip and thus may lead to a degraded estimation performance. It has to be noted that classical approaches rely on a dynamic vehicle model while GNSS-based vehicle state estimators are in general pure kinematic filters.

In the following, an EKF-based estimator to determine the longitudinal and lateral velocity at CG as well as the yaw rate is proposed. Thereby, the estimator is designed in such a way that it is adaptive with respect to uncertainties in the tire-road contact. To achieve the adaptive behavior, two additional estimator states are introduced to scale longitudinal and lateral tire forces. While the basic idea is comparable to the approach in [72, 73], there are distinguishable differences. This work generally scales tire forces, which are determined through a nonlinear tire model, instead of solely adapting the cornering stiffness. In this way, the adaptation is more general and also appropriate when tires are saturated while the local approximation of the cornering stiffness actually changes its sign at the friction limit, see section 2.1.2.4. As stated in [75], the observability and finally the stability of the observer inherently depend on the excitation, i.e. the variation in the longitudinal and lateral velocity and acceleration due to steering and accelerating respectively braking. To solve this issue, [72, 73] tune the filter covariances appropriately such that adaptation happens conservatively respectively in certain sideslip angle intervals. As a major contribution, this thesis proposes a concept for proving the local observability of the adaptation states online and keep them constant by introducing these states as virtual measurement variables when loosing local observability. By using this concept, the

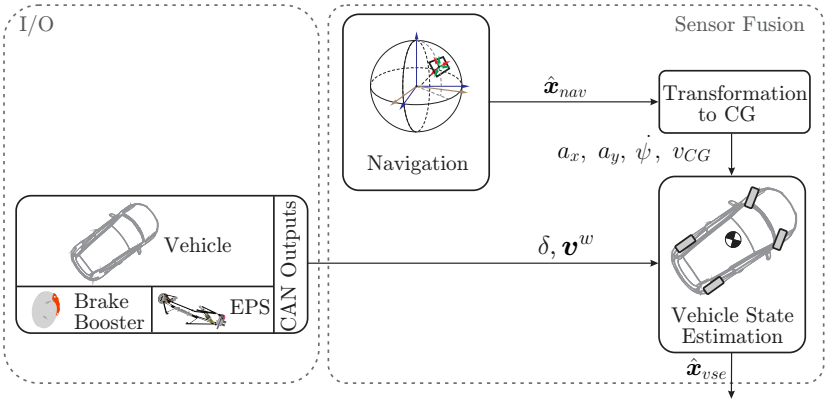

Figure 4.1: Vehicle state estimation scheme

adaptation is only conducted when the estimation problem is considered to be well-conditioned based on its local observability. Thereby, other basic model parameters like the vehicle mass or the mass moment of inertia are not considered to be subject to uncertainty in the scope of this research work. Thus, the estimator is not especially designed to be adaptive or robust with respect to uncertainties in these model parameters. Furthermore, the estimator employs the GNSS-based horizontal velocity estimate which is derived from the navigation solution as aiding measurement, thus being independent of wheel slip. In this way, classical and GNSS-based approaches that can be found in literature are combined. As a further advantage, the employed sensor fusion scheme allows for processing the bias compensated IMU measurements in the estimator. However, it has to be stated that long-term GNSS outages could seriously affect the estimator performance while short-term outages can be compensated by the navigation filter. Consequently, a filter reconfiguration has to be considered for long-term GNSS outages. Due to the fact that at least four satellites are assumed to be available in experimental tests (see section 3.1), this issue has been neglected in the scope of this thesis but can be seen as part of future work.

The particular part of the entire system scheme in section 2.4 that is

related to vehicle state estimation is depicted in Figure 4.1. More precisely, the navigation filter's outputs $\hat{\boldsymbol{x}}_{nav}$ are transferred to CG to determine the longitudinal acceleration a_x, lateral acceleration a_y, yaw rate $\dot{\psi}$ and horizontal velocity v_{CG}. These measurements together with the wheel steering angle δ and the four wheel velocities $\boldsymbol{v}^w$ which are obtained from the vehicle CAN bus are used as input variables to the vehicle state estimator. Finally, the estimated vehicle states $\hat{\boldsymbol{x}}_{vse}$ are supplied to the application with a sampling rate of 100 Hz.

4.2 Transformation of Navigation Outputs

While the navigation solution refers to the mounting position of the IMU and the navigation filter's b-frame is directed forward, right and downwards, the vehicle state estimator's body-fixed reference frame is directed forward, left and upwards having the origin at CG. These different definitions are common in the field of navigation and vehicle dynamics. In this section, a brief outline is given how to determine the longitudinal acceleration a_x, lateral acceleration a_y, yaw rate $\dot{\psi}$ and horizontal velocity v_{CG} at CG based on the navigation solution $\hat{\boldsymbol{x}}_{nav}$. Particularly, bias compensated accelerations $\boldsymbol{f}_{ib}^{b,*}$ are transferred to CG by

$$\boldsymbol{f}_{ib,CG}^{b,*} = \begin{bmatrix} f_{ib,CG,x}^{b,*} \\ f_{ib,CG,y}^{b,*} \\ f_{ib,CG,z}^{b,*} \end{bmatrix} = \boldsymbol{f}_{ib}^{b,*} + \boldsymbol{\omega}_{ib}^{b,*} \times (\boldsymbol{\omega}_{ib}^{b,*} \times \boldsymbol{r}_{IMU,CG}^{b}) \tag{4.1}$$

where $\boldsymbol{\omega}_{ib}^{b,*}$ indicates the bias compensated angular rates and $\boldsymbol{r}_{IMU,CG}^{b}$ the vector pointing from the IMU to CG. Finally, the reference frame has to be rotated by 180 deg with respect to the x^b-axis to obtain the required reference frame orientation (i.e. forward, left and upwards), thus obtaining the longitudinal and lateral acceleration at CG

$$a_x = f_{ib,CG,x}^{b,*} \quad \text{and} \quad a_y = -f_{ib,CG,y}^{b,*}. \tag{4.2}$$

When performing the reference frame rotation, for the yaw rate in the vehicle body frame holds

$$\dot{\psi} = -\omega_{ib,z}^{b,*}. \tag{4.3}$$

As previously indicated, the horizontal velocity v_{CG} at CG, which can be deduced from the navigation solution, will be used as aiding measurement. In this way, independence from tire slip can be achieved which promises an improved estimation performance. In order to obtain v_{CG}, the n-frame velocity $\boldsymbol{v}_{eb}^{n}$ is determined at CG by

$$\boldsymbol{v}_{eb,CG}^{n} = \begin{bmatrix} v_{eb,CG,n}^{n} \\ v_{eb,CG,e}^{n} \\ v_{eb,CG,d}^{n} \end{bmatrix} = \boldsymbol{v}_{eb}^{n} + \boldsymbol{R}_{b}^{n}(\boldsymbol{\omega}_{ib}^{b,*} \times \boldsymbol{r}_{IMU,CG}^{b}) \tag{4.4}$$

where $\boldsymbol{R}_{b}^{n}$ denotes the DCM transferring a vector from the b- to the n-frame. Finally, for the horizontal velocity v_{CG} at CG holds

$$v_{CG} = \sqrt{{v_{eb,CG,n}^{n}}^{2} + {v_{eb,CG,e}^{n}}^{2}}. \tag{4.5}$$

4.3 Modeling

4.3.1 Vehicle Model

In order to implement the estimator outlined above, a nonlinear two-track model according to section 2.1.1.2 is used to describe vehicle dynamics. In this context, rolling resistances, aerodynamic drag as well as road bank and road grade are neglected. The corresponding free-body diagram is depicted in Fig. 4.2. Particularly, (4.6)-(4.7) describe the longitudinal and lateral momentum with respect to CG while (4.8) refers to yaw dynamics.

$$\begin{aligned} f_1 = \dot{v}_x = \dot{\psi} v_y + \frac{1}{m}\Big(& (F_{x,fl} + F_{x,fr})\cos(\delta) \\ & - (F_{y,fl} + F_{y,fr})\sin(\delta) + F_{x,rl} + F_{x,rr}\Big) \end{aligned} \tag{4.6}$$

$$\begin{aligned} f_2 = \dot{v}_y = -\dot{\psi} v_x + \frac{1}{m}\Big(& (F_{y,fl} + F_{y,fr})\cos(\delta) \\ & + (F_{x,fl} + F_{x,fr})\sin(\delta) + F_{y,rl} + F_{y,rr}\Big) \end{aligned} \tag{4.7}$$

$$f_3 = \ddot{\psi} = \frac{1}{J_z}\Big[(F_{x,rr} - F_{x,rl})\frac{tw_r}{2} - (F_{y,rl} + F_{y,rr})l_r \tag{4.8}$$
$$+ \Big((F_{x,fr} - F_{y,fl})\cos(\delta) + (F_{y,fl} - F_{y,fr})\sin(\delta)\Big)\frac{tw_f}{2}$$
$$+ \Big((F_{y,fl} + F_{y,fr})\cos(\delta) + (F_{x,fl} + F_{y,fr})\sin(\delta)\Big)l_f\Big]$$

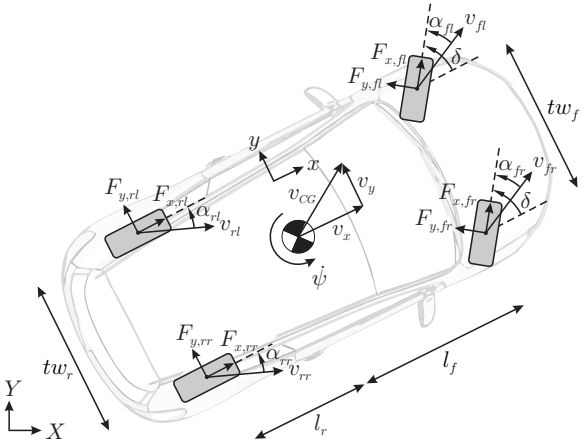

Figure 4.2: Free-body diagram of the employed estimator model

4.3.2 Tire Model

4.3.2.1 Longitudinal and Lateral Tire Forces

To determine longitudinal and lateral tire forces in (4.6)-(4.8), the Pacejka magic formula tire model according to section 2.1.2 is employed. Longitudinal tire forces $F_{x,i}$ with $i \in \{fl,fr,rl,rr\}$ at pure longitudinal slip can be expressed as

$$F_{x,i} = \theta_{F_x} \cdot \mu F_{z,i} \cdot f_{x,i}(\lambda_i) \tag{4.9}$$

where $f_{x,i}(\lambda_i)$ indicates the normalized Pacejka Magic Formula depending on the longitudinal slip ratio λ_i and $\mu F_{z,i}$ the maximum feasible tire force according to Coulomb's law of friction. Thereby, μ denotes the maximum friction coefficient and $F_{z,i}$ the vertical tire load. Furthermore, θ_{F_x} is introduced to adapt longitudinal tire forces as described in the end of this section. Referring to section 2.1.2.1, the longitudinal tire slip ratio λ_i is defined as

$$\lambda_i = \begin{cases} 1 - \frac{v^w_{x,i,free}}{v^w_{x,i}} & , v^w_{x,i} - v^w_{x,i,free} \geq 0 \text{ (acceleration slip)} \\ \frac{v^w_{x,i}}{v^w_{x,i,free}} - 1 & , v^w_{x,i} - v^w_{x,i,free} < 0 \text{ (braking slip).} \end{cases} \tag{4.10}$$

Due to the fact that wheel velocities v^w_i that are obtained from the vehicle's CAN bus refer to the direction of travel, the longitudinal velocity $v^w_{x,i}$ in the wheel reference frame is determined by

$$v^w_{x,i} = v^w_i \cos(\alpha_i) \tag{4.11}$$

where α_i denotes the corresponding tire sideslip angle. Referring to section 2.1.2.6, the dynamic vertical tire load is approximated by

$$F_{z,fl/fr} = m \left(\frac{l_r}{l} g - \frac{h_{CG}}{l} a_x \right) \left(\frac{1}{2} \mp \frac{h_{CG}}{tw_f \cdot g} a_y \right), \tag{4.12}$$

$$F_{z,rl/rr} = m \left(\frac{l_f}{l} g + \frac{h_{CG}}{l} a_x \right) \left(\frac{1}{2} \mp \frac{h_{CG}}{tw_r \cdot g} a_y \right) \tag{4.13}$$

where a_x and a_y denote the measured longitudinal and lateral acceleration at CG and $l = l_f + f_r$ the wheel base. Lateral tire forces $F_{y,i,0}$ with $i \in \{fl,fr,rl,rr\}$ at pure cornering are determined similar to (4.9) by

$$F_{y,i,0} = \theta_{F_y} \cdot \mu F_{z,i} \cdot f_{y,i}(\alpha_i) \tag{4.14}$$

where $f_{y,i}(\alpha_i)$ denotes the normalized Pacejka Magic Formula in dependence of the tire sideslip angle α_i and θ_{F_y} indicates the adaptation state to scale lateral tire forces.

4.3.2.2 Combined Slip

To incorporate combined slip, i.e. the simultaneous transmission of longitudinal and lateral forces, lateral tire forces $F_{y,i,0}$ with $i \in \{fl,fr,rl,rr\}$

at pure cornering are reduced depending on the transmission of longitudinal forces in accordance to the friction ellipse as introduced in section 2.1.2.5, i.e.

$$F_{y,i} = F_{y,i,0}\sqrt{1 - \left(\frac{F_{x,i}}{F_{x,i,max}}\right)^2} = F_{y,i,0}\sqrt{1 - {f_{x,i}}^2}. \tag{4.15}$$

4.3.2.3 Adaptation States

Obviously, the employed vehicle and tire model contain several parameters that are difficult to be determined and may vary during operation. Especially tire parameters are an inherently uncertain parameter set. Therefore, two additional estimator states θ_{F_x} and θ_{F_y} are introduced in (4.9) and (4.14) to take model uncertainties into account. Thus, this approach allows the estimator to scale tire forces, e.g. when the friction coefficient changes. Investigations have shown that employing two separate adaptation states for longitudinal and lateral tire forces leads to an improved estimation performance. In this context, the dynamic behavior of θ_{F_x} and θ_{F_y} is assumed to be a random walk process, i.e.

$$f_4 = \dot{\theta}_{F_x} = 0, \tag{4.16}$$

$$f_5 = \dot{\theta}_{F_y} = 0. \tag{4.17}$$

4.3.3 Resulting Vehicle Dynamics Model

When substituting longitudinal and lateral tire forces (4.9) and (4.15) in (4.6)-(4.8), the resulting nonlinear estimator model describing vehicle dynamics can be written as

$$\dot{\boldsymbol{x}}(t) = \begin{bmatrix} \dot{\bar{\boldsymbol{x}}}(t) \\ \dot{\boldsymbol{\theta}}(t) \end{bmatrix} = \boldsymbol{f}(\boldsymbol{x}(t), \boldsymbol{u}(t)) \tag{4.18}$$

with $\boldsymbol{f}^T = [f_1,\, f_2,\, f_3,\, f_4,\, f_5]$. In this regard,

$$\boldsymbol{x}^T = [\bar{\boldsymbol{x}}^T,\, \boldsymbol{\theta}^T] \tag{4.19}$$

denotes the augmented state vector comprising the actual state vector

$$\bar{\boldsymbol{x}}^T = [v_x,\, v_y,\, \dot{\psi}] \tag{4.20}$$

where v_x indicates the longitudinal velocity, v_y the lateral velocity and $\dot{\psi}$ the yaw rate as well as the adaptation states

$$\boldsymbol{\theta}^T = [\theta_{F_x},\, \theta_{F_y}]. \tag{4.21}$$

Furthermore,

$$\boldsymbol{u}^T = [\delta,\, v_{fl}^w,\, v_{fr}^w,\, v_{rl}^w,\, v_{rr}^w,\, a_x,\, a_y] \tag{4.22}$$

denominates the input vector containing the wheel steering angle δ, the absolute wheel velocities v_i^w with $i \in \{fl,fr,rl,rr\}$ and the longitudinal and lateral acceleration a_x and a_y at CG respectively.

4.4 Model Validation

As the EKF-based estimator determines a weighted mean value of the model-based predictions and the corresponding measurements, estimation results inherently depend on the accuracy of the introduced plant model, see [17]. For this reason, the plant model's validity is assessed consecutively. Therefore, a manually driven maneuver starting with an acceleration period with longitudinal accelerations of up to $7\,\mathrm{m/s^2}$ and a following double lane change maneuver with lateral accelerations of up to $9\,\mathrm{m/s^2}$ is employed as test maneuver. In this way, the estimator model's ability to describe longitudinal as well as lateral vehicle dynamics is evaluated. For evaluation purposes, the nonlinear plant model (4.18) is integrated numerically in offline simulations using MATLAB/Simulink's ODE45 solver [80]. Thereby, the measured inputs $\boldsymbol{u}$, which are illustrated in Figure 4.3, are employed as input variables. As tire sideslip angles take unreasonable values for velocities close to zero (due to the division by the longitudinal velocity v_x, see section 2.1.2.2), the model validation is initiated for a longitudinal velocity of $2\,\mathrm{m/s}$ at $t = 1\,\mathrm{s}$.

When examining the open-loop estimation results in Figure 4.4, it is apparent that the longitudinal velocity v_x is tracked nearly perfectly

even for longitudinal accelerations of 5 to 7 m/s^2. The lateral velocity v_y shows larger errors while the qualitative behavior is estimated very well without any significant phase shifts for lateral accelerations of about 9 m/s^2. Likewise, the yaw rate $\dot{\psi}$ matches the qualitative behavior of its reference convincingly while larger quantitative estimation errors are apparent for high lateral accelerations. The reason for these quantitative deviations can be seen in the strong nonlinear tire behavior for absolute accelerations greater than 6 m/s^2. It has to be stated that the same scenario has been evaluated for lateral accelerations of 5 m/s^2. In this case, the lateral velocity as well as the yaw rate are tracked nearly perfectly. However, experimental results in section 4.7 demonstrate that the introduced model is well suited to estimate these vehicle states even at the handling limits when operating the filter closed-loop. Finally, it has to be stated that the adaptation states θ_{F_x} and θ_{F_y}, whose

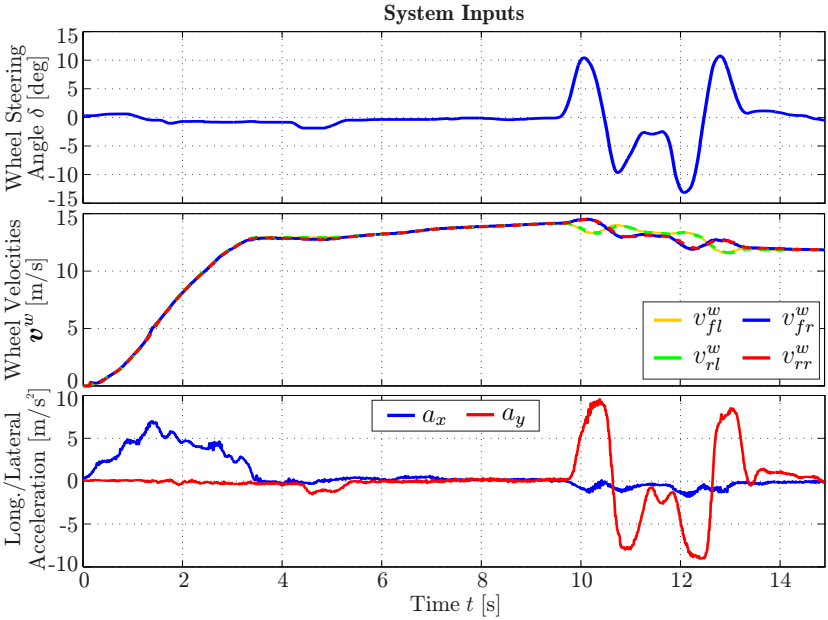

Figure 4.3: Model validation: System inputs

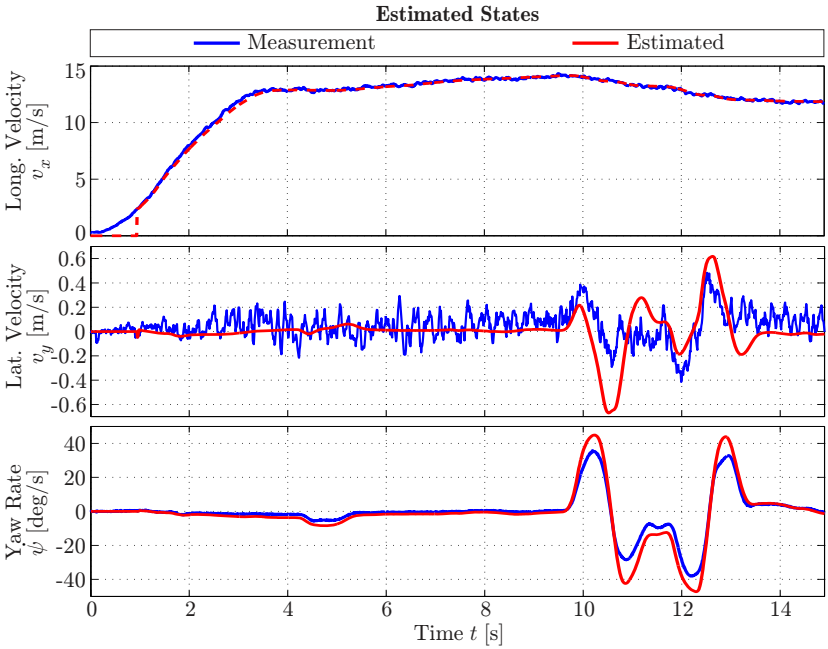

Figure 4.4: Model validation: Estimated states

dynamic behavior is assumed to be a random walk process, have been omitted for reasons of clarity as their estimated values remain constant during the entire simulation.

4.5 Estimator Design

As outlined in section 4.1, the estimation of key vehicle states is performed through an EKF-based approach. The basic concept of EKF-based estimators is to predict an a priori state estimate using a nonlinear plant model and to correct this estimate when a measurement $\tilde{\boldsymbol{y}}$ is available, see [17]. Therefore, the measurements have to be put into context

to the states of the nonlinear plant model (4.18). For the purpose of vehicle state estimation,

$$h_1 = \tilde{a}_x = \frac{1}{m}\Big((F_{x,fl} + F_{x,fr})\cos(\delta) - (F_{y,fl} + F_{y,fr})\sin(\delta) + F_{x,rl} + F_{x,rr}\Big) \tag{4.23}$$

$$h_2 = \tilde{a}_y = \frac{1}{m}\Big((F_{y,fl} + F_{y,fr})\cos(\delta) + (F_{x,fl} + F_{x,fr})\sin(\delta) + F_{y,rl} + F_{y,rr}\Big) \tag{4.24}$$

$$h_3 = \tilde{\dot{\psi}} = \dot{\psi} \tag{4.25}$$

$$h_4 = \tilde{v}_{CG} = \sqrt{{v_x}^2 + {v_y}^2} \tag{4.26}$$

are employed as measurement equations where h_1 corresponds to the longitudinal acceleration a_x at CG, h_2 to the lateral acceleration a_y at CG, h_3 to the yaw rate $\dot{\psi}$ and h_4 to the horizontal velocity v_{CG} which is derived from the navigation solution (see section 4.2). Referring to section 4.3.2.3, θ_{F_x} and θ_{F_y} have been introduced to scale tire forces and thus to be adaptive with respect to uncertainties in the tire-road contact. In this regard, excitation plays a vital role as far as observability of these adaptation states is concerned. When loosing observability, θ_{F_x} and θ_{F_y} might take arbitrary values which can even lead to filter divergence. Therefore, two additional artificial measurement variables

$$h_5 = \tilde{\theta}_{F_x} = \begin{cases} 0 & \text{, if } \theta_{F_x} \text{ is observable} \\ \theta_{F_x} & \text{, otherwise} \end{cases} \tag{4.27}$$

$$h_6 = \tilde{\theta}_{F_y} = \begin{cases} 0 & \text{, if } \theta_{F_y} \text{ is observable} \\ \theta_{F_y} & \text{, otherwise} \end{cases} \tag{4.28}$$

are introduced to keep θ_{F_x} respectively θ_{F_y} constant if these state variables are considered to be unobservable. To achieve this aim, the corresponding measurement noise covariances have to be chosen small enough. A detailed observability analysis as well as the assessment of (local) observability is provided in section 4.6. Assuming that the measured inputs and outputs are superimposed by zero-mean Gaussian white noise, the stochastic nonlinear estimator model can be derived

from (4.18) and (4.23)-(4.28) as

$$\dot{\boldsymbol{x}}(t) = \boldsymbol{f}(\boldsymbol{x}(t), \boldsymbol{u}(t), \boldsymbol{w}(t)) \tag{4.29}$$

$$\boldsymbol{y}(t) = \boldsymbol{h}(\boldsymbol{x}(t), \boldsymbol{u}(t)) + \boldsymbol{v}(t) \tag{4.30}$$

where

$$\boldsymbol{w}^T = [w_\delta,\, w_{v_{fl}^w},\, w_{v_{fr}^w},\, w_{v_{rl}^w},\, w_{v_{rr}^w},\, w_{a_x},\, w_{a_y},\, w_{\theta_{F_x}},\, w_{\theta_{F_y}}] \tag{4.31}$$

denotes the process noise resulting from the inputs $\boldsymbol{u}$ and the adaptation states $\boldsymbol{\theta}$ acting on the state vector $\boldsymbol{x}$,

$$\boldsymbol{v}^T = [v_{a_x},\, v_{a_y},\, v_{\dot{\psi}},\, v_{v_{CG}},\, v_{\theta_{F_x}},\, v_{\theta_{F_y}}] \tag{4.32}$$

the measurement noise affecting the outputs

$$\boldsymbol{y}^T = [a_x,\, a_y,\, \dot{\psi},\, v_{CG},\, \theta_{F_x},\, \theta_{F_y}] \tag{4.33}$$

and $\boldsymbol{h}^T = [h_1,\, h_2,\, h_3,\, h_4,\, h_5,\, h_6]$. Thereby, $\boldsymbol{w}$ and $\boldsymbol{v}$ are assumed to be zero-mean Gaussian white noise, i.e. $\boldsymbol{w} \sim \mathcal{N}(\boldsymbol{0},\boldsymbol{Q})$ and $\boldsymbol{v} \sim \mathcal{N}(\boldsymbol{0},\boldsymbol{R})$ where $\boldsymbol{Q}$ and $\boldsymbol{R}$ denote the corresponding covariance matrices.

Considering the input and measurement vector, it can be noticed that the longitudinal and lateral acceleration are contained in both vectors. Hence, the assumption of uncorrelated input and measurement noise, i.e. $E[\boldsymbol{w}\boldsymbol{v}^T] = \boldsymbol{0}$, is no longer fulfilled and has to be accounted for in the filter equations. This issue results from the fact that a_x and a_y are used to determine the vertical tire load as well as to aid the state prediction. In fact, the tire load could be computed outside the filter, but nevertheless there would be a strong cross-correlation of input and measurement variables. As this can indeed be handled inside the filter, the update equations are modified as described subsequently to take this cross-correlation into account. At the same time, the cross-correlation of the yaw rate $\dot{\psi}$ and the horizontal velocity at CG v_{CG} respectively the yaw rate and longitudinal as well as lateral acceleration a_x and a_y that is introduced when transferring the outputs of the navigation filter to CG (see section 4.2) is assumed to be negligible.

To be used in the EKF-based estimator, (4.29)-(4.30) are linearized along the estimated state trajectory and transferred to a discrete-time

linear representation, thus obtaining

$$\boldsymbol{x}_{k+1} = \boldsymbol{F}_k \boldsymbol{x}_k + \boldsymbol{B}_k \boldsymbol{u}_k + \boldsymbol{G}_k \boldsymbol{w}_k \tag{4.34}$$

$$\boldsymbol{y}_k = \boldsymbol{H}_k \boldsymbol{x}_k + \boldsymbol{D}_k \boldsymbol{u}_k + \boldsymbol{v}_k. \tag{4.35}$$

According to [17], the prediction step at time k consists of determining the a priori state estimate $\hat{\boldsymbol{x}}_k^-$ as well as the corresponding estimation error covariance matrix $\boldsymbol{P}_k^-$

$$\hat{\boldsymbol{x}}_k^- = \hat{\boldsymbol{x}}_{k-1}^+ + \int_{(k-1)\cdot T_s}^{k\cdot T_s} \boldsymbol{f}(\hat{\boldsymbol{x}}_{k-1}^+, \boldsymbol{u}_{k-1})\, dt \tag{4.36}$$

$$\boldsymbol{P}_k^- = \boldsymbol{F}_{k-1} \boldsymbol{P}_{k-1}^+ \boldsymbol{F}_{k-1}^T + \boldsymbol{G}_{k-1} \boldsymbol{Q}_{k-1} \boldsymbol{G}_{k-1}^T \tag{4.37}$$

where $\boldsymbol{Q}_k = \boldsymbol{Q}/T_s$ and $\boldsymbol{R}_k = \boldsymbol{R}$ denote the discrete-time covariance matrices of the process noise $\boldsymbol{w}_k$ and the measurement noise $\boldsymbol{v}_k$ while T_s indicates the EKF's sampling time. In order to solve (4.36) numerically, an explicit forth-order Runge-Kutta integration technique [59] is applied. When a measurement $\tilde{\boldsymbol{y}}_k$ is available at time k, the a posteriori state estimate $\hat{\boldsymbol{x}}_k^+$ and covariance matrix $\boldsymbol{P}_k^+$ are obtained by

$$\begin{aligned} \boldsymbol{K}_k = (\boldsymbol{P}_k^- \boldsymbol{H}_k^T + \boldsymbol{G}_k \boldsymbol{S}_k)(\boldsymbol{H}_k \boldsymbol{P}_k^- \boldsymbol{H}_k^T + \boldsymbol{R}_k \\ + \boldsymbol{H}_k \boldsymbol{G}_k \boldsymbol{S}_k + \boldsymbol{S}_k^T \boldsymbol{G}_k^T \boldsymbol{H}_k^T)^{-1} \end{aligned} \tag{4.38}$$

$$\hat{\boldsymbol{x}}_k^+ = \hat{\boldsymbol{x}}_k^- + \boldsymbol{K}_k(\tilde{\boldsymbol{y}}_k - \boldsymbol{h}(\hat{\boldsymbol{x}}_k^-, \boldsymbol{u}_k)) \tag{4.39}$$

$$\boldsymbol{P}_k^+ = (\boldsymbol{I} - \boldsymbol{K}_k \boldsymbol{H}_k)\boldsymbol{P}_k^- - \boldsymbol{K}_k \boldsymbol{S}_k^T \boldsymbol{G}_k^T \tag{4.40}$$

where $\boldsymbol{K}_k$ denominates the Kalman gain. To account for the cross-correlation of the input noise $\boldsymbol{w}_k$ and the measurement noise $\boldsymbol{v}_k$, measurement update equations (4.38)-(4.40) have been modified according to [17] by introducing the cross-covariance matrix $\boldsymbol{S}_k = E[\boldsymbol{w}_k \boldsymbol{v}_k^T]$.

4.6 Observability Analysis

4.6.1 Local Observability

As far as the observability of the introduced estimation problem is concerned, a detailed consideration of this issue is carried out in this section.

In general, a nonlinear system is locally observable if and only if

$$\boldsymbol{\mathcal{O}}_{nl} = \frac{\partial}{\partial \boldsymbol{x}} \begin{bmatrix} \mathcal{L}_{\boldsymbol{f}}^{0}(\boldsymbol{h}) \\ \vdots \\ \mathcal{L}_{\boldsymbol{f}}^{(n-1)}(\boldsymbol{h}) \end{bmatrix}_{(\boldsymbol{x}_0, \boldsymbol{u}_0)} \tag{4.41}$$

has rank n where n denotes the number of state variables and $\mathcal{L}_{\boldsymbol{f}}^{j}(\boldsymbol{h})$ the j-th Lie derivative of $\boldsymbol{h}$ along the vector field $\boldsymbol{f}$, see [81]. Focusing on the estimation problem introduced in this section, the nonlinear system (4.29)-(4.30) becomes locally unobservable if the vehicle is standing still or if there is an insufficient longitudinal or lateral excitation as indicated in section 4.5. In case of low vehicle velocity, the estimator is disabled if the velocity decreases further than a certain threshold and is reinitialized when exceeding this threshold again. Thus, observability issues have subsequently only to be taken into account when having insufficient excitation. Particularly, when longitudinal or lateral tire forces are close to zero, θ_{F_x} respectively θ_{F_y} might take arbitrary values due to the loss of local observability. Then the estimation problem becomes ill-conditioned which can even lead to filter divergence. Therefore, the local observability of θ_{F_x} and θ_{F_y} has to be investigated in real-time for each iteration of the estimator. Finally, if one of these states is considered to be locally unobservable, the corresponding state has to be kept constant as described in section 4.5.

As the rank of (4.41) cannot be evaluated online for the given nonlinear system, the local observability is proven in accordance to [82]. In particular, [82] proposes to obtain an indication of the local observability of the nonlinear system by investigating the rank of the observability matrix for discrete-time linear systems

$$\boldsymbol{\mathcal{O}}_{LTI} = \begin{bmatrix} \boldsymbol{H}_k \\ \vdots \\ \boldsymbol{H}_k \boldsymbol{F}_k{}^{(n-1)} \end{bmatrix} \tag{4.42}$$

assuming that the linearized system remains near the current operating point. If $\boldsymbol{\mathcal{O}}_{LTI}$ has full rank, the nonlinear system is assumed to be locally observable near the current operating point.

4.6.2 Assessment of Local Observability

Due to noisy input and measurement variables in real-world applications, it is not reasonable to apply a pure rank test of $\boldsymbol{\mathcal{O}}_{LTI}$ to assess local observability. Instead, a common approach in literature is to consider the condition number

$$\text{cond}(\boldsymbol{\mathcal{O}}_{LTI}) = \frac{\overline{\sigma}(\boldsymbol{\mathcal{O}}_{LTI})}{\underline{\sigma}(\boldsymbol{\mathcal{O}}_{LTI})} \tag{4.43}$$

of the observability matrix $\boldsymbol{\mathcal{O}}_{LTI}$ to decide whether the system is assumed to be locally observable or not, see [83]. In this context, $\overline{\sigma}$ denotes the maximum and $\underline{\sigma}$ the minimum singular value of $\boldsymbol{\mathcal{O}}_{LTI}$. Roughly speaking, the system can be said to be less observable when the condition number increases and vice versa. To finally differ between a locally observable and unobservable estimation problem, a condition number threshold is commonly employed such that the nonlinear system is assumed be locally observable if the condition number is less than or equal to this threshold and unobservable otherwise. To assess the local observability at time k for the vehicle state estimation problem, the observability matrix is determined at the current operating point for the following three cases

1. θ_{F_x} and θ_{F_y} are locally observable.
2. θ_{F_x} is locally observable while θ_{F_y} is not.
3. θ_{F_y} is locally observable while θ_{F_x} is not.

Consequently, three observability matrices are obtained, i.e. $\boldsymbol{\mathcal{O}}_{LTI,F_x,F_y}$ assuming that θ_{F_x} and θ_{F_y} are locally observable, $\boldsymbol{\mathcal{O}}_{LTI,F_x}$ considering only θ_{F_x} to be locally observable and $\boldsymbol{\mathcal{O}}_{LTI,F_y}$ assuming that only θ_{F_y} is locally observable. Particularly, the system matrix $\boldsymbol{F}_k$ in (4.42) is equal for each case while the measurement matrix $\boldsymbol{H}_k$ depends on the assumption regarding the local observability of the adaptation states, see section 4.5.

Hence, θ_{F_x} and θ_{F_y} are assessed to be locally observable at the same time if the condition number $\text{cond}(\boldsymbol{\mathcal{O}}_{LTI,F_x,F_y})$ of the observability matrix $\boldsymbol{\mathcal{O}}_{LTI,F_x,F_y}$ is less than or equal to the threshold $c_{F_x,F_y,thld}$, i.e.

$$\text{cond}(\boldsymbol{\mathcal{O}}_{LTI,F_x,F_y}) \leq c_{F_x,F_y,thld}. \tag{4.44}$$

If (4.44) is not fulfilled, it has to be investigated whether θ_{F_x}, θ_{F_y} or none of them are assumed to be locally observable. Therefore, the condition numbers of the observability matrices $\boldsymbol{\mathcal{O}}_{LTI,F_x}$ and $\boldsymbol{\mathcal{O}}_{LTI,F_y}$ are computed. Due to the fact that different thresholds might be required to assess the local observability of θ_{F_x} and θ_{F_y}, the condition numbers are divided by the corresponding thresholds $c_{F_x,thld}$ respectively $c_{F_y,thld}$ to allow for an appropriate comparison, i.e.

$$\overline{\text{cond}}(\boldsymbol{\mathcal{O}}_{LTI,F_i}) = \frac{\text{cond}(\boldsymbol{\mathcal{O}}_{LTI,F_i})}{c_{F_i,thld}} \tag{4.45}$$

with $i \in \{x,y\}$. Consequently, $\overline{\text{cond}}(\boldsymbol{\mathcal{O}}_{LTI,F_i}) > 1$ with $i \in \{x,y\}$ indicates that θ_{F_i} is locally unobservable. Consecutively, it has to be decided whether θ_{F_x} or θ_{F_y} are considered to be locally observable based on $\overline{\text{cond}}(\boldsymbol{\mathcal{O}}_{LTI,F_x})$ respectively $\overline{\text{cond}}(\boldsymbol{\mathcal{O}}_{LTI,F_y})$. In particular, θ_{F_x} is assumed to be locally observable if

$$\overline{\text{cond}}(\boldsymbol{\mathcal{O}}_{LTI,F_x}) < \overline{\text{cond}}(\boldsymbol{\mathcal{O}}_{LTI,F_y}) \ \wedge \ \overline{\text{cond}}(\boldsymbol{\mathcal{O}}_{LTI,F_x}) \leq 1, \tag{4.46}$$

i.e. if θ_{F_x} is assessed to be locally observable and the estimation problem is assumed to have a better condition if θ_{F_y} is kept constant. Likewise, θ_{F_y} is considered to be locally observable if

$$\overline{\text{cond}}(\boldsymbol{\mathcal{O}}_{LTI,F_y}) \leq \overline{\text{cond}}(\boldsymbol{\mathcal{O}}_{LTI,F_x}) \ \wedge \ \overline{\text{cond}}(\boldsymbol{\mathcal{O}}_{LTI,F_y}) \leq 1. \tag{4.47}$$

Of course, the case of $\overline{\text{cond}}(\boldsymbol{\mathcal{O}}_{LTI,F_x}) = \overline{\text{cond}}(\boldsymbol{\mathcal{O}}_{LTI,F_y})$ can be handled arbitrarily. This contribution assumes θ_{F_y} to be locally observable in that case.

To give an example, Figure 4.5 depicts the (normalized) condition numbers for a sinusoidal maneuver. For the following considerations it is assumed that either θ_{F_x} or θ_{F_y} are locally observable at time t (but not both at the same time). When considering $\text{cond}(\boldsymbol{\mathcal{O}}_{LTI,F_x})$ and $\text{cond}(\boldsymbol{\mathcal{O}}_{LTI,F_y})$ it can be recognized that for certain time intervals, e.g. at $t = 7.9\,\text{s}$ and $t = 11.7\,\text{s}$, both condition numbers are less that their observability thresholds $c_{F_x,thld}$ respectively $c_{F_y,thld}$ and might thus be locally observable. Obviously, if the corresponding thresholds are not equal to each other, a reasonable assessment whether θ_{F_x} or θ_{F_y} is locally observable cannot be conducted. Contrarily, using normalized

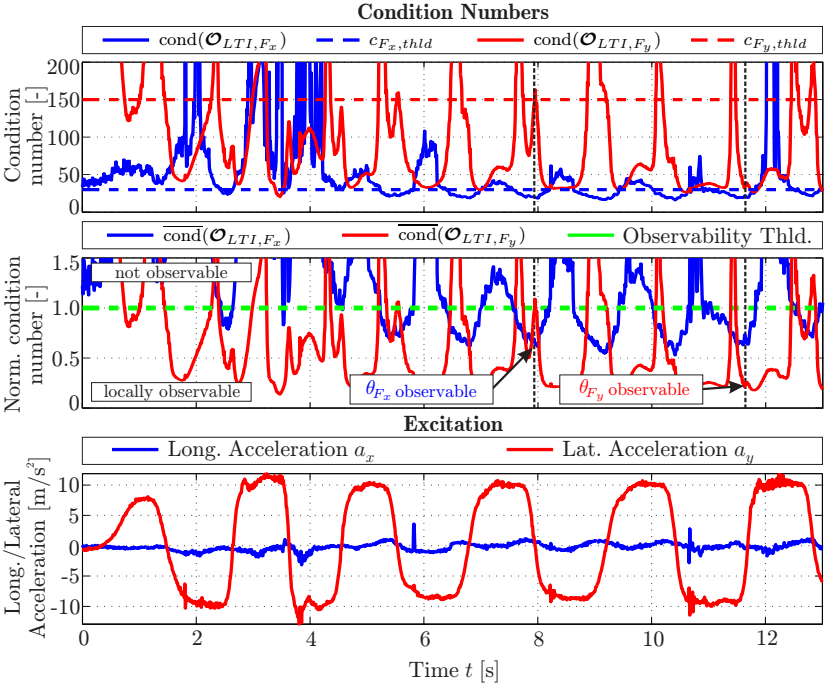

Figure 4.5: (Normalized) condition numbers and assessment of observability

condition numbers allows for evaluating θ_{F_x} to be locally observable at $t = 7.9\,\text{s}$ and θ_{F_y} at $t = 11.7\,\text{s}$ according to (4.46)-(4.47).

Finally, if (4.44), (4.46) and (4.47) are not fulfilled, θ_{F_x} and θ_{F_y} are assessed to be locally unobservable and thus have to be kept constant in the next estimator step. Obviously, the condition number thresholds have to be determined appropriately during filter parameterization to prevent the estimator from undesired and unreasonable adaptations. Nonetheless, investigations have shown that a reasonable parameterization can quickly be obtained when evaluating the filter performance for a few crucial maneuvers, see section 4.7.1.

4.7 Experimental Results

4.7.1 Test Scenarios and Filter Parameterization

To evaluate the performance of the introduced estimator, a manually driven double lane change and a manually driven sinusoidal maneuver on a dry road have been chosen as test scenarios. Due to dry road conditions on high friction surface, a maximum tire-road friction coefficient of $\mu = 1$ is assumed. While both test maneuvers are commonly investigated for evaluation purposes, the double lane change maneuver is also employed as reference evasion path for autonomous vehicle guidance in chapter 6. For both maneuvers, lateral accelerations have a magnitude of $\pm 1g$ which allows for a filter evaluation at the vehicle handling limits corresponding to the operating conditions of CA. Furthermore, the sinusoidal maneuver is examined for the nominal as well as the adaptive case. In the adaptive case, tire parameters are distorted intentionally to achieve a model mismatch that has to be compensated by the estimator. For the subsequent assessment of the adaptive estimator performance, the sinusoidal maneuver is preferred to the double lane change as the maneuver duration is significantly longer and is thus better suited for an extensive analysis. Nevertheless, the estimator is indeed able to compensate the model mismatch for the double lane change maneuver as well.

For reasons of reproducibility, the following results have been gained through offline simulations in MATLAB/Simulink that rely on actual measurement data which have been recorded in the test vehicle. As previously mentioned, the estimator is executed with a sampling rate of 100 Hz. In order to prove the general applicability of the proposed estimation concept for GNSS-based vehicle state estimation, the navigation filter is operated in the conventional closed-loop operating mode instead of LWM (see section 3.7.2). As a consequence, the estimation of the horizontal velocity v_{CG} which is an input to the vehicle state estimator becomes slightly worse compared to LWM for increasing accelerations. Nevertheless, the following estimation results show a convincing performance when the navigation filter is operated conventionally and thus the general applicability of the proposed concept. Furthermore, studies

have shown that estimation results are almost equal when LWM is used as navigation mode.

To determine the estimator's parameterization, different test maneuvers comprising double lane change, sinusoidal and accelerating/braking maneuvers have been analyzed. While the major part of the process noise matrix $\boldsymbol{Q}$, the measurement noise matrix $\boldsymbol{R}$ and the cross-covariance matrix $\boldsymbol{S}$ can basically be derived from sensor specification, the adaptation states' noise has to be determined carefully. Thereby, the covariance of the adaptation states has to be chosen small enough in order to prevent the estimator from false adaptations and large enough to actually allow for an adaptation. Likewise, the condition number thresholds that define when an adaptation state is considered to be locally observable have to be chosen appropriately. For this purpose, maneuvers with high longitudinal and lateral accelerations have been examined. These covariances and thresholds have been tuned such that the estimator performance basically corresponds to the non-adaptive filter in the nominal case and a reasonable adaptation is obtained when tire parameters are distorted. For further information on filter tuning, see section D.1.

4.7.2 Nominal Estimator Results

4.7.2.1 Double Lane Change Maneuver

Figure 4.6 illustrates the estimation results for the double lane change maneuver when using nominal tire parameters. It can be recognized that the reference values of the longitudinal velocity v_x and the lateral velocity v_y are tracked very well. As the yaw rate $\dot{\psi}$ is employed as aiding measurement the estimation matches its reference perfectly. In this context, it has to be noted that the velocity reference values originate from the optical Correvit sensor (see section 2.2.1) while the reference yaw rate corresponds to the actual IMU measurement. Figure 4.7 depicts the adaptation states that are considered to be locally observable as well as the corresponding excitation in terms of longitudinal and lateral accelerations. In this regard, θ_{F_y} is assessed to be locally observable almost always when having large lateral excitation. Just before the maneuver, i.e. from $t = 0$ to 0.3 s, θ_{F_x} is evaluated to be locally observable

although the longitudinal acceleration a_x is approximately zero. The reason can be seen in an immediately preceding steering maneuver in which the driver compensates the loss of velocity by hitting the gas pedal. Consequently, this part of the maneuver is composed of combined steering and braking thus that longitudinal and lateral tire forces

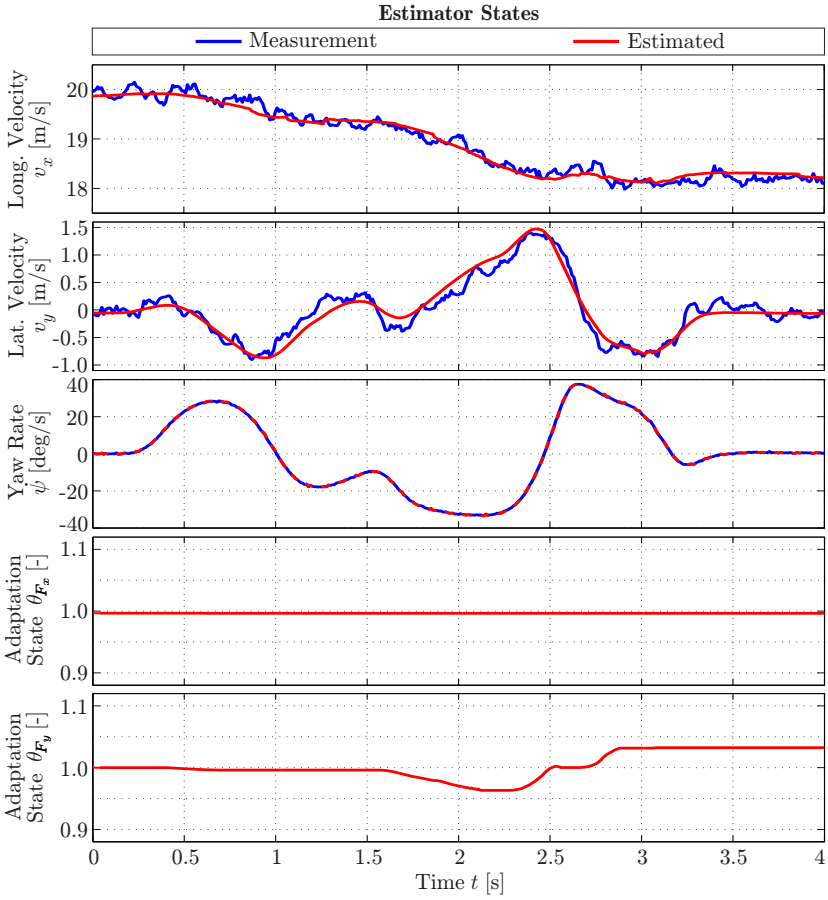

Figure 4.6: Double lane change maneuver: State estimates

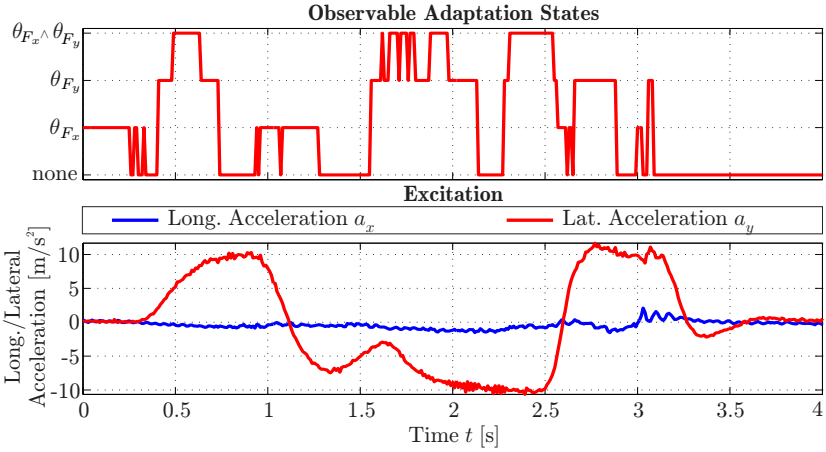

Figure 4.7: Double lane change maneuver: Flags and accelerations

are different from zero. In this way, the estimator decides that θ_{F_x} can be determined unambiguously and is thus assessed to be locally observable. Likewise, θ_{F_x} becomes locally observable for several time intervals during the maneuver as the driver still holds the gas pedal to reduce the loss of velocity. However, as expected, no significant changes of θ_{F_x} and θ_{F_y} can be observed in the nominal case. Furthermore, adaptation parameters are successfully held constant in the case of low excitation as it can be observed during the last second of the maneuver. Overall, a convincing performance can be gained for the double lane change maneuver.

4.7.2.2 Sinusoidal Maneuver

Figure 4.8 shows the nominal estimation results for the sinusoidal maneuver. As the driver tries to compensate the loss of velocity during the maneuver by hitting the gas pedal, the scenario is also appropriate to assess the estimator performance for combined longitudinal and lateral excitation. Similar to the double lane change maneuver, the longitudinal velocity v_x and the lateral velocity v_y are tracked very well.

The largest errors, which are still considerably small, can be recognized when the tires enter the region of sliding friction at $t = 3$ and 12 s. The fact that tires begin to skid is indicated by noisy lateral accelerations (see Figure 4.9) as well as larger lateral velocities while having the same maximum lateral acceleration as in other time intervals. Furthermore,

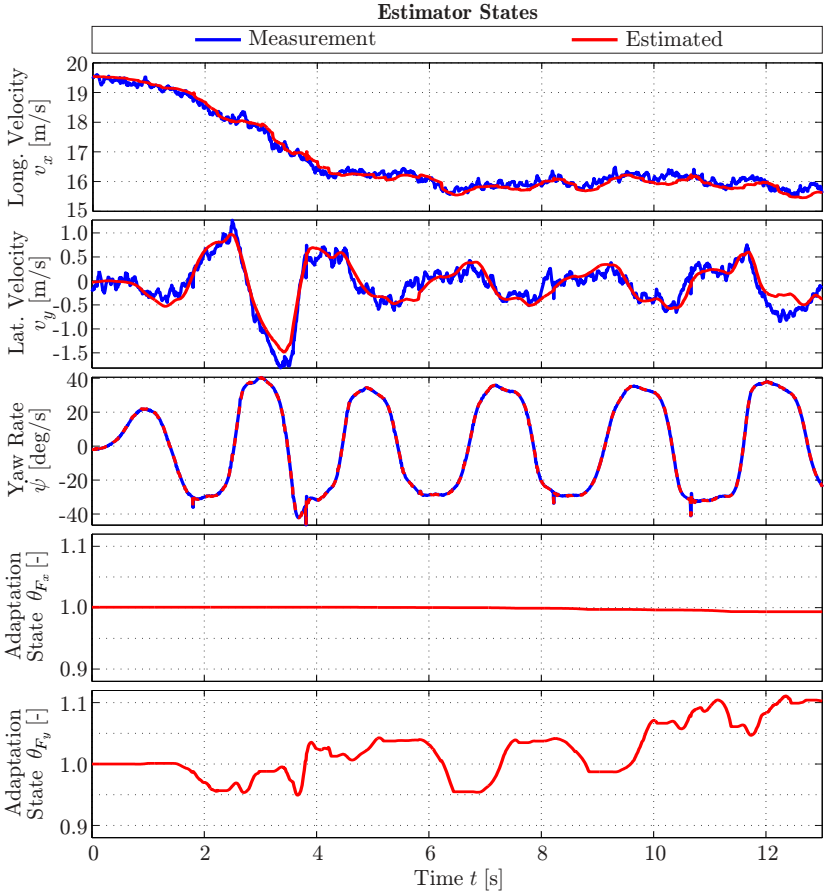

Figure 4.8: Sinusoidal maneuver: State estimates

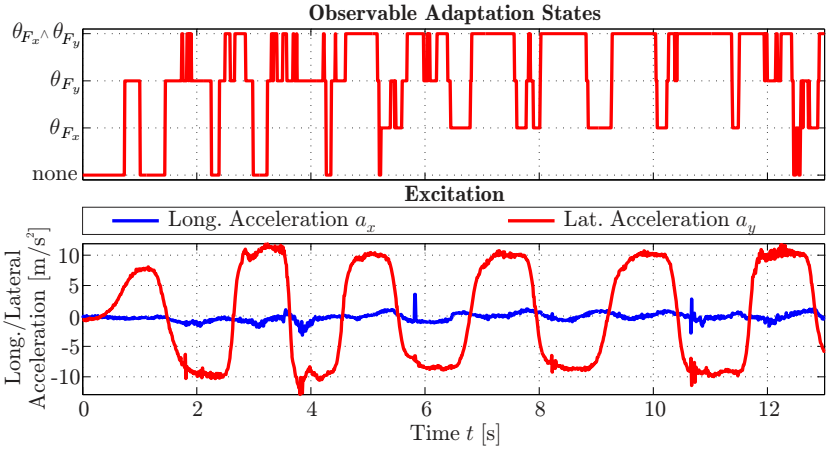

Figure 4.9: Sinusoidal maneuver: Flags and accelerations

θ_{F_y} is evaluated to be locally observable most of the time due to high lateral accelerations. At the same time, θ_{F_x} becomes locally observable for several time intervals although the longitudinal acceleration a_x is close to zero. This behavior is indeed reasonable as the driver hits the gas pedal to prevent the vehicle from slowing down due to significant resistance forces which result from the sinusoidal steering maneuver. According to Figure 4.8, θ_{F_x} and θ_{F_y} do not vary significantly in time which corresponds to the expectation in the nominal case. As for the double lane change maneuver, the reference values are tracked very convincingly at the vehicle handling limits and even when the tires enter the region of sliding friction. Thus, the nominal estimator performance is assessed to be appropriate for autonomous vehicle guidance at the handling limits.

4.7.3 Adaptive Estimator Results

To evaluate the effectivness of the filter adaptation, the adaptive estimator is compared to the non-adaptive when tire parameters are distorted intentionally. Particularly, the maximum friction coefficient μ is

multiplied by 2, the nominal cornering stiffness (i.e. the slope at the origin of $F_{y,i}$, see section 2.1.2.4) by 1.5 while the nominal longitudinal tire stiffness (i.e. the slope at the origin of $F_{x,i}$, see section 2.1.2.3) remains unchanged. To achieve non-adaptive filter behavior, the condition number thresholds are chosen small enough to keep adaptation

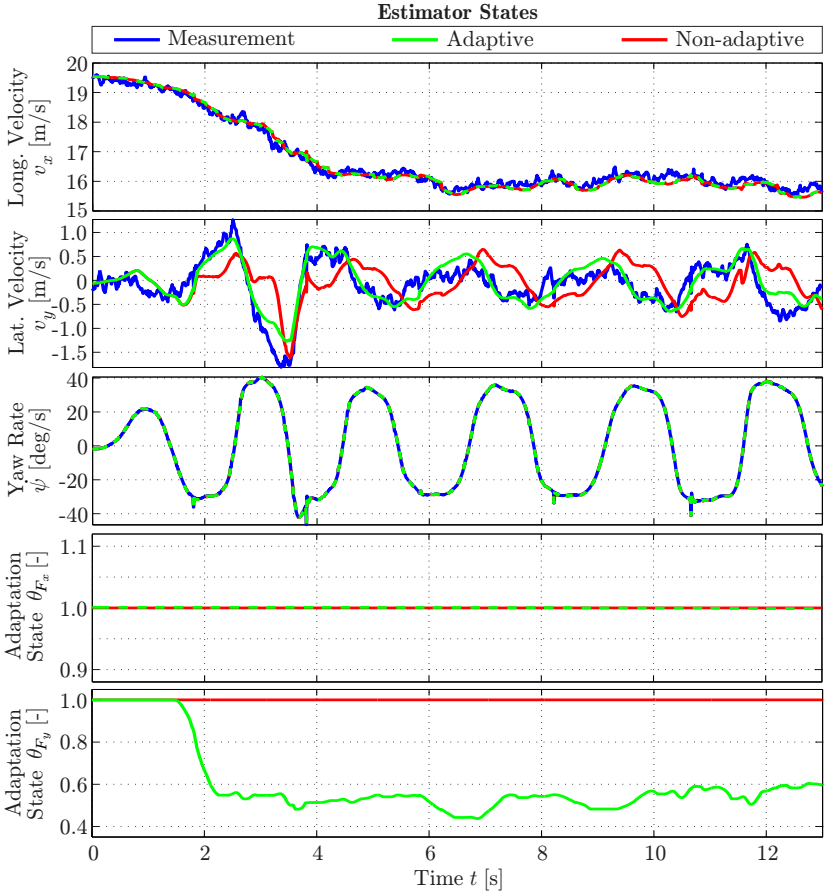

Figure 4.10: Adaptive vs. non-adaptive estimator results: State estimates

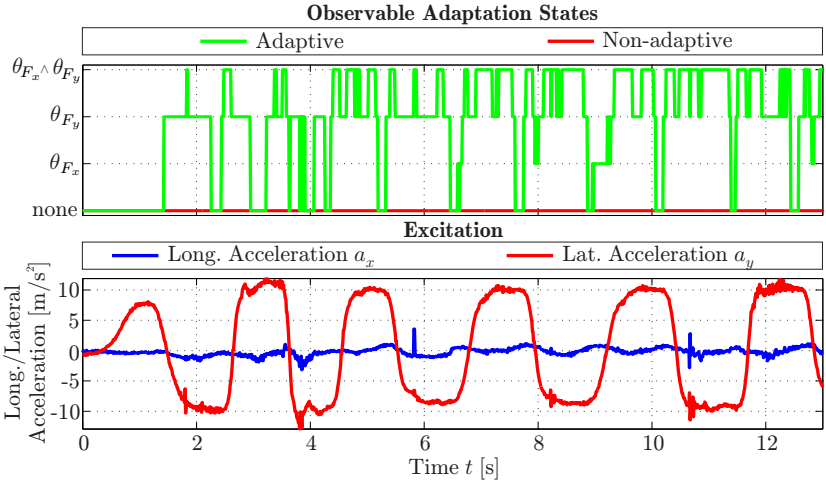

Figure 4.11: Adaptive vs. non-adaptive estimator results: Flags and accelerations

states constant. A comparison of the adaptive and the non-adaptive estimator results is depicted in Figure 4.10. While the longitudinal velocity v_x is still tracked very well in both cases, the lateral velocity v_y shows noticeable differences. While distinguishable phase shifts can be recognized for the non-adaptive estimator, these can completely be compensated in the adaptive case. Furthermore, amplitude errors are also less than in the non-adaptive case. As a quantitative measure, the RMSE of v_y amounts to 0.23 m/s in the adaptive case and is thus 54% less than the RMSE of 0.50 m/s in the non-adaptive case. This result shows the effectiviness of the filter adaptation. When considering θ_{F_y} in Figure 4.11, it can be noticed that the adaptation state reaches values between 0.45 and 0.6 quickly. This interval corresponds to the distortion of tire parameters. At the same time, θ_{F_x} remains constant as the longitudinal tire slip does not leave the non-distorted linear region of the tire model. Finally, it has to be stated that the convergence speed of the adaptation states inherently depends on the excitation which is indeed large for the investigated test scenarios. Nevertheless, this ex-

citation corresponds to the operating conditions of CA. Summing up, the estimator shows a very satisfying performance in the adaptive case even when tire parameters are significantly distorted.

5 Optimal Vehicle Dynamics Control

5.1 Motivation and Related Work

While the two previous chapters are related to sensor fusion, this chapter mainly focuses on vehicle control for autonomous vehicle guidance at the handling limits. In literature, a diversity of concepts can be found in the context of autonomous vehicle guidance comprising amongst others proportional-integral-derivative (PID) plus feed-forward controllers [14, 84], linear quadratic regulators (LQR) [85], input-output linearization based control [86, 87], sliding-mode control [87, 88] and flatness-based control [15]. Due to the fact that the evasion path respectively trajectory is considered to be given over a finite time horizon and physical constraints like actuator limitations and the tire-road friction limit are taken into account, a model predictive control scheme [19, 20] is investigated. The main advantage of employing an MPC-based control scheme is the possibility to explicitly account for constraints on the input, state and output variables. Furthermore, multiple-input multiple-output (MIMO) systems are inherently decoupled and reference as well as disturbance trajectories can be included in the computation of control inputs.

In general, the main idea of MPC-based control schemes is to employ a mathematical plant model to predict the plant's outputs $\boldsymbol{y}_{(k+j|k)}$, $j = 1,..,H_p$ over a finite prediction horizon of length H_p, see Figure 5.1. In this regard, $\{\cdot\}_{(k+j|k)}$ indicates that at time k the future value of variable $\{\cdot\}$ is predicted for time $k + j$. Moreover, the notation $\{\cdot\}_{(\cdot|k)}$ is employed if the entire prediction horizon is considered. According to the prediction of the plant's outputs, the control inputs are chosen in such a way over a finite control horizon of length H_u that the deviation of the

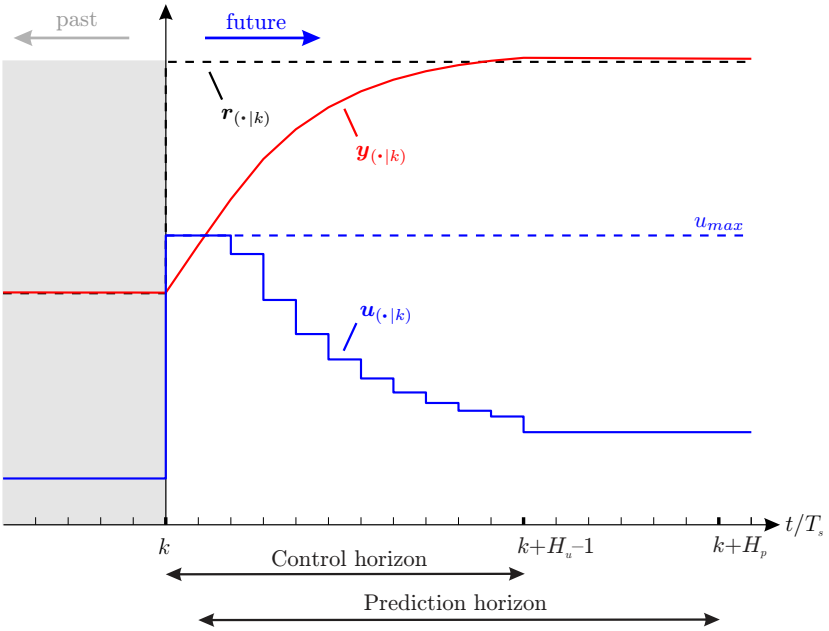

Figure 5.1: Model predictive control scheme

control outputs from a reference trajectory $\boldsymbol{r}_{(k+j|k)}$, $j = 1,...,H_p$ is minimized according to a quadratic cost function. This open-loop control problem is solved at each sampling time k, thus obtaining an optimal input step sequence $\boldsymbol{\Delta u}^*_{(k|k)},...,\boldsymbol{\Delta u}^*_{(k+H_u-1|k)}$. Finally, the control input $\boldsymbol{u}_k = \boldsymbol{u}_{k-1} + \boldsymbol{\Delta u}^*_{(k|k)}$ is applied to the plant where $\boldsymbol{u}_{k-1}$ denotes the control input of the preceding time step $k-1$. At the next time step, this optimization is repeated over a shifted prediction horizon.

For the purpose of autonomous vehicle guidance as well as vehicle stabilization MPC-based control schemes have previously been studied in literature. In the context of yaw stability control, [89, 90] introduce a hybrid MPC (HMPC) scheme to track a driver-intended yaw rate while stabilizing the vehicle at the static friction limit. In a similar context, [91] proposes a MPC-based envelope controller to track the drivers in-

tend in terms of yaw rate and sideslip while keeping the vehicle in a stable (state) envelope. Regarding MPC-based vehicle guidance, [92] introduces a nonlinear steering-only MPC controller (NMPC) to follow a given path in the scope of an obstacle avoidance maneuver as well as a side-wind rejection maneuver. In the same context, [93] proposes a hybrid parameter-varying MPC (HPV-MPC) which aims at reducing the computational complexity of [92]. A linear time-varying MPC (LTV-MPC) approach using successive linearizations of the nonlinear prediction model is investigated in [13]. In [21, 94], the additional use of differential braking by demanding the longitudinal tire slip respectively brake torque at each wheel is studied for the purpose of path following. As an extension of [21], the author shows in [4] that anticipating dynamic load transfer over the prediction horizon leads to an improved control performance when considering maneuvers with high lateral accelerations. From a conceptual point of view, [94] compares the approach of a (simple) low-level vehicle controller in combination with a trajectory replanning module to a single (complex) low-level MPC control law. It turns out that the latter approach is superior to stabilize the vehicle in complex counter-steering situations and in order to account for tire saturation. Therefore, a single complex MPC control law is preferred in the following.

In this chapter, a LTV-MPC based steering-only path following controller and a steering/braking trajectory following controller for combined longitudinal and lateral vehicle guidance is introduced. These approaches are based on the personal publications [2, 5]. Thereby, the formulation as LTV-MPC control scheme has been preferred to cover model nonlinearities while being able to apply the controller in real-time on the target dSPACE RCP hardware during experimental tests. As far as vehicle control in general is concerned, the main contribution of this thesis can be seen in extending previous LTV-MPC based approaches to guide and stabilize the vehicle in the nonlinear region of the tire model and even at the limits of static friction. In this regard, [13,21] limit the tire sideslip angles to the linear region of the tire model as the vehicle cannot always be stabilized in the nonlinear region when using LTV-MPC schemes. Furthermore, a disturbance estimator is presented to compensate steady-state offsets of the lateral displacement from the evasion path (at the end of the maneuver) that are caused by

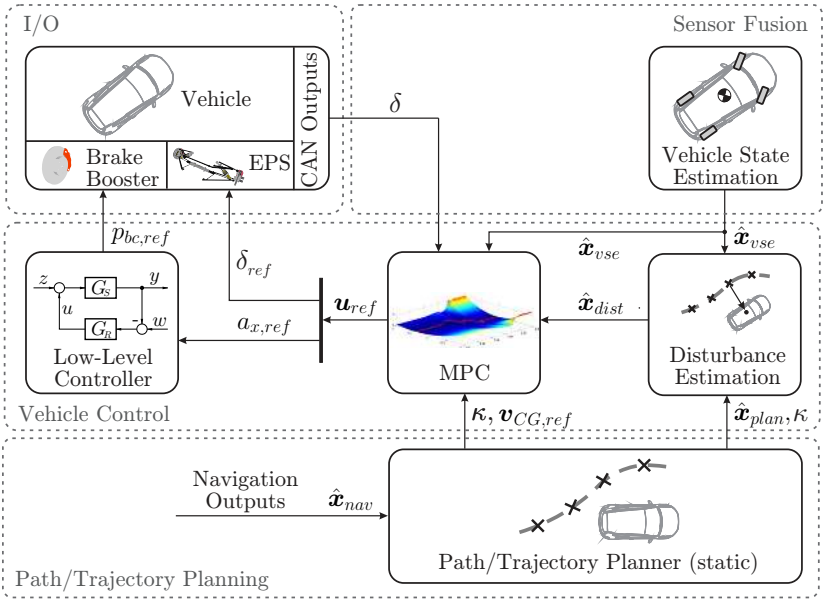

Figure 5.2: Optimal vehicle dynamics control scheme

time-varying yaw angle offsets in the navigation solution. This issue has not been solved in previous publications like [13]. For the path following steering-only controller, the ability to guide the vehicle at the handling limits as well as the inclusion of the vehicle state estimator's adaptation state θ_{F_y} (see section 4.5) into the control design is of major interest. In this way, an adaptive MPC-based control scheme is gained which is able to account for uncertainties in the tire-road contact and which has not been considered in previous contributions. As for the vehicle state estimator, it is assumed that other basic model parameters like the vehicle mass or mass moment of inertia are not subject to uncertainty. Finally, the steering/braking trajectory following controller is designed in the sense of an integrated vehicle dynamics control approach. Thereby, the trajectory following problem is decomposed in a path following problem and a velocity trajectory tracking problem.

The control scheme employs the wheel steering angle and the vehicle's longitudinal acceleration (in contrast to differential braking in [21]) as control inputs to follow an evasion trajectory at the handling limits. As the underlying application aims at avoiding accidents, only negative accelerations are considered to be reasonable as positive accelerations might even worsen the consequences of a collision. This particular formulation of the control problem has not been considered in previous publications.

Figure 5.2 focuses on the parts of the autonomous vehicle guidance scheme in section 2.4 that refer to vehicle control respectively serve as an input to the control scheme. In this regard, the controller's state vector is composed of outputs originating from the vehicle state estimator, the vehicle CAN bus and the disturbance estimator (see section 5.6). Moreover, reference as well as disturbance trajectories are supplied by the path/trajectory planner (see section 5.5). The control inputs, i.e the reference wheel steering angle δ_{ref} and the deceleration $a_{x,ref}$ (when applying the steering/braking controller), which are determined through an online-optimization are made available to the actuators. In this context, an update rate of 50 Hz is used for the steering-only controller while just 25 Hz are feasible for the steering/braking controller due to its higher computational complexity.

5.2 Lateral Vehicle Guidance

5.2.1 Problem Statement

This section mainly focuses on the design of an (adaptive) steering-only MPC-based controller for guiding the vehicle along an a priori known evasion path. The main objective of the predictive controller is to follow the evasion path with minimum lateral deviations by manipulating the wheel steering angle while stabilizing the vehicle during the entire maneuver. As outlined in section 5.1, the inclusion of the vehicle state estimator's adaptation state θ_{F_y} is additionally studied. In this way, the controller is able to account for (time-varying) model uncertainties in the tire-road contact.

5.2.2 Modeling

5.2.2.1 Vehicle Model and Relative Kinematics

To apply the predictive control scheme outlined above, an appropriate plant model that is capable of describing vehicle dynamics as well as relative kinematics of the vehicle and the evasion path is required. For this purpose, a nonlinear single-track model according to section 2.1.1.1 is employed, see Figure 5.3. Thereby, it is assumed that the height of CG is zero, thus neglecting roll and pitch dynamics, no longitudinal forces are transmitted neither at the front nor at the rear tire and that rolling resistances, aerodynamic drag as well as road bank and grade are negligible. Hence, the longitudinal, lateral and yaw momentum can be described by

$$\dot{v}_x = \dot{\psi} v_y - \frac{1}{m} F_{y,f} \sin(\delta) \tag{5.1}$$

$$\dot{v}_y = -\dot{\psi} v_x + \frac{1}{m} \Big(F_{y,f} \cos(\delta) + F_{y,r} \Big) \tag{5.2}$$

$$\ddot{\psi} = \frac{1}{J_z} \Big(F_{y,f} \cos(\delta) l_f - F_{y,r} l_r \Big). \tag{5.3}$$

With respect to section 2.2.2.1, the dynamic behavior of the steering actuator is approximated by a first-order lag element

$$\dot{\delta} = -\frac{1}{T_\delta} \delta + \frac{1}{T_\delta} \delta_{ref} \tag{5.4}$$

where T_δ denotes the dynamic time constant, δ_{ref} the demanded and δ the actual wheel steering angle. Finally, relative kinematics of the vehicle and the evasion path are modeled with respect to section 2.1.3 by

$$\Delta\dot{\psi} = \dot{\psi} - \kappa \sqrt{{v_x}^2 + {v_y}^2} \tag{5.5}$$

$$\Delta\dot{y} = \sqrt{{v_x}^2 + {v_y}^2} \sin(\Delta\psi) + v_y + d_{\Delta\dot{y}}. \tag{5.6}$$

In this context, $\Delta\psi$ denotes the relative yaw angle, Δy the lateral displacement of the vehicle's CG from the evasion path perpendicular to

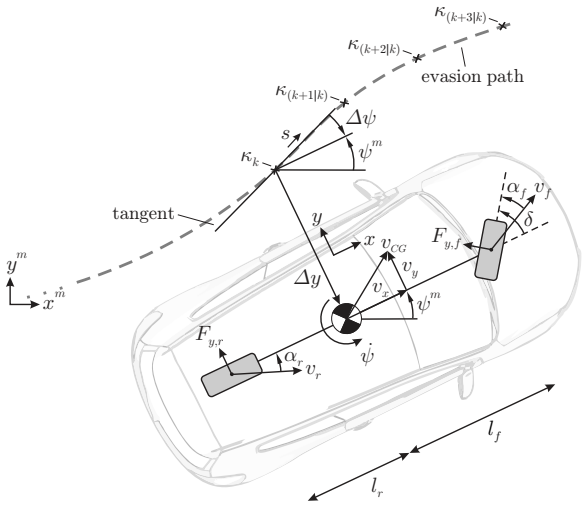

Figure 5.3: Free-body diagram of the employed prediction model

the longitudinal vehicle axis and κ the path's curvature. As discussed in [13], yaw angle offsets can be observed in the navigation solution during experimental tests. Regarding this control problem, a yaw angle offset would cause a relative yaw angle offset which can be interpreted as a lateral velocity disturbance $d_{\Delta\dot{y}}$ acting on the relative lateral velocity $\Delta\dot{y}$ in (5.6) and thus as a ramp disturbance on the control output Δy. To achieve steady-state offset-free tracking and to improve the transient tracking performance, the relative yaw angle offset is modeled as a lateral velocity disturbance $d_{\Delta\dot{y}}$. As no further knowledge about the dynamic behavior is available a common approach is to assume the disturbance to be constant, i.e.

$$\dot{d}_{\Delta\dot{y}} = 0. \tag{5.7}$$

Further information on disturbance estimation for the purpose of offset-free tracking is provided in section 5.6.

5.2.2.2 Tire Model

Compliant with section 2.1.2.4, a Pacejka Magic Formula tire model is applied to describe lateral tire forces $F_{y,f}$ and $F_{y,r}$ in (5.1)-(5.3). When assuming pure cornering, the lateral tire forces $F_{y,i}$ with $i \in \{f,r\}$ can be expressed as

$$F_{y,i} = \theta_{F_y} \cdot \mu F_{z,i} \cdot f_{y,i}(\alpha_i) \tag{5.8}$$

where $\mu F_{z,i}$ indicates the maximum feasible lateral tire force according to Coulomb's law of friction and $f_{y,i}(\alpha_i)$ the normalized Pacejka Magic Formula. In this regard, α_i denotes the tire sideslip angle at the front respectively rear axle with respect to section 2.1.2.2, μ the maximum friction coefficient and

$$F_{z,f} = \frac{m \cdot g \cdot l_r}{l_f + l_r}, \quad F_{z,r} = \frac{m \cdot g \cdot l_f}{l_f + l_r} \tag{5.9}$$

the nominal tire load according to section 2.1.2.6. Furthermore, it is assumed that the lateral tire forces that are transmitted at the front respectively rear axle in (5.1)-(5.3) are approximately the same as for the vehicle state estimator when summing up the lateral tire forces at the corresponding axle. For this reason, incorporating θ_{F_y} as adaptation parameter in (5.8) to account for (time-varying) uncertainties in the tire-road contact is assessed to be reasonable.

5.2.2.3 Resulting Prediction Model

Finally, replacing $F_{y,f}$ and $F_{y,r}$ in (5.1)-(5.3) with (5.8) and using the lateral displacement Δy from the evasion path as controlled output, the resulting nonlinear prediction model can be rewritten in state space representation as

$$\dot{\boldsymbol{x}}(t) = \boldsymbol{f}(\boldsymbol{x}(t),u(t),z(t),\theta^*(t)) \tag{5.10}$$

$$y(t) = g(\boldsymbol{x}(t)) = \Delta y(t) \tag{5.11}$$

where

$$\boldsymbol{x}^T = [v_x,\, v_y,\, \dot{\psi},\, \delta,\, \Delta\psi,\, \Delta y,\, d_{\Delta\dot{y}}] \tag{5.12}$$

denominates the state vector,

$$u = \delta_{ref} \tag{5.13}$$

the control input,

$$z = \kappa \tag{5.14}$$

the system disturbance and $\theta^* = \theta_{F_y}$ the adaptation parameter. In order to be used in the predictive control scheme, the nonlinear prediction model (5.10)-(5.11) has to be linearized at the current operating point $(\boldsymbol{x}_0, u_0, z_0)$ and to be transferred into a discrete-time representation. Finally, the resulting discrete-time linear affine prediction model can be written as

$$\boldsymbol{x}_{k+1} = \boldsymbol{A}_k(\theta_k^*)\boldsymbol{x}_k + \boldsymbol{B}_k(\theta_k^*)u_k + \boldsymbol{E}_k z_k + \boldsymbol{\Gamma}_k(\theta_k^*) \tag{5.15}$$

$$y_k = [0 \;\; 0 \;\; 0 \;\; 0 \;\; 0 \;\; 1 \;\; 0]\, \boldsymbol{x}_k = \Delta y_k \tag{5.16}$$

where $\boldsymbol{A}_k(\theta_k^*) \in \mathbb{R}^{7\times 7}$, $\boldsymbol{B}_k(\theta_k^*) \in \mathbb{R}^7$, $\boldsymbol{E}_k \in \mathbb{R}^7$ and $\boldsymbol{\Gamma}_k(\theta_k^*) \in \mathbb{R}^7$ indicate time-variant matrices and vectors with respect to time k depending on the adaptation parameter $\theta_k^* = \theta_{F_y,k}$. In this context, $\boldsymbol{A}_k(\theta_k^*)$ denotes the system matrix, $\boldsymbol{B}_k(\theta_k^*)$ the input matrix, $\boldsymbol{E}_k$ describes the influence of the system disturbance z on the state variables and $\boldsymbol{\Gamma}_k(\theta_k^*)$ denotes an affine term that results from the linearization of (5.10)-(5.11) and is employed to obtain absolute instead of error variables.

5.2.3 Model Validation

As the control performance of a model predictive control strategy inherently depends on the accuracy of the employed internal plant model [19], its validity is examined in the following. For this purpose, an autonomously driven double lane change maneuver is investigated. In this regard, Figure 5.4 depicts the corresponding reference wheel steering angle δ_{ref} as well as the associated lateral accelerations. It can be noticed that lateral accelerations increase up to $8.3\,\mathrm{m/s^2}$ such that the maneuver is appropriate to examine the model's accuracy at the vehicle handling limits.

For validation purposes, the reference wheel steering angle δ_{ref} is used as input variable to integrate the nonlinear prediction model (5.10) numerically in MATLAB/Simulink using the ODE45 solver for ordinary differential equations. When examining (5.5)-(5.6), it can be recognized that the relationship between the input δ_{ref} and the output $\Delta\psi$ contains a single integrator while two integrators are present as far as the relationship of δ_{ref} and Δy is concerned. Consequently, estimation results show reasonable values only for a short time interval as numerical integration errors increase in time. Therefore, the evaluation of $\Delta\psi$ and Δy is omitted consecutively thus that mainly the ability of the prediction model to describe vehicle dynamics is investigated. Nevertheless, the predictive controller generally considers just a short time interval in which integration errors are considerably small. Furthermore, these errors are eliminated in each time step due to the feedback of the state vector. Beside the relative orientation and lateral displacement, the disturbance state $d_{\Delta\dot{y}}$ is discarded for reasons of clarity as it remains constant over the integration interval.

The results of the open-loop estimation outlined above are illustrated

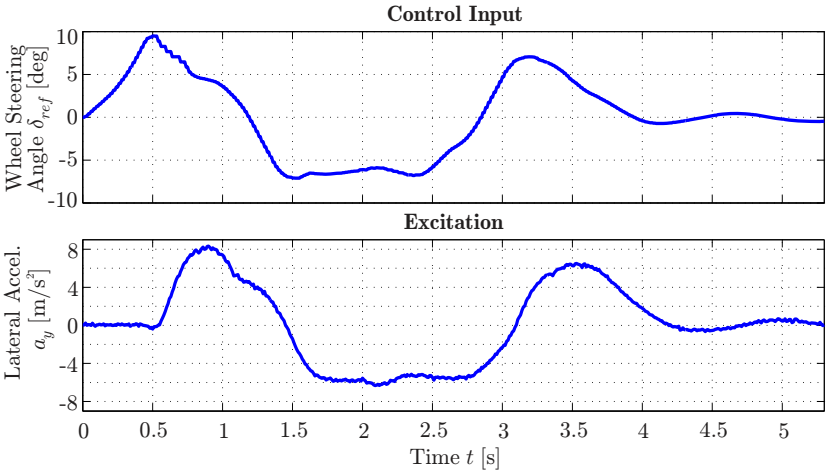

Figure 5.4: Model validation: Control inputs and excitation

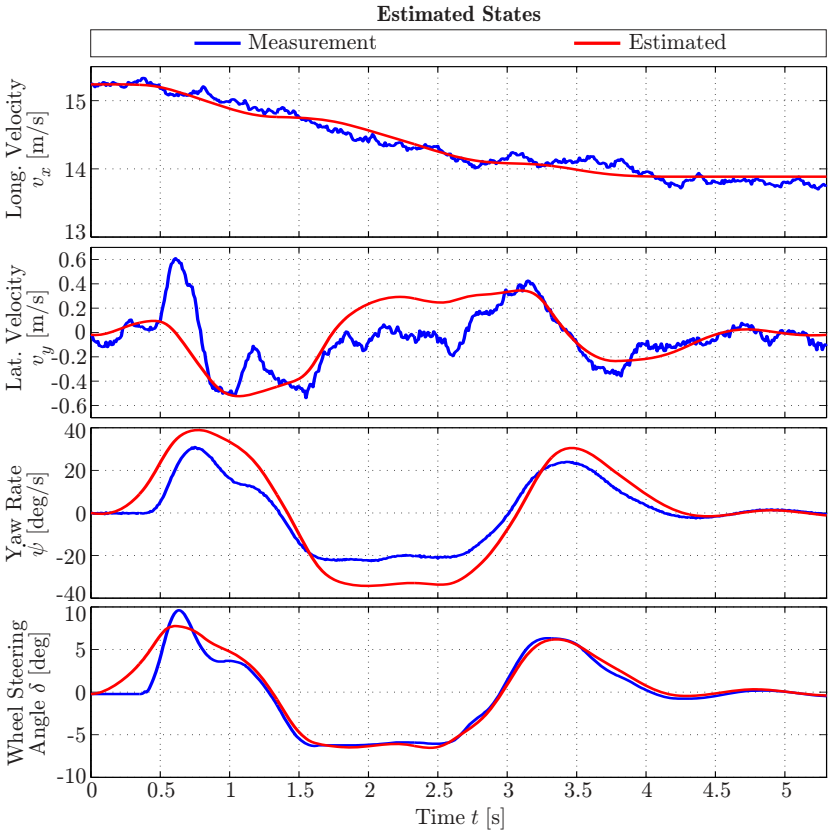

Figure 5.5: Model validation: Estimated states

in Figure 5.5. It is apparent that the longitudinal velocity v_x is tracked nearly perfectly. In contrast, the lateral velocity v_y as well as the yaw rate $\dot{\psi}$ show larger deviations from the actual measurement. In this context, initial estimation errors are noticeable larger as the low-level steering interface shows an initial activation time delay. This issue can unfortunately not be avoided with the available steering interface, which has actually been designed for the park assist, as the update rate of the

activation CAN message is too low. The delayed activation causes initial errors in the estimated wheel steering angle δ and thus in the lateral velocity as well as the yaw rate. However, this initial delay is not a serious issue for the considered application as the vehicle is driving almost straight during this time interval. For the rest of the maneuver, the wheel steering angle is tracked closely such that only minor quantitative errors are present. Although a larger model mismatch is apparent for the lateral velocity and the yaw rate, experimental control results in chapter 6 confirm that the accuracy of prediction model is adequate to be used in the predictive control scheme.

5.2.4 Predictive Control Problem

For the single-input single-output (SISO) path following problem, the main objective of the controller is to minimize the lateral path displacement Δy from the evasion path by demanding the wheel steering angle δ_{ref} to follow the evasion path in an optimal way. Consequently, the reference value $r_{(k+j|k)}$, $j = 1,...,H_p$ of the controlled output $y = \Delta y$ is set to zero. As the prediction model is inherently nonlinear, especially when operating at the vehicle handling limits, successive linearizations of the nonlinear plant model (5.10)-(5.11) are determined at the operating point

$$(\boldsymbol{x}_0 = \boldsymbol{x}_k,\, u_0 = \delta_{ref,k-1},\, z_0 = \kappa_k) \tag{5.17}$$

and in dependence of the adaptation parameter $\theta_k^* = \theta_{F_y,k}$ in each sampling step at time k. In this regard, $\boldsymbol{x}_k$ denotes the state vector at time k, $\delta_{ref,k-1}$ the control input that has been applied to the plant at time $k-1$ and κ_k the path's curvature at time k. Thereby, an adaptive LTV-MPC scheme is gained when θ_{F_y} is assigned in accordance to the corresponding vehicle state estimator's adaptation state. Contrarily, the predictive controller shows nominal behavior if θ_{F_y} is set to 1. The required state variables $\boldsymbol{x}_k$ are supplied by the vehicle state estimator (see chapter 4), the disturbance estimator (see section 5.6) and the vehicle's CAN bus. The resulting discrete-time linear affine prediction model (5.15)-(5.16) is used to determine the free response of the plant and to formulate the constrained finite-time optimal control problem

(CFTOC). When predicting the free response of the plant, the path curvature κ_k at time k results from the perpendicular projection of the vehicle's CG on the evasion path, see Figure 5.3. For the remaining prediction horizon, $\kappa_{(k+j|k)}$ with $j = 1,...,H_p - 1$ is estimated assuming that the vehicle follows the evasion path in an optimal way along the path coordinate s, see section 5.5. Using the quadratic cost function

$$J(\boldsymbol{\Delta u}, \epsilon_f, \epsilon_r) = Q \cdot \sum_{j=1}^{H_p-1} {y_{(k+j|k)}}^2 \tag{5.18a}$$

$$+ Q_{H_p} \cdot {y_{(k+H_p|k)}}^2 \tag{5.18b}$$

$$+ R \cdot \sum_{j=0}^{H_u-1} {\Delta u_{(k+j|k)}}^2 \tag{5.18c}$$

$$+ \rho_f \cdot \epsilon_f + \rho_r \cdot \epsilon_r, \tag{5.18d}$$

the CFTOC of the path following problem can be formulated as

$$\min_{\boldsymbol{\Delta u}, \epsilon_f, \epsilon_r} J(\boldsymbol{\Delta u}, \epsilon_f, \epsilon_r) \tag{5.19a}$$

subject to
dynamic constraints

$$\boldsymbol{x}_{k+1} = \boldsymbol{A}_k(\theta_k^*)\boldsymbol{x}_k + \boldsymbol{B}_k(\theta_k^*)u_k + \boldsymbol{E}_k z_k + \boldsymbol{\Gamma}_k(\theta_k^*) \tag{5.19b}$$

$$y_k = [0 \;\; 0 \;\; 0 \;\; 0 \;\; 0 \;\; 1 \;\; 0]\, \boldsymbol{x}_k = \Delta y_k \tag{5.19c}$$

input constraints

$$\Delta u_{(k+j|k)} \geq \Delta\delta_{ref,min}, \qquad j = 0,...,H_u - 1 \tag{5.19d}$$

$$\Delta u_{(k+j|k)} \leq \Delta\delta_{ref,max}, \qquad j = 0,...,H_u - 1 \tag{5.19e}$$

$$u_{(k+j|k)} \geq \delta_{ref,min}, \qquad j = 0,...,H_u - 1 \tag{5.19f}$$

$$u_{(k+j|k)} \leq \delta_{ref,max}, \qquad j = 0,...,H_u - 1 \tag{5.19g}$$

and state constraints

$$\alpha_{f,(k+j|k)} \geq \alpha_{f,min} - \epsilon_f, \qquad j = 1,...,H_p \tag{5.19h}$$

$$\alpha_{f,(k+j|k)} \leq \alpha_{f,max} + \epsilon_f, \qquad j = 1,...,H_p \tag{5.19i}$$

$$\alpha_{r,(k+j|k)} \geq \alpha_{r,min} - \epsilon_r, \qquad j = 1,...,H_p \tag{5.19j}$$

$$\alpha_{r,(k+j|k)} \leq \alpha_{r,max} + \epsilon_r, \qquad j = 1,...,H_p \tag{5.19k}$$

$$\epsilon_f \geq 0,\ \epsilon_r \geq 0 \tag{5.19l}$$

where $\boldsymbol{\Delta u}^T = [\Delta u_{(k|k)},...,\Delta u_{(k+H_u-1|k)}]$. In the quadratic cost function (5.18), (5.18a)-(5.18b) prune the deviation of the control output from its reference value over the prediction horizon, (5.18c) the control input's change per time step over the control horizon and (5.18d) the use of the slack variables ϵ_f and ϵ_r that are employed to formulate soft constraints (5.19h)-(5.19k). To apply the control scheme in real-time, the control horizon H_u is always chosen shorter than the prediction horizon H_p to reduce computation time. In this context, investigations have shown that using terminal cost (5.18b), i.e. a significantly increased weight at the end of the prediction horizon, leads to a noticeable improvement of the control performance. Thereby, it has to be noted that the control scheme is stable without any appropriately chosen terminal cost. Indeed, the main intention of employing (5.18b) is to force the control outputs to tend towards their reference values at the end of the prediction horizon which has turned out to be beneficial for the control performance.

As far as optimization constraints are concerned, dynamic constraints (5.19b-5.19c) specify the discrete-time linear affine prediction model that is used at the current operating point. Furthermore, input constraints (5.19d)-(5.19g) are introduced to account for physical limitations of steering system. In particular, (5.19f)-(5.19g) limit the absolute value of the wheel steering angle while (5.19d)-(5.19e) constrain the corresponding maximum and minimum change per time step. According to [13] and [2], constraints (5.19h)-(5.19k) on the tire sideslip angles have to be incorporated in the CFTOC to ensure vehicle stability when operating in the nonlinear region of the tire model. As the tire sideslip angles are a nonlinear function of the state variables, α_f and α_r are linearized at the current operating point to obtain linear constraints and thus a convex optimization problem. The particular choice of the maximum and minimum tire sideslip angles is essential to ensure vehicle stability at the handling limits. A detailed discussion on how to determine these limits can be found in section 5.4. Due to the fact that tire sideslip angle constraints depend on the state variables, input as well as dynamic constraints might prevent that (5.19h)-(5.19k) are fulfilled which would cause an infeasible optimization problem, see [19]. To ensure feasibility of the CFTOC (5.19), state constraints (5.19h)-(5.19k) are softened by introducing slack variables ϵ_f and ϵ_r. Finally $Q \in \mathbb{R}$,

$Q_{H_p} \in \mathbb{R}$, $R \in \mathbb{R}$, $\rho_f \in \mathbb{R}$ and $\rho_r \in \mathbb{R}$ in (5.18) denote weighting coefficients. The resulting convex optimization problem subject to linear constraints is a quadratic program (QP) that can be solved numerically e.g. by active set or interior point methods, see [95].

Finally, it has to be stated that sideslip angle constraints (5.19h)-(5.19k) are always formulated for the nominal case. When the tire-road contact changes significantly, e.g. from a dry to a wet road, the static friction limit in terms of maximum/minimum tire sideslip angles will decrease/increase to smaller/larger values, see [22]. Even though the adaptive controller is able to scale tire forces, it is not able to actually prevent the tire from entering the region of sliding friction although the prediction model assumes to be within the region of static friction. This is only possible when the maximum/minimum tire sideslip angles are identified online. Solving this issue is part of future work.

5.3 Combined Longitudinal and Lateral Vehicle Guidance

5.3.1 Problem Statement

While the previous section focuses on a steering-only controller for a path following problem, this section investigates the design of a steering/braking controller for a trajectory following problem. Thereby, the trajectory following problem is decomposed in a path following problem, as described in section 5.2, and a velocity trajectory following problem. In particular, the main objective of the controller is to minimize the lateral displacement from the evasion path while tracking the velocity reference as close as possible by manipulating the wheel steering angle as well as the vehicle's longitudinal acceleration. As the application of CA aims at avoiding accidents, only negative accelerations are applied by the controller as positive accelerations increase the kinetic energy of the vehicle and thus may worsen the consequences of a collision. Furthermore, the combined transmission of longitudinal and lateral tire forces is explicitly considered in the employed plant model. Thus, the

MIMO trajectory following problem is handled in the sense of an integrated vehicle dynamics control approach. While the steering-only controller allows for a model adaptation, this possibility has not yet been examined for the steering/braking case and is still part of future work.

5.3.2 Modeling

5.3.2.1 Vehicle Model and Relative Kinematics

Similar to section 5.2, a nonlinear single-track model is employed to describe vehicle dynamics, see Figure 5.6. Referring to section 2.1.1.1, Newton-Euler equations (5.20)-(5.22) describe the longitudinal and lateral momentum with respect to CG in the vehicle reference frame while yaw dynamics are considered by (5.22). Compared to the steering-only approach in section 5.2, the longitudinal deceleration $a_{x,br}$ as well as the corresponding longitudinal tire forces $F_{x,f}$ and $F_{x,r}$ are additionally incorporated in (5.20)-(5.22). The particular computation of $F_{x,f}$ and $F_{x,r}$ in dependence of $a_{x,br}$ is introduced in section 5.3.2.2.

$$\dot{v}_x = \dot{\psi} v_y - \frac{1}{m} F_{y,f} \sin(\delta) + a_{x,br} \tag{5.20}$$

$$\dot{v}_y = -\dot{\psi} v_x + \frac{1}{m}\Big(F_{y,f} \cos(\delta) + F_{y,r} + F_{x,f} \sin(\delta) \Big) \tag{5.21}$$

$$\ddot{\psi} = \frac{1}{J_z}\Big(F_{y,f} \cos(\delta) l_f + F_{x,f} \sin(\delta) l_f - F_{y,r} l_r \Big) \tag{5.22}$$

With respect to section 2.2.2.1, the dynamic behavior of the steering actuator is approximated by a first-order lag element

$$\dot{\delta} = -\frac{1}{T_\delta}\delta + \frac{1}{T_\delta}\delta_{ref} \tag{5.23}$$

where T_δ denotes the dynamic time constant, δ_{ref} the demanded and δ the actual wheel steering angle. Likewise, the dynamic behavior of the braking system is modeled in accordance to section 2.2.2.2

$$\dot{a}_{x,br} = -\frac{1}{T_{a_{x,br}}} a_{x,br} + \frac{1}{T_{a_{x,br}}} a_{x,br,ref} \tag{5.24}$$

where $T_{a_{x,br}}$ denotes the dynamic time constant, $a_{x,br,ref}$ the demanded and $a_{x,br}$ the actual longitudinal deceleration due to braking. As the trajectory following problem is decomposed in a path following and a velocity trajectory following problem, relative kinematics of the vehicle's CG and the evasion path are modeled in the same way as in section 5.2, i.e.

$$\Delta\dot{\psi} = \dot{\psi} - \kappa\sqrt{{v_x}^2 + {v_y}^2} \tag{5.25}$$

$$\Delta\dot{y} = \sqrt{{v_x}^2 + {v_y}^2}\sin(\Delta\psi) + v_y + d_{\Delta\dot{y}} \tag{5.26}$$

$$\dot{d}_{\Delta\dot{y}} = 0 \tag{5.27}$$

where $\Delta\psi$ denotes the relative yaw angle, Δy the lateral distance between the vehicle's CG and the evasion path perpendicular to the longitudinal vehicle axis and κ the path's curvature. The disturbance state $d_{\Delta\dot{y}}$ is employed to compensate relative yaw-angle offsets as further outlined in section 5.6. For the second control output, i.e. the velocity v_{CG} at CG, disturbance estimation is considered not to be reasonable

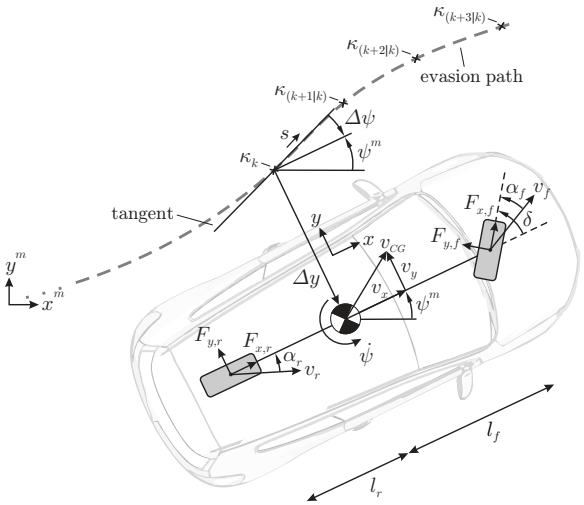

Figure 5.6: Free-body diagram of the employed prediction model

as the velocity can just be decreased by braking but not be increased by accelerating.

5.3.2.2 Tire Model

Longitudinal Tire Forces As outlined in section 5.3.2.1, longitudinal tire forces $F_{x,f}$ and $F_{x,r}$ have to be determined in dependence of $a_{x,br}$. The longitudinal momentum due to braking can be expressed as

$$m \cdot a_{x,br} = F_{x,f} \cos(\delta) + F_{x,r}. \tag{5.28}$$

Defining the tire force distribution i_{br} between front and rear axle as

$$i_{br} = \frac{F_{x,f}}{F_{x,f} + F_{x,r}}, \tag{5.29}$$

the corresponding longitudinal front and rear tire forces can be formulated as

$$F_{x,f} = \frac{i_{br}}{1 - i_{br}} F_{x,r}, \quad F_{x,r} = \frac{1 - i_{br}}{i_{br}} F_{x,f} \tag{5.30}$$

when reorganizing (5.29) with respect to $F_{x,f}$ and $F_{x,r}$. When substituting (5.30) in (5.28), $F_{x,f}$ and $F_{x,r}$ can be determined as a nonlinear function of $a_{x,br}$

$$F_{x,f} = \frac{m}{\cos(\delta) + \frac{1-i_{br}}{i_{br}}} \cdot a_{x,br}, \quad F_{x,r} = \frac{m}{1 + \frac{i_{br}}{1-i_{br}} \cos(\delta)} \cdot a_{x,br}. \tag{5.31}$$

For the sake of simplicity, it is assumed that the ideal brake force distribution [22]

$$i_{br} = \frac{F_{z,f}}{F_{z,f} + F_{z,r}} = \frac{l_r}{l_f + l_r} \tag{5.32}$$

is applied by the braking system, where

$$F_{z,f} = \frac{m \cdot g \cdot l_r}{l_f + l_r}, \quad F_{z,r} = \frac{m \cdot g \cdot l_f}{l_f + l_r} \tag{5.33}$$

denotes the nominal tire load neglecting load transfer, see section 2.1.2.6.

Lateral Tire Forces Similar to section 5.2.2.2, lateral tire forces $F_{y,f}$ and $F_{y,r}$ in (5.20)-(5.22) are determined through a Pacejka Magic Formula tire model. When assuming pure cornering, the corresponding lateral tire forces $F_{y,i,0}$ with $i \in \{f,r\}$ can be expressed as

$$F_{y,i,0} = \mu F_{z,i} \cdot f_{y,i}(\alpha_i) \tag{5.34}$$

where $\mu F_{z,i}$ indicates the maximum feasible lateral tire force according to Coulomb's law of friction and $f_{y,i}(\alpha_i)$ the normalized Pacejka Magic Formula. Thereby, α_i denotes the tire sideslip angle at the front respectively rear tire according to section 2.1.2.2, μ the maximum tire-road friction coefficient and $F_{z,i}$ the nominal tire load as defined in (5.33).

Combined Slip With respect to section 2.1.2.5, the simultaneous transmission of longitudinal and lateral tire forces is considered by reducing the lateral tire force $F_{y,i,0}$ with $i \in \{f,r\}$ at pure cornering depending on the transmission of longitudinal forces in accordance to the friction ellipse

$$F_{y,i} = F_{y,i,0}\sqrt{1 - \left(\frac{F_{x,i}}{F_{x,i,max}}\right)^2} \tag{5.35}$$

where

$$F_{x,i,max} = \begin{cases} \mu F_{z,i} \ , & |F_{x,i}| < \mu F_{z,i} \\ \xi_{F_x} |F_{x,i}| \ , & |F_{x,i}| \geq \mu F_{z,i} \end{cases} \tag{5.36}$$

with $\xi_{F_x} > 1$ describes the maximum feasible longitudinal tire force. As the maximum friction coefficient μ is not known exactly and load transfer is neglected, the longitudinal tire forces that are determined by (5.31) in dependence of $a_{x,br}$ may exceed the assumed friction limit $\mu F_{z,i}$. At the same time, $F_{x,i}/F_{x,i,max} < 1$ has to be ensured to avoid linearization and numerical issues. For this reason, the maximum feasible force $F_{x,i,max}$ is increased to a slightly larger value than the absolute value of the longitudinal tire force $F_{x,i}$ if $|F_{x,i}| \geq \mu F_{z,i}$. For this purpose, ξ_{F_x} is introduced in (5.36) and has to be chosen slightly greater than one.

5.3.2.3 Resulting Prediction Model

Finally, replacing $F_{x,i}$ and $F_{y,i}$ in (5.20)-(5.22) with (5.31) and (5.35) while using the lateral displacement Δy from the evasion path as well as the absolute velocity $v_{CG} = \sqrt{v_x^2 + v_y^2}$ at CG as control outputs, the resulting nonlinear prediction model can be rewritten in state space representation as

$$\dot{\boldsymbol{x}}(t) = \boldsymbol{f}(\boldsymbol{x}(t), \boldsymbol{u}(t), z(t)) \tag{5.37}$$

$$\boldsymbol{y}(t) = \boldsymbol{g}(\boldsymbol{x}(t)) = \begin{bmatrix} \Delta y(t) \\ v_{CG}(t) \end{bmatrix} \tag{5.38}$$

where

$$\boldsymbol{x}^T = [v_x,\, v_y,\, \dot{\psi},\, \delta,\, a_{x,br},\, \Delta\psi,\, \Delta y,\, d_{\Delta\dot{y}}] \tag{5.39}$$

denotes the state vector,

$$\boldsymbol{u}^T = [\delta_{ref},\, a_{x,br,ref}] \tag{5.40}$$

the control input vector and

$$z = \kappa \tag{5.41}$$

the system disturbance. To be applied in the predictive control strategy, the nonlinear prediction model (5.37)-(5.38) has to be linearized at the current operating point $(\boldsymbol{x}_0, \boldsymbol{u}_0, z_0)$ and to be transferred into a discrete-time representation. Hence, the resulting discrete-time linear affine prediction model can be written as

$$\boldsymbol{x}_{k+1} = \boldsymbol{A}_k \boldsymbol{x}_k + \boldsymbol{B}_k \boldsymbol{u}_k + \boldsymbol{E}_k z_k + \boldsymbol{\Gamma}_k \tag{5.42}$$

$$\boldsymbol{y}_k = \boldsymbol{C}_k \boldsymbol{x}_k + \boldsymbol{\Pi}_k \tag{5.43}$$

where $\boldsymbol{A}_k \in \mathbb{R}^{8\times 8}$ denotes the system matrix, $\boldsymbol{B}_k \in \mathbb{R}^{8\times 2}$ the input matrix, $\boldsymbol{C}_k \in \mathbb{R}^{2\times 8}$ the output matrix, $\boldsymbol{E}_k \in \mathbb{R}^8$ describes the influence of the system disturbance z on the state variables and $\boldsymbol{\Gamma}_k \in \mathbb{R}^8$ as well as $\boldsymbol{\Pi}_k \in \mathbb{R}^2$ indicate affine terms that result from the linearization of (5.37)-(5.38). Thereby, these matrices and vectors are time-varying with respect to time k.

5.3.3 Model Validation

Now that the vehicle and tire model for combined steering and braking has been deduced, its validity is proven consecutively. For this purpose, an autonomously driven double lane change maneuver with simultaneous steering and braking is considered. The plant's inputs, i.e. the demanded wheel steering angle δ_{ref} and the demanded longitudinal deceleration due to braking $a_{x,br,ref}$, as well as the maneuver accelerations are depicted in Figure 5.7. In this context, horizontal accelerations have a maximum magnitude of $8.9\,\mathrm{m/s^2}$ during combined steering and braking. Furthermore, lateral accelerations are in the range of $\pm 6.7\,\mathrm{m/s^2}$ while longitudinal accelerations take values up to $-9.3\,\mathrm{m/s^2}$. Hence, the scenario is appropriate to assess the model's validity in the operating range of CA.

Figure 5.8 illustrates the results when the nonlinear plant model (5.37) is integrated numerically by using MATLAB/Simulink's ODE45 solver. As the additional deceleration due to braking $a_{x,br}$ cannot be measured directly, no reference value is available thus that the longitudinal acceleration a_x at CG has been used as reference value instead. The auxiliary reference value a_x is compared to the estimated longitudinal acceleration at CG. Similar to the steering-only control scheme, $\Delta\psi$ and Δy are not depicted due to their integrating behavior. Likewise, $d_{\Delta\dot{y}}$ is discarded as it remains constant over the integration interval.

When examining the estimation results, the reference values of the longitudinal velocity v_x and lateral velocity v_y are tracked closely even during simultaneous steering and braking in the time interval from $t = 0.5$ to 1.5 s and from $t = 4$ to 4.5 s. Thereby, larger estimation errors of the lateral velocity from $t = 0$ to 0.7 s are once again caused by the initial time delay of the steering actuator. As the horizontal velocities v_x and v_y are estimated sufficiently well, it can be concluded that the same holds for the horizontal velocity v_{CG}. Thus, v_{CG} has been omitted for reasons of clarity as it basically corresponds to v_x. At the same time, the yaw rate $\dot{\psi}$ shows larger deviations from its reference while the qualitative behavior is still described convincingly. Moreover, the actual wheel steering angle is again estimated without any significant quantitative errors with the exception of the initial time delay. Finally,

the estimated longitudinal acceleration coincides with the actual measurement very well while larger errors are only apparent when the brake booster shows a significantly delayed response. However, this issue can only be observed for small longitudinal accelerations (due to the buildup of the brake pressure) and is almost not apparent for larger accelerations. Even though the yaw rate shows a larger model mismatch for the considered maneuver, experimental control results verify that the plant

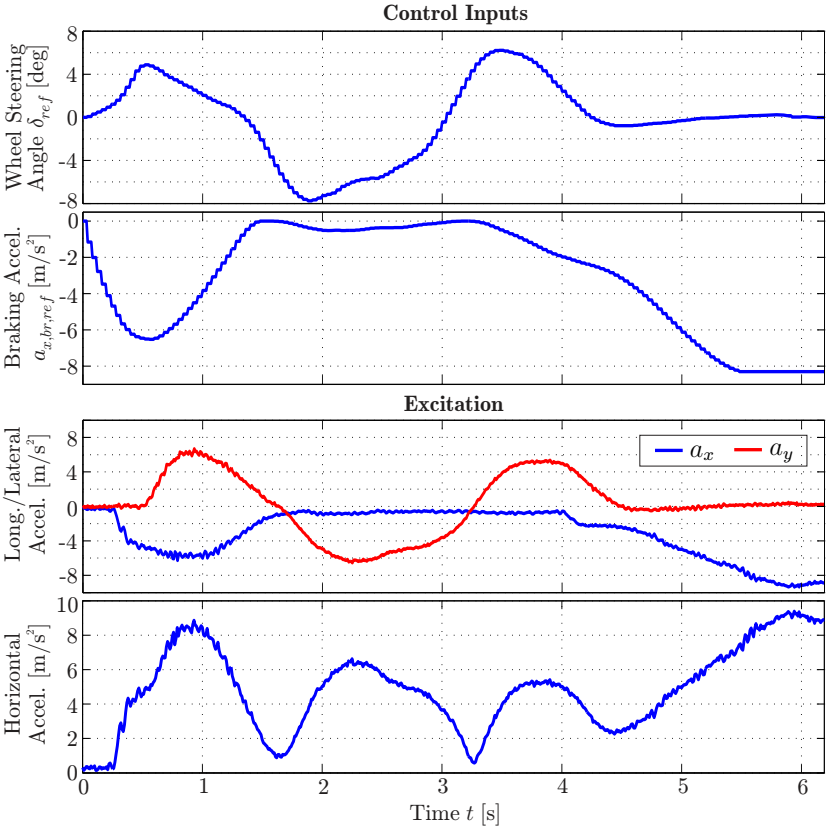

Figure 5.7: Model validation: Control inputs and excitation

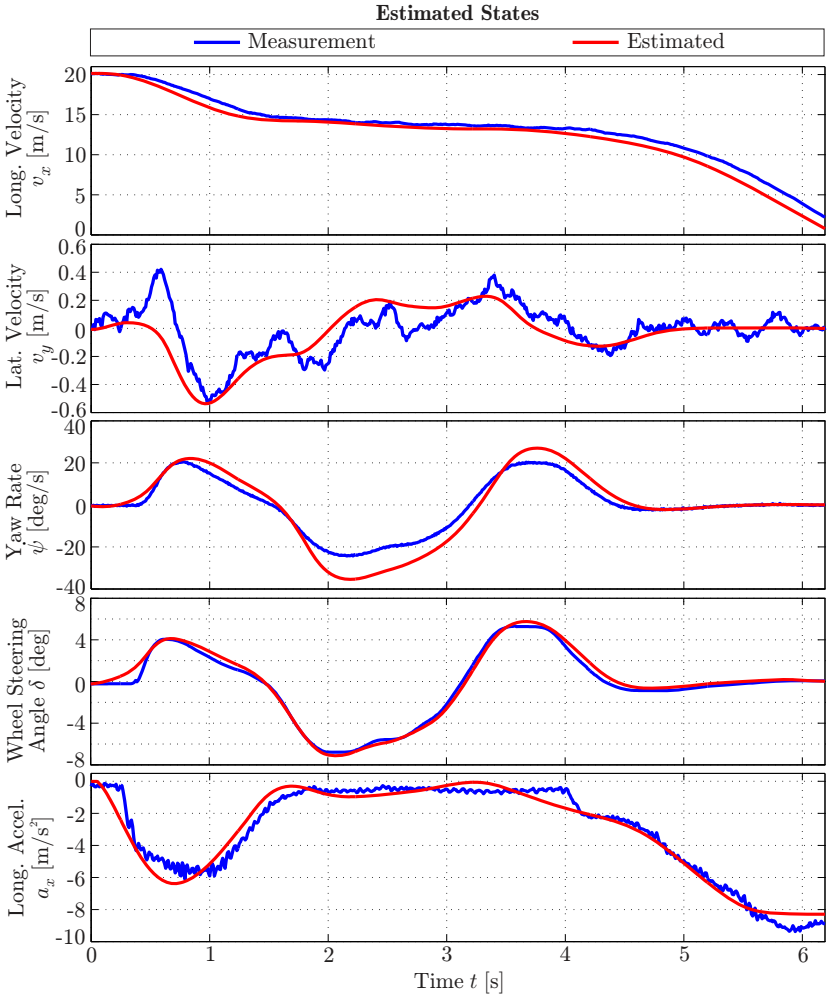

Figure 5.8: Model validation: Estimated states

model is appropriate to be employed in the steering/braking control scheme.

5.3.4 Predictive Control Problem

For the trajectory following problem, the main aim of the controller can be described as minimizing the lateral deviation Δy from the evasion path while tracking the horizontal velocity v_{CG} at CG as close as possible by demanding the wheel steering angle δ_{ref} as well as the vehicle's longitudinal deceleration due to braking $a_{x,br,ref}$. In this way, the MIMO control problem is decomposed in a path following problem and a velocity trajectory tracking problem. While the reference value of the lateral deviation $r_{\Delta y,(k+j|k)}$, $j = 1,...,H_p$ is set to zero, the velocity reference value $r_{v_{CG},(k+j|k)}$, $j = 1,...,H_p$ is provided by the path/trajectory planner. As the employed prediction model is inherently nonlinear, especially when operating at the vehicle handling limits, successive linearizations of the nonlinear plant model (5.37)-(5.38) are determined at the current operating point

$$(\boldsymbol{x}_0 = \boldsymbol{x}_k,\, \boldsymbol{u}_0 = \boldsymbol{u}_{k-1},\, z_0 = \kappa_k) \tag{5.44}$$

in each sampling step at time k, thus obtaining a LTV-MPC control scheme. In this regard, $\boldsymbol{x}_k$ denotes the state vector at time k, $\boldsymbol{u}_{k-1}$ the control input that has been applied to the plant at time $k-1$ and κ_k the path's curvature at time k. Similar to the steering-only controller, the state variables are gained from the vehicle state estimator (see chapter 4), the disturbance estimator (see section 5.6) and the vehicle's CAN bus. Thereby, the longitudinal acceleration due to braking is not directly estimated but derived from (5.20) as

$$a_{x,br} = a_x + \frac{1}{m} F_{y,f} \sin(\delta) \tag{5.45}$$

where a_x indicates the measured longitudinal acceleration at CG (see section 4.2) and $F_{y,f} = F_{y,fl} + F_{y,fr}$ the estimated applied lateral tire force at the front axle which is deduced from the vehicle state estimator's outputs.

To predict the free response of the plant and formulate the corresponding CFTOC, the discrete-time linear affine plant model (5.42)-(5.43) is applied. Furthermore, the path's curvature κ_k at time k results from the perpendicular projection of the vehicle's CG on the evasion path while $\kappa_{(k+j|k)}$ with $j = 1,...,H_p - 1$ is estimated assuming that the vehicle follows the evasion path in an optimal way along the path coordinate s, see section 5.5. Using the quadratic cost function

$$J(\boldsymbol{\Delta u}, \epsilon_f, \epsilon_r) = \sum_{j=1}^{H_p-1} \boldsymbol{e}_{(k+j|k)}^T \boldsymbol{Q} \boldsymbol{e}_{(k+j|k)} \tag{5.46a}$$

$$+ \boldsymbol{e}_{(k+H_p|k)}^T \boldsymbol{Q}_{H_p} \boldsymbol{e}_{(k+H_p|k)} \tag{5.46b}$$

$$+ \sum_{j=0}^{H_u-1} \boldsymbol{\Delta u}_{(k+j|k)}^T \boldsymbol{R} \boldsymbol{\Delta u}_{(k+j|k)} \tag{5.46c}$$

$$+ \rho_f \cdot \epsilon_f + \rho_r \cdot \epsilon_r \tag{5.46d}$$

with $\boldsymbol{e}_{(k+j|k)} = \boldsymbol{y}_{(k+j|k)} - \boldsymbol{r}_{(k+j|k)}$, the CFTOC of the trajectory following problem can be formulated as

$$\min_{\boldsymbol{\Delta u}, \epsilon_f, \epsilon_r} J(\boldsymbol{\Delta u}, \epsilon_f, \epsilon_r) \tag{5.47a}$$

subject to
dynamic constraints

$$\boldsymbol{x}_{k+1} = \boldsymbol{A}_k \boldsymbol{x}_k + \boldsymbol{B}_k \boldsymbol{u}_k + \boldsymbol{E}_k z_k + \boldsymbol{\Gamma}_k \tag{5.47b}$$

$$\boldsymbol{y}_k = \boldsymbol{C}_k \boldsymbol{x}_k + \boldsymbol{\Pi}_k \tag{5.47c}$$

input constraints

$$\boldsymbol{\Delta u}_{(k+j|k)} \geq \boldsymbol{\Delta u}_{min}, \qquad j = 0,...,H_u - 1 \tag{5.47d}$$

$$\boldsymbol{\Delta u}_{(k+j|k)} \leq \boldsymbol{\Delta u}_{max}, \qquad j = 0,...,H_u - 1 \tag{5.47e}$$

$$\boldsymbol{u}_{(k+j|k)} \geq \boldsymbol{u}_{min}, \qquad j = 0,...,H_u - 1 \tag{5.47f}$$

$$\boldsymbol{u}_{(k+j|k)} \leq \boldsymbol{u}_{max}, \qquad j = 0,...,H_u - 1 \tag{5.47g}$$

and state constraints

$$\alpha_{f,(k+j|k)} \geq \alpha_{f,min} - \epsilon_f, \qquad j = 1,...,H_p \tag{5.47h}$$
$$\alpha_{f,(k+j|k)} \leq \alpha_{f,max} + \epsilon_f, \qquad j = 1,...,H_p \tag{5.47i}$$
$$\alpha_{r,(k+j|k)} \geq \alpha_{r,min} - \epsilon_r, \qquad j = 1,...,H_p \tag{5.47j}$$
$$\alpha_{r,(k+j|k)} \leq \alpha_{r,max} + \epsilon_r, \qquad j = 1,...,H_p \tag{5.47k}$$
$$\epsilon_f \geq 0,\ \epsilon_r \geq 0 \tag{5.47l}$$

where $\boldsymbol{\Delta u}^T = [\boldsymbol{\Delta u}_{(k|k)}^T,...,\boldsymbol{\Delta u}_{(k+H_u-1|k)}^T]$. As far as the quadratic cost function (5.46) is concerned, (5.46a)-(5.46b) weight the deviation of the control outputs from their reference values over the prediction horizon, (5.46c) the control input's change per time step over the control horizon and (5.46d) the use of the slack variables ϵ_f and ϵ_r that are employed in soft constraints (5.47h)-(5.47i). To reduce the computational complexity of the optimization problem for the purpose of real-time capability, the control horizon H_u is chosen shorter than the prediction horizon H_p. In this context, it has turned out that using terminal cost (5.46b) leads to a noticeable improvement of the control performance, see section 5.2.1. Thereby, the control scheme is stable without any appropriately chosen terminal cost.

While dynamic constraints (5.47b-5.47c) denote the discrete-time linear affine prediction model that is considered to be valid at the current operating point, input constraints (5.47d)-(5.47g) are introduced to account for physical limitations of the steering as well as the braking system. Particularly, (5.47f)-(5.47g) are employed to limit the absolute values of the control inputs while (5.47d)-(5.47e) constrain the corresponding maximum and minimum change per time step. As discussed in section 5.2.4, state constraints (5.47h)-(5.47k) on the tire sideslip angles are required to stabilize the vehicle at the handling limits. To prevent the CFTOC from becoming infeasible, these state-dependent constraints have to be softened by utilizing slack variables ϵ_f and ϵ_r. Further details on how to determine the upper and lower sideslip angle limits are provided in section 5.4. Finally,

$$\boldsymbol{Q} = \begin{bmatrix} Q_{\Delta y} & 0 \\ 0 & Q_{v_{CG}} \end{bmatrix} \in \mathbb{R}^{2\times 2}, \tag{5.48}$$

$$\boldsymbol{Q}_{H_p} = \begin{bmatrix} Q_{\Delta y, H_p} & 0 \\ 0 & Q_{v_{CG}, H_p} \end{bmatrix} \in \mathbb{R}^{2\times 2}, \tag{5.49}$$

$$\boldsymbol{R} = \begin{bmatrix} R_{\Delta \delta_{ref}} & 0 \\ 0 & R_{\Delta a_{x,br,ref}} \end{bmatrix} \in \mathbb{R}^{2\times 2}, \tag{5.50}$$

$\rho_f \in \mathbb{R}$ and $\rho_r \in \mathbb{R}$ in (5.46) denote weighting matrices respectively coefficients. As in the case of the predictive control problem for lateral vehicle guidance, a quadratic optimization problem subject to linear constraints is gained whose solution can be obtained by QP optimization methods, see [95].

In the end, a final remark on providing reference values to the low-level deceleration interface has to be given. As the control input $a_{x,br,ref}$ refers to an additional deceleration due to braking while the low-level deceleration controller regulates the actual longitudinal acceleration at CG, a reasonable reference value $a_{x,ref}$ has to be derived for the low-level controller. Particularly, the reference value $a_{x,ref}$ is obtained according to (5.45), i.e.

$$a_{x,ref} = a_{x,br,ref} - \frac{1}{m} F_{y,f} \sin(\delta). \tag{5.51}$$

5.4 Constraints on Tire Sideslip Angles

Constraints on the tire sideslip angles, as employed in (5.19h)-(5.19j) and (5.47h)-(5.47j), have first been introduced in [13] to limit the tire sideslip angles to the linear region of the tire model. In [2], the authors propose an extension of [13] that allows for guiding the vehicle in the nonlinear region of the tire model and even at the friction limit. The main ideas will be introduced subsequently. Due to the fact that successive linearizations of the nonlinear prediction model are determined when the LTV-MPC controller is executed at time k, the authors propose to define the tire sideslip angle limits $\alpha_{f,max/min}$ at the front and $\alpha_{r,max/min}$ at the rear axle in such a way that they depend on the current operating point. Therefore, the linearization of the Pacejka tire

model (2.21) has to be investigated at the operating point $(\alpha_{i,0},\ F_{y,i,0})$ with $i \in \{f,r\}$, i.e.

$$F_{y,i} = (\alpha_i - \alpha_{i,0}) \cdot k_{\alpha_i} + F_{y,i,0}. \tag{5.52}$$

In this regard, $k_{\alpha_i} = \partial F_{y,i}/\partial \alpha_i|_{\alpha_{i,0}}$ denotes the linearization coefficient while $\alpha_{i,0}$ and $F_{y,i,0}$ refer to the particular values of α_i and $F_{y,i}$ at the current operating point. Figure 5.9 illustrates that employing (5.52) (i.e. the red dashed line) for determining tire forces $F_{y,i}$ over the prediction horizon would cause lateral tire forces that are greater/less than the maximum/minimum feasible force $F_{y,i,max/min}$ for $\alpha_i > \alpha_{i,LIN,max}$ respectively $\alpha_i < \alpha_{i,LIN,min}$. In order to prevent the predictive controller from assuming lateral forces that are not physically feasible and to ensure that tires saturate in a conservative way, maximum and minimum values of the tire sideslip angles are defined in dependence of the current operating point. Hence, if tire sideslip angles are located in the stable region of the tire model, i.e. region 2 in Figure 5.9 for $\alpha_{i,PMF,min} < \alpha_{i,0} < \alpha_{i,PMF,max}$, upper and lower sideslip angle limits $\alpha_{i,max/min}$ are determined by

$$\alpha_{i,max} = \min\{\xi_\alpha \cdot \alpha_{i,PMF,max},\ \alpha_{i,LIN,max}\}, \tag{5.53}$$

$$\alpha_{i,min} = \max\{\xi_\alpha \cdot \alpha_{i,PMF,min},\ \alpha_{i,LIN,min}\} \tag{5.54}$$

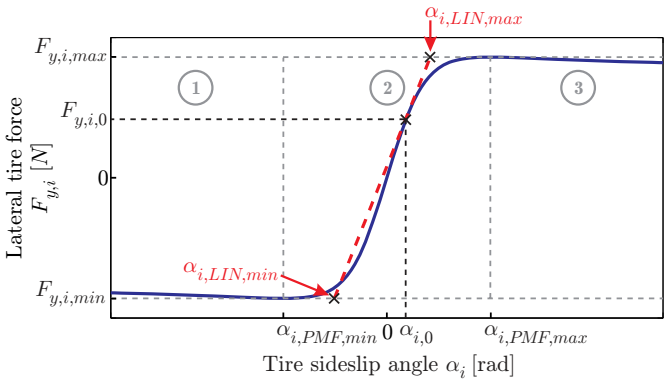

Figure 5.9: Assignment of tire sideslip angle limits (solid blue line: Pacejka tire model, dashed red line: local linearization)

where $0 < \xi_\alpha < 1$. Moreover,

$$\alpha_{i,LIN,max/min} = \frac{F_{y,i,max/min} - F_{y,i,0}}{k_{\alpha_i}} + \alpha_{i,0} \tag{5.55}$$

indicates the tire sideslip angle that corresponds to the intersection of the tangent to $F_{y,i}$ at the operating point ($\alpha_{i,0}$,$F_{y,i,0}$), i.e. the red dashed line in Figure 5.9, and the maximum/minimum feasible tire force $F_{y,i,max/min}$. As extensive analysis has shown, it is reasonable if tire sideslip angles are slightly less than $\alpha_{i,PMF,max}$ respectively greater than $\alpha_{i,PMF,min}$. Therefore, $0 < \xi_\alpha < 1$ is additionally introduced in (5.53)-(5.54). Especially, if the lateral and yaw momentum in (5.2)-(5.3) and (5.21)-(5.22) are linearized close to $\alpha_{f,PMF,max/min}$, the linearization coefficient of the actual wheel steering angle δ may change its sign and may thus cause false control actions, especially in counter-steering situations. Obviously, ξ_α has to be chosen close to one to operate at the limits of vehicle dynamics. Contrarily, if tire sideslip angles are located in the unstable region of the tire model, i.e. region 1 or 3 in Figure 5.9 for $\alpha_{i,0} \leq \alpha_{i,PMF,min}$ or $\alpha_{i,0} \geq \alpha_{i,PMF,max}$, the main objective is to force tire sideslip angles back into the stable region. Therefore, upper and lower tire sideslip angle limits are chosen as

$$\alpha_{i,max/min} = \xi_\alpha \cdot \alpha_{i,PMF,max/min}. \tag{5.56}$$

The parameter ξ_α can be determined through experimental tests for the steering-only and steering/braking control scheme. Furthermore, it can also be derived in advance through a conservative deduction for the steering-only case, see section E.1.

5.5 Static Path/Trajectory Planning

5.5.1 Basic Principles

As outlined in section 2.4, this contribution assumes the evasion path respectively trajectory to be given over a finite time horizon thus that

no online computation is required. In this regard, the path is stored as an injective function

$$f_{path} : x^m \in \mathbb{R}^{\geq 0} \longmapsto y^m \in \mathbb{R}, \tag{5.57}$$

i.e. the mapping of a x^m-coordinate to a y^m-coordinate in the maneuver reference frame is always unambiguous. At the same time, the velocity reference trajectory $\boldsymbol{v}_{CG,ref}$ which is additionally required for the trajectory following problem is stored in discrete-time steps for the entire maneuver duration. Moreover, the relative orientation $\Delta\psi$ and the displacement Δy from the evasion path are computed online and supplied to the disturbance estimator as

$$\hat{\boldsymbol{x}}_{plan}^T = [\Delta\psi,\, \Delta y], \tag{5.58}$$

see Figure 5.2. Therefore, the path/trajectory planner has to transfer the navigation solution to the m-frame as outlined in section 3.7.1. Finally, the current path curvature as well as the future values are determined online and delivered as a curvature vector $\boldsymbol{\kappa}$. In the following, the computation of the relative orientation and the lateral displacement as well as the prediction of the path's curvature over the prediction horizon is discussed in detail.

5.5.2 Path Displacement and Relative Orientation

At each sampling step k, the relative yaw angle $\Delta\psi$ between the vehicle and the evasion path as well as the lateral displacement Δy from the evasion path have to be provided to the disturbance estimator, see Figure 5.2. As depicted in Figure 5.10, $\Delta\psi$ is defined as the difference between the vehicle's yaw angle ψ^m and the path tangent's yaw angle ψ_{path}^m in the m-frame. As the path is given as $y^m = f_{path}(x^m)$, for the relative yaw angle holds

$$\Delta\psi = \psi^m - \underbrace{\arctan\left(\left.\frac{df_{path}}{d(x^m)}\right|_{x_k^m}\right)}_{\psi_{path}^m} \tag{5.59}$$

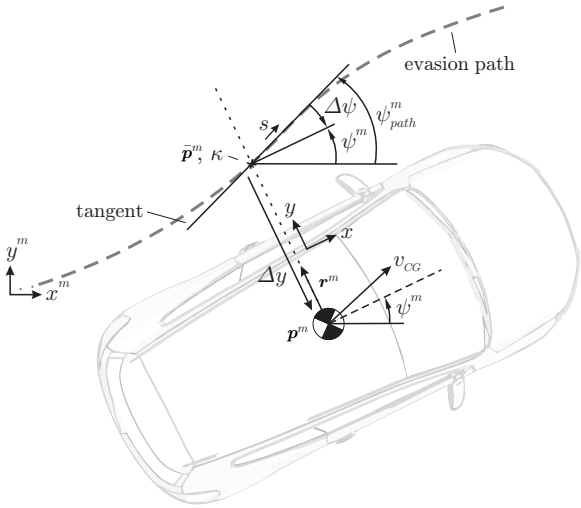

Figure 5.10: Free-body diagram illustrating path displacement and relative orientation

for $-\pi/2 < \psi^m_{path} < \pi/2$ where x^m_k indicates the x^m-coordinate of the CG position at time k. The lateral displacement Δy is gained by projecting the vehicle's CG position $\boldsymbol{p}^{m,T} = [x^m,\, y^m]$ perpendicular to the longitudinal vehicle axle onto the evasion path, thus yielding its projected position $\bar{\boldsymbol{p}}^{m,T} = [\bar{x}^m,\, \bar{y}^m]$. In particular, $\bar{\boldsymbol{p}}^{m,T} = [\bar{x}^m,\, \bar{y}^m]$ is computed by solving the equation

$$\begin{bmatrix} \bar{x}^m \\ \bar{y}^m \end{bmatrix} = \begin{bmatrix} x^m \\ y^m \end{bmatrix} + \gamma\, \boldsymbol{r}^m \tag{5.60}$$

$$\Leftrightarrow \begin{bmatrix} \bar{x}^m \\ f_{path}(\bar{x}^m) \end{bmatrix} = \begin{bmatrix} x^m \\ y^m \end{bmatrix} + \gamma \begin{bmatrix} \tan(\psi^m) \\ -1 \end{bmatrix}$$

for $\gamma \in \mathbb{R}$ where $\boldsymbol{r}^m$ denotes the vector directing perpendicular to the longitudinal vehicle axis. When multiplying (5.60) with the normal vector

$$\boldsymbol{n} = \begin{bmatrix} 1 \\ \tan(\psi^m) \end{bmatrix}, \tag{5.61}$$

the scalar function

$$\begin{bmatrix} 1 \\ \tan(\psi^m) \end{bmatrix}^T \begin{bmatrix} \bar{x}^m \\ f_{path}(\bar{x}^m) \end{bmatrix} - \begin{bmatrix} 1 \\ \tan(\psi^m) \end{bmatrix}^T \begin{bmatrix} x^m \\ y^m \end{bmatrix} = 0 \tag{5.62}$$

is gained where $\bar{x}^m$ is the only unknown variable. Finally, (5.62) is solved using Newton's method [96] with x^m as initial solution. However, using Newton's method does not implicate any real-time issues as only few iterations are needed. Finally, the lateral displacement Δy corresponds to the Euclidean distance $\|\boldsymbol{p}^m - \bar{\boldsymbol{p}}^m\|$ and is positive if the vehicle's CG is located left and negative if it is located right from the evasion path, i.e.

$$\Delta y = \|\boldsymbol{p}^m - \bar{\boldsymbol{p}}^m\| \cdot \text{sign}(y^m - \bar{y}^m). \tag{5.63}$$

5.5.3 Prediction of Path Curvature

In order to account for the path curvature's trajectory

$$\kappa^T = [\kappa_{(k|k)},...,\kappa_{(k+H_p-1|k)}] \tag{5.64}$$

over the prediction horizon, the current as well as the future values of the path curvature are required at each sampling time k. According to [39], the path curvature $\kappa_{(k|k)}$ at time k can be determined in dependence of the projected CG position $\bar{\boldsymbol{p}}^{m,T}_{(k|k)} = [\bar{x}^m_{(k|k)},\ \bar{y}^m_{(k|k)}]$ by

$$\kappa_{(k|k)} = \frac{\left.\frac{d^2 f_{path}}{d(x^m)^2}\right|_{\bar{x}^m_{(k|k)}}}{\left(1 + \left.\frac{df_{path}}{d(x^m)}\right|^2_{\bar{x}^m_{(k|k)}}\right)^{3/2}}. \tag{5.65}$$

For the remaining prediction horizon, $\kappa_{(k+j|k)}$ with $j = 1,...,H_p - 1$ can be obtained by predicting the CG position $\boldsymbol{p}^{m,T}_{(k+j|k)} = [x^m_{(k+j|k)},\ y^m_{(k+j|k)}]$ successively assuming that the vehicle follows the evasion path in an optimal way without any displacement starting at $\bar{\boldsymbol{p}}^m_{(k|k)}$, see Figure 5.11. For the sake of simplicity, the vehicle's horizontal velocity v_{CG} is considered to be constant over the prediction horizon, i.e.

$$v_{CG,(k|k)} = ... = v_{CG,(k+H_p-1|k)} = \text{const.} \tag{5.66}$$

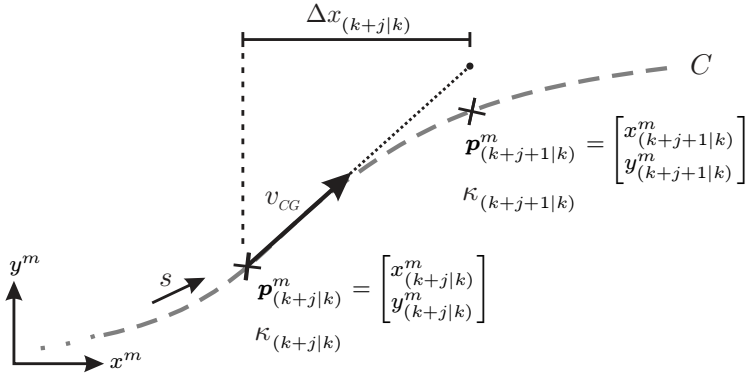

Figure 5.11: Curvature prediction scheme

Indeed, this assumption is a simplification as the vehicle is able to decelerate significantly in the steering/braking case. But the analysis whether further improvement can be gained when the vehicle's velocity varies over the prediction horizon, e.g. in dependence of the current deceleration, is part of future work. In order to predict the future positions $\boldsymbol{p}^m_{(k+j|k)}$, the curve integral of $\mathcal{C}$ is solved along the path coordinate s, i.e.

$$\int_{\mathcal{C}} ds = \int_{x^m_{(k+j|k)}}^{x^m_{(k+j+1|k)}} \sqrt{1 + \left(\frac{df_{path}}{d(x^m)}\right)^2}\, d(x^m) \tag{5.67}$$

where $\mathcal{C}$ refers to the path segment between $x^m_{(k+j|k)}$ and $x^m_{(k+j+1|k)}$. Therefore, (5.67) is approximated numerically by applying Euler integration [59]

$$\int_{x^m_{(k+j|k)}}^{x^m_{(k+j+1|k)}} \sqrt{1 + \left(\frac{df_{path}}{d(x^m)}\right)^2}\, d(x^m) \approx \Delta x^m_{(k+j|k)} \sqrt{1 + \left.\frac{df_{path}}{d(x^m)}\right|^2_{x^m_{(k+j|k)}}} \tag{5.68}$$

where $\Delta x^m_{(k+j|k)} = x^m_{(k+j+1|k)} - x^m_{(k+j|k)}$. For a constant vehicle velocity v_{CG}, the length of $\mathcal{C}$ can be approximated by the traveling distance $v_{CG} \cdot T_s$ between two subsequent discrete time steps, i.e.

$$\Delta x^m_{(k+j|k)} \sqrt{1 + \left.\frac{df_{path}}{d(x^m)}\right|^2_{x^m_{(k+j|k)}}} \approx v_{CG} \cdot T_s \tag{5.69}$$

where T_s denotes the sampling time of the predictive controller. When rewriting (5.69) with respect to $\Delta x^m_{(k+j|k)}$, i.e.

$$\Delta x^m_{(k+j|k)} = \frac{v_{CG} \cdot T_s}{\sqrt{1 + \left.\frac{df_{path}}{d(x^m)}\right|^2_{x^m_{(k+j|k)}}}}, \tag{5.70}$$

for the CG position $\boldsymbol{p}^{m,T}_{(k+j+1|k)} = [x^m_{(k+j+1|k)},\, y^m_{(k+j+1|k)}]$ holds

$$x^m_{(k+j+1|k)} = x^m_{(k+j|k)} + \Delta x^m_{(k+j|k)}, \tag{5.71}$$

$$y^m_{(k+j+1|k)} = f_{path}(x^m_{(k+j+1|k)}). \tag{5.72}$$

Finally, the predicted path curvature $\kappa_{(k+j|k)}$ can be determined in accordance to (5.65).

5.6 Disturbance Estimation

5.6.1 Estimation Problem

Referring to [13], experimental tests have shown that (time-varying) yaw angle offsets can be observed in the navigation solution. A yaw angle offset would consequently cause a relative yaw angle offset which can be interpreted as a lateral velocity disturbance with respect to the evasion path. Hence, (relative) yaw angle offsets act as a ramp disturbance on the control output Δy, i.e. the lateral displacement from the evasion path. To achieve offset-free tracking in MPC-based control schemes, an appropriate disturbance estimator is required if the plant itself does not contain enough integrators, see [97].

Therefore, an additional EKF-based disturbance estimator has been implemented to compensate the ramp disturbance on Δy in order to achieve steady-state offset-free tracking and to improve the transient control performance of both control schemes. As the filter has to be executed only during an evasive maneuver, the disturbance estimator has been implemented as a separate EKF and not been included into the vehicle state estimator in chapter 4. In this way, the system design has been simplified and further issues with assessing the observability of the adaptation states θ_{F_x} and θ_{F_y} due to switching model equations (of the integrated disturbance estimator) have been avoided. By applying the disturbance estimator, the lateral displacement Δy and the relative yaw angle $\Delta\psi$ which are determined by the path/trajectory planner (based on the navigation solution) are additionally filtered considering relative kinematics between the vehicle and the evasion path.

5.6.2 Modeling

To design the disturbance estimator, the relative kinematics model, which is used in both MPC-based control schemes, is employed as estimator model, i.e.

$$f_1 = \Delta\dot{\psi} = \dot{\psi} - \kappa\sqrt{{v_x}^2 + {v_y}^2}, \tag{5.73}$$

$$f_2 = \Delta\dot{y} = \sqrt{{v_x}^2 + {v_y}^2}\sin(\Delta\psi) + v_y + d_{\Delta\dot{y}}. \tag{5.74}$$

Thereby, f_1 models the relative rotational and f_2 the relative translational movement between the vehicle's CG and the evasion path. When investigating (5.74), it can be noticed that the actual relative yaw angle disturbance is modeled as a lateral velocity disturbance $d_{\Delta\dot{y}}$. If a relative yaw angle disturbance $d_{\Delta\psi}$ acting on $\Delta\psi$ would have been introduced instead, an unobservable estimation problem would have been obtained. Contrarily, using the disturbance state $d_{\Delta\dot{y}}$ yields an observable estimation problem, see section 5.6.4. As indicated in 5.2.2.1, its dynamic behavior is assumed to be a random walk process, i.e.

$$f_3 = \dot{d}_{\Delta\dot{y}} = 0. \tag{5.75}$$

Summarizing, the nonlinear estimator model can be written as

$$\dot{\boldsymbol{x}}(t) = \boldsymbol{f}(\boldsymbol{x}(t),\boldsymbol{u}(t)) \tag{5.76}$$

where

$$\boldsymbol{x}^T = [\Delta\psi,\ \Delta y,\ d_{\Delta\dot{y}}] \tag{5.77}$$

denotes the state vector and

$$\boldsymbol{u}^T = [v_x,\ v_y,\ \dot{\psi},\ \kappa] \tag{5.78}$$

the input vector and $\boldsymbol{f}^T = [f_1,\ f_2,\ f_3]$.

5.6.3 Estimator Design

As previously mentioned, an EKF-based estimator relies on a prediction/correction scheme. For this reason, a relationship between the state variables of the nonlinear estimator model and the measured outputs $\tilde{\boldsymbol{y}}$ is required. For the disturbance estimator, the relative yaw angle $\Delta\psi$ and the lateral displacement Δy which are provided by the static path/trajectory planner are the measured variables

$$h_1 = \Delta\tilde{\psi} = \Delta\psi, \tag{5.79}$$

$$h_2 = \Delta\tilde{y} = \Delta y. \tag{5.80}$$

The stochastic nonlinear estimator model can be deduced from (5.76) and (5.79)-(5.80) and be formulated in state space representation as

$$\dot{\boldsymbol{x}}(t) = \boldsymbol{f}(\boldsymbol{x}(t),\boldsymbol{u}(t)) + \boldsymbol{w}(t) \tag{5.81}$$

$$\boldsymbol{y}(t) = \boldsymbol{h}(\boldsymbol{x}(t)) + \boldsymbol{v}(t) \tag{5.82}$$

where

$$\boldsymbol{y}^T = [\Delta\psi,\ \Delta y] \tag{5.83}$$

indicates the measurement vector, $\boldsymbol{w}$ the process noise, $\boldsymbol{v}$ the measurement noise, $\boldsymbol{f}^T = [f_1,\ f_2,\ f_3]$ and $\boldsymbol{h}^T = [h_1,\ h_2]$. In this regard, $\boldsymbol{w}$ and $\boldsymbol{v}$ are assumed to be zero-mean Gaussian white noise, i.e $\boldsymbol{w} \sim \mathcal{N}(\boldsymbol{0},\boldsymbol{Q})$

and $\boldsymbol{v} \sim \mathcal{N}(\boldsymbol{0},\boldsymbol{R})$ where $\boldsymbol{Q}$ and $\boldsymbol{R}$ denote the corresponding covariance matrices. As illustrated in Figure 5.2, the measurement vector $\boldsymbol{y}$ and the path curvature κ and are provided by the path/trajectory planner while the remaining inputs v_x, v_y and $\dot{\psi}$ are supplied by the vehicle state estimator.

To employ the continuous-time nonlinear model in the EKF-based estimator, (5.81)-(5.82) are linearized along the estimated state trajectory and transferred to a discrete-time linear representation, thus yielding

$$\boldsymbol{x}_{k+1} = \boldsymbol{F}_k \boldsymbol{x}_k + \boldsymbol{B}_k \boldsymbol{u}_k + \boldsymbol{w}_k \tag{5.84}$$

$$\boldsymbol{y}_k = \boldsymbol{H}_k \boldsymbol{x}_k + \boldsymbol{D}_k \boldsymbol{u}_k + \boldsymbol{v}_k. \tag{5.85}$$

With respect to [17], the prediction step at time k comprises the computation of the a priori state estimate $\hat{\boldsymbol{x}}_k^-$ and the corresponding estimation error covariance matrix $\boldsymbol{P}_k^-$

$$\hat{\boldsymbol{x}}_k^- = \hat{\boldsymbol{x}}_{k-1}^+ + \int_{(k-1)\cdot T_s}^{k\cdot T_s} \boldsymbol{f}(\hat{\boldsymbol{x}}_{k-1}^+, \boldsymbol{u}_{k-1})\, dt \tag{5.86}$$

$$\boldsymbol{P}_k^- = \boldsymbol{F}_{k-1} \boldsymbol{P}_{k-1}^+ \boldsymbol{F}_{k-1}^T + \boldsymbol{Q}_{k-1} \tag{5.87}$$

where $\boldsymbol{Q}_k = \boldsymbol{Q}/T_s$ and $\boldsymbol{R}_k = \boldsymbol{R}$ denote the discrete-time covariance matrices of the process noise $\boldsymbol{w}_k$ and the measurement noise $\boldsymbol{v}_k$ while T_s indicates the EKF's sampling time. To solve the integral in (5.86) numerically, an explicit forth-order Runge-Kutta integration technique [59] is applied. When a measurement $\tilde{\boldsymbol{y}}_k$ is obtained at time k, the a posteriori state estimate $\hat{\boldsymbol{x}}_k^+$ and covariance matrix $\boldsymbol{P}_k^+$ are determined by

$$\boldsymbol{K}_k = (\boldsymbol{P}_k^- \boldsymbol{H}_k^T)(\boldsymbol{H}_k \boldsymbol{P}_k^- \boldsymbol{H}_k^T + \boldsymbol{R}_k)^{-1} \tag{5.88}$$

$$\hat{\boldsymbol{x}}_k^+ = \hat{\boldsymbol{x}}_k^- + \boldsymbol{K}_k(\tilde{\boldsymbol{y}}_k - \boldsymbol{h}(\hat{\boldsymbol{x}}_k^-)) \tag{5.89}$$

$$\boldsymbol{P}_k^+ = (\boldsymbol{I} - \boldsymbol{K}_k \boldsymbol{H}_k)\boldsymbol{P}_k^-. \tag{5.90}$$

5.6.4 Observability Analysis

Referring to section 4.6, the local observability of the nonlinear system (5.81)-(5.82) can be proven by investigating the rank of the observability

matrix

$$\boldsymbol{\mathcal{O}} = \frac{\partial}{\partial \boldsymbol{x}} \begin{bmatrix} \boldsymbol{\mathcal{L}}_{\boldsymbol{f}}^{0}(\boldsymbol{h}) \\ \vdots \\ \boldsymbol{\mathcal{L}}_{\boldsymbol{f}}^{(n-1)}(\boldsymbol{h}) \end{bmatrix}_{(\boldsymbol{x}_0, \boldsymbol{u}_0)} \tag{5.91}$$

where $\mathcal{L}_{\boldsymbol{f}}^{j}(\boldsymbol{h})$ denominates the j-th Lie derivative of $\boldsymbol{h}$ along the vector field $\boldsymbol{f}$. As the number of states amounts to three for this particular estimation problem, the underlying nonlinear system is locally observable if and only if $\operatorname{rank}(\boldsymbol{\mathcal{O}}) = 3$ is satisfied. With respect to [81], the j-th Lie derivative $\mathcal{L}_{\boldsymbol{f}}^{j}(\boldsymbol{h})$ is defined as

$$\begin{aligned} \boldsymbol{\mathcal{L}}_{\boldsymbol{f}}^{0}(\boldsymbol{h}) &= \boldsymbol{h}, \\ &\vdots \\ \boldsymbol{\mathcal{L}}_{\boldsymbol{f}}^{(n-1)}(\boldsymbol{h}) &= \boldsymbol{h}^{(n-1)} = \frac{\partial}{\partial \boldsymbol{x}} [\boldsymbol{\mathcal{L}}_{\boldsymbol{f}}^{(n-2)}(\boldsymbol{h})] \ \boldsymbol{f}. \end{aligned} \tag{5.92}$$

As shown subsequently, the consideration of the 0-th and 1-st Lie derivative is sufficient to prove local observability. With regard to (5.92), for these Lie derivatives it holds

$$\boldsymbol{\mathcal{L}}_{\boldsymbol{f}}^{0}(\boldsymbol{h}) = \boldsymbol{h} = \begin{bmatrix} \Delta\psi \\ \Delta y \end{bmatrix}, \tag{5.93}$$

$$\boldsymbol{\mathcal{L}}_{\boldsymbol{f}}^{1}(\boldsymbol{h}) = \dot{\boldsymbol{h}} = \begin{bmatrix} \dot{\psi} - \kappa \sqrt{{v_x}^2 + {v_y}^2} \\ \sqrt{{v_x}^2 + {v_y}^2} \sin(\Delta\psi) + v_y + d_{\Delta\dot{y}} \end{bmatrix}. \tag{5.94}$$

To obtain the observability matrix (5.91), the Jacobians of (5.93)-(5.94) have to be determined at the current operating point $(\boldsymbol{x}_0, \boldsymbol{u}_0)$, thus yielding

$$\frac{\partial}{\partial \boldsymbol{x}} \boldsymbol{\mathcal{L}}_{\boldsymbol{f}}^{0}(\boldsymbol{h}) \bigg|_{(\boldsymbol{x}_0, \boldsymbol{u}_0)} = \begin{bmatrix} 1 & 0 & 0 \\ 0 & 1 & 0 \end{bmatrix}, \tag{5.95}$$

$$\frac{\partial}{\partial \boldsymbol{x}} \boldsymbol{\mathcal{L}}_{\boldsymbol{f}}^{1}(\boldsymbol{h}) \bigg|_{(\boldsymbol{x}_0, \boldsymbol{u}_0)} = \begin{bmatrix} 0 & 0 & 0 \\ \sqrt{{v_{x,0}}^2 + {v_{y,0}}^2} \cos(\Delta\psi_0) & 0 & 1 \end{bmatrix}. \tag{5.96}$$

It can be recognized that

$$\frac{\partial}{\partial \boldsymbol{x}} \begin{bmatrix} \boldsymbol{\mathcal{L}}_{\boldsymbol{f}}^{0}(\boldsymbol{h}) \\ \boldsymbol{\mathcal{L}}_{\boldsymbol{f}}^{1}(\boldsymbol{h}) \end{bmatrix}_{(\boldsymbol{x}_0, \boldsymbol{u}_0)} \tag{5.97}$$

has already rank 3 for an arbitrary operating point. Hence, the nonlinear system (5.81)-(5.82) is locally observable everywhere.

6 Experimental Control Results

6.1 Scenarios and Controller Parameterization

In this chapter, experimental results for the optimal control approaches that have been introduced in chapter 5 are examined. Thereby, the operability of the entire system comprising the low-cost GNSS-based navigation filter, vehicle state estimator, disturbance estimator as well as the MPC-based controller will be evaluated. For these tests, the driver just sets up the initial vehicle velocity and manually initiates the evasion maneuver. During the maneuver, the vehicle acts autonomously without any driver input. When the maneuver is ended, the driver takes over control again. All the tests have been conducted on a dry (high friction) road, thus assuming a maximum friction coefficient of $\mu = 1$. Furthermore, electronic safety systems like ABS and ESC (ESC cannot totally be turned off) have been enabled during experimental tests.

The steering-only control scheme is investigated for the nominal as well as the adaptive case, i.e. when using a nominal and a distorted tire parameter set. The adaptive case shows that using the adaptation parameter θ_{F_y} in the MPC-based control scheme leads to a noticeable improved control performance when having a tire model mismatch. The steering/braking control scheme is only considered for the nominal case as controller adaptation has not yet been incorporated into the control scheme. In order to assess the influence of the position solution's accuracy on the control results, each nominal scenario is additionally considered when using the OxTS RT3003 reference navigation system instead of the low-cost navigation solution. In this case, the reference frame transformation relies on the OxTS RT3003 outputs while the vehicle state estimator still relies on the low-cost navigation solution, see section 2.4. The OxTS RT3003 navigation solution is also employed for the adaptive case to reduce the influence of navigation issues on the

control results and thus to enable for reproducible conditions for subsequent test maneuvers. For both control schemes, a double lane change maneuver is employed as evasion path which corresponds to evading an obstacle by changing to an adjacent and back to the initial lane. Driving back to the initial lane can e.g. be interpreted as a scenario with oncoming traffic. As stated in section 5.5.1, the evasion path has to be given as an injective function. In the scope of this thesis, it is chosen similar to [13] as

$$y^m = f_{path}(x^m) = \Delta y_1 \left(1 + \tanh(z_1)\right) - \Delta y_2 \left(1 + \tanh(z_1)\right) \tag{6.1}$$

where

$$z_1 = \frac{z_{11}}{z_{12}}(x^m - z_{13}) - z_{14}, \quad z_2 = \frac{z_{21}}{z_{22}}(x^m - z_{23}) - z_{24} \tag{6.2}$$

and z_{ij} with $i \in \{1,2\}$, $j \in \{1,2,3,4\}$ respectively Δy_i with $i \in \{1,2\}$ are coefficients that specify the particular geometry of the evasion path. These coefficients have been chosen such that the resulting path corresponds to the track paintings on the proving ground, thus having an optical reference during the evasion maneuver, see Figure 6.1. Furthermore, the particular values have been determined by fitting (6.1) to a manually driven maneuver in order to ensure that the path is physically feasible, i.e. $\Delta y_1 = \Delta y_2 = 3.5$, $z_{11} = z_{21} = 1.7$, $z_{12} = z_{22} = 11.4$,

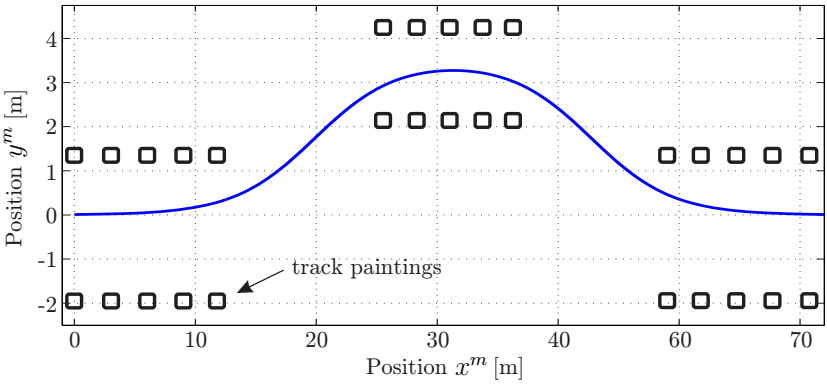

Figure 6.1: Reference evasion path

$z_{13} = 6.5$, $z_{23} = 29.3$ and $z_{24} = 2.0$. Besides the evasion path, a velocity trajectory is required for the evaluation of the steering/braking control scheme. Its particular design is discussed in section 6.3.

The controller parameters have been optimized in experimental test. For both controllers, the control horizon H_u and the prediction horizon H_p have been varied over a wide range. It has turned out that prediction horizons of about 1 s show the best results while shorter horizons of less than 0.5 s lead to a degraded control performance. Simulation based investigations have shown that very short horizons can even lead to an unstable system behavior. In order to solve the constrained convex optimization problems in real-time, the control horizon is always chosen shorter that the prediction horizon. Furthermore, a sample time of 0.02 s is used for the steering-only controller. Due to the higher computational complexity of the MIMO steering/braking control problem, the corresponding sample time has been increased to 0.04 s. Thereby, qpOASES [98] is employed as (active-set) QP solver. For both control schemes, a solution of the CFTOC can always be obtained within the sampling interval and within the maximum number of iterations. The particular parameterization of control and prediction horizons, optimization constraints and weighting matrices respectively coefficients is addressed in the following sections. Finally, the navigation filter and the vehicle state estimator are executed with a sample time of 0.01 s while a sampling interval of 0.02 s is applied for the path/trajectory planner and the disturbance estimator. For the navigation filter and the vehicle state estimator, the same filter parameters as discussed in section 3.8.1 and section 4.7.1 are used while the disturbance estimator parameterization has been part of the controller tuning. For both control schemes, the disturbance estimator employs the same filter parameters, see section E.2.

6.2 Lateral Vehicle Guidance

In the following, experimental results that have been gained for the steering-only control scheme in the nominal (i.e. using nominal tire parameters) as well as the adaptive case (i.e. using artificially distorted

Table 6.1: Steering-only controller parameterization

Parameter	Value	Description
T_s	0.02 s	Sample time
H_u	25	Control horizon
H_p	50	Prediction horizon
Q	1	Weight on lat. displacement
Q_{H_p}	1000	Terminal weight on lat. displacement
R	400, 100*	Weight on change of δ_{ref}
ρ_f, ρ_r	10000	Weight on slack variables
$\delta_{ref,max/min}$	±15 deg	Max./min. wheel steering angle δ_{ref}
$\Delta\delta_{ref,max/min}$	±0.6 deg	Max./min. change of δ_{ref}

* nominal RTK-based steering-only controller

tire parameters) are investigated. The corresponding MPC parameters have been chosen according to Table 6.1. Although, the maximum and minimum change of the wheel steering angle per time step has a physical limit that is greater respectively less than ±0.6 deg, it has turned out to be beneficial to assign these limits to ±0.6 deg to reduce oscillations in the steering system. Investigations have shown that these oscillations are likely to happen at the beginning of the maneuver due to the initial time delay that occurs when the actuator is activated, see section 5.2.3.

6.2.1 Nominal Controller

6.2.1.1 Low-cost GNSS-based Control Results

Figure 6.2 depicts the control results for a maneuver with an initial velocity of 15.5 m/s when relying on the low-cost navigation solution. To evaluate the actual path displacement, the OxTS RT3003 reference position as well as the corresponding lateral deviation from the evasion path are additionally illustrated. Particularly, a maximum absolute lateral deviation of 0.33 m with respect to the low-cost navigation solution can be observed while the RMSE amounts to 0.18 m. With respect to

the OxTS RT3003 reference sensor, the maximum absolute lateral displacement is equal while the RMSE decreases slightly to 0.17 m. In this regard, the maximum absolute difference between the reference and the estimated path displacement is less than 0.2 m while stepwise changes are less than 0.05 m. Thus, (relative) position accuracy and smoothness requirements on the low-cost navigation solution that have been defined in section 3.2 are fulfilled during the entire maneuver. Furthermore, the resulting maximum navigation and control errors which amount

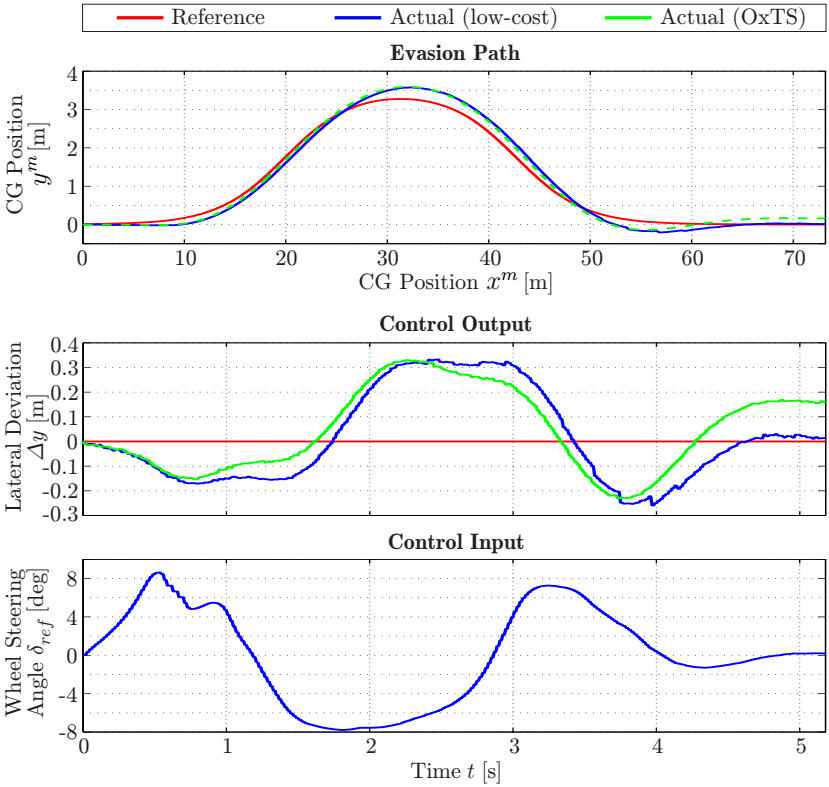

Figure 6.2: Experimental results for nominal steering-only controller using low-cost navigation: Control input and output

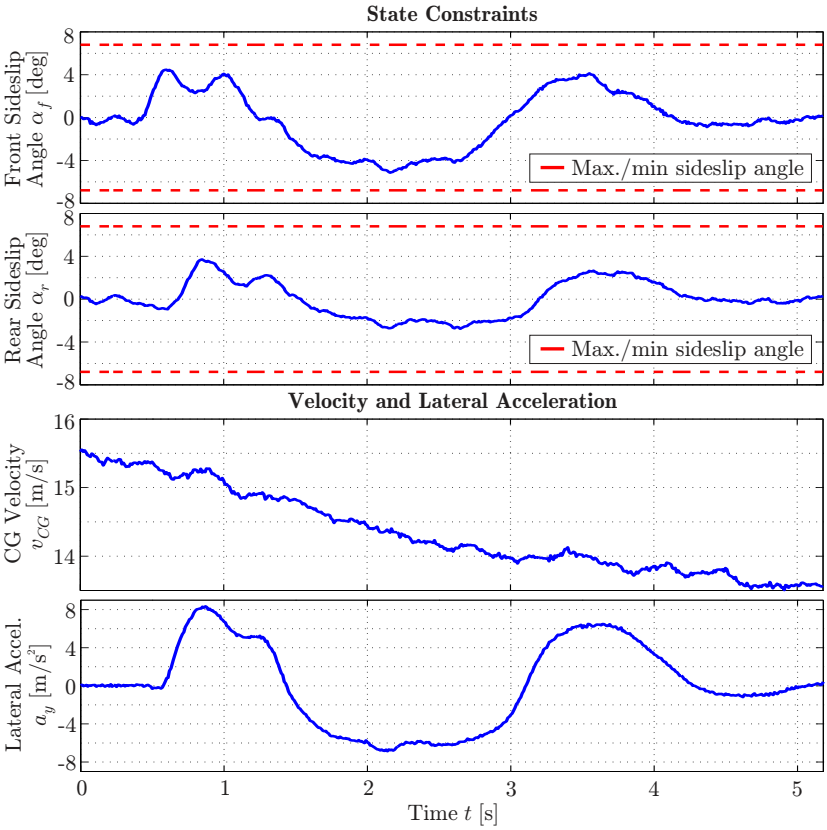

Figure 6.3: Experimental results for nominal steering-only controller using low-cost navigation: State constraints and vehicle states

to 0.33 m are far less than the maximum acceptable error. Moreover, steady-state offsets of the control output Δy can actually be avoided by using the disturbance estimator.

Figure 6.3 shows the tire sideslip angles at the front and the rear axle that are deduced from the Correvit measurements. It can be recognized that tire sideslip angle constraints are always fulfilled while maximum

lateral accelerations of $8.4\,\mathrm{m/s^2}$ can be observed during the maneuver. Thereby, it is apparent that the maximum tire sideslip angle at the front axle amounts to 5.2 deg while the limit of static friction corresponds to 7 deg. In this context, it has to be stated that linear tire behavior can be assumed for $-3\,\mathrm{deg} \leq \alpha_i \leq 3\,\mathrm{deg}$ and that 95% of the maximum feasible tire force is transmitted for sideslip angles of ± 5 deg. The fact that maximum respectively minimum tire sideslip angles are not entirely reached on the high friction surface results from the slight conservatism that is introduced through the definition of the tire sideslip angle limits (see section 5.4) that are necessary to stabilize the vehicle. This conservatism is especially apparent due to the low gradient $\partial F_{y,i}/\partial \alpha_i|_{\alpha_0}$, $i \in \{f,r\}$ near the maximum feasible tire force on the high friction surface, i.e. only 5% of the maximum feasible tire force are transmitted between 5 deg and 7 deg sideslip. On low friction surfaces, e.g. on a snow covered road, this conservatism is not apparent as the region of sliding friction is reached with much steeper gradients. Simulation results that verify this statement and demonstrate vehicle guidance when tires are saturated during long-term intervals on a snow covered road have been presented by the author in [2]. Hence, it can be concluded that the controller is able to guide the vehicle in the nonlinear region of the tire model and even at the handling limits.

6.2.1.2 OxTS-based Control Results

The same maneuver has been conducted using the OxTS RT3003 navigation solution to assess the improvement in control performance when using the best position information that is available. As illustrated in Figure 6.5, both maneuvers have approximately the same initial velocity (i.e. 15.3 m/s and 15.5 m/s) as well as maximum lateral accelerations (i.e. $8.4\,\mathrm{m/s^2}$ and $8.3\,\mathrm{m/s^2}$). Thus, these maneuvers are considered to be suitable for a reasonable comparison. Due to the fact that the OxTS RT3003 position information has a better positional accuracy and is slightly smoother than the low-cost solution, it has been possible to decrease the weight R on the control input δ_{ref} without causing any severe steering interventions or oscillations. In this regard, minor oscillations have sometimes been observed when using the low-cost navigation solution and a lower weight on R. Particularly, R is decreased to 100 while

all the other parameters remain unchanged.

According to Figure 6.4, it is apparent that the maximum absolute lateral displacement can be reduced to 0.22 m and the RMSE to 0.10 m when using the centimeter-precision navigation solution. In this regard, the displacement of 0.03 m at the end of the maneuver is negligible as it is caused by deactivating the controller slightly too early. Similar to the previous maneuver, the controller is able to stabilize the vehicle

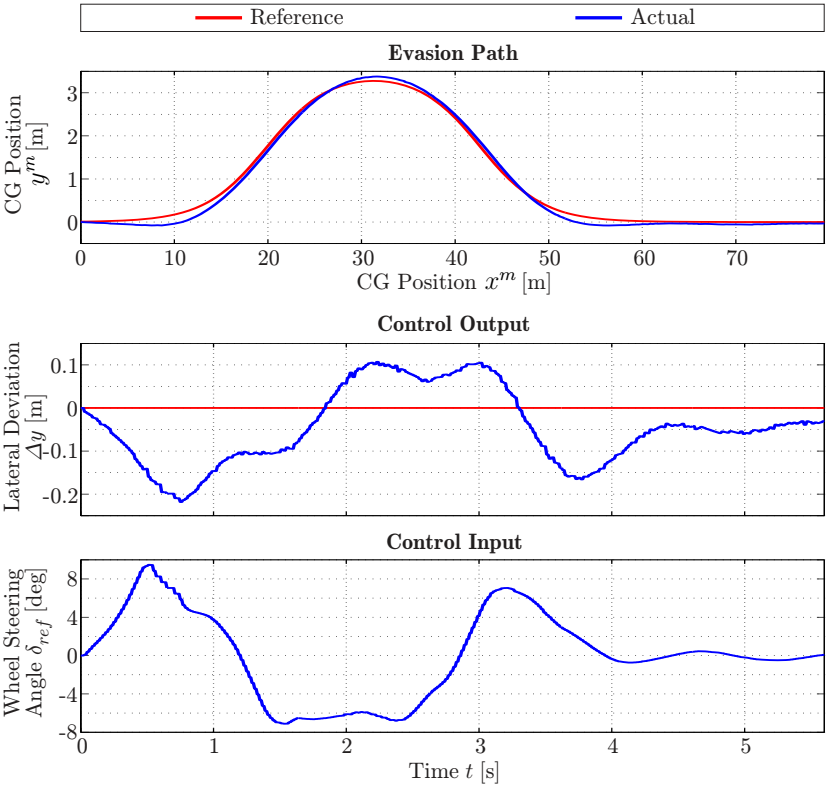

Figure 6.4: Experimental results for nominal steering-only controller using OxTS RT3003: Control input and output

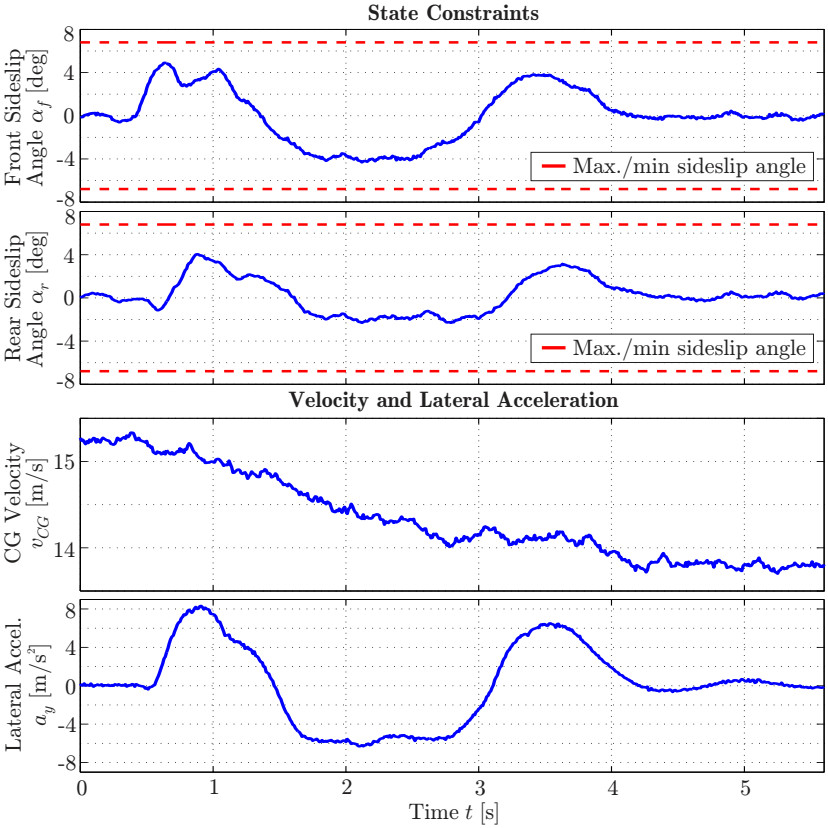

Figure 6.5: Experimental results for nominal steering-only controller using OxTS RT3003: State constraints and vehicle states

during the entire evasion maneuver which shows maximum lateral accelerations of $8.3\,\mathrm{m/s^2}$, see Figure 6.5. Concluding, a convincing control performance can be achieved in both cases while a further improvement can be gained when relying on the OxTS RT3003 navigation solution. However, the feasibility of autonomous evasion maneuvers when relying on the low-cost navigation solution has thus been proven for the steering-only controller.

6.2.2 Adaptive Controller

In the following, experimental control results for the adaptive control scheme that employs the vehicle state estimator's state θ_{F_y} for adaptation purposes are evaluated. Especially when the tire-road contact varies significantly during an evasion maneuver (e.g. when changing from a dry to a wet road), controller adaptation can be advantageous as shown subsequently. In the particular test scenario, tire parameters have been distorted by multiplying the maximum friction coefficient by 2.5 and the nominal cornering stiffness (i.e. the slope at the origin of $F_{y,i}$, see section 2.1.2.4) by 1.5. Thus, the controller assumes the friction coefficient as well as the tire cornering stiffness to be too large. The employed distortion can be interpreted as a transition from a dry to a snow covered road. While the maximum/minimum tire sideslip angle $\alpha_{i,max/min}$ decreases/increases for an actually decreased maximum friction coefficient, this is not the case when tire parameters are artificially distorted. Therefore, $\alpha_{i,max/min}$ have been kept constant. As far as future research is concerned, the influence of actually increased or decreased maximum/minimum sideslip angles (compared to those in the tire model) has to be investigated. Especially for an actually decreased maximum friction coefficient, the tires will enter the region of sliding friction while the controller still assumes static friction. Moreover, it has to be noted that the nominal as well as the adaptive control scheme rely on the adaptive vehicle state estimator while the corresponding adaptation state θ_{F_y} is only used by the adaptive controller. Particularly, the nominal controller assumes θ_{F_y} to be 1. In order to improve the reproducibility of subsequent test maneuvers, the OxTS RT3003 instead of the low-cost navigation solution is employed to reduce the influence of navigation issues on the control results. As tire parameters have been distorted, the weight R on the control input is increased to 400 (as for the low-cost steering-only case) to avoid severe steering interventions and oscillations, see Table 6.1.

Figure 6.6 shows a comparison of the experimental control results for the adaptive and nominal control scheme. Thereby, both maneuvers have approximately the same initial velocity of 15.9 m/s as well as similar maximum lateral accelerations of $\pm 8\,\mathrm{m/s^2}$ which allows for a reasonable conclusion. With respect to the lateral deviation from the evasion

path, a noticeably improved control performance can be recognized in the adaptive case. In particular, the maximum absolute lateral deviation can be reduced by 17.6% from 0.74 m to 0.61 m and the RMSE by 17.1% from 0.35 m to 0.29 m. Moreover, the control input shows a smoother trajectory and the entire maneuver is ended 0.8 s earlier when

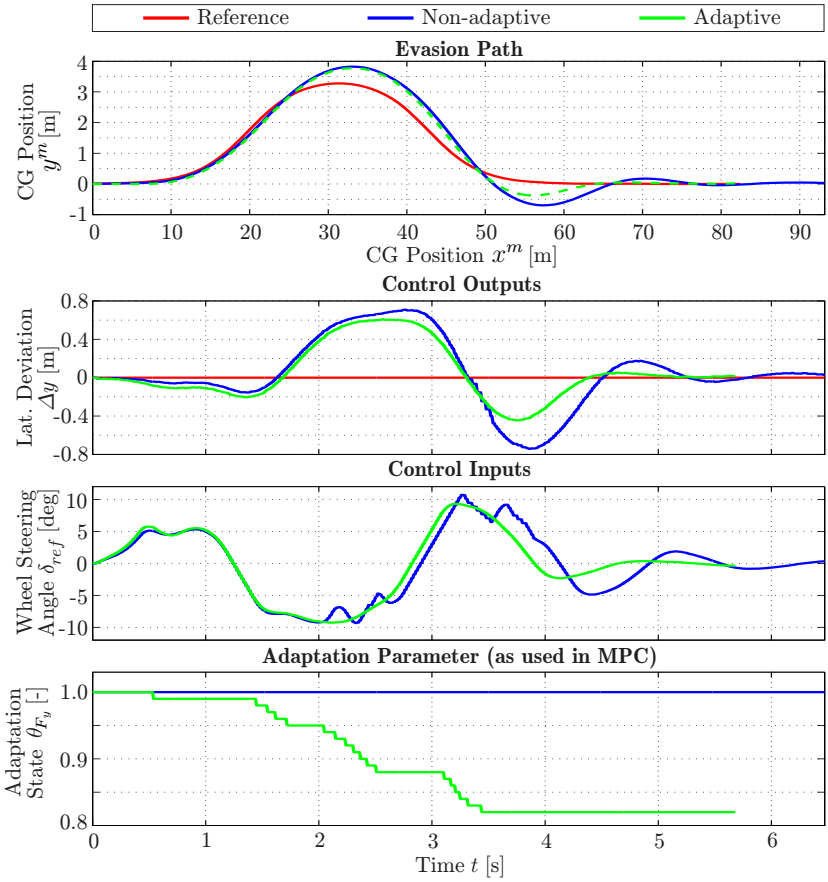

Figure 6.6: Experimental results for adaptive steering-only controller using OxTS RT3003: Control input and output

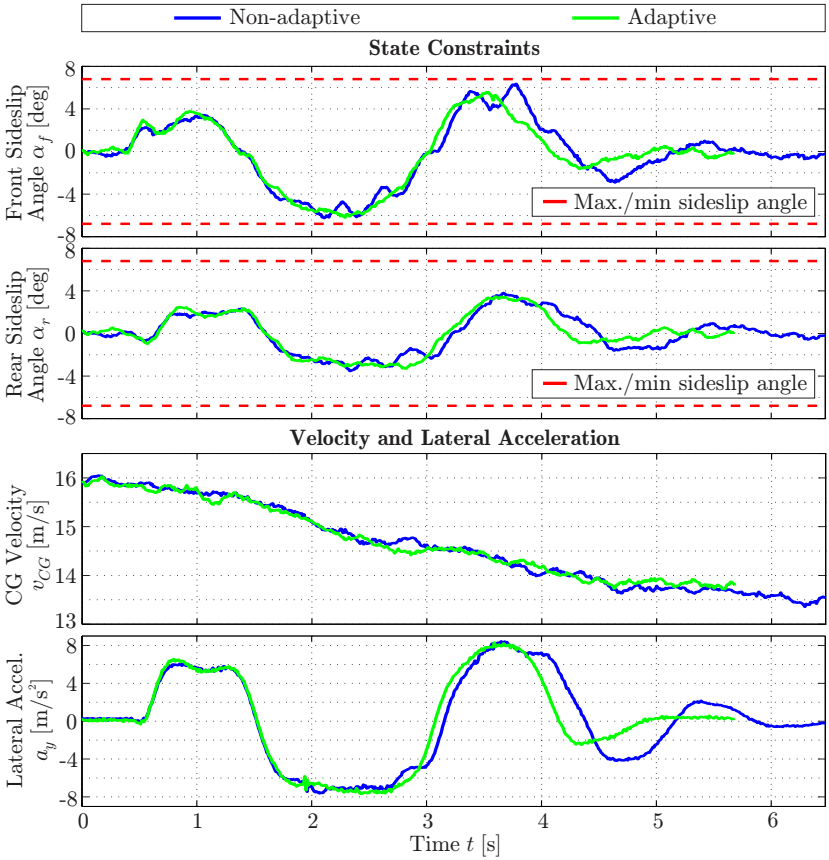

Figure 6.7: Experimental results for adaptive steering-only controller using OxTS RT3003: State constraints and vehicle states

applying the adaptive control scheme. The adaptation parameter θ_{F_y}, as it is used in the predictive control scheme, is additionally depicted in Figure 6.6. In this context, it has to be noted that θ_{F_y} is assigned to 1 in the nominal case to achieve non-adaptive controller behavior while θ_{F_y} (provided by the vehicle state estimator) actually differs from 1. For the adaptive case, it can be recognized that the adaptation pa-

rameter θ_{F_y} just converges to a value of 0.83 while the distortion of tire parameters corresponds to an interval of $1/2.5 = 0.4$ (maximum friction coefficient) to $1/1.5 = 0.66$ (nominal cornering stiffness). In the nominal case, θ_{F_y} (provided by the vehicle state estimator) actually converges to 0.44. When assessing the corresponding results of the vehicle state estimator, which have been omitted for reasons of clarity at this point, it has to be noted that the reference values are tracked noticeably better for this particular maneuver. Nevertheless, a recognizable gain in control performance can be achieved in the adaptive case although the adaptation is not as large as expected, thus demonstrating the potential of the proposed control scheme. With respect to Figure 6.7, it can finally be recognized that both control schemes are capable of fulfilling tire sideslip angle constraints.

6.3 Combined Longitudinal and Lateral Vehicle Guidance

6.3.1 Velocity Reference Generation

To evaluate the steering/braking control scheme, a velocity trajectory is required in addition to the evasion path that has been introduced in section 6.1. Therefore, the following scenario on a rural road with two lanes, oncoming traffic and a speed limit of 70 km/h is examined. The ego-vehicle is driving on a dry road ($\mu = 1$) with an initial velocity of $v_{CG} = 20\,\mathrm{m/s}$ when a non-moving broken vehicle occurs in the lane. At the same time, oncoming traffic on the other lane and a vehicle that is standing still on the same lane for a left turn (50 m behind the first obstacle) are part of the scenario, see Figure 6.8. For the evasion maneuver, the ego-vehicle has to evade the first obstacle as well as the oncoming traffic and has to decelerate to standstill before colliding with the turning vehicle. To evade the oncoming traffic and to follow the evasion path, the initial velocity is decreased by braking with $-5\,\mathrm{m/s^2}$ from $t = 0$ to 0.8 s and with $-1.5\,\mathrm{m/s^2}$ from $t = 0.8$ to 1.3 s when lateral accelerations increase. During this time interval, braking and steering are applied simultaneously to investigate the potential of the proposed

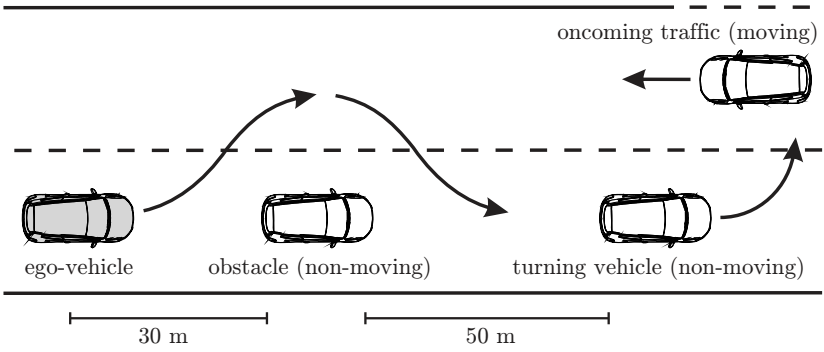

Figure 6.8: Steering/braking scenario

integrated vehicle dynamics control approach. From $t = 1.3$ to 3 s, no further braking is applied to complete the main part of the maneuver as fast as possible. Finally, the vehicle is decelerated to standstill while braking is initiated with $-2\,\mathrm{m/s^2}$ from $t = 3$ to 5 s when the vehicle approaches its original lane. For $t > 5\,\mathrm{s}$, the velocity is reduced to zero by braking with $-8\,\mathrm{m/s^2}$. The corresponding reference velocity trajectory $\boldsymbol{v}_{CG,ref}$ is gained by applying these accelerations in the corresponding time intervals neglecting further steering and rolling resistances.

Moreover, it has to be noted that an additional stop logic is required if the vehicle has to be decelerated to low velocities. The main reason can be seen in the fact that the controller assumes the vehicle to drive backward over the prediction horizon when the actual velocity decreases to far. Therefore, the reference velocity that is provided to the predictive controller is saturated such that it does not decrease further than 1 m/s. Furthermore, the deceleration is kept constant by the stop logic when standstill is detected at the end of the prediction horizon. To avoid numerical issues, the vehicle state and disturbance estimator as well as the predictive controller are disabled for velocities less than 2 m/s.

In the following, experimental control results are examined for the proposed integrated vehicle dynamics control scheme. As for the steering-only case, the same maneuver is conducted using the low-cost and the OxTS RT3003 navigation solution to assess the influence of navigation

Table 6.2: Steering/braking controller parameterization

Parameter	Value	Description
T_s	0.04 s	Sample time
H_u	15	Control horizon
H_p	25	Prediction horizon
$Q_{\Delta y}$	1	Weight on lateral displacement
$Q_{\Delta y,H_p}$	10	Terminal weight on lat. displacement
$Q_{v_{CG}}$	0.15	Weight on velocity
Q_{v_{CG},H_p}	1.5	Terminal weight on velocity
$R_{\delta_{ref}}$	200	Weight on change of δ_{ref}
$R_{a_{x,br,ref}}$	1	Weight on change of $a_{x,br,ref}$
ρ_f, ρ_r	1000	Weight on slack variables
$\delta_{ref,max/min}$	± 15 deg	Max./min. wheel steering angle δ_{ref}
$\Delta\delta_{ref,max/min}$	± 0.8 deg	Max./min. change of δ_{ref}
$a_{x,br,ref,max}$	$0g$	Max. braking acceleration
$a_{x,br,ref,min}$	$-1g$	Min. braking acceleration ($\mu = 1$)
$\Delta a_{x,br,ref,max}$	$1g$	Max. change of $a_{x,br,ref}$ ($\mu = 1$)
$\Delta a_{x,br,ref,max}$	$-1g$	Min. change of $a_{x,br,ref}$ ($\mu = 1$)

issues on the control performance. For the subsequent test scenario, the MPC parameters which are listed in Table 6.2 are used to parameterize the predictive controller.

6.3.2 Low-cost GNSS-based Control Results

Figure 6.9 illustrates the experimental results that have been gained in experimental tests when using the low-cost navigation solution. As far as the control outputs are concerned, a maximum absolute lateral deviation of 0.42 m and a RMSE of 0.20 m with respect to the low-cost navigation solution is obtained. According to the OxTS RT3003 reference sensor, a maximum absolute lateral deviation of 0.41 m and a RMSE of 0.20 m can be observed. Thereby, the maximum absolute difference between the estimated and reference path displacement is less than 0.20 m while stepwise changes are less than 0.05 m. As for

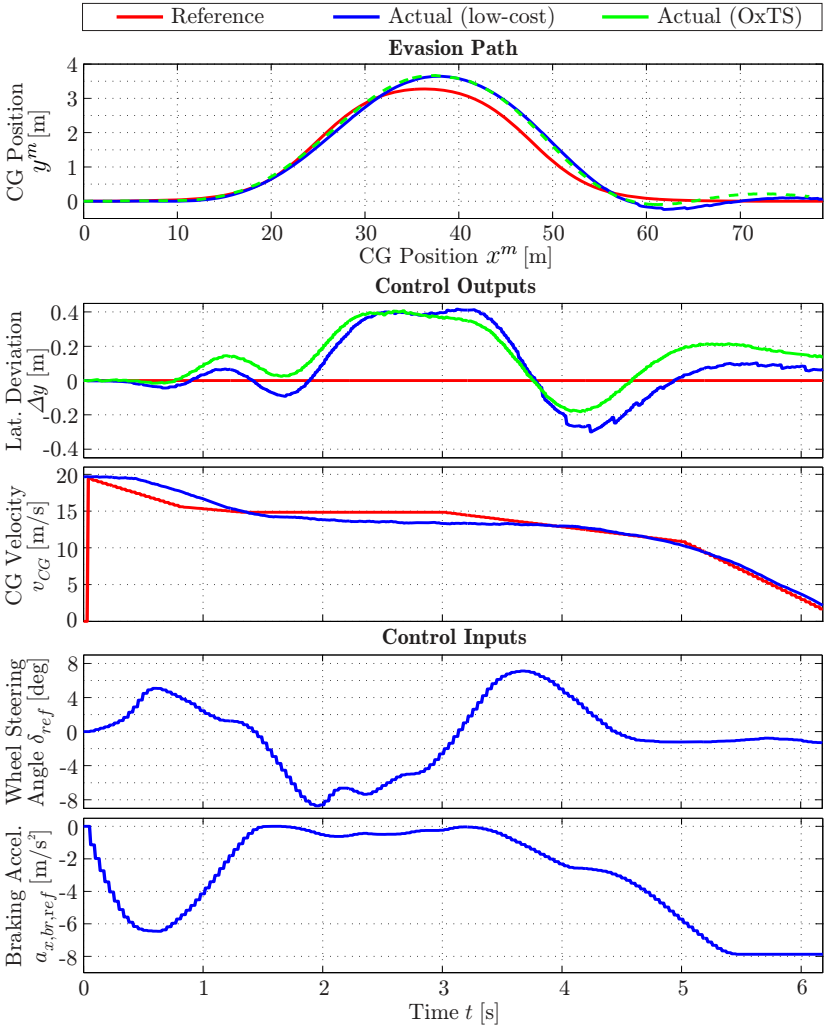

Figure 6.9: Experimental results for nominal steering/braking controller using low-cost navigation: Control inputs and outputs

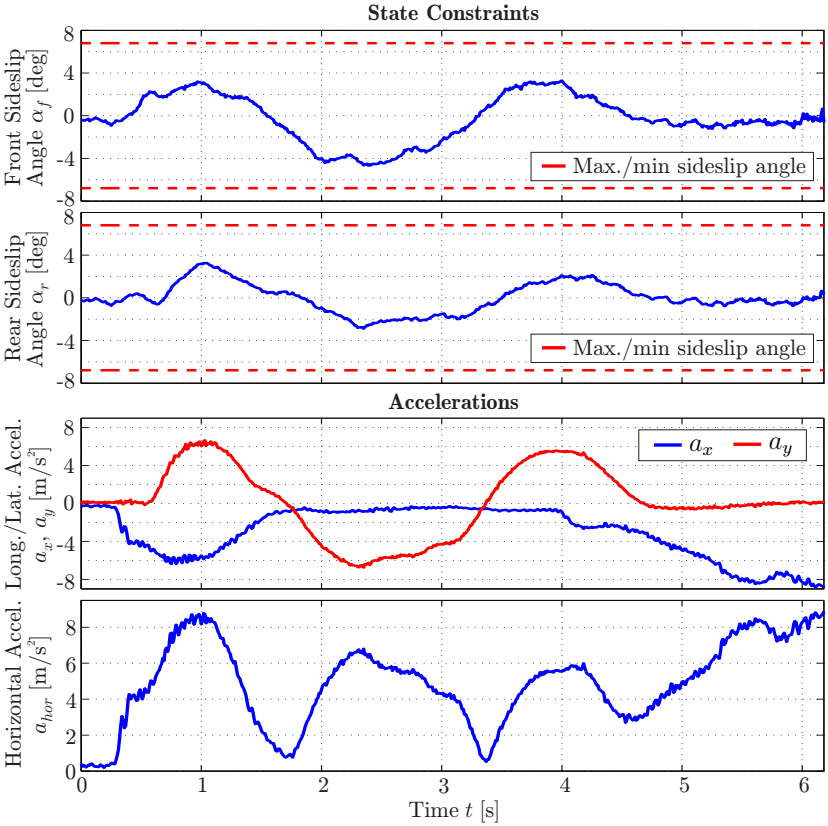

Figure 6.10: Experimental results for nominal steering/braking controller using low-cost navigation: State constraints and vehicle states

the steering-only control scheme, (relative) position accuracy as well as smoothness requirements according to section 3.2 are fulfilled for the entire maneuver. Moreover, the maximum error resulting from navigation and control amounts to 0.41 m and is thus significantly less than the maximum acceptable error. At the end of the maneuver, a small steady-state offset of 0.07 m can be recognized which can occur when the lateral displacement is not entirely compensated before the velocity

decreases too far. The absolute velocity v_{CG} at CG shows a maximum absolute tracking error of 1.53 m/s and a RMSE of 0.97 m/s. In this regard, the actual velocity v_{CG} is derived from the Correvit reference sensor measurements. The velocity errors as well as the delayed response of v_{CG} from $t = 0$ to 0.3 s are mainly caused by the initial buildup of the brake pressure and cannot be avoided, see section 2.2.2.2. As the controller is not able to accelerate, the velocity decreases from $t = 1.3$ to 3.3 s due to steering and rolling resistances. For $t \geq 3.3$, the velocity reference is tracked very well. With regard to section 6.3.1, it can be recognized that the maneuver ends at a velocity of about 2 m/s instead of standstill to avoid numerical issues.

During the maneuver, horizontal accelerations increase up to 8.8 m/s^2 when steering and braking is applied simultaneously which corresponds to the limits of vehicle dynamics, see Figure 6.10. Thereby, longitudinal accelerations have a magnitude of -8.8 m/s^2 while lateral accelerations are in the range of ± 6.8 m/s^2. At the same time, the controller is able to keep tire sideslip angles in the stable region of static friction. According to the main focus of this contribution, it can be concluded that the controller is able to guide the vehicle at the handling limits when combined steering and braking is applied (i.e. for $t = 0.5$ to 1.4 s) as well as in the nonlinear region of the (lateral) tire model (i.e. for $t = 1.9$ to 3.0 s and $t = 3.7$ to 4.0 s) while achieving a convincing control performance.

6.3.3 OxTS-based Control Results

Similar to the steering-only case, the same maneuver is performed using the OxTS RT3003 navigation solution to assess the gain in control performance when using the centimeter-precision navigation system. According to Figure 6.12, both maneuvers have an initial velocity of about 20 m/s and horizontal accelerations are approximately of the same magnitude. Thus, these maneuvers are considered to be suited for an appropriate assessment. The corresponding experimental control results are depicted in Figure 6.11. In particular, the maximum absolute lateral deviation can be reduced to 0.25 m and the RMSE to 0.12 m. Moreover, it can be noticed that the steady-state offset in the

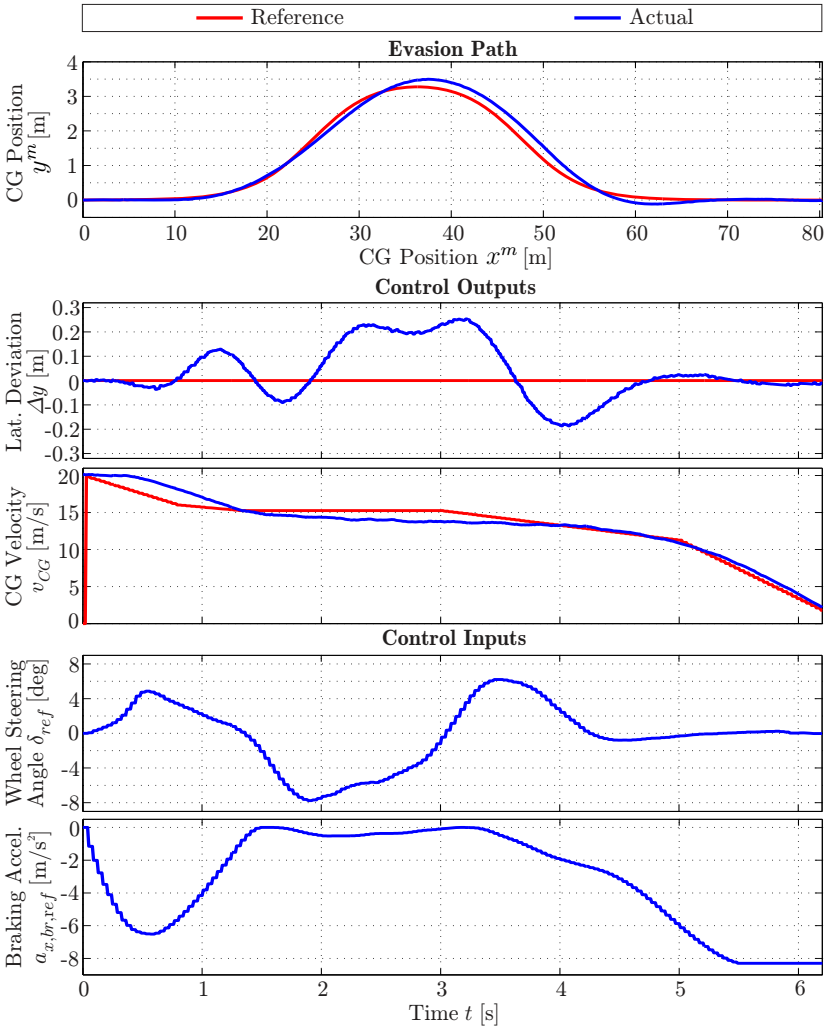

Figure 6.11: Experimental results for nominal steering/braking controller using OxTS RT3003: Control inputs and outputs

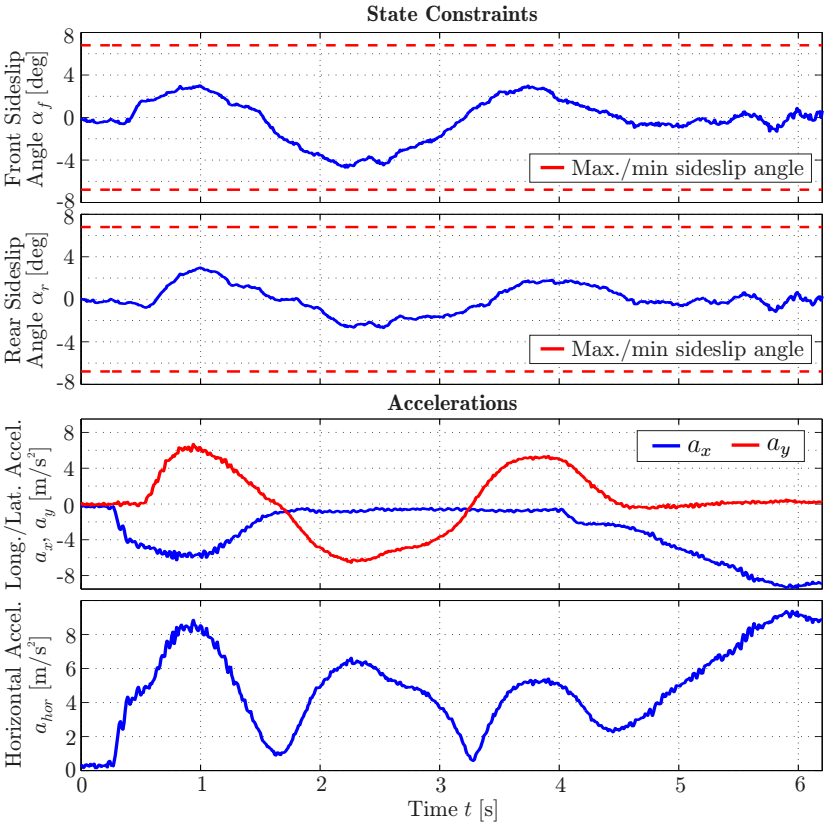

Figure 6.12: Experimental results for nominal steering/braking controller using OxTS RT3003: State constraints and vehicle states

lateral displacement at the end of the maneuver can indeed be avoided by employing the disturbance estimator. As the velocity v_{CG} at CG is derived from the vehicle state estimator's outputs whose inputs do not change when using the OxTS RT3003 (in both cases the estimator relies on the low-cost navigation solution), no significant difference in the velocity tracking error can be recognized compared to the preceding maneuver. In this regard, a maximum absolute velocity tracking error

of 1.55 m/s and a RMSE of 0.99 m/s are obtained. Similar to the preceding maneuver, the magnitude of the velocity tracking error and the delayed response of v_{CG} from $t = 0$ to 0.3 s originate from the initial buildup of the brake pressure and are unavoidable.

According to Figure 6.12, horizontal accelerations have a magnitude of $8.9\,\mathrm{m/s^2}$ when combined steering and braking is applied thus that the control scheme is evaluated at the vehicle handling limits. In this context, longitudinal accelerations have a magnitude of $-9.3\,\mathrm{m/s^2}$ while lateral accelerations are in the range of $\pm 6.7\,\mathrm{m/s^2}$. Thereby, the predictive controller is capable of keeping the tire sideslip angles in the region of static friction. As for the preceding maneuver, it can be concluded that the vehicle can be guided at the vehicle handling limits when steering and braking is applied simultaneously (i.e. for $t = 0.5$ to 1.5 s) as well as in the nonlinear region of the (lateral) tire model (i.e. for $t = 1.8$ to 2.8 s) while achieving a convincing control performance. Although a noticeable decrease of the lateral deviation can again be observed when employing the OxTS RT3003 navigation solution, autonomous vehicle guidance by steering and braking based on low-cost navigation has been approved to be feasible.

6.4 Assessment of Control Results

Table 6.3 summarizes the control results that have been obtained in experimental tests. Generally, it can be concluded that a further improvement in control performance can be gained when position errors decrease, i.e. when relying on the OxTS RT3003 reference sensor. Although experimental results show the sensitivity of the control performance on navigation issues, all the requirements that have been defined in section 3.2 are met for the steering-only as well as the steering/braking controller. Moreover, it has to be noted that this aim has been achieved for maneuvers with maximum horizontal accelerations of $8.4\,\mathrm{m/s^2}$ for the steering-only controller and $8.9\,\mathrm{m/s^2}$ for simultaneous steering and braking. The considered range of maximum horizontal accelerations is indeed a challenging task as far as navigation, vehicle state estimation and vehicle control is concerned. Particularly, the maximum

horizontal position error due to navigation and control issues is far less than the specified maximum admissible error of 1 m, i.e. 0.33 m in the steering-only and 0.41 m in the steering/braking case. Thus, the feasibility of low-cost GNSS-based autonomous evasion maneuvers has been demonstrated.

Additionally, the potential of applying an adaptive MPC-based control scheme, which has not been considered in previous publications, is examined. For experimental evaluations, tire parameters are distorted artificially by increasing the maximum friction coefficient as well as the nominal cornering stiffness. The particular parameterization can be interpreted as actually driving on a snow covered road while the controller assumes a dry road. Control results show that the maximum lateral displacement from the evasion path can be reduced by 17.6% while the RMSE is decreased by 17.1%. Thus, it is apparent that the adaptive control scheme has the potential to significantly improve the control performance when the nominal plant model is subject to uncertainties, especially in the tire-road contact.

Table 6.3: Overview of experimental control results

	Lat. dev. error $e_{\Delta y}$ [m]		Velocity error $e_{v_{CG}}$ [m/s]	
	Max.	RMSE	Max.	RMSE
Nominal steering-only controller				
Low-cost	0.33	0.18	-	-
OxTS	0.22	0.10	-	-
Adaptive steering-only controller				
Non-adapt.	0.74	0.35	-	-
Adaptive	0.61	0.29	-	-
Nominal steering/braking controller				
Low-cost	0.41	0.20	1.53	0.97
OxTS	0.25	0.12	1.55	0.99

7 Conclusion and Outlook

7.1 Conclusion

According to the new European road safety programme in 2010 [8], the number of road casualties is intended to be reduced by 50% until 2020. While passive safety systems like seat belts or constructive measures are already implemented in almost each vehicle, a special emphasis is put on ADAS which are supposed to contribute significantly to achieve this aim. In this regard, RWTH Aachen University conducts research on a GNSS-based CA system in the context of the project *Galileo above*. The system decides whether to warn the driver or intervene autonomously by an emergency braking respectively evasion maneuver when a collision with surrounding vehicles is imminent. Among the main research topics, this thesis focuses on the issues that are related to *navigation*, *vehicle state estimation* and *vehicle control*. Thereby, the feasibility of low-cost GNSS-based autonomous vehicle guidance at the handling limits in the context of autonomous evasion maneuvers is demonstrated.

In order to guide the vehicle autonomously, an appropriate navigation concept is required that supplies the vehicle's pose in terms of position, velocity and attitude. Thereby, the navigation solution has to fulfill requirements on accuracy, bandwidth, availability, integrity and smoothness. In this regard, this contribution assumes that the requirements regarding availability and integrity are always met. For the feasibility of autonomous evasion maneuvers, the upper bound of the admissible horizontal position error is assessed to be 0.5 m. As the low-cost navigation solution does not have the ability to fulfill this requirement when considering absolute positioning, relative positioning with respect to the initial maneuver position is investigated. Particularly, the navigation concept relies on a loosely coupled GNSS/INS integration concept that complements the properties of an INS (high update rate, sensor drift) and a GNSS (low update rate, no sensor drift). Moreover, a

real-time capable solution to cope with time delayed GNSS measurements according to [28] is introduced and an extension to aid and thus to improve the yaw angle estimate is proposed. Though, larger position errors and even disadvantageous discontinuities (stepwise changes in the horizontal position) can be observed when operating the vehicle at the handling limits. These errors are either caused by discontinuities in GNSS measurements or result from simplifications in the filter design (e.g. for real-time compensation of time delays). To solve this issue, it is proposed to decrease the weight on GNSS position and velocity measurements appropriately in the filter update step during the maneuver. Experimental results show that all the requirements on the navigation solution are satisfied and a convincing estimation performance is achieved. Particularly, a maximum horizontal position error of 0.24 m is obtained for a maneuver at the handling limits which is significantly less than the specified feasibility limit. Thus, the navigation concept is assessed to be appropriate for autonomous evasion maneuvers at the vehicle handling limits.

Besides an accurate and smooth navigation solution, drive dynamic states like the longitudinal and lateral velocity at CG as well as the yaw rate are essential to apply the considered optimal vehicle dynamics control schemes. For this purpose, an EKF-based vehicle state estimator is proposed which is able to cope with uncertainties in the tire-road contact. To achieve the adaptive behavior, two additional estimator states are introduced to scale tire forces if necessary. Thereby, the local observability of the estimation problem is a major issue. For this purpose, an approach to assess the local observability as well as to handle the loss of local observability online is introduced. Moreover, the horizontal velocity estimate, which is derived from the navigation solution and thus independent from wheel slip, is processed by the estimator as aiding measurement. In this way, classical and GNSS-based approaches that can be found in literature are combined. Experimental results prove the validity of the proposed concept for the nominal as well as the adaptive case.

To guide the vehicle autonomously along an a priori known evasion path respectively trajectory, a steering-only path following and a steering/braking trajectory following MPC-based control scheme is introduced. Both controllers are designed such that the vehicle can be guided

and stabilized in the nonlinear region of the tire model and even at the vehicle handling limits. For the steering-only controller, the inclusion of the vehicle state estimator's adaptation state θ_{F_y} to account for uncertainties in the tire-road contact is additionally investigated. Furthermore, the steering/braking controller is designed in the sense of an integrated vehicle dynamics control approach employing the wheel steering angle as well as the vehicle's deceleration as control inputs. Moreover, a disturbance estimator to compensate (relative) yaw angle offsets and thus steady-state offsets in the lateral displacement from the evasion path is proposed.

Finally, experimental control results for the steering-only as well as steering/braking control scheme using the low-cost navigation solution show a convincing control performance. For the steering-only control scheme, the adaptive case (i.e. when tire parameters are distorted artificially) is additionally investigated. Thereby, it is apparent that a noticeable improvement of the control performance can be achieved when the tire model is adapted online. Furthermore, the influence of navigation issues on the control performance is analyzed by using the OxTS RT3003 reference navigation system instead of the low-cost navigation solution. Particularly, it is obvious that a further improvement can be achieved when applying the centimeter-precision navigation solution. However, experimental control results demonstrate the feasibility of the proposed concept for low-cost GNSS-based evasion maneuvers at the vehicle handling limits in the context of CA that relies on the proposed navigation, vehicle state estimation and control algorithms.

7.2 Outlook

Although low-cost GNSS-based autonomous evasion maneuvers have been proven to be feasible, there is still future work left. In the following, a brief outline will be given for each field of research that has been considered in this contribution.

As far as navigation is concerned, further concepts to improve the GNSS time delay compensation for maneuvers with high horizontal accelerations have to be evaluated. In this way, a further improvement of the

(relative) position accuracy as well as the smoothness of the navigation solution might be gained. Moreover, the use of additional aiding measurements that originate from sensors like LiDARs, radars or cameras have to be considered to obtain an enhanced (relative) positioning accuracy, reliability and availability, see [63,64]. Furthermore, tight coupling integration schemes have to be taken into account when GNSS-denied environments like urban canyons become a potential field of operation. Finally, research has to be conducted in determining a reliable quality measure of the current position accuracy such that a safety margin can be incorporated into path planning algorithms. A first investigation in this direction has been carried out by the author in [6].

For the purpose of vehicle state estimation, a DEKF-based concept for estimating vehicle states and tire parameters in parallel is considered to be reasonable. Particularly, nominal tire parameters are intended to be identified during normal operation and fixed during an evasion maneuver while short-term uncertainties can still be compensated by the adaptation states θ_{F_x} and θ_{F_y}. Finally, filter reconfiguration has to be studied when the horizontal velocity estimate is assessed to have an insufficient accuracy due to long-term GNSS outages. This issue has been neglected in the scope of this contribution.

Regarding vehicle control, further investigations should take into account that the adaptive controller actually cannot prevent the tires from entering the region of sliding friction when the tire-road friction coefficient decreases, e.g. when changing from a dry to a wet road surface. In this case, the actual maximum tire sideslip angle will decrease to smaller values [22] while the predictive controller assumes it to be constant. Therefore, an online estimation of the physical tire sideslip limits and finally an online adaptation of the corresponding MPC constraints should be part of future work. For the steering/braking controller, it has to be analyzed whether an improved control performance can be gained when load transfer due to braking is additionally incorporated into the prediction model.

A Nomenclature

A.1 Symbols and Notations

Vehicle Dynamics and Relative Kinematics

m	Vehicle mass
J_z	Mass moment of inertia (vertical axis)
l_f, l_r	Distance between CG and front/rear axle
tw_f, tw_r	Front / rear track width
h_{CG}	Height of CG
g	Gravitational acceleration
μ	Maximum tire-road friction coefficient
T_δ	Dynamic time constant of steering system
$T_{a_{x,br}}$	Dynamic time constant of braking system
i_{br}	Brake force distribution front/rear axle
v_x	Longitudinal velocity at CG in veh. ref. frame
v_y	Lateral velocity at CG in veh. ref. frame
v_{CG}	Horizontal velocity at CG
β	Vehicle sideslip angle
$\dot{\psi}$	Yaw rate
ψ	Yaw angle
κ	Path curvature
$\Delta\psi$	Difference angle between vehicle and evasion path
Δy	Lateral displacement of CG from evasion path
$d_{\Delta\dot{y}}$	Lateral velocity disturbance
δ	Actual steering angle at the front axle
δ_{ref}	Demanded steering angle at the front axle
a_x	Actual longitudinal acceleration at CG
$a_{x,ref}$	Demanded acceleration at CG
$a_{x,br}$	Actual deceleration due to braking at CG
$a_{x,br,ref}$	Demanded deceleration due to braking at CG
a_y	Actual lateral acceleration at CG

$p_{bc,ref}$	Demanded brake pressure in main braking cylinder
v_f, v_r	Horizontal velocity at front/rear axle
v_{fl}, v_{fr}	Horizontal velocity at front left/right tire
v_{rl}, v_{rr}	Horizontal velocity at rear left/right tire
v_i^w	Horizontal velocity of wheel i in wheel ref. frame
$v_{i,free}^w$	Abs. velocity of free rolling front/rear left/right wheel
α_i	Sideslip angle at tire i
λ_i	Longitudinal tire slip at tire i
$F_{x,i}$	Applied longitudinal force at tire i
$F_{y,i}$	Applied lateral force at tire i
$F_{z,i}$	Vertical tire load at tire i
θ_x, θ_y	Adaptation variables to compensate model uncertainties
$B_{x,i}$, $B_{y,i}$	Pacejka parameter: slope at the origin
$C_{x,i}$, $C_{y,i}$	Pacejka parameter: shape factor
$D_{x,i}$, $D_{y,i}$	Pacejka parameter: max./min. tire force
$E_{x,i}$, $E_{y,i}$	Pacejka parameter: curvature near max./min. tire force

State Estimation

$\{\hat{\cdot}\}$	Estimated variable
$\{\bar{\cdot}\}$	Measured variable
$\{\cdot\}^-$	A priori estimation
$\{\cdot\}^+$	A posteriori estimation
$\boldsymbol{Q}$, $\boldsymbol{Q}_k$	Cont.-/discr.-time process noise cov. matrix
$\boldsymbol{R}$, $\boldsymbol{R}_k$	Cont.-/discr.-time measurement noise cov. matrix
$\boldsymbol{S}$, $\boldsymbol{S}_k$	Cont.-/discr.-time cross-cov. matrix
$\boldsymbol{P}_k$	Estimation error covariance matrix
$\boldsymbol{K}_k$	Kalman gain
$\boldsymbol{\mathcal{O}}_{nl}$	Observability matrix of nonlinear system
$\boldsymbol{\mathcal{O}}_{LTI}$	Observability matrix of LTI system
$\mathcal{L}_{\boldsymbol{f}}^j(\boldsymbol{h})$	j-th Lie derivative of $\boldsymbol{h}$ along vector field $\boldsymbol{f}$

Navigation

$\{\cdot\}_k^{k-n}$	Variable that is valid at time $k-n$ but avail. at time k
$\{\cdot\}_{ij}^{l}$	Variable describing a movement of the j-frame w.r.t. the i-frame in coordinates of the l-frame

$\boldsymbol{p}^e$	Position vector in e-frame
$\boldsymbol{p}^n$	Position vector in n-frame
$\boldsymbol{p}^m$	Position vector in m-frame
φ	Longitude (WGS84)
λ	Latitude (WGS84)
h	Altitude (WGS84)
$\boldsymbol{v}_{eb}^n$	Velocity vector in n-frame
$v_{eb,n}^n$	Velocity north in n-frame
$v_{eb,e}^n$	Velocity east in n-frame
$v_{eb,d}^n$	Velocity downwards in n-frame
ϕ	Roll angle
θ	Pitch angle
ψ	Yaw angle
ψ_{course}	GNSS course angle (direction of travel w.r.t. true north)
$\boldsymbol{\sigma}_i^j$	Vector describing rel. orientation of i- and j-frame
$\boldsymbol{q}_i^j$	Quaternion describing rel. orientation of i- and j-frame
$\boldsymbol{R}_i^j$	Direction cosine matrix transferring the i- to the j-frame
$\boldsymbol{b}_a$	Accelerometer biases
$\boldsymbol{b}_\omega$	Gyroscope biases
$\boldsymbol{f}_{ib}^b$	Specific force measured by IMU in b-frame
$\boldsymbol{f}_{ib}^{b,*}$	Bias compensated specific force
$\boldsymbol{\omega}_{ib}^b$	Angular rates measured by IMU in b-frame
$\boldsymbol{\omega}_{ib}^{b,*}$	Bias compensated angular rates
$\boldsymbol{r}_{IMU,A}^b$	Vector pointing from IMU to antenna in b-frame
$\boldsymbol{r}_{IMU,CG}^b$	Vector pointing from IMU to CG in b-frame
$\boldsymbol{\omega}_{ie}^n$	Earth rotation rate in n-frame
$\boldsymbol{\omega}_{en}^n$	Earth transportation rate in n-frame
$\boldsymbol{g}^n$	Gravity vector in n-frame
R_n	North-south radius of curvature of WGS84 ref. ellipsoid
R_e	East-west radius of curvature of WGS84 ref. ellipsoid

Vehicle State Estimation

$c_{F_x,thld}$	Cond. number threshold for observability of θ_{F_x}
$c_{F_y,thld}$	Cond. number threshold for observability of θ_{F_y}
$c_{F_x,F_y,thld}$	Cond. number threshold for observability of θ_{F_x} and θ_{F_y}

Optimal Vehicle Dynamics Control

$\{\cdot\}_{(k+j\|k)}$	Prediction of variable $\{\cdot\}$ at time $k+j$ when the actual sample time is k
ϵ_f, ϵ_r	Slack variables to soften sideslip angle constraints
ξ_{F_x}	Parameter to adjust max. longitudinal tire force
ξ_α	Parameter to adjust tire sideslip angle limits
$\boldsymbol{Q}$	Weight matrix/coefficient for controlled output(s)
$\boldsymbol{Q}_{H_p}$	Terminal cost on controlled output(s)
$\boldsymbol{R}$	Weight matrix for control input(s)
ρ_f, ρ_r	Weight coefficients for slack variables

A.2 Acronyms

ABS	Anti-lock Braking System
ADAS	Advanced Driver Assistance Systems
CAN	Controller Area Network
CA	Collision Avoidance
CM	Collision Mitigation
CW	Collision Warning
CFTOC	Constrained Finite Time Optimal Control
CG	Center of Gravity
DCM	Direction Cosine Matrix
DEKF	Dual Extended Kalman Filter
DR	Dead Reckoning
ECEF	Earth-Centered, Earth-Fixed
EGNOS	European Geostationary Navigation Overlay Service
ECU	Electronic Control Unit
EKF	Extended Kalman Filter
EPS	Electric Power Steering
ESC	Electronic Stability Control
ESS-KF	Error State Space Kalman Filter
FCW	Forward Collision Warning
GPS	Global Positioning System
GNSS	Global Navigation Satellite System
HPV	Hybrid Parameter-varying
IMU	Inertial Measurement Unit
INS	Inertial Navigation System
KF	Kalman Filter
LCCW	Lane Change Collision Warning
LTI	Linear Time-Invariant
LTV	Linear Time-Varying
LWM	Low-weight Measurement (Covariance Matrix)
MEMS	Micro-Electro-Mechanical Systems
MIMO	Multiple-Input Multiple-Output
MPC	Model Predictive Control
NMPC	Nonlinear Model Predictive Control
OxTS	Oxford Technical Systems
PF	Particle Filter

PI	Proportional-Integral
PID	Proportional-Integral-Derivative
QP	Quadratic Program
RMSE	Root Mean Square Error
RCP	Rapid Control Prototyping
RTK	Real-Time Kinematics
SPKF	Sigma-Point Kalman Filter
SISO	Single-Input Single-Output
TTC	Time to Collision
UAV	Unmanned Aerial Vehicle
UTC	Universal Time Coordinated
V2V	Vehicle-to-Vehicle
WGS84	World Geodetic System 1984

B Parameters of Experimental Setup

The following parameters are either given by construction or have been measured respectively identified in experimental tests.

Table B.1: Vehicle and tire parameters

Parameter	Value	Unit	Description
Vehicle Parameters			
m	2098	kg	Vehicle mass (full tank, 2 persons)
J_z	3639.3	$\mathrm{kg} \cdot \mathrm{m}^2$	Mass moment of inertia
l_f	1.35	m	Distance bw. CG and front axle
l_r	1.36	m	Distance bw. CG and rear axle
tw_f	1.55	m	Front track width
tw_r	1.56	m	Rear track width
h_{CG}	0.53	m	Height of CG
T_δ	0.15	s	Time constant steering system
$T_{a_{x,br}}$	0.15	s	Time constant braking system
Tire Parameters			
μ	1	-	Max. friction coefficient
$c_{\alpha,fl/fr}$	50	kN/rad	Cornering stiff. front left/right
$c_{\alpha,f}$	100	kN/rad	Cornering stiff. front axle
$c_{\alpha,rl/rr}$	50	kN/rad	Cornering stiff. rear left/right
$c_{\alpha,r}$	100	kN/rad	Cornering stiff. rear axle
$\alpha_{max/min}$	7	deg	Max./min. sideslip angle
$c_{\lambda,fl/fr}$	35	kN	Long. stiff. front left/right
$c_{\lambda,f}$	70	kN	Long. stiff. front axle
$c_{\lambda,rl/rr}$	35	kN	Long. stiff. rear left/right
$c_{\lambda,r}$	70	kN	Long. stiff. rear axle
$\lambda_{max/min}$	0.2	-	Max./min. long. slip

The sensor mounting positions refer to the definition of the navigation b-frame that is orientated forward, right and downwards.

Table B.2: Sensor mounting parameters

Parameter	Value	Unit	Description
$\boldsymbol{r}^b_{IMU,CG,x}$	1.44	m	Vector IMU to CG, x-coord.
$\boldsymbol{r}^b_{IMU,CG,y}$	0.05	m	Vector IMU to CG, y-coord.
$\boldsymbol{r}^b_{IMU,CG,z}$	0.10	m	Vector IMU to CG, z-coord.
$\boldsymbol{r}^b_{IMU,A,x}$	0.28	m	Vector IMU to antenna, x-coord.
$\boldsymbol{r}^b_{IMU,A,y}$	0.19	m	Vector IMU to antenna, y-coord.
$\boldsymbol{r}^b_{IMU,A,z}$	-0.88	m	Vector IMU to antenna, z-coord.

C Appendix to Navigation

In chapter 3, several issues have been omitted for reasons of clarity. The most relevant details that are necessary to comprehend the particular implementation are introduced subsequently in accordance to [28].

C.1 Direction Cosine Matrix

The relative orientation of two Cartesian reference frames can be expressed by the corresponding Euler angles. These angles describe three subsequent rotations to transfer one reference frame to the other. In order to transfer the i- to the j-frame, the z^i-axis is rotated by the yaw angle ψ, the resulting $y^{i'}$-axis by the pitch angle θ and finally the resulting $x^{i''}$-axis by the roll angle ϕ. These subsequent rotations can be formulated in terms of a direction cosine matrix (DCM), i.e.

$$\boldsymbol{R}_i^j = \boldsymbol{R}_{i,x}^j(\phi)\ \boldsymbol{R}_{i,y}^j(\theta)\ \boldsymbol{R}_{i,z}^j(\psi) \tag{C.1}$$

where

$$\boldsymbol{R}_{i,z}^j(\psi) = \begin{bmatrix} \cos\psi & -\sin\psi & 0 \\ \sin\psi & \cos\psi & 0 \\ 0 & 0 & 1 \end{bmatrix} \tag{C.2}$$

corresponds to the rotation with respect to the z^i-axis,

$$\boldsymbol{R}_{i,y}^j(\theta) = \begin{bmatrix} \cos\theta & 0 & \sin\theta \\ 0 & 1 & 0 \\ -\sin\theta & 0 & \cos\theta \end{bmatrix} \tag{C.3}$$

to the rotation with respect to the resulting $y^{i'}$-axis and

$$\boldsymbol{R}_{i,x}^j(\phi) = \begin{bmatrix} 1 & 0 & 0 \\ 0 & \cos\phi & -\sin\phi \\ 0 & \sin\phi & \cos\phi \end{bmatrix} \tag{C.4}$$

to the rotation with respect to the resulting $x^{i''}$-axis.

C.2 Quaternions

With respect to section 3.3.2, a major issue of Euler angles are singularities. To solve this issue, a common approach is the use of an orientation vector $\boldsymbol{\sigma}^T = [\sigma_x,\, \sigma_y,\, \sigma_z] \in \mathbb{R}^3$ which specifies the axis in the three dimensional space to transfer a reference frame to the other by a single rotation. Generally, this orientation vector is stored as a nomalized quaternion

$$\boldsymbol{q} = \begin{bmatrix} \cos(\|\boldsymbol{\sigma}\|/2) \\ (\sigma_x/\|\boldsymbol{\sigma}\|)\sin(\|\boldsymbol{\sigma}\|/2) \\ (\sigma_y/\|\boldsymbol{\sigma}\|)\sin(\|\boldsymbol{\sigma}\|/2) \\ (\sigma_z/\|\boldsymbol{\sigma}\|)\sin(\|\boldsymbol{\sigma}\|/2) \end{bmatrix}. \tag{C.5}$$

Subsequently, the most important quaternion operations and transformations that are used in the context of this contribution are introduced.

C.2.1 Quaternion Multiplication

Let $\boldsymbol{q}_1^T = [q_{1,a},\, q_{1,b},\, q_{1,c},\, q_{1,d}] \in \mathbb{R}^4$ and $\boldsymbol{q}_2^T = [q_{2,a},\, q_{2,b},\, q_{2,c},\, q_{2,d}] \in \mathbb{R}^4$ denote two quaternions. Then, the product $\circ$ of $\boldsymbol{q}_1$ and $\boldsymbol{q}_2$ is defined as

$$\boldsymbol{q}_1 \circ \boldsymbol{q}_2 = \begin{bmatrix} q_{1,a} \\ q_{1,b} \\ q_{1,c} \\ q_{1,d} \end{bmatrix} \circ \begin{bmatrix} q_{2,a} \\ q_{2,b} \\ q_{2,c} \\ q_{2,d} \end{bmatrix} \tag{C.6}$$

$$= \begin{bmatrix} q_{1,a} & -q_{1,b} & -q_{1,c} & -q_{1,d} \\ q_{1,b} & q_{1,a} & -q_{1,d} & q_{1,c} \\ q_{1,c} & q_{1,d} & q_{1,a} & -q_{1,b} \\ q_{1,d} & -q_{1,c} & q_{1,b} & q_{1,a} \end{bmatrix} \begin{bmatrix} q_{2,a} \\ q_{2,b} \\ q_{2,c} \\ q_{2,d} \end{bmatrix}. \tag{C.7}$$

C.2.2 Quaternion to Direction Cosine Matrix

Let $\boldsymbol{q}_i^{j,T} = [a,\, b,\, c,\, d] \in \mathbb{R}^4$ denote a quaternion that describes a rotation from the i- to the j-frame. For the corresponding direction cosine matrix

$\boldsymbol{R}_i^j(\boldsymbol{q}_i^j)$ holds

$$\boldsymbol{R}_i^j(\boldsymbol{q}_i^j) = \begin{bmatrix} a^2+b^2-c^2-d^2 & 2(bc-ad) & 2(bd+ac) \\ 2(bc+ad) & a^2-b^2+c^2-d^2 & 2(cd-ab) \\ 2(bd-ac) & 2(cd+ab) & a^2-b^2-c^2+d^2 \end{bmatrix}. \tag{C.8}$$

C.3 Skew Symmetric Matrix

For two vectors $\boldsymbol{a}^T = [a_x,\, a_y,\, a_z] \in \mathbb{R}^3$ and $\boldsymbol{b}^T = [b_x,\, b_y,\, b_z] \in \mathbb{R}^3$, the cross product $\boldsymbol{a} \times \boldsymbol{b}$ can be represented as matrix-vector multiplication, i.e.

$$\boldsymbol{a} \times \boldsymbol{b} = \boldsymbol{A} \cdot \boldsymbol{b} \tag{C.9}$$

where

$$\boldsymbol{A} = [\boldsymbol{a}\times] = \begin{bmatrix} 0 & -a_z & a_y \\ a_z & 0 & -a_x \\ -a_y & a_x & 0 \end{bmatrix}. \tag{C.10}$$

C.4 Model Equations

In section 3.5.1, the linear time-continuous model equations of the error estimator have not entirely been specified for reasons of clarity. As various implementations can be found in literature, an overview of the particular model equations without considering aided heading is provided subsequently. With respect to [28], the estimator model of a

loosely coupled GNSS/INS integration scheme is specified as follows

$$\underbrace{\frac{d}{dt}\begin{bmatrix}\delta\boldsymbol{p}^n\\ \delta\boldsymbol{v}^n_{eb}\\ \delta\boldsymbol{\epsilon}\\ \delta\boldsymbol{b}_a\\ \delta\boldsymbol{b}_\omega\end{bmatrix}}_{\delta\boldsymbol{x}(t)} = \underbrace{\begin{bmatrix}\boldsymbol{F}_{p,p} & \boldsymbol{I} & \boldsymbol{0} & \boldsymbol{0} & \boldsymbol{0}\\ \boldsymbol{F}_{v,p} & \boldsymbol{F}_{v,v} & \boldsymbol{F}_{v,\epsilon} & -\boldsymbol{R}^n_b & \boldsymbol{0}\\ \boldsymbol{F}_{\epsilon,p} & \boldsymbol{F}_{\epsilon,v} & \boldsymbol{F}_{\epsilon,\epsilon} & \boldsymbol{0} & -\boldsymbol{R}^n_b\\ \boldsymbol{0} & \boldsymbol{0} & \boldsymbol{0} & \boldsymbol{0} & \boldsymbol{0}\\ \boldsymbol{0} & \boldsymbol{0} & \boldsymbol{0} & \boldsymbol{0} & \boldsymbol{0}\end{bmatrix}}_{\boldsymbol{F}}\underbrace{\begin{bmatrix}\delta\boldsymbol{p}^n\\ \delta\boldsymbol{v}^n_{eb}\\ \delta\boldsymbol{\epsilon}\\ \delta\boldsymbol{b}_a\\ \delta\boldsymbol{b}_\omega\end{bmatrix}}_{\delta\boldsymbol{x}(t)} + \underbrace{\begin{bmatrix}\boldsymbol{0} & \boldsymbol{0} & \boldsymbol{0} & \boldsymbol{0}\\ -\boldsymbol{R}^n_b & \boldsymbol{0} & \boldsymbol{0} & \boldsymbol{0}\\ \boldsymbol{0} & -\boldsymbol{R}^n_b & \boldsymbol{0} & \boldsymbol{0}\\ \boldsymbol{0} & \boldsymbol{0} & \boldsymbol{I} & \boldsymbol{0}\\ \boldsymbol{0} & \boldsymbol{0} & \boldsymbol{0} & \boldsymbol{I}\end{bmatrix}}_{\boldsymbol{G}}\underbrace{\begin{bmatrix}\boldsymbol{n}_a\\ \boldsymbol{n}_\omega\\ \boldsymbol{n}_{b_a}\\ \boldsymbol{n}_{b_\omega}\end{bmatrix}}_{\boldsymbol{w}(t)} \tag{C.11}$$

$$\underbrace{\begin{bmatrix}\delta\boldsymbol{p}^n_A\\ \delta\boldsymbol{v}^n_{eA}\end{bmatrix}}_{\delta\boldsymbol{y}(t)} = \underbrace{\begin{bmatrix}\boldsymbol{I} & \boldsymbol{0} & \boldsymbol{H}_{p,\epsilon} & \boldsymbol{0} & \boldsymbol{0}\\ \boldsymbol{0} & \boldsymbol{I} & \boldsymbol{H}_{v,\epsilon} & \boldsymbol{0} & \boldsymbol{H}_{v,b_\omega}\end{bmatrix}}_{\boldsymbol{H}}\underbrace{\begin{bmatrix}\delta\boldsymbol{p}^n\\ \delta\boldsymbol{v}^n_{eb}\\ \delta\boldsymbol{\epsilon}\\ \delta\boldsymbol{b}_a\\ \delta\boldsymbol{b}_\omega\end{bmatrix}}_{\delta\boldsymbol{x}(t)} + \underbrace{\begin{bmatrix}\boldsymbol{n}_p\\ \boldsymbol{n}_v\end{bmatrix}}_{\boldsymbol{v}(t)}. \tag{C.12}$$

where $\boldsymbol{0}$ and $\boldsymbol{I}$ denote the zero matrix and the identity matrix of appropriate dimension. In accordance to [28], the following submatrices $\boldsymbol{F}_{i,j}$ of the system matrix $\boldsymbol{F}$ are employed in the scope of this contribution

$$\boldsymbol{F}_{p,p} = \begin{bmatrix}0 & 0 & \frac{v^n_{eb,n}}{R_n - h}\\ \frac{v^n_{eb,e}\tan(\phi)}{R_n - h} & 0 & \frac{v^n_{eb,e}}{R_e - h}\\ 0 & 0 & 0\end{bmatrix} \tag{C.13}$$

$$\boldsymbol{F}_{v,p} = [\boldsymbol{v}^n_{eb}\times](2\cdot\boldsymbol{F}_1 + \boldsymbol{F}_2)\boldsymbol{F}_3 \tag{C.14}$$

$$\boldsymbol{F}_{v,v} = -(2\cdot[\boldsymbol{\omega}^n_{ie}\times] + [\boldsymbol{\omega}^n_{en}\times] + [\boldsymbol{v}^n_{eb}\times]\boldsymbol{F}_4 \tag{C.15}$$

$$\boldsymbol{F}_{v,\epsilon} = -[\boldsymbol{R}^n_b\boldsymbol{f}^b_{ib}\times] \tag{C.16}$$

$$\boldsymbol{F}_{\epsilon,p} = -(\boldsymbol{F}_1 + \boldsymbol{F}_2)\boldsymbol{F}_3 \tag{C.17}$$

$$\boldsymbol{F}_{\epsilon,v} = -\boldsymbol{F}_4 \tag{C.18}$$

$$\boldsymbol{F}_{\epsilon,\epsilon} = -[(\boldsymbol{\omega}^n_{ie} + \boldsymbol{\omega}^n_{en})\times] \tag{C.19}$$

where

$$\boldsymbol{\omega}_{ie}^{n,T} = [\Omega\cos(\varphi),\ 0,\ -\Omega\sin(\varphi)] \tag{C.20}$$

denotes the earth rotation rate,

$$\boldsymbol{\omega}_{en}^{n,T} = \left[\frac{v_{eb,e}^{n}}{R_e - h},\ -\frac{v_{eb,n}^{n}}{R_n - h},\ -\frac{v_{eb,e}^{n}\tan(\varphi)}{R_e - h}\right] \tag{C.21}$$

the transport rate, Ω the angular earth rotation rate, R_n the north-south and R_e the east-west radius of curvature of the WGS84 earth reference ellipsoid. The particular definition of R_n and R_e can be found in [28]. For the auxiliary matrices $\boldsymbol{F}_i$ holds

$$\boldsymbol{F}_1 = \begin{bmatrix} -\Omega\sin(\varphi) & 0 & 0 \\ 0 & 0 & 0 \\ -\Omega\cos(\varphi) & 0 & 0 \end{bmatrix} \tag{C.22}$$

$$\boldsymbol{F}_2 = \begin{bmatrix} 0 & 0 & \frac{v_{eb,e}^{n}}{(R_e-h)^2} \\ 0 & 0 & -\frac{v_{eb,n}^{n}}{(R_n-h)^2} \\ \frac{v_{eb,e}^{n}}{(R_e-h)\cos^2(\varphi)} & 0 & \frac{v_{eb,e}^{n}\tan(\varphi)}{(R_e-h)^2} \end{bmatrix} \tag{C.23}$$

$$\boldsymbol{F}_3 = \begin{bmatrix} \frac{1}{R_n-h} & 0 & 0 \\ 0 & \frac{1}{(R_e-h)\cos(\varphi)} & 0 \\ 0 & 0 & 1 \end{bmatrix} \tag{C.24}$$

$$\boldsymbol{F}_4 = \begin{bmatrix} 0 & \frac{1}{R_e-h} & 0 \\ -\frac{1}{R_n-h} & 0 & 0 \\ 0 & -\frac{\tan(\varphi)}{R_e-h} & 0 \end{bmatrix} \tag{C.25}$$

As far as the measurement equations are concerned, for the matrices $\boldsymbol{H}_{i,j}$ the following definition is used in the scope of this thesis

$$\boldsymbol{H}_{p,\epsilon} = -[\boldsymbol{R}_b^n \boldsymbol{r}_{IMU,A}^b \times] \tag{C.26}$$

$$\boldsymbol{H}_{v,\epsilon} = -[\boldsymbol{R}_b^n \boldsymbol{\Omega}_{ib}^{b,*} \boldsymbol{r}_{IMU,A}^b \times] \tag{C.27}$$

$$\boldsymbol{H}_{v,b_\omega} = \boldsymbol{R}_b^n [\boldsymbol{r}_{IMU,A}^b \times] \tag{C.28}$$

where

$$\boldsymbol{\Omega}_{ib}^{b,*} = [\boldsymbol{\omega}_{ib}^{b,*} \times] = [(\boldsymbol{\omega}_{ib}^{b} - \boldsymbol{b}_\omega) \times]. \tag{C.29}$$

denotes the skew matrix of the bias compensated angular rate measurement. Finally, the state variables have to be substituted by the current state estimate $\hat{\boldsymbol{x}}$ to obtain the Jacobian of the system matrix $\boldsymbol{F}$, measurement matrix $\boldsymbol{H}$ and process noise matrix $\boldsymbol{G}$ at the current operating point.

C.5 Filter Parameterization

The time-continuous process noise covariance matrix $\boldsymbol{Q}$ and measurement noise covariance matrix $\boldsymbol{R}_i$ with $i \in \{nom, lw\}$ (nominal and low weight measurement noise covariance matrix) are diagonal matrices having the variance of the noise terms on its main diagonal, i.e.

$$\boldsymbol{Q} = \mathrm{diag}(\boldsymbol{\sigma}^2_{Q,n_a}, \boldsymbol{\sigma}^2_{Q,n_\omega}, \boldsymbol{\sigma}^2_{Q,n_{b_a}}, \boldsymbol{\sigma}^2_{Q,n_{b_\omega}}), \tag{C.30}$$

$$\boldsymbol{R}_i = \mathrm{diag}(\boldsymbol{\sigma}^2_{Q,p}, \boldsymbol{\sigma}^2_{Q,v}, \sigma^2_{Q,\psi_{course}}). \tag{C.31}$$

The process noise standard deviations σ_j that have been derived from sensor specification respectively have been optimized in experimental test are summarized in Table C.1.

Table C.1: Navigation filter process noise standard deviations

Symbol	Standard deviation of	Value
$\boldsymbol{\sigma}_{Q,n_a}$	Acceleration noise (each axis)	$5 \cdot 10^{-2}$
$\boldsymbol{\sigma}_{Q,n_\omega}$	Angular rate noise (each axis)	$1 \cdot 10^{-1} \cdot \pi/180$
$\boldsymbol{\sigma}_{Q,n_{b_a}}$	Acceleration bias noise (each axis)	$5 \cdot 10^{-3}$
$\boldsymbol{\sigma}_{Q,n_{b_\omega}}$	Angular rate bias noise (each axis)	$5 \cdot 10^{-3} \cdot \pi/180$

In order to fulfill the requirements on the navigation solution for autonomous evasion maneuvers, a nominal and a low-weight measurement noise covariance matrix $\boldsymbol{R}_{nom}$ and $\boldsymbol{R}_{lw}$ are employed in the navigation concept. Their corresponding standard deviations are listed in Table C.2.

Table C.2: Navigation filter measurement noise standard deviations

Symbol	Standard deviation of	Value (nom)	Value (lw)
$\boldsymbol{\sigma}_{Q,p}$	Position (λ,φ,h)	(0.5, 0.5, 1)	(10, 10, 10)
$\boldsymbol{\sigma}_{Q,v}$	Velocity (each axis)	$5 \cdot 10^{-2}$	1
$\sigma_{Q,\psi_{course}}$	GNSS course angle	$0.5 \cdot \pi/180$	$0.5 \cdot \pi/180$

As the EKF is a discrete-time filter, the covariance matrices $\boldsymbol{R}_i$ and $\boldsymbol{Q}$ have to be transferred to a discrete-time representation as well. While the discrete-time measurement noise covariance matrix $\boldsymbol{R}_{i,k}$ is equal to $\boldsymbol{R}_i$, the discrete-time process noise covariance matrix $\boldsymbol{Q}_k$ is gained when dividing $\boldsymbol{Q}$ by the estimator's sample time T_s, i.e. $\boldsymbol{Q}_k = \boldsymbol{Q}/T_s$.

As far as the aided heading estimation is concerned, a horizontal velocity threshold $v_{hor,thld}$ of 2 m/s and an absolute yaw rate threshold $\dot{\psi}_{thld}$ of 2 deg/s have been applied for all the experimental tests.

D Appendix to Vehicle State Estimation

D.1 Filter Parameterization

The time-continuous process noise covariance matrix $\boldsymbol{Q}$ and measurement noise covariance matrix $\boldsymbol{R}$ are diagonal matrices having the variance of the noise terms on its main diagonal, i.e.

$$\boldsymbol{Q} = \mathrm{diag}(\sigma^2_{Q,\delta},\, \boldsymbol{\sigma}^2_{Q,v^w},\, \sigma^2_{Q,a_x},\, \sigma^2_{Q,a_y},\, \sigma^2_{Q,\theta_{F_x}},\, \sigma^2_{Q,\theta_{F_y}}), \tag{D.1}$$

$$\boldsymbol{R} = \mathrm{diag}(\sigma^2_{R,a_x},\, \sigma^2_{R,a_y},\, \sigma^2_{R,\dot{\psi}},\, \sigma^2_{R,v_{CG}},\, \sigma^2_{R,\theta_{F_x}},\, \sigma^2_{R,\theta_{F_y}}). \tag{D.2}$$

The standard deviations σ_i that have been obtained in experimental tests are summarized in Table D.1.

Table D.1: Vehicle state estimator standard deviations

Symbol	Standard deviation of	Value
$\sigma_{Q,\delta}$	Wheel steering angle	$5 \cdot 10^{-3} \cdot \pi/180$
$\boldsymbol{\sigma}_{Q,v^w}$	Wheel velocities (each wheel)	$1 \cdot 10^{-1}$
σ_{Q,a_x}	Longitudinal acceleration	$5 \cdot 10^{-1}$
σ_{Q,a_y}	Lateral acceleration	$5 \cdot 10^{-1}$
$\sigma_{Q,\theta_{F_x}}$	Adaptation state θ_{F_x}	$1 \cdot 10^{-3}$
$\sigma_{Q,\theta_{F_y}}$	Adaptation state θ_{F_y}	$1 \cdot 10^{-2}$
σ_{R,a_x}	Longitudinal acceleration	$5 \cdot 10^{-1}$
σ_{R,a_y}	Lateral acceleration	$5 \cdot 10^{-1}$
$\sigma_{R,\dot{\psi}}$	Yaw rate	$1 \cdot 10^{-1} \cdot \pi/180$
$\sigma_{R,v_{CG}}$	Horizontal velocity	$1 \cdot 10^{-2}$
$\sigma_{R,\theta_{F_x}}$	Virtual measurement θ_{F_x}	$1 \cdot 10^{-5}$
$\sigma_{R,\theta_{F_y}}$	Virtual measurement θ_{F_y}	$1 \cdot 10^{-5}$

As the EKF is a discrete-time filter, the covariance matrices $\boldsymbol{R}$ and $\boldsymbol{Q}$ have to be transferred to a discrete-time representation as well. While the discrete-time measurement noise covariance matrix $\boldsymbol{R}_k$ is equal to $\boldsymbol{R}$, the discrete-time process noise covariance matrix $\boldsymbol{Q}_k$ is gained when dividing $\boldsymbol{Q}$ by the estimator's sample time T_s, i.e. $\boldsymbol{Q}_k = \boldsymbol{Q}/T_s$.

Due to the fact that the longitudinal acceleration a_x and lateral acceleration a_y are contained in the input and measurement vector, the assumption of uncorrelated input and measurement noise, i.e. $E[\boldsymbol{w}\boldsymbol{v}^T] = \boldsymbol{0}$, is no longer fulfilled and has to be accounted for in the filter equations, see section 4.5. Therefore, the cross-covariance matrix $\boldsymbol{S}_k = E[\boldsymbol{w}_k\boldsymbol{v}_k^T]$ has been introduced. In $\boldsymbol{S}_k$, only the entries that specify the covariance $E[w_{a_x,k}v_{a_x,k}]$ respectively $E[w_{a_y,k}v_{a_y,k}]$ are different from zero and are approximated by

$$E[w_{a_x,k}v_{a_x,k}] = \sigma_{Q_k,a_x} \cdot \sigma_{R_k,a_x}, \tag{D.3}$$

$$E[w_{a_y,k}v_{a_y,k}] = \sigma_{Q_k,a_y} \cdot \sigma_{R_k,a_y}. \tag{D.4}$$

The observability thresholds that are used to assess the local observability of θ_{F_x}, θ_{F_y} or both adaptation states at the same time are given in Table D.2.

Table D.2: Observability thresholds

Symbol	Threshold to assess that	Value
$c_{F_x,F_y,thld}$	θ_{F_x} and θ_{F_y} are locally observable	80
$c_{F_x,thld}$	Only θ_{F_x} is locally observable	30
$c_{F_y,thld}$	Only θ_{F_y} is locally observable	150

E Appendix to Optimal Vehicle Dynamics Control

E.1 Sideslip Angle Limits for Steering-only Controller

For the steering-only controller, the maximum value of ξ_α can be derived in advance through a conservative deduction such that the linearization coefficient of the actual wheel steering angle δ does not change its sign when linearizing the lateral and yaw momentum (5.2)-(5.3) close to $\alpha_{f,PMF,max/min}$. To determine ξ_α as large as possible, the linearization of (5.2)-(5.3) with respect to the wheel steering angle δ has to be investigated. In this regard, the longitudinal momentum (5.1) can be neglected in the subsequent considerations as the linearization coefficient of the wheel steering angle just influences the resistance due to steering and will not cause any false control actions when changing its sign. Consecutively, the term $F_{y,f}\cos\delta$ in (5.2)-(5.3), is crucial to determine the maximum value of ξ_α. Particularly, linearizing $F_{y,f}\cos\delta$ at the operating point $(\boldsymbol{x}_0,\, u_0)$ with respect to δ yields

$$\begin{aligned} c_\delta &= \left.\frac{\partial F_{y,f}\cos(\delta)}{\partial\delta}\right|_{\boldsymbol{x}_0} \\ &= \left.\frac{\partial F_{y,f}}{\partial\alpha_f}\frac{\partial\alpha_f}{\partial\delta}\right|_{\boldsymbol{x}_0}\cos(\delta_0) - F_{y,f}(\alpha_{f,0})\sin(\delta_0) \\ &= \left.\frac{\partial F_{y,f}}{\partial\alpha_f}\right|_{\boldsymbol{x}_0}\cos(\delta_0) - F_{y,f}(\alpha_{f,0})\sin(\delta_0). \end{aligned} \tag{E.1}$$

To prevent the controller from false control actions, ξ_α has to be determined such that $c_\delta > 0$ holds. While the first term in (E.1) is a monotonically increasing function in $\alpha_{f,0}$ for a constant wheel steering angle δ_0, the second term is a monotonically decreasing function

in α_f for a constant value of δ_0. For a conservative assessment of the maximum value of ξ_α such that $c_\delta > 0$, it is assumed that the maximum/minimum wheel steering angle δ according to input constraints (5.19f)-(5.19g) is currently applied. Then, the maximum/minimum tire sideslip angle $\alpha_{f,max/min,0}$ that causes $c_\delta = 0$ can be obtained by solving the nonlinear equation in $\alpha_{f,0}$

$$\begin{aligned} &\left.\frac{\partial F_{y,f}}{\partial \alpha_f}\right|_{\boldsymbol{x}_0} \cos(\delta_0) - F_{y,f}(\alpha_{f,0}) \sin(\delta_0) = 0 \\ \Leftrightarrow &\left.\frac{\partial f_{y,f}}{\partial \alpha_f}\right|_{\boldsymbol{x}_0} \cos(\delta_0) - f_{y,f}(\alpha_{f,0}) \sin(\delta_0) = 0 \end{aligned} \tag{E.2}$$

where $f_{y,i}$ denotes the normalized Pacejka Magic Formula. Thereby, it has to be noted that (E.2) can be solved unambiguously. Finally, ξ_α has to be chosen such that

$$\xi_\alpha < \frac{\alpha_{f,0,max}}{\alpha_{f,PMF,max}} = \frac{\alpha_{f,0,min}}{\alpha_{f,PMF,min}}. \tag{E.3}$$

where $\alpha_{f,PMF,max}$ and $\alpha_{f,PMF,min}$ indicate the maximum and minimum tire sideslip angle that correspond to the limit of static friction, see Figure 5.9. Besides the linearization coefficient of the wheel steering angle δ, it is also reasonable to consider the linearization coefficients of v_x, v_y and $\dot{\psi}$. As these change their sign or become zero for $\alpha_{f,0} \geq \alpha_{f,PMF,max}$ and $\alpha_{f,0} \leq \alpha_{f,PMF,min}$, the computation of ξ_α according to (E.3) is sufficient.

When linearizing the rear tire force $F_{y,r}$ in (5.2)-(5.3), it is also reasonable to prevent the corresponding linearization coefficients of v_x, v_y and $\dot{\psi}$ from becoming zero. Therefore, the maximum/minimum tire sideslip angle limit is chosen slightly less than $\alpha_{r,PMF,max}$ respectively larger than $\alpha_{r,PMF,min}$. As the resulting value of ξ_α according to (E.3) is always close to one, ξ_α is also employed in (5.53)-(5.54) to determine the upper and lower sideslip angle limits at the rear axle. Finally, it has to be stated that the preceding theoretical deduction of ξ_α is only valid for the steering-only controller. For the steering/braking control scheme, ξ_α has to be gained through experimental tests.

E.2 Disturbance Estimator Parameterization

The time-continuous process noise covariance matrix $\boldsymbol{Q}$ and measurement noise covariance matrix $\boldsymbol{R}$ are diagonal matrices having the variance of the noise terms on its main diagonal, i.e.

$$\boldsymbol{Q} = \begin{bmatrix} \sigma^2_{Q,\Delta\dot{\psi}} & 0 & 0 \\ 0 & \sigma^2_{Q,\Delta\dot{y}} & 0 \\ 0 & 0 & \sigma^2_{Q,\dot{d}_{\Delta\dot{y}}} \end{bmatrix}, \quad \boldsymbol{R} = \begin{bmatrix} \sigma^2_{R,\Delta\psi} & 0 \\ 0 & \sigma^2_{R,\Delta y} \end{bmatrix}. \tag{E.4}$$

The standard deviations σ_i that have been obtained in experimental tests are summarized in Table E.1.

Table E.1: Disturbance estimator standard deviations

Symbol	Standard deviation of	Value
$\sigma_{Q,\Delta\dot{\psi}}$	Relative yaw rate	$1 \cdot 10^{-3}$
$\sigma_{Q,\Delta\dot{y}}$	Relative lateral velocity	$1 \cdot 10^{-2}$
$\sigma_{Q,\dot{d}_{\Delta\dot{y}}}$	Lateral velocity disturbance	$1 \cdot 10^{-3}$
$\sigma_{R,\Delta\psi}$	Relative yaw angle	$2 \cdot 10^{-5}$
$\sigma_{R,\Delta y}$	Lateral displacement	$1 \cdot 10^{-4}$

As the EKF is a discrete-time filter, the covariance matrices $\boldsymbol{R}$ and $\boldsymbol{Q}$ have to be transferred to a discrete-time representation as well. While the discrete-time measurement noise covariance matrix $\boldsymbol{R}_k$ is equal to $\boldsymbol{R}$, the discrete-time process noise covariance matrix $\boldsymbol{Q}_k$ is gained when dividing $\boldsymbol{Q}$ by the estimator's sample time T_s, i.e. $\boldsymbol{Q}_k = \boldsymbol{Q}/T_s$.

Personal Publications

[1] A. Katriniok, M. Reiter, D. Abel, F. Christen, and L. Eckstein, "Collision Avoidance using Galileo - The automotiveGATE as Development and Testing Center for Galileo based Applications," in *Aachener Colloquium Automobile and Engine Technology*, 2010.

[2] A. Katriniok and D. Abel, "LTV-MPC Approach for Lateral Vehicle Guidance by Front Steering at the Limits of Vehicle Dynamics," in *IEEE Conference on Decision and Control and European Control Conference*, 2011, pp. 6828–6833.

[3] F. Christen, C. Ewald, L. Eckstein, D. Abel, A. Katriniok, and P. Duysinx, "Traffic Situation Assessment and Intervention Strategy of a Collision Avoidance System based on Galileo Satellite Positioning," in *SAE 2012 World Congress & Exhibition, SAE Technical Paper 2012-01-0280*, 2012.

[4] A. Katriniok, J. Yuan, and D. Abel, "Modellgestützte Prädiktive Regelung zur Fahrzeugquerführung mittels Lenk- und radselektiven Bremseingriffen," in *AUTOREG 2011 - Steuerung und Regelung von Fahrzeugen und Motoren*, 2011, pp. 209–220.

[5] A. Katriniok, J. P. Maschuw, F. Christen, L. Eckstein, and D. Abel, "Optimal Vehicle Dynamics Control for Combined Longitudinal and Lateral Autonomous Vehicle Guidance," in *IEEE European Control Conference*, 2013, pp. 974–979.

[6] A. Katriniok, J. P. Maschuw, D. Abel, F. Christen, and L. Eckstein, "Uncertainty Aware Sensor Fusion for a GNSS-based Collision Avoidance System," in *24th International Technical Meeting of The Satellite Division of the Institute of Navigation (ION GNSS 2011)*, 2011, pp. 968–978.

Bibliography

[7] European Commission / Directorate General Energy and Transport, "Road safety evolution in the EU," in *CARE (EU road accidents database)*, 2012.

[8] European Commission, "Towards a European road safety area: policy orientations on road safety 2011-2020," in *COM(2010) 389 final, Brussels*, 2010.

[9] Statistisches Bundesamt, Wiesbaden, "Verkehrsunfälle 2012," in *Fachserie 8, Reihe 7*, 2013.

[10] R. Isermann, R. Mannale, and K. Schmitt, "Collision-avoidance systems PRORETA: Situation analysis and intervention control," *Control Engineering Practice*, vol. 20, no. 11, pp. 1236–1246, 2012.

[11] R. Schubert, M. Schlingelhof, H. Cramer, and G. Wanielik, "Accurate Positioning for Vehicular Safety Applications - The SAFESPOT Approach," in *IEEE Vehicular Technology Conference*, april 2007, pp. 2506 –2510.

[12] P. Papadimitratos, A. La Fortelle, K. Evenssen, R. Brignolo, and S. Cosenza, "Vehicular communication systems: Enabling technologies, applications, and future outlook on intelligent transportation," *IEEE Communications Magazine*, vol. 47, no. 11, pp. 84–95, 2009.

[13] P. Falcone, F. Borrelli, J. Asgari, H. E. Tseng, and D. Hrovat, "Predictive Active Steering Control for Autonomous Vehicle Systems," *IEEE Transactions on Control Systems Technology*, vol. 15, no. 3, pp. 566–580, 2007.

[14] K. Zindler, S. Hahn, S. Zecha, and G. Jürgens, "Lateral Vehicle Control for Reproducible Tests of Safety Systems," *Automatisierungstechnik*, vol. 60, no. 2, pp. 61–73, 2012.

[15] M. Schorn, "Quer- und Längsregelung eines Personenkraftwagens für ein Fahrerassistenzsystem zur Unfallvermeidung," Ph.D. dissertation, TU Darmstadt, Institut für Automatisierungstechnik, 2007.

[16] J. A. Farrell, *Aided Navigation: GPS with High Rate Sensors*. McGraw Hill, 2008.

[17] D. Simon, *Optimal State Estimation: Kalman, H Infinity, and Nonlinear Approaches*. John Wiley & Sons, Inc., 2006.

[18] D. Bevly, J. Gerdes, C. Wilson, and G. Zhang, "The Use of GPS Based Velocity Measurements for Improved Vehicle State Estimation," in *Proceedings of the American Control Conference*, 2000, pp. 2538–2542.

[19] J. Maciejowski, *Predictive Control with Constraints*. Prentice Hall, Harlow, 2002.

[20] E. Camacho and C. Bordons, *Model predictive control*. Springer, 2007.

[21] P. Falcone, F. Borrelli, J. Asgari, H. Tseng, and D. Hrovat, "A model predictive control approach for combined braking and steering in autonomous vehicles," in *Mediterranean Conference on Control Automation*, 2007, pp. 1–6.

[22] M. Mitschke and H. Wallentowitz, *Dynamik der Kraftfahrzeuge*. Springer Verlag, 2004.

[23] R. Rajamani, *Vehicle Dynamics and Control*. Springer, 2005.

[24] H. Pacejka and E. Bakker, "The magic formular tire model," *Vehicle System Dynamics: International Journal of Vehicle Mechanics and Mobility*, vol. 21, no. 1, pp. 1–18, 1992.

[25] B. Johansson and M. Gäfvert, "Untripped SUV Rollover Detection and Prevention," in *IEEE Conference on Decision and Control*, 2004, pp. 5461–5466.

[26] u-Blox, *u-Blox 6 GPS Modules, LEA-6T Data Sheet, 2010*.

[27] B. W. Parkinson and J. J. Spilker, *Global Positioning System: Theory and Applications Volume I/II*. American Institute of Aeronautics & Astronautics (AAIA), 1996.

[28] J. Wendel, *Integrierte Navigationssysteme: Sensordatenfusion, GPS und Inertiale Navigation*. Oldenbourg Wissenschaftsverlag, 2011.

[29] P. D. Solomon, J. Wang, and C. Rizos, "Latency Determination and Compensation in Real-Time GNSS/INS Integrated Navigation Systems," in *Proceedings of the International Conference on Unmanned Aerial Vehicle in Geomatics (UAV-g)*, 2011.

[30] Oxford Technical Solutions, *RT3003, User Manual, 2011*.

[31] R. Toledo-Moreo, D. Betaille, and F. Peyret, "Lane-Level Integrity Provision for Navigation and Map Matching With GNSS, Dead Reckoning, and Enhanced Maps," *IEEE Transactions on Intelligent Transportation Systems*, vol. 11, no. 1, pp. 100 –112, 2010.

[32] P. Bonnifait, J. Laneurit, C. Fouque, and G. Dherbomez, "Multi-hypothesis map-matching using particle filtering," in *16th World Congress of ITS Systems and Services*, 2009.

[33] T. Herpel, C. Lauer, R. German, and J. Salzberger, "Multi-sensor data fusion in automotive applications," in *International Conference on Sensing Technology*, 2008, pp. 206–211.

[34] A. Amditis, A. Polychronopoulos, I. Karaseitanidis, G. Katsoulis, and E. Bekiaris, "Multiple sensor collision avoidance system for automotive applications using an IMM approach for obstacle tracking," in *Proceedings of the Fifth International Conference on Information Fusion*, vol. 2, 2002, pp. 812–817.

[35] C. Urmson, J. Anhalt, and D. Bagnell et al., "Autonomous driving in urban environments: Boss and the urban challenge," *Journal of Field Robotics: Special Issues on the 2007 DARPA Urban Challenge*, vol. 25, no. 8, pp. 425–466, 2008.

[36] C. Stiller, S. Kammel, I. Lulcheva, and J. Ziegler, "Probabilistic Methods for Environment Perception of Cognitive Automobiles," *at - Automatisierungstechnik*, vol. 56, no. 11, pp. 563–574, 2008.

[37] U. Stählin, "Eingriffsentscheidung für ein Fahrerassistenzsystem zur Unfallvermeidung," Ph.D. dissertation, TU Darmstadt, Institut für Automatisierungstechnik, 2008.

[38] J. Jansson and F. Gustafsson, "A framework and automotive application of collision avoidance decision making," *Automatica*, vol. 44, no. 9, pp. 2347–2351, 2008.

[39] T. Brandt, T. Sattel, and J. Wallaschek, "On Automatic Collision Avoidance Systems," in *SAE 2005 World Congress & Exhibition, SAE Technical Paper 2005-01-1479*, 2005.

[40] E. Bauer, F. Lotz, M. Pfromm, M. Schreier, S. Cieler, A. Eckert, A. Hohm, S. Lüke, P. Rieth, B. Abendroth, V. Willert, J. Adamy, B. Bruder, U. Konigorski, and H. Winner, "PRORETA 3: An Integrated Approach to Collision Avoidance and Vehicle Automation," *at - Automatisierungstechnik*, vol. 60, no. 12, pp. 755–765, 2012.

[41] P. Falcone, F. Borrelli, H. Tsengz, J. Asgari, and D. Hrovat, "A hierarchical model predictive control framework for autonomous ground vehicles," in *American Control Conference*, 2008, pp. 3719–3724.

[42] S. Anderson and S. Peters, "An optimal-control-based framework for trajectory planning, threat assessment, and semi-autonomous control of passenger vehicles in hazard avoidance scenarios," *International Journal of Vehicle Autonomous Systems*, vol. 8, pp. 190–216, 2010.

[43] S. Schmidt and R. Kasper, "A Hierarchical Approach to Optimal Path-Planning and Path Control for an Autonomous Vehicle," *at - Automatisierungstechnik*, vol. 60, no. 12, pp. 743–754, 2012.

[44] A. Gray, Y. Gao, T. Lin, J. Hedrick, H. Tseng, and F. Borrelli, "Predictive control for agile semi-autonomous ground vehicles using motion primitives," in *American Control Conference*, 2012, pp. 4239–4244.

[45] U. Franke, D. Gavrila, S. Gorzig, F. Lindner, F. Puetzold, and C. Wohler, "Autonomous driving goes downtown," *IEEE Intelligent Systems and their Applications*, vol. 13, no. 6, pp. 40–48, 1998.

[46] L. Huang and M. Barth, "A novel multi-planar LIDAR and computer vision calibration procedure using 2D patterns for automated

navigation," in *IEEE Intelligent Vehicles Symposium*, 2009, pp. 117–122.

[47] J. Goldbeck, B. Huertgen, S. Ernst, and L. Kelch, "Lane following combining vision and DGPS," *Image and Vision Computing*, vol. 18, no. 5, pp. 425 – 433, 2000.

[48] J. Becker and A. Simon, "Sensor and navigation data fusion for an autonomous vehicle," in *IEEE Intelligent Vehicles Symposium*, 2000, pp. 156–161.

[49] I. Skog and P. Handel, "In-Car Positioning and Navigation Technologies - A Survey," *IEEE Transactions on Intelligent Transportation Systems*, vol. 10, no. 1, pp. 4–21, 2009.

[50] M. Obst, E. Richter, and G. Wanielik, "Accurate Relative Localization for Land Vehicles with SBAS Corrected GPS/INS Integration and V2V Communication," in *24th International Technical Meeting of The Satellite Division of the Institute of Navigation (ION GNSS 2011)*, 2011.

[51] G. Elkaim, M. Lizarraga, and L. Pedersen, "Comparison of low-cost GPS/INS sensors for Autonomous Vehicle applications," in *IEEE/ION Position, Location and Navigation Symposium*, 2008, pp. 1133–1144.

[52] J. Santa, R. Toledo-Moreo, M. Zamora-Izquierdo, B. Úbeda, and A. Gómez-Skarmeta, "An analysis of communication and navigation issues in collision avoidance support systems," *Transportation Research Part C: Emerging Technologies*, vol. 18, no. 3, pp. 351 – 366, 2010.

[53] H.-S. Tan and J. Huang, "DGPS-Based Vehicle-to-Vehicle Cooperative Collision Warning: Engineering Feasibility Viewpoints," *IEEE Transactions on Intelligent Transportation Systems*, vol. 7, no. 4, pp. 415–428, 2006.

[54] S. Shladover and S.-K. Tan, "Analysis of Vehicle Positioning Accuracy Requirements for Communication-Based Cooperative Collision Warning," *Journal of Intelligent Transportation Systems: Technology, Planning, and Operations*, vol. 10, no. 3, pp. 131–140, 2006.

[55] M. Lu, K. Wevers, and R. Van Der Heijden, "Technical Feasibility of Advanced Driver Assistance Systems (ADAS) for Road Traffic Safety," *Transportation Planning and Technology*, vol. 28, no. 3, pp. 167–187, 2005.

[56] F. Wegman and M. Slop, "Safety Effects of Road Design Standards in Europe," *Transportation Research Circular*, pp. 1–10, 1998.

[57] R. van der Merwe and E. Wan, "Sigma-Point Kalman Filters for Integrated Navigation," in *Proceedings of the 60th Annual Meeting of The Institute of Navigation (ION)*, 2004.

[58] F. Gustafsson, F. Gunnarsson, N. Bergman, U. Forssell, J. Jansson, R. Karlsson, and P.-J. Nordlund, "Particle filters for positioning, navigation, and tracking," *IEEE Transactions on Signal Processing*, vol. 50, no. 2, pp. 425–437, 2002.

[59] J. C. Butcher, *Numerical Methods for Ordinary Differential Equations*. John Wiley & Sons, Inc., 2008.

[60] T. D. Larsen, N. A. Andersen, O. Ravn, and N. K. Poulsen, "Incorporation of Time Delayed Measurements in a Discrete-time Kalman Filter," in *IEEE Conference on Decision and Control*, 1998, pp. 3972–3977.

[61] Y. Li, A. Dempster, B. Li, J. Wang, and C. Rizos, "A low-cost attitude heading reference system by combination of GPS and magnetometers and MEMS inertial sensors for mobile applications," *Journal of Global Positioning Systems*, vol. 5, no. 1-2, pp. 88–95, 2006.

[62] J. Huang and H.-S. Tan, "A Low-Order DGPS-Based Vehicle Positioning System Under Urban Environment," *IEEE/ASME Transactions on Mechatronics*, vol. 11, no. 5, pp. 567–575, 2006.

[63] K. Krishnaswamy, S. Susca, R. McCroskey, P. Seiler, J. Lukas, O. Kotaba, V. Bageshwar, and S. Ganguli, "Sensor fusion for GNSS denied navigation," in *IEEE/ION Position, Location and Navigation Symposium*, 2008, pp. 541–551.

[64] A. Fernandez, M. Wis, F. Dovis, K. Ali, P. Silva, P. Friess, I. Colomina, E. Pares, and J. Lindenberger, "GNSS/INS/LiDAR integration in urban environment: Algorithm description and results from ATENEA test campaign," in *ESA Workshop on Satellite Navigation Technologies and European Workshop on GNSS Signals and Signal Processing, (NAVITEC)*, 2012, pp. 1–8.

[65] U. Kiencke and A. Deiß, "Observation of lateral vehicle dynamics," *Control Engineering Practice*, vol. 5, no. 8, pp. 1145 – 1150, 1997.

[66] A. von Vietinghoff, M. Hiemer, and U. Kiencke, "Nonlinear observer design for lateral vehicle dynamics," in *IFAC World Congress*, 2005.

[67] L. Imsland, T. A. Johansen, T. I. Fossen, H. F. Grip, J. C. Kalkkuhl, and A. Suissa, "Vehicle velocity estimation using nonlinear observers," *Automatica*, vol. 42, no. 12, pp. 2091 – 2103, 2006.

[68] M. Satria and M. C. Best, "Comparison Between Kalman Filter and Robust Filter for Vehicle Handling Dynamics State Estimation," in *SAE World Congress*, 2002.

[69] J. Dakhlallah, S. Glaser, S. Mammar, and Y. Sebsadji, "Tire-road forces estimation using extended Kalman filter and sideslip angle evaluation," in *American Control Conference*, 2008, pp. 4597–4602.

[70] L. R. Ray, "Nonlinear state and tire force estimation for advanced vehicle control," *IEEE Transactions on Control Systems Technology*, vol. 3, no. 1, pp. 117–124, 1995.

[71] L. R. Ray, "Nonlinear Tire Force Estimation and Road Friction Identification: Simulation and Experiments," *Automatica*, vol. 33, no. 10, pp. 1819–1833, 1997.

[72] M. C. Best, T. J. Gordon, and P. J. Dixon, "An Extended Adaptive Kalman Filter for Real-time State Estimation of Vehicle Handling Dynamics," *Vehicle System Dynamics*, vol. 34, no. 1, pp. 57–75, 2000.

[73] G. Baffet, A. Charara, and D. Lechner, "Estimation of vehicle sideslip, tire force and wheel cornering stiffness," *Control Engineering Practice*, vol. 17, no. 11, pp. 1255–1264, 2009.

[74] S.-H. You, J.-O. Hahn, and H. Lee, "New adaptive approaches to real-time estimation of vehicle sideslip angle," *Control Engineering Practice*, vol. 17, no. 12, pp. 1367–1379, 2009.

[75] H. F. Grip, L. Imsland, T. A. Johansen, T. I. Fossen, J. C. Kalkkuhl, and A. Suissa, "Nonlinear vehicle side-slip estimation with friction adaptation," *Automatica*, vol. 44, no. 3, pp. 611–622, 2008.

[76] T. A. Wenzel, K. J. Burnham, M. V. Blundell, and R. A. Williams, "Dual extended Kalman filter for vehicle state and parameter estimation," *Vehicle System Dynamics: International Journal of Vehicle Mechanics and Mobility*, vol. 44, no. 2, pp. 153–171, 2006.

[77] D. M. Bevly, J. C. Gerdes, and C. Wilson, "The Use of GPS Based Velocity Measurements for Measurement of Sideslip and Wheel Slip," *Vehicle System Dynamics: International Journal of Vehicle Mechanics and Mobility*, vol. 38, no. 2, pp. 127–147, 2003.

[78] D. M. Bevly, J. Ryu, and J. C. Gerdes, "Integrating INS Sensors With GPS Measurements for Continuous Estimation of Vehicle Sideslip, Roll, and Tire Cornering Stiffness," *IEEE Transactions on Intelligent Transportation Systems*, vol. 7, no. 4, pp. 483–493, 2006.

[79] J. Ryu and J. C. Gerdes, "Integrating Inertial Sensors With Global Positioning System (GPS) for Vehicle Dynamics Control," *Journal of Dynamic Systems, Measurement, and Control*, vol. 126, no. 2, pp. 243–254, 2004.

[80] L. Shampine and M. Reichelt, "The MATLAB ODE Suite," *SIAM journal on scientific computing: a publication of the Society for Industrial and Applied Mathematics*, vol. 18, pp. 1–22, 1997.

[81] R. Hermann and A. J. Krener, "Nonlinear controllability and observability," *IEEE Transactions on Automatic Control*, vol. 22, no. 5, pp. 728–740, 1977.

[82] F. Aghili, "3D SLAM using IMU and its observability analysis," in *International Conference on Mechatronics and Automation (ICMA)*, 2010, pp. 377–383.

[83] Z. Chen, "Local observability and its application to multiple measurement estimation," *IEEE Transactions on Industrial Electronics*, vol. 38, no. 6, pp. 491–496, 1991.

[84] K. Kritayakirana, "Autonomous vehicle control at the limits of handling," Ph.D. dissertation, Standford University, 2012.

[85] D. Kim, J. Kang, and K. Yi, "Control strategy for high-speed autonomous driving in structured road," in *International IEEE Conference on Intelligent Transportation Systems (ITSC)*, 2011, pp. 186–191.

[86] M. Werling, L. Gröll, and G. Bretthauer, "Trajectory Tracking of Time-Critical Driving Maneuvers," *at - Automatisierungstechnik*, vol. 60, no. 1, pp. 28–37, 2012.

[87] L. König, "Ein virtueller Testfahrer für den querdynamischen Grenzbereich," Ph.D. dissertation, University of Stuttgart, 2009.

[88] J. Guldner, V. Utkin, and J. Ackermann, "A sliding mode control approach to automatic car steering," in *American Control Conference*, vol. 2, 1994, pp. 1969–1973.

[89] D. Bernardini, S. Di Cairano, A. Bemporad, and H. Tseng, "Drive-by-wire vehicle stabilization and yaw regulation: a hybrid Model Predictive Control design," in *Decision and Control, 2009 held jointly with the 2009 28th Chinese Control Conference. CDC/CCC 2009. Proceedings of the 48th IEEE Conference on*, 2009, pp. 7621–7626.

[90] S. Di Cairano, H. Tseng, D. Bernardini, and A. Bemporad, "Vehicle Yaw Stability Control by Coordinated Active Front Steering and Differential Braking in the Tire Sideslip Angles Domain," *IEEE Transactions on Control Systems Technology*, vol. 21, no. 4, pp. 1236–1248, 2013.

[91] C. Beal and J. Gerdes, "Model Predictive Control for Vehicle Stabilization at the Limits of Handling," *IEEE Transactions on Control Systems Technology*, vol. 21, no. 4, pp. 1258–1269, 2013.

[92] T. Keviczky, P. Falcone, F. Borrelli, J. Asgari, and D. Hrovat, "Predictive control approach to autonomous vehicle steering," in *American Control Conference*, 2006, pp. 4670–4675.

[93] T. Besselmann and M. Morari, "Hybrid Parameter-varying Model Predictive Control for Autonomous Vehicle Steering," *European Journal of Control*, vol. 14, no. 5, pp. 418–431, 2008.

[94] L. Del Re, F. Allgöwer, L. Glielmo, C. Guardiola, and I. Kolmanovsky, *Automotive Model Predictive Control: Models, Methods and Applications*. Springer, 2010.

[95] S. Boyd and L. Vandenberghe, *Convex Optimization*. Cambridge University Press, 2004.

[96] J. Nocedal and S. J. Wright, *Numerical Optimization*. Springer, 2006.

[97] M. Morari and U. Maeder, "Nonlinear offset-free model predictive control," *Automatica*, vol. 48, no. 9, pp. 2059 – 2067, 2012.

[98] H. J. Ferreau, "qpOASES User's Manual (Version 3.0beta)," *Optimization in Engineering Center (OPTEC) and Department of Electrical Engineering, KU Leuven*, 2012.